Superwetting surfaces derived from sustainable materials for environmental and energy applications

by

Weinan Zhao

A thesis

presented to the University of Waterloo

in fulfillment of the

thesis requirement for the degree of

Doctor of Philosophy

in

Chemical Engineering

Waterloo, Ontario, Canada, 2023

Examining Committee Membership

The following served on the Examining Committee for this thesis. The decision of the Examining Committee is by majority vote.

External Examiner	NAME: Qingye (Gemma) Lu Title: Associate Professor
Supervisor	NAME: Michael K. C. Tam Title: Full Professor
Internal Member	NAME: Ting Tsui Title: Associate Professor
Internal Member	NAME: Mario Ioannidis Title: Full Professor
Internal-external Member	NAME: Juewen Liu Title: Full Professor

Author's Declaration

This thesis consists of material all of which I authored or co-authored: see Statement of Contributions included in the thesis. This is a true copy of the thesis, including any required final revisions, as accepted by my examiners.

I understand that my thesis may be made electronically available to the public.

Statement of Contributions

Chapter 2 of this thesis consists of a manuscript that was co-authored by myself, two PhD students Yi Wang, Mei Han and Dr. Jiaxin Xu. I conceptualized the study and manuscript writing. My coauthors reviewed the manuscript and provided feedback on the draft document.

Chapter 3 of this thesis consists of a manuscript that was co-authored by myself, my supervisor, Dr. Michael Tam, two PhD student Yi Wang, Lian Han and Dr. Jiaxin Xu. I wrote the entire manuscript, and planned and executed the experiments, Yi Wang planned and executed some of the experiments, Lian Han and Dr. Jiaxin Xu assisted in the execution of some experiments My coauthors reviewed the manuscript and provided feedback on the draft document.

Chapter 4 of this thesis consists of a manuscript that was co-authored by myself, my supervisor, Dr. Michael Tam, two PhD student Yi Wang, Lian Han and Dr. Jiaxin Xu. I wrote the entire manuscript, and planned and executed the experiments, Yi Wang planned and executed some of the experiments, Lian Han and Dr. Jiaxin Xu assisted in the execution of some experiments My coauthors reviewed the manuscript and provided feedback on the draft document.

Chapter 5 of this thesis consists of a manuscript that was co-authored by myself, my supervisor, Dr. Michael Tam, three PhD student Yi Wang, Lian Han and Mei Han, Dr. Jiaxin Xu. I wrote the entire manuscript, and planned and executed the experiments, Yi Wang planned and executed some of the experiments, Lian Han, Mei Han and Dr. Jiaxin Xu assisted in the execution of some experiments My coauthors reviewed the manuscript and provided feedback on the draft document.

Chapter 6 of this thesis consists of a manuscript that was co-authored by myself, my supervisor, Dr. Michael Tam, two PhD student Yi Wang and Mei Han, Dr. Jiaxin Xu. I wrote the entire manuscript, and planned and executed the experiments, Yi Wang planned and executed some of the experiments, Lian Han and Dr. Jiaxin Xu assisted in the execution of some experiments. My coauthors reviewed the manuscript and provided feedback on the draft document.

Abstract

This thesis focuses on the utilization of sustainable materials, including cellulose nanocrystals (CNC), cellulose nanofibers (CNF), and modified lycopodium pollen particles, for the development of superwettable surfaces with diverse properties. By incorporating surface modifications, such as grafting CNC with positively charged functional materials and incorporating superhydrophobic modified lycopodium pollen particles, these sustainable materials were used to fabricate superhydrophobic, superlyophobic, highly hydrophilic, and superhydrophilic surfaces. These superwettable surfaces hold great potential for environmental and energy applications, such as non-loss micro droplet transfer, oil/water emulsion separation, ions transfer and salinity energy harvesting.

In the first study (**Chapter 3**), positively charged functionalized CNC stabilized wax-in-water Pickering emulsions were prepared. These emulsion particles, with adjustable sizes (2~33 μm), served as building blocks for constructing superhydrophobic surfaces via spray coating onto substrates. By altering the concentration of the CNC-Glycidyltrimethylammonium chloride (CNC-GTMAC) water suspension, the surface coverage of Pickering emulsion particles could be tuned, resulting in a wide range of adhesive forces toward water droplets. Surface topography, CNC coverage, and particle size played significant roles in determining the variation in the adhesive force (ranging from 47.7 μN to 79 μN for the superhydrophobic surfaces and 110 μN for the hydrophobic surface). Additionally, by fabricating surfaces using emulsion particles of two different sizes, the adhesion force could be significantly reduced to 5.7 μN, achieving self-cleaning characteristics. Finally, because of the switchable adhesion behavior, the superhydrophobic surface prepared by mixing different size emulsion particles (33) could be used for the non-loss micro droplet transportation.

The sustainable materials not only could be utilized for preparing superhydrophobic surfaces as described in chapter 3, specific surface functionalization could be implemented to expand the utilization of sustainable materials in dual superlyophobic surface. **Chapter 4** explores the utilization of sustainable materials in the construction of superlyophobic surfaces. A hybrid membrane consisting of cellulose nanofibers (CNF) and octadecylamine (ODA) modified lycopodium sporopollenin extine shell (ODA.SES) was developed by incorporating

superhydrophilic CNF and superhydrophobic modified lycopodium pollen particles (ODA.SES). The wettability and surface free energy of the system depended on the proportion of the two components. The unique 3D re-entrant structure formed by ODA.SES particles enabled the membrane to simultaneously exhibit superhydrophobicity under oil and superoleophobicity under water due to the formation of metastable oil-water-solid interface. This surface characteristic allowed the CNF-ODA.SES membrane to efficiently separate oil-water mixtures and filter highly stable oil/water emulsions.

The sustainable materials (CNC with different surface charges) could also be incorporated into the 2-dimension graphene-oxide (2D GO) system that significantly enhanced its hydrophilicity and charge capacity, which could be utilized in energy harvesting applications. In **Chapter 5**, sustainable materials grafted with different surface charges, such as positively and negatively charged CNCs, were incorporated into a graphene oxide (GO) system to enhance its hydrophilicity and charge capacity. A 1D/2D composite membrane consisting of intercalated CNCs and GO sheets was developed for ion transport and osmotic energy harvesting. The intercalated CNCs could effectively improved the hydrophilicity and mechanical properties of the system. Due to the special geometry and architecture of the intercalated CNC, it could expand the interlayer spacing of the nanochannel, allowing for a higher electrolyte flux and reducing energy barrier for ion transport. All these beneficial properties resulted in a high osmotic power generation of up to 4.73 W m^{-2} at room temperature under a controlled salt gradient (50 folds) in KCl electrolyte solution. Additionally, the oppositely charged tandem CNC/GO pair produced high voltages of up to 1.8V when 10 units were connected in series, indicating the commercial viability of the composite membranes.

Chapter 6 focuses on enhancing the hydrophilicity and water transport capability of sustainable systems through structural reorganization. CNF was dispersed in epichlorohydrin-NaOH-urea solution and reconstructed in H_2SO_4 solution to generate an align-distributed morphology and anisotropic surface characteristics. The resulting A-CNF membrane exhibited both strong mechanical strength and elasticity due to the double-crosslinked structure, making it suitable for real-world applications. The highly aligned structure facilitated rapid water conduction (>5mm s^{-1}), and the nano-sized CNF diameter allowed for the rapid transport of different types of ions, mono-valent (Li^+, Na^+ and K^+) and even multi-valent ions (Ca^{2+} and Mg^{2+}), inside the nanochannels. The

A-CNF membrane demonstrated excellent performance in osmotic energy harvesting, achieving a high-power density of 3.95 W m^{-2} power density in 50-fold salt gradient.

Acknowledgments

Time flies, thesis writing here means the invaluable journey of my Ph.D. study is coming to an end. Here I would like to express my sincere gratitude to my supervisor, Professor Michael Tam, who provided me with strong support, guidance and advice during my Ph.D. study. He gave me the freedom to pursue various research ideas; without his support, I would never have accomplished so much. His insightful guidance for me is not only on the research but also on the way of thinking and solving problems in life.

Also, I would like to thank my Ph.D. thesis examining committee members, including Professor Ting Tsui, Professor Mario Ioannidis, Professor Juewen Liu from the University of Waterloo, who provided me with the guidance during my comprehensive examination, and Professor as the external examiner from the for the valuable time and insights

In addition, I would like to thank all the group members who were always there to help in my project. I appreciate my outstanding colleagues including but not limited to Lian Han, Mei Han, Dr. Jiaxin Xu, Dr. Nathan Grishkewich, Dr. Yebin Lee, Dr Chunxia Tang for their valuable advice on my research.

Finally, I would like to give my sincere gratitude to my parents and fiancee Eva Wang for their unconditional support, encouragement and love. I would also like to thank all those lovely and close friends that I have made here in Waterloo. Thank you all for their generous support whenever and wherever I needed.

The memory I had here in Waterloo will last forever.

Table of Contents

Examining Committee Membership ii
Author's Declaration iii
Statement of Contributions iv
Abstract v
Acknowledgments viii
List of Figures xi
List of Tables xvii
Chapter 1. Introduction 1
1.1 Overview 1
1.2 Motivation and challenges 2
1.3 Research Objectives 3
1.4 Thesis outline 2
Chapter 2. Literature Review. 4
2.1 Introduction. 4
2.2 Wettability: Definition 4
2.2.1 Flat surface and Young's equation 4
2.2.2 Rough surface: Wenzel's and Cassie's models 6
2.2.3 Sliding angle 7
2.2.4 Superhydrophobic states 7
2.3 Superhydrophobic treatment. 9
2.3.1 Chemical functionalization 9
2.3.2 Design of topography 12
2.4 Superhydrophilic treatment 18
2.5 The superwettable surface 22
2.5.1 Tunable adhesion of superhydrophobic surface 22
2.5.2 Hydrophilic/superhydrophobic Hybrid surface 31
2.4.3 Smart superhydrophobic/superhydrophilic surface 35
Chapter 3. Tunable adhesion superhydrophobic surface based on wax-in-water Pickering emulsion 46
3.1 Introduction 46
3.2 Materials and method 47
3.3 Result and discussion 51
3.3.1 The modification of cellulose nanocrystal (CNC) 51
3.3.2 Time-evolution of interfacial tension change 53
3.3.3 Wax-in-water Pickering emulsion 56
3.3.4 Construction of superhydrophobic surface 58
3.3.5 Mapping of the surface adhesive force 71
3.3.6 Non-loss micro droplet transportation 73
3.4 Conclusions 74
Chapter 4. Unusual under liquid dual superlyophobic surface 75
4.1 Introduction 75
4.2 Materials and method 77
4.3 Result and discussion 80

4.3.1 The modification of superhydrophobic ODA.SES particles 80
4.3.2 Preparation of CNF-ODA.SES membrane and corresponding wetting behavior in air . 85
4.3.3 The wetting behaviour of CNF-ODA.SES membrane under oil and water 89
4.3.4 The surface free energy induced under liquid superlyophobicity 95
4.3.5 Water-in-Oil and Oil-in-Water Emulsion Separation 100
4.4 Conclusions 101
Chapter 5. Highly hydrophilic and oppositely charged cellulose nanocrystal intercalating GO membranes for ions transport and osmotic energy harvesting 103
5.1 Introduction 103
5.2 Materials and method 105
5.3 Result and discussion 107
5.3.1 Synthesis of oppositely charged CNC/GO membranes 107
5.3.2 Structure characteristic and mechanical viability of the oppositely charged membrane 112
5.3.3 Charge governed ion transport property 114
5.3.4 The mechanism of high-power generation of composites membrane. 122
5.4 Conclusion 131
Chapter 6. Superhydrophilic and aligned CNF array for selective ion transport and salinity energy harvesting 132
6.1 Introduction 132
6.2 Materials and method 133
6.3 Results and discussion 135
6.3.1 The construction of align distributed CNF membrane 135
6.3.2 The properties of A-CNF membrane 139
6.3.3 The ion transport behavior of A-CNF membrane 145
6.3.4 The osmotic energy harvesting of A-CNF membrane 152
6.4 Conclusions 153
Chapter 7 Conclusions and recommendation for future studies 155
7.1 Conclusions 155
7.2 Future recommendations 158
Letters of Copyright Permissions 160
References 161

List of Figures

Figure 1-1. The surface modification, topography design, mechanical understanding and application of superwettable surfaces. 3
Figure 2-1. The illustration of wettability for a modified surface. 5
Figure 2-2. (a) Modulation of the surface chemistry with different chemical functionalities. (b) Schematic illustration of surface topographies design using different technologies and in distinct length scale.....11
Figure 2-3. The relationship between the minimum porosity required for achieving superhydrophilicity on porous surfaces and the intrinsic contact angle.....19
Figure 2-4. Effect of surface roughness on water spreading on superhydrophilic surface.....20
Figure 2-5. The examples of superhydrophobic surfaces with tuable adhesive force. 27
Figure 2-6. The examples of patterned superhydrophobic/superhydrophilic surface. 33
Figure 2-7. The examples of smart superwettable surface with tunable superhydrophobicity and superhydrophilicity.....38
Figure 2-8. The various application of superwettable surfce in real-world applications. 43
Figure 3-1. Schematic illustration of droplet geometry for water adhesive force analysis. 51
Figure 3-2. (a) Schematic illustration of surface modification of CNC with GTMAC. (b) The FT-IR spectra of pure CNC and CNC-GTMAC. (c) The zeta potentials of CNC and cationic modified CNC-GTMAC. (d) the hydration diameter of CNC-GTMAC in different zeta potential. (e) Vial containing 0.5%w/w CNC-GTMAC in water and (f) Corresponding TEM image and (g) AFM image of the dispersion. The scale bar is 100 nm. 53
Figure 3-3. (a) The time-evolution interfacial tension change of pure wax-water, pristine CNC and CNC-GTMAC with different concentration by using Wilhelmy plate method. (b) The CNC-GTMAC stabilized oil/water interface and the buckling effect during volume decrease. (c) The oil/water interfacial variation at different concentration of CNC-GTMAC by using pendant drop method. (d) the hydration diameter of CNC-GTMAC in different zeta potential. (e) Vial containing 0.5%w/w CNC-GTMAC in water and (f) Corresponding TEM image and (g) AFM image of the dispersion. The scale bar is 100 nm. 55
Figure 3-4. (a) and (b) The emulsion particle size changes via the variation of CNC-GTMAC concentration. 56
Figure 3-5. The microscopic images of Pickering emulsions particles when the concentration of CNC-GTMAC is (a) 0.2wt%, (b) 0.4wt, (c) 0.5wt% and (d) 2wt%. 57
Figure 3-6. The core-shell CNC-GTMAC stabilized Pickering emulsion particle, (a) 0.2wt% and (b) 0.5wt%, observed by fluorescent optical microscopy. The scale bar, (a) 10μm and (b) 5μm. ..58
Figure 3-8. The static contact angle of water-repellent surface coated with emulsion particles of (a) 33μm and (b) 2μm. (c), (d) The size distribution of emulsion particles and corresponding static contact angle of different superhydrophobic surface. 59
Figure 3-9. The SEM images of (a) CGPE-2 and (b) CGPE-33, respectively. The zoom-in SEM images of (c) CGPE-2 and (d) CGPE-33 and the clear observation of rapped CNC at their surface (The red arrow). 61
Figure 3-10. (a) The diagram of droplet holder for testing water adhesive force. (b) The graphical illustration of adhesive force measurement protocol for the surface prepared with CGPE-33. (c) Schematic illustration of testing process of surface adhesive force. 62

Figure 3-11. (a) The adhesive force profiles (as a function of droplet separation and substrate) for (low to high concentration from front to back in the graph). (b) The relationship between adhesive force and emulsion particle sizes. 63
Figure 3-12. The schematic illustration of adhesive force generation for emulsion particles with different sizes. (a) The Cassie wetting state. (b) The Wenzel wetting state. 64
Figure 3-13. (a) The laser confocal microscopy images of three phase contact line when CGPE-5 was in contact with droplet and (c) the three phase contact line after stabilized with 30s. (b) The laser confocal microscopy images of three phase contact line when CGPE-2 was in contact with droplet and (d) the three phase contact line after stabilized with 30s. 65
Figure 3-14. (a) The adhesion behavior of CGPE-2 when contacted by a 5 μL liquid droplet. (b) The adhesive force characterization of CGPE-2. (c) The adhesion behavior of CGPE-5 when contacted by a 5 μL liquid droplet. (d) The adhesive force characterization of CGPE-5. 65
Figure 3-15. Different stages of advancing contact angle (ACA) and receding contact angle (RCA) measurement. 66
Figure 3-16. (a) Schematic of a sessile liquid drop on a hydrophilic/superhydrophobic surface made of highly porous aggregates of microspheres. The schematic illustrates the definition of the static contact angle. The term “edge” is used to distinguish the formation of three-phase contact line (TPCL) between nanostructure and microstructure. (b) The advancing contact angles, receding contact angles and contact angle hysteresis of different surfaces. (c) The static contact angles and sliding angles of different surfaces. 68
Figure 3-17. (a) Schematic diagram of CPE-2 with negative charge attracted by positive charged CGPE-33. (b) Adhesive force profiles of ME-1-3, ME-1-1, ME-3-1, ME-1-7, ME-7-1, ME-8-0 and ME-0-8. (c)The value of different mixing superhydrophobic surface). 70
Figure 3-18. (a) Static contact angle of superhydrophobic surface prepared using ME-1-1 and (b) droplet sliding off the surface as the substrate was tilted. (c) Dynamics of a 5μL falling water droplet on the ME-1-1 surface. (d) The adhesion behavior of ME-1-1 when contacted by a 5 μL liquid droplet. 71
Figure 3-19. The microscopic images and corresponding illustration of force scan maps (The scale bar is 200μm, the red color indicates the high adhesive force and blue color shows low adhesive force). 72
Figure 3-20. The adhesive force mapping of (a) CGPE-33, (b) CGPE-29, (c) CGPE-18, (d) CGPE-8, (e) CGPE-5 and (f) ME-1-1. 73
Figure 3-21. Transportation of a water droplet from superhydrophobic surface with low adhesion to a hydrophilic surface using a superhydrophobic surface with high adhesion. 73
Figure 4-1. The wetting behavior of hydrophilic, hydrophobic and super-lyophobic surface under dual liquid (water and oil). 76
Figure 4-2. The Schematic of transforming Lycopodium clavatum pollen into a hollow Lycopodium sporopollenin extine shell following the defatted and extraction process. 80
Figure 4-3. The digital microscopic images and scanning electron microscopic (SEM) images of (a) nature pollens, (b) defatted pollens and (c) extracted lycopodium sporopollenin extine shell (SES) particles. 82
Figure 4-4. (a) The FT-IR spectrum of CNF, Pure SES and SES modified with different contents of ODA. (b) The high resolution XPS spectrum of Pure SES and SES.ODA-5. 83
Figure 4-5. The detail morphology of three different ODA.SES particles, including (a) SES.ODA-

1, (b) SES.ODA-5 and (c) SES.ODA-10. And the corresponding static contact angle of three different particles (d), (e) and (f).....84
Figure 4-6. The (a) AFM image and (b) the characterization of height of prepared CNF. (c) The TEM image of CNF made from cotton fiber by TEMPO oxidization method. 85
Figure 4-7. Illustration of the preparation of CNF-ODA.SES superlyophobic surface for oil/water separation. 86
Figure 4-8. The static contact angle of (a) CNF-ODA.SES-0.1, (b) CNF-ODA.SES-0.2 and (c) CNF-ODA.SES-0.3, and the corresponding SEM images of three membrane shown in (d), (e), and (f) respectively.....87
Figure 4-9. The contact angle measurements in air for the (a) CNF-ODA.SES-0.4 membrane and (b) CNF-ODA.SES-0.5 membrane. 88
Figure 4-10. The SEM images of (a) CNF-ODA.SES-0.4 and (b) CNF-ODA.SES-0.5, and the corresponding zoom-in image (c) and (d), respectively. 88
Figure 4-11. (a) Illustration of oil static contact angle measurement underwater. (b) The hexane contact angle on CNF-ODA.SES-0.9 surface under water. (c) Illustration of superoleophobic state underwater. (d) The hexane contact angle on CNF-ODA.SES-0.4 surface under water. (e) Illustration of partially oil wetted state underwater. (f) The hexane contact angle measurement of various CNF-ODA.SES membranes under water. 90
Figure 4-12. Time-dependent variation of under water hexane contact angle on CNF-ODA.SES-0.2. 90
Figure 4-13. Time-dependent variation of under water hexane contact angle on CNF-ODA.SES-0.2. 91
Figure 4-14. (a) Illustration of water static contact angle measurement underoil. (b) The hexane contact angle on CNF-ODA.SES-0.2 surface under water. (c) Illustration of superoleophobic state underwater. (d) The hexane contact angle on CNF-ODA.SES-0.7 surface under water. (e) Illustration of partially oil wetted state underwater. (f) The hexane contact angle measurement of various CNF-ODA.SES membranes under water. 92
Figure 4-15. The under liquid wetting behavior of series of CNF-ODA.SES (from CNF-ODA.SES-0.1 to CNF-ODA.SES-0.9) surface in the hexane-water system. 93
Figure 4-16. Illustration of sliding angle measurements of (a) water droplet under hexane environment and (c) hexane droplet under water environment. (b) and (d) The digital images showed that both water droplet or oil droplet could easily move away from the CNF-ODA.SES-0.5 surface with a slightly inclined degree in oil-water system. 94
Figure 4-17. Adhesion measurement of CNF-ODA.SES-0.5 surface. The image shows a controlled experiment where either (a) a water droplet or (b) hexane was brought into contact with the CNF-ODA.SES-0.5 surface and exhibited no pinning effect under hexane or water, respectively. 94
Figure 4-18. Thermodynamic wetting models analysis of the CNF-ODA.SES membrane under liquid. 95
Figure 4-19. The Dual superlyophobic properties of the CNF-ODA.SES-0.5 in different oil water system. The blue columns indicate the water contact angle under different oil and brown columns represent the oil contact angle under water. 99
Figure 4-20. The potential application of CNF-ODA.SES-0.5 membrane for the water-in-oil and oil-in-water emulsion separation and their optical images of feed emulsion and filtrate. 101
Figure 4-21. The stability measurement of separation flux of CNF-ODA.SES-0.5 for the water-in-

hexane and hexane-in-water emulsion. 101
Figure 5-1. (a) Schematic depiction of oppositely charged NCNC/GO and PCNC/pGO nanofluidic energy harvesting device. (b) NCNC/GO and PCNC/pGO solution with typical Tyndall effect, indicating the excellent dispersibility of colloidal particles. (c) The zeta-potential of different colloidal particle solutions. (d) The zeta-potential and conductivity (G) as a function of the salt concentration in colloidal solution. (e) The zeta-potential variation with changes in pH. 108
Figure 5-2. (a) Typical AFM image of NCNC distributed on substrate. The TEM image of NCNC and the inset image show the dimension of single distributed NCNC. The high-resolution AFM image of NCNC and height profile of different position on the image: (Profile 1) The longitudinal section of NCNC; (Profile 2 and Profile 3). The cross section of NCNC. (b) Typical AFM image of PCNC distributed on substrate. The TEM image of PCNC and the inset image shows the dimension of a single distributed PCNC. The high-resolution AFM image of PCNC and height profile of different position on the image: (Profile 1, Profile 2 and Profile 3). The cross section of NCNC. (c) Characterization of GO nanosheets. Particle size distribution of exfoliated GO suspension (scale bar: 300nm). AFM height image of graphene oxide. Cross-section profile of different position on the AFM height image (1) and (2). 109
Figure 5-3. (a), (d) Photographs of self-standing and flexible NCNC/GO and PCNC/pGO membranes, respectively. (b), (e) Cross-section SEM characterizations of NCNC/GO and PCNC/pGO membranes. The thickness of the membranes was about 20 μm. (c), (f) XRD patterns of NCNC/GO and PCNC/pGO membranes. (g) Tensile stress-strain curve of the NCNC/GO, PCNC/pGO, CMC/GO and pure GO membranes. (h) The ultimate strength and toughness of NCNC/GO and PCNC/pGO composite membranes with different CNC contents. (i) Comparison of mechanical performance in terms of stress, strain, Young's modulus, thickness and toughness. . 111
Figure 5-4. (a) Fourier transform infrared spectrum acquired from Pure CNC, NCNC/GO and PCNC/pGO membrane, in which the characteristic peaks were marked to represent the functional groups. (b) The AFM image, height profile and the schematic structure of the several layers of stacked GO nanosheet. (c) The TEM image and AFM image NCNC wrapped on the surface of GO. The height profile shows the covering of NCNC that induces the formation of artificial wrinkles on GO (The scale bar is 1μm). (d) The TEM and AFM image of PCNC wrapped on the surface of pGO. The height profile shows the covering of PCNC that induces the formation of additional artificial wrinkles on pGO (The scale bar is 1μm). (e) The schematic structure of the NCNC/GO and PCNC/pGO, and schematic illustration of the wrinkles when NCNC and PCNC is trapped in GO basal planes. (f) TEM images of the fractured regions with wavy cracks, pulled sheets, and bridged NCNC and PCNC. 114
Figure 5-5. (a) Small rectangular strips for nanofluidic testing. (b) Schematic illustration for the encapsulation of the 2D membrane (NCNC/GO andPCNC/pGO) into the epoxy resin. 114
Figure 5-6. (a), (c) Current-Voltage (I-V) curves of NCNC/GO and PCNC/pGO at different electrolyte concentrations. (b) Schematic illustration of ion transport testing. (d), (f) Measurement of Current-Voltage (I-V) curves for NCNC/GO and PCNC/pGO membranes recorded in 1000-fold KCl concentration gradient. The low concentration side was set to 1 mM. (e) Schematic illustration of the ion transport testing setup under a concentration gradient. The diffusion current is consistent with the net flow from high to low concentration. 115
Figure 5-7. Surface profile image of the section of (a) NCNC/GO and (c) PCNC/pGO membrane and (c), (d) the corresponding height profile. (e) Ionic conductance variation versus salt

concentration of the NCNC/GO and PCNC/pGO. 117
Figure 5-8. (a), (b) Open-circuit potential and short-circuit current variations with the concentration gradient difference. (c), (d) Ion selectivity (t+) and conversion efficiency. 117
Figure 5-9. Element mapping of prepared PCNC/pGO and NCNC/GO. For PCNC/pGO membrane, showing the binding of chloride ions, and repulsion of potassium ions. On the contrary, the potassium ions are condensed in NCNC/GO membrane, showing the anion selectivity. The scale bar is 2μm 118
Figure 5-10. (a) The nanofluidic reverse electrodialysis of the combination of oppositely charged ChCNC/GO (NCNC/GO and PCNC/pGO composites membrane) pair. (b) I-V responses for single-unit nanofluidic reverse eletrodialysis device measured under two configurations methods, High concentration (HC) in the central or low concentration (LC) in the central compartment. (c) Current density and (d) output power of ChCNC/GO based RED system as function of load resistance under the placement of different electrolyte solution (KCl, NaCl and LiCl) in the central cell. (e) Comparison of the power density and internal resistance with the reported intercalated 2D nanofluidic membranes. (f) Short-circuit current and (g) output power density of ChCNC/GO pair membrane for continuous 7 days. 119
Figure 5-11. Short-circuit current testing for epoxy resin confined GO membrane pair for continuous 7 days. 122
Figure 5-12. The surface zeta potential of four different types of membrane. 123
Figure 5-13. (a) Schematic illustration of the mechanisms of different intercalating agents for the improvement of performance. (a-1), adding neutral charged NeCNC to the GO system. (a-2), adding CMC to the GO system. (a-3), introduction of oppositely charged ChCNC to the GO system. (b) and (c) The electrochemical performance variation for ChCNC/GO, NeCNC/GO, CMC/GO and pure GO system. (d) Dependence of output power density on the electrolyte pH. 124
Figure 5-14. The AFM image of CMC/GO and the corresponding profile. 125
Figure 5-15. Schematic illustration of the ion transport pathway for (a) vertically stacked ChCNC/GO membrane (ion diffusion direction parallel to the 2D membrane) and (b) horizontally stacked ChCNC/GO (ion diffusion direction perpendicular to the 2D membrane) membrane. (c) the dimension of single ChCNC/GO membrane for the estimation of ion transport length. The (d) current density and (e) output power density of the H-ChCNC/GO as functions of load resistance under the placement of different electrolyte solution (KCl, NaCl and LiCl) in the central cell. ..127
Figure 5-16. (a) Influence of the weight content of ChCNC on the output power density. Error bars represent s.d. (b) The AFM image of densely coated (10.5% weight content) NCNC on GO surface. 128
Figure 5-17. (a) Ionic conductance as a function of temperature. The inset shows the Arrhenius-type plot of the ion conductance versus temperatures. (b) The maximum output power density as a function of temperature in 50-fold KCl concentration gradient. (c) Schematic illustration of the tandem stacks of ChCNC/GO pair RED device. (d) The output voltage of 10 units. The inset image shows the voltage of 5 connected RED units and power a 0.8V thermo/hygro clock. 128
Figure 5-18. (a) Ionic conductance variation with temperatures. (b) The Arrhenius-type plot of the conductance as a function of temperature. 129
Figure 6-1. Schematic image of the bottom-up approach for fabricating aligned distributed CNF. 135
Figure 6-2. (a) Storage (G′) and loss (G″) modulus as a function of time during the cross-linking of

the hydrogel precursor solution (6 wt% cellulose with 2.75mL ECH) at -12 °C. (b) and (c) The amplitude sweep of diverse sample with different contents of EPI. (d) single-frequency measurements of gelation progress with 2.75ml EPI crosslinker. 136
Figure 6-3. (a) The mechanical properties of membrane after structural re-organization in acid solution and dried in air. (b) The ruptured stress and toughness of the different membranes prepared by different contents of EPI. 137
Figure 6-4. The AFM images of the surface of the anisotropic cellulose films with various prestretching strains, including 40%, 80%, 120%, and 160% respectively. 139
Figure 6-5. The SEM images of anisotropic TEMPO oxidized CNF membranes. (a) the illustration of observed A-CNF membrane from (b) xy plane, (c) xz plane and (d) yz plane. 140
Figure 6-6. Characterization of tunable optical properties of the A-CNF membrane. Illustrations and optimal images showing the light scattering effect of the A-CNF membrane without stretching (0% strain) (a) and (c), as well as with 160% strain (b) and (d), respectively. 140
Figure 6-7. The superhydrophilic characteristics of A-CNF membrane. 141
Figure 6-8. Superhydrophilic A-CNF membrane demonstrating directional fluidic transport against the gravity. 142
Figure 6-9. The water transport behavior inside the nanochannel of A-CNF 143
Figure 6-10. (a) The transmittance of the dry and wet A-CNF membrane. (b) Photos of wet and dried A-CNF membrane wrapped around a rod. 144
Figure 6-11. (a) Illustration of the differences in surface functional groups between carboxylated A-CNF and hydroxylated A-CNF-OH. (b) The zeta potential of A-CNF and A-CNF-OH under neutral pH at a concentration of approximately 0.1%. 145
Figure 6-12. Ion conductance measurement in KCl electrolyte for the membrane between (a) A-CNF and A-CNF-OH, and (b) A-CNF and A-CNF-Freeze dried samples, respectively. 147
Figure 6-13. The current-voltage (I-V) curves of A-CNF membrane in KCl electrolyte at different concentrations. (b) Measurement of current-voltage (I-V) curve for A-CNF membrane recorded in 50-fold salinity gradient. The low concentration side was set to 1 mM. 147
Figure 6-14. The I-V curves of A-CNF membrane recorded in different types of electrolyte, including KCl, NaCl and LiCl. (b) Measurement of current-voltage (I-V) curves for A-CNF membrane recorded in 50-fold salinity gradient in three types of electrolyte. The low concentration side was set to 1 mM. 149
Figure 6-15. (a) The illustration of in-situ Raman observation device for ion transport in A-CNF membrane. (b) The Raman spectrum measurement for A-CNF, A-CNF-FD and A-CNF-OH membrane. (c) The 2D Raman image obtained by in-situ analyzing changes in the carboxyl signal intensity, showing the incorporation between the K^+ and A-CNF membrane. 150
Figure 6-16. Current density (a) and output power density (d) of A-CNF, A-CNF-FD and A-CNF-OH based reverse electrochemical dialysis system as function of load resistance under the placement of electrolyte solution (artificial sea water and river water, 0.5M/0.01M KCl electrolyte) in the central cell. (b) and (c) Current density measurement of A-CNF membrane under different electrolyte systems. (e) and (f) The output power density of A-CNF membrane under different electrolyte systems. 152

List of Tables

Table 1-1. The construction of low adhesive force superhydrophobic surface by mixing CGPE-33 and CPE-2 69
Table 4-1. Total interfacial energy calculation on various CNF-ODA.SES membranes. 95
Table 4-2. Components of Surface Energy for various CNF-ODA.SES membranes..... 98
Table 4-3. Physical properties of four tested oils. 99
Table 5-1. Measured open-circuit potential, redox potential and diffusion potential for NCNC/GO and PCNC/pGO, respectively..... 118
Table 6-1. The electrophoretic mobility of different type of ion and the relative mobility compare to K^+. 148

Chapter 1. Introduction

1.1 Overview

Wettability is central to numerous biological processes, and this topic on wettability is highly relevant to many engineering and industrial applications.[1] The academic research on the surface wettability phenomena can be traced to 1805 when the Tomas Young proposed the contact angle and define the notion of surface wetting.[2] And surface wetting research encounter an exponential growth in the past decades, especially the study of the extreme wetting phenomena of superhydrophilic surface (where water contact angle close to 0˚) and superhydrophobic surface (where water contact angle above 150˚) in the past decades.[3] Discovering and revealing the mechanism of extreme wetting surface allows researchers to gain new insights into the design and fabrication of materials with tailored wetting properties. In recent years, the integration of surface chemistry and rough topography has created new avenues for the development of novel superwettable surfaces with diverse characteristics and properties suitable for emerging applications. These include responsive superhydrophobic/hydrophilic surfaces[4], under liquid superlyophobic surfaces[5], superhydrophilic surfaces with fast water transport[6], among others. However, the complex requirements of surface topography and properties pose challenges in the construction and processing of superwettable surfaces, resulting in methods that are not environmentally friendly and that hinder large-scale production and potential commercialization.[7, 8] These limitations have highlighted the need to explore the effective utilization of sustainable materials in the construction of superwetting systems.

Bio-based sustainable materials, such as cellulose nanocrystal (CNC), cellulose nanofiber (CNF) and plant pollens, represent an interesting nature-derived and renewable feedstock for advanced material applications.[9] Especially, the effective utilization of nano and micro-scale particles in material applications represents a major breakthrough due to their multifaceted benefits in preparing delicate morphology compared to bulk matter. For instance, the morphology of CNC can be considered as stiff crystallites with a high aspect ratio.[10] The CNF exhibits a high aspect ratio and it's length can expand to several micrometers.[11] The plant pollens have diverse and unique 3D topography depending on the species with sizes micrometres.[12] Moreover, the abundant hydroxyl (-OH) and carboxyl groups (-COOH) present on the surface of these sustainable materials offer

numerous opportunities for functionalization and coating, enabling customization of superwettability for specific applications.

1.2 Motivation and challenges

The primary motivation behind this research is to harness the potential of sustainable materials, such as CNC, CNF, and plant pollens, in the development of superwettable surfaces. These materials offer unique advantages, including their renewable nature and low environmental impact, making them promising candidates for addressing sustainability challenges in surface engineering. By leveraging the properties of sustainable materials and employing surface functionalization techniques, we will modify their surface characteristics, such as altering the functional groups, enhancing or altering the surface charges, combining them with other compounds or re-organizing their structure, to fabricate superwettable surfaces with diverse properties. The goal is to apply these superwettable systems in environmental and energy applications, contributing to sustainable solutions and addressing pressing challenges in these fields.

One key motivation is the desire by various stake holders to seek for sustainable alternatives in surface engineering. Traditional methods on superwettable surface construction often rely on non-renewable resources and environmentally harmful processes with large carbon footprints to produce the special surface topographies.[13] These sustainable materials possess unique properties and morphology needed to engineer the desired microstructure that minimizes the environmental impact associated with surface construction. Also, the utilization of sustainable materials for superwettable systems aligns with the global sustainable requirement that minimize their dependence on finite resources.

Another key motivation is to understand the fundamental principles and mechanisms associated with the properties of modified sustainable materials in superwettable systems. By unraveling the interactions between surface functional groups, wettability properties, and structural reconstructions, we will gain insights into the basic interfacial science and guide the design of advanced superwettable surfaces. This knowledge is crucial to optimize the performance, durability, and versatility of these surfaces in environmental and energy related applications, such as tiny droplet transfer, oil-water separation, ions transfer and salinity energy harvesting as shown in Figure 1-1.

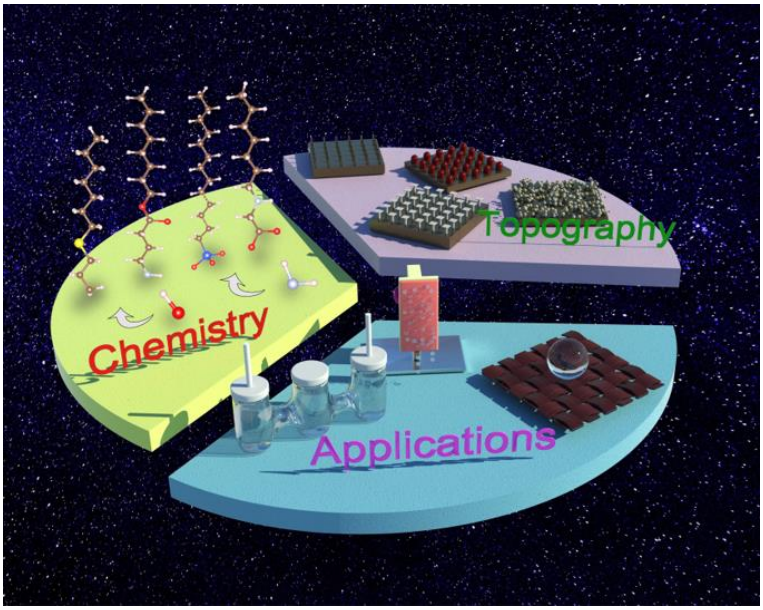

Figure 1-1. The surface modification, topography design, mechanical understanding and application of superwettable surfaces.

There are however several challenges that need to be addressed in order to achieve the research motivations outlined above.

(i) ***Surface functionality.*** The effective functionalization and scalable techniques that can control surface wettability, surface charge, and structure while maintaining the integrity and unique structure of the sustainable materials is crucial.

(ii) ***Material compatibility***. The main challenge here is how to incorporate the raw and modified sustainable materials into the superwettable systems to achieve the desired properties and avoid undesired interactions that could compromise the characteristics of the superwettable surfaces.

(iii) ***Controlling mechanisms***. Investigating the underlying mechanisms and establishing the structure-property relationships require comprehensive characterization techniques and multi-disciplinary approaches. Overcoming this challenge is essential for designing and tailoring superwettable surfaces with precise and desired properties.

1.3 Research Objectives

The research objective of this thesis is to explore the effective utilization of sustainable materials in the development of superwetting systems for application in the environmental and energy fields. By

incorporating sustainable materials into various superwetting surfaces, we will investigate their role, contributions and performance through effective modifications. We will focus on fabricating four types of superwettable surfaces, namely superhydrophobic, superlyophobic, as well as highly hydrophilic and superhydrophilic surfaces. This involves functionalizing the sustainable materials with specific functional groups, altering their surface charges, or modifying their wettability properties. Through these modifications, we will examine how these sustainable materials actively participate in the superwetting systems, and how they can enhance or introduce new properties to existing or new applications. Furthermore, we seek to investigate and gain insights into the mechanisms associated with performance of these modified sustainable materials in superwetting systems, as well as unravel the underlying principles that will pave the way for future research opportunities. Thus, the objectives of this thesis are:

(1) The preparation of positively charge functionalized CNC stabilized wax-in-water Pickering emulsion and their capacity to construct superhydrophobic surfaces with tunable adhesive force toward water droplets.
(2) A facile method for the construction of novel under liquid superlyophobic surface with controlled surface free energy.
(3) Synthesis of highly hydrophilic and oppositely charged CNC intercalated graphene oxide membranes for ion transport and salinity energy harvesting.
(4) The development of “bottom-up” method for the construction of superhydrophilic CNF membranes for superior ion conducting and osmotic energy harvesting.

1.4 Thesis outline

The contents of this thesis are organized into 7 chapters, each focusing on different aspects of the research. Chapter 1 provides a brief introduction on the superwetting surfaces, sustainable materials, and potential applications of superwettable systems. The chapter also outlines the goals as well as the contents of the thesis. Chapter 2 examines the wetting theory and characterization methods related to surface wettability. A comprehensive literature review was conducted, covering the development of superwetting systems, efficient surface chemistry and topography modifications, as well as associated applications when combined with a superwetting system. Chapter 3 investigates the interfacial assembly of positively charged CNC at the oil/water interface, as well as the

preparation of paraffin wax Pickering emulsions of different particle sizes and surface coverage. The underlying mechanism behind the tunable adhesive force of superhydrophobic surfaces prepared from these Pickering emulsions was also studied. Chapter 4 presents a novel and facile method for controlling the surface free energy to produce a new type of under liquid superlyophobic surface. This is achieved through the combination of superhydrophilic CNF and superhydrophobically modified lycopodium pollen particles. Also, the oil-water emulsion separation was investigated to illustrate the potential application of this new type of surface. Chapter 5 describes the utilization of superhydrophilic and highly charged CNC for the modification of graphene oxide nanosheets. The enhanced surface wettability and charge capacity of CNC/GO system could be applied to ion transport and salinity energy harvesting in water. Chapter 6 outlines a "bottom-up" approach for constructing superconducting, superhydrophilic, and anisotropic CNF membranes. The chapter highlights their superior ion conductivity, even in the presence of multivalent ions, and their ability to harvest osmotic energy in water systems. Chapter 7 provides a comprehensive conclusion derived from the results described in Chapter 3-6 and suggests future research directions for superwettable surfaces.

Chapter 2. Literature Review.

2.1 Introduction.

This chapter presents a review of the literature relevant to the understanding of the research contained in this thesis. Firstly, the introduction of fundamental theories about wettability will be discussed, including hydrophilic, hydrophobic, superhydrophilic, and superhydrophobic and details regarding to the Young's equation, rough surface, sliding angle and contact angle hysteresis. Secondly, the introduction of sustainable materials, including CNF, CNC, chitin, chitosan and pollen. This will include discussions on the definition, properties and modification of surface. Then, superhydrophobic surface will be presented. This will include discussions on the definition, properties, characterizations of superhydrophobic surface. In order to achieve the aforementioned superhydrophobic characteristic, the surface construction strategies, including chemical functionalization and topography design, will also be mentioned. Thirdly, the special superhydrophobicity, including the tunable adhesion superhydrophobic surface, hybrid superhydrophobic surface and smart superhydrophobic surface, would be reviewed. Also, the relevant various applications would be introduced. Fourthly, the under-liquid superlyophobicity would be introduced. In this part, we will talk about the definition, characterization and potential applications. Finally, the superhydrophilicity would be introduced. We will talk about the recent promising applications that achieved by utilizing the properties of superhydrophilic surface.

2.2 Wettability: Definition

2.2.1 Flat surface and Young's equation

The history of surface wetting and wettability research could be traced back to two centuries ago. Thomas Young (a pioneer researcher in this field) proposed the concept of contact angle of a liquid droplet and defined the surface wettability. When placing a droplet in contact with a flat surface, the droplet will form a cap-like semi-sphere if it does not completely wet the surface. As illustrated in Figure 2-1a, when the whole system reaches to the thermal dynamical equilibrium state, the static contact angle (CA) can be defined as the angle of intersection between the solid-liquid interfacial and liquid-gas interfacial.

Traditionally, the hydrophobic surface is defined when CA (θ) >90° and those with CA (θ) <90°

is described as hydrophilic. Additionally, some recent studies about interfacial water structure indicate that the intrinsic wetting threshold for hydrophilic/hydrophobic is close to the ~65°.[14] It can be interpreted that the water molecules at solid/liquid interface intended to form denser structure, like trihedral or tetrahedral configuration, on hydrophilic surface, while the water molecules will show weak interaction with hydrophobic surface, assembling into looser or non-hydrogen-bond water structure.[15]

Young's equation quantitatively represents the relationship between the CA, the liquid surface tension γ_{Lv} (N/m or J/m^2), the solid surface tension γ_{sv} (N/m or J/m^2) and the solid-liquid interfacial tension γ_{sL} (N/m or J/m^2) for an ideal flat surface with homogeneous physical/chemical properties, which can be described by Equation (2-1):

$$\gamma_{sv} = \gamma_{sL} + \gamma_{Lv} \cos\theta \qquad (2\text{-}1)$$

Additionally, it can be easily concluded that the apparent contact angle can be enhanced by grafting a low free energy chemical onto the surface. Previous research indicated that the largest contact angle achievable for a smooth surface was ~120˚ by grafting lowest surface free energy compounds, such as CF_3 groups (6.7mJ m^{-2}) to the solid surface.[16] However, there are numerous natural water-resisting materials, displaying much higher CA and liquid repellency, like the Lotus leaves display a CA 162° and a CA 155° shown by duck feather).[17] Therefore, a deeper understanding and better mathematical model is necessary to understand the various types of solid-liquid surfaces.

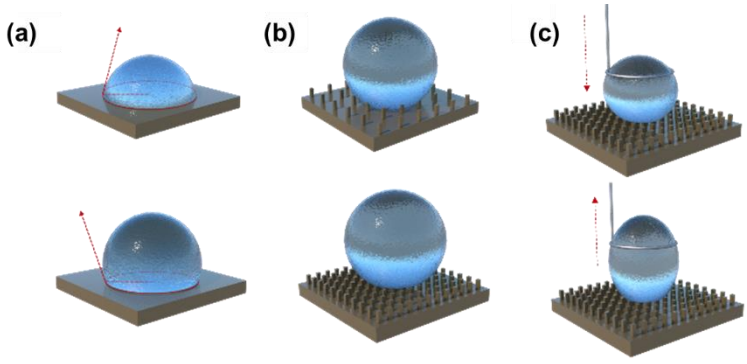

Figure 2-1. The illustration of wettability for a modified surface. (a) The water droplet shape and formation of static contact angle on a hydrophilic surface (upper) and hydrophobic surface (bottom). (b) The water droplet contacts with rough surface in a Wenzel's state (upper) or Cassie's state (bottom). (c) The illustration of surface adhesive force measurement with the snap-in (upper)

and pull-off (bottom) process.

2.2.2 Rough surface: Wenzel's and Cassie's models

In practice, very few solid surfaces are truly smooth, thus the apparent CA detected on rough surfaces deviates from the values predicted from the Young's equation. This deviation is caused by the complicated solid-air-liquid interface interaction. Therefore, the roughness and topography factor (R) should be considered when evaluating the surface wettability. Two models have been developed to describe this phenomenon. Firstly, in the Wenzel's model, the water is assumed to penetrate into the 'grooves' or 'cavities' of the surfaces since water will closely follow the topography of the surface and form a continuous liquid-solid interaction interface (Figure 2-1b).[18] Thus, the CA can be calculated using the Wenzel's equation (Eq. (2-2))

$$\cos\theta' = r\cos\theta \tag{2-2}$$

where the θ' is the apparent contact angle of a rough surface, r is the roughness factor (defined as the actual surface area of the rough surface to the apparent area) and θ refers to the intrinsic CA described by the Young's equation. Obviously, the roughness factor increases both the surface wetting and anti-wetting properties, depending on the intrinsic hydrophobicity of the corresponding materials. If the surface has a contact angle smaller than 90°, and r will reduce this value further however if the CA greater than 90°, the roughness will increase the apparent CA.

Based on the extensive investigation of natural superhydrophobic materials, Cassie and Baxter proposed another superhydrophobic model in 1944.[19] They proposed that for a highly water repellent surface, the liquid will suspend on the rough surface structure and the interface is composed of protrusions and trapped air-pockets beneath the liquid droplets. In this case, the apparent CA can be calculated using the Cassie' equation described by Eq. (2-3):

$$\cos'\theta = f_1\cos\theta_1 + f_2\cos\theta_2 \tag{2-3}$$

where f_1 and f_2 correspond to the fraction of materials and pores on the surface respectively. Besides, $f_1+f_2=1$, $\theta_1 = \theta$ (corresponding to the intrinsic CA for materials 1) and $\theta_2=180°$ (Considering the vapor as the ideal hydrophobic media). Thus, Eq. (2-3) can be rewritten as Eq. (2-4):

$$\cos\theta' = f_1(1+\cos\theta_1) - 1 \tag{2-4}$$

In this state, the droplet will only rest on the topmost region of rough structure, exhibiting a much

larger apparent CA than flat surface (Figure 2-1b). Therefore, the surface morphology and topography play a crucial role in the surface wettable phenomenon.

2.2.3 Sliding angle

The static contact angle can be utilized to characterize the hydrophobicity of flat and slightly rough surface due to its continuous solid-liquid contact line. However, for surfaces with extremely highly heterogeneous and irregular structure, such as textile or filament surface, it is difficult to determine the accurate CA value since the contact line of the solid-liquid is covered by protruding bumps. In such cases, dynamic methods, such as sliding angle (SA) is necessary in addition to the static CA measurement.

2.2.4 Superhydrophobic states

Intermediate state between Cassie and Wenzel state

On a rough surface, the water droplet possesses a wet contact mode with surface that generates a high adhesive force, where the liquid does not slide from the surface. In contrast, for the Cassie state, the contact line liquid-solid surface is discrete, and the droplet adopts a non-wet contact mode resulting in a high static CA with an extremely low sliding angle (normally smaller than 5°), generating a self-cleaning effect like the Lotus leaves. In practice, most of the surfaces exist in between the Cassie and Wenzel state, where the surface would produce an adhesive force on the droplet due to the partially wetted textile structure, such as surfaces with hybrid hydrophobic/hydrophilic functional groups and multi-scale hierarchical structure.[20] The coexistence of the Wenzel's and Cassie's state in the structure would prevent the spontaneous wetting transition due to the existence of the Gibbs energy barrier. However, external stimuli, such as pressure, electrical force, and magnetic field may be necessary to drive the droplet from one wetting state to another by adjusting the solid-liquid interaction force.

Contact angle hysteresis and adhesion detection

It has been widely demonstrated that the contact angle hysteresis (CAH) is an important parameter to characterize the water repellent surface.[21, 22] Typically, for a chemically uneven and heterogenous superhydrophobic surface, the migration of the contact line could lead to changes in the static CA. Therefore, the advancing contact angle (θ_{adv}) is used to describe the highest CA when

the solid-vapor interface is replaced by the solid-liquid interface. On the contrary, the receding contact angle is used to define the smallest CA observed before the three-phase contact line recedes. Normally, the θ_{adv} is greater than θ_{rec} and the difference between them is defined as contact angle hysteresis (CAH, Eq. (2-5)).

$$CAH = \theta_{adv} - \theta_{rec} \quad (2\text{-}5)$$

Additionally, for superhydrophobic surface with special wetting characteristics, the movement of the droplet is different at distinct points and directions and generating large differences in CAH. There are several reported studies that suggested that adhesion force are related to the advancing and receding angles.[23] According to the Young-Duprè equation (Eq. (6)), the work of adhesion (w_{ad}, J/m^2) involved in the movement of the droplet on a superhydrophobic surface can be related to the interfacial tension and intrinsic CA and expressed as below:

$$w_{ad} = \gamma_{LV}(1 + cos\theta) \quad (2\text{-}6)$$

Besides, assuming the w_{ad} represents the work done by the lateral adhesion force (F, mN) that making droplet move at a certain distance (δ, mm).[24] Therefore, the F can be represented by the w_{ad}, contact angle hysteresis (CAH), The droplet/surface contact radius (R) and CA as below (Eq. (2-7) and Eq. (2-8)):

$$F\delta = w_{ad}\delta\pi R \quad (2\text{-}7)$$

$$\gamma_{LV}\,(\theta_{adv} - \theta_{rec})2R = \gamma_{LV} f_1(1 + cos\theta)\delta\pi R \quad (2\text{-}8)$$

Besides, the droplet touching and separating from anisotropic superhydrophobic surface in a vertical direction will not be affected by the position difference in the frictional force. Therefore, the wetting properties, like Cassie transition state (also called meta-stable Cassie state) and Wenzel state, can also be characterized by determining the droplet adhesive force.[25] The adhesive force for a certain hydrophobic surface can be evaluated via dynamic contact angle apparatus. Specifically, a platinum holder that connect to a high sensitivity micro-force balance hang with a testing droplet was controlled to contact with solid surface at constant speed. During the movement, the snap-in force (the droplet touch the surface) generated once droplet in contact with surface and the maximum force the droplet required when it deviated from surface was pull-off force (the droplet separate from the surface, also called maximum adhesive force as shown in Figure 2-1c.

2.3 Superhydrophobic treatment.

With the detailed knowledge on the mechanism of surface wettability, researchers have identified two key factors, namely, low surface energy and roughness structure in preparing superhydrophobic surface. In the following section, we will discuss the chemical functionalization and topographical design in the modification of solid surfaces.

2.3.1 Chemical functionalization

The surface energy of the solid substrate plays a key role in determining the surface wettability. To date, low surface energy materials such as long chain fatty acids, organic silanes and fluorinated compounds are the most used materials to introduce hydrophobicity to a surface. The controlled and precise modulation of the surface chemistry with the desired functional groups is active strategy to prepare smart and advanced liquid wettability system. In this section, we will introduce and summarize the methods for hydrophobic modification based on various reactive functional groups on the surface (Figure 2-2a).

Hydroxyl groups modification

The hydroxyl groups (-OH), as anchoring points for surface modification are widely used due to the ease of functionalization and moderate reactivity. Alkylsilanes modification is one of the most common methods used to prepare hydrophobic monolayers, where reactions of organosilanes ($RSiX_3$, R_2SiX_2, or R_3SiX, where R is an alkyl group and X is a leaving group, such as chloride, alkoxy, or hydride) with OH-bearing surfaces.[26] Specifically, the surface modification with silanes can be conducted under different conditions in either in solution or vapor phase. For liquid-based modification reaction, several factors needed to be considered at room temperature, including the solvent viscosity and polarity, which heavily influence the dispersity of materials. In addition, the amount of water in the liquid medium is also necessary to hydrolyze the silane molecules for further reaction. Sagivs and co-workers[27] were the first to report on the preparation of silane monolayers from the solution phase, and other researchers have also focused on developing other synthetic methods. Lee et al.[28] proposed a simple strategy to fabricate hierarchical structure via a one-step microwave irradiation and the superhydrophobic surfaces were obtained after coating the surfaces with octadecyl-tetrachlorosilane (ODTS) in toluene solution. Recently, Zhang et al.[29]

reported a superhydrophobic coating technique based on a single-step, stoichiometrically controlled reaction of octadecyltrichlorosilane (OTS) in hexane/water, which produced micro-to nano-scale hierarchical siloxane aggregates with a low surface tension. For vapor-phase modification, the prepared surface usually required to expose to a silane reagent for several hours or days at elevated temperatures (50–120˚C). Deng's group[30] developed an effective and reproducible approach to fabricate robust super coating via vapor-phase deposition of semi-fluorinated silane. Besides, hydrophobic modification with fatty acids, such as paraffin wax, steric acid, cinnamic acid, octylphosphonic acid (OP) or myristic acid, are other effective methods to fabricate superhydrophobic surface.[31]

Other hydrophilic groups modification

In addition, chemically reactive interfaces were introduced following facile chemistries including UV-assisted click chemistries, azlactone ring opening reaction, and Michael addition reaction. Accordingly, the surface with different orthogonal reactive functional groups (e.g., NH_2, or COOH) could be easily functionalized using these reactions, after a simple pre-modification step. Specifically, when the surface possesses reactive alkyne groups (-C≡C-) the surface could be reacted with thiols (thioglycerol, 1-adamantanethiol, thiochlolesterol, 3-mercaptopropyl polyhedral oligomeric silsequioxane) through the rapid thiol-yne click reaction to impart superhydrophobic characteristic to the surface.[32, 33] Levkin and co-workers reported on the modification of poly(2-hydroxyethyl methacrylate-co-ethylene dimethacrylate) surface with tetrazole moieties, which allowed the exploitation of UV-induced tetrazole-thiol reaction to prepare superhydrophobic-hydrophilic micropatterns with a site-selective hydrophobic/hydrophobic thiol functionalization.[34]

Besides, the azlactone ring-opening reaction between primary amine-containing hydrophilic small molecules and azlactone groups can be utilized to facilitate the chemical patterning on the hierarchically featured polymeric film, followed by the modification with a hydrophobic amine (decylamine, decafluoroundecylamine, propylamine, octylamine) without any additional catalysts or UV radiation.[35-37] For example, Buck et al.[38] exploited the azlactone ring opening chemistry to prepare covalently crosslinked, chemically reactive interfaces. The films fabricated from alternating layers of azlactone functionalized polymer poly(2-vinyl-4,4-dimethylazlactone) (PVDMA) and poly(ethyleneimine) (PEI) exhibit micro- and nanoscale surface features that

resulted in superhydrophobic character to the surface. Further, Carter et al.[39] reported that the azlactone groups in these covalently crosslinked materials could be functionalized using less nucleophilic alcohol- or thiol-containing compounds, such as an organic catalyst, or converted to reactive acylhydrazine groups by direct treatment with hydrazine.

For the surface with acrylates groups, the reactive polymeric coating could be subjected to post-modification with alkylamines via the facile Michael addition reaction. For example, the alkylamines of increasing chain length used for post-functionalization with various amines, ranging from propylamine to octadecylamine, yielded hydrophobic (pentyl, hexyl, heptyl), and superhydrophobic (octyl, decyl, dodecyl, octadecyl) coatings.[40] Jana et al.[41] developed a switchable superhydrophobic to underwater superoleophobic polymeric materials on exposure to acidic media. The prepared chitosan gel materials, with amine groups on chitosan allowed for a rare pathway to the catalyst-free Michael addition-assisted covalent crosslinking with a multifunctional acrylate crosslinker to obtain a chemically reactive materials for post modification. Recently, the catalyst-free Michael addition reaction was also utilized to integrate naturally derived components to prepare functional bio-inspired materials with tailorable mechanical property and water wettability. Li et al.[42] presented durable superhydrophobic photothermal coatings via the modification of carbon nanotubes with dodecylamine (DDA) and dopamine via Michael addition reaction.

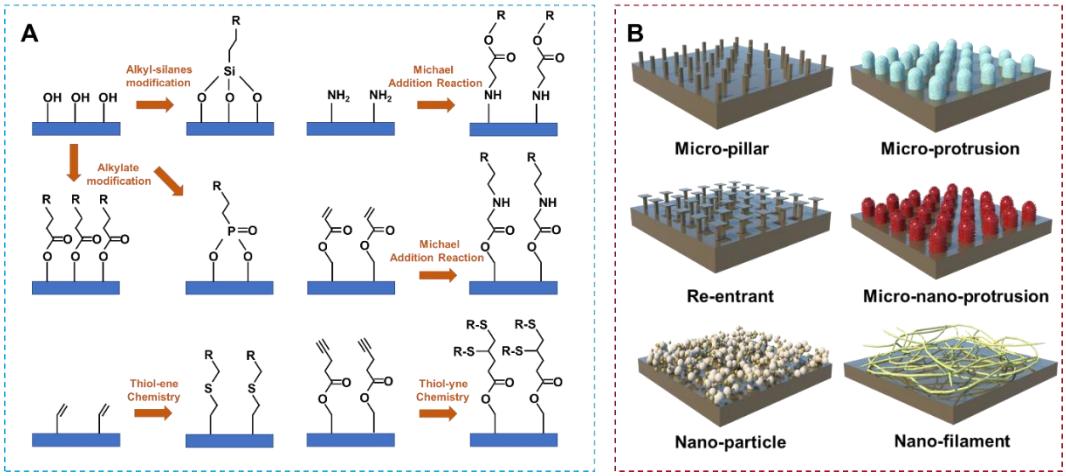

Figure 2-2. (a) Modulation of the surface chemistry with different chemical functionalities. (b) Schematic illustration of surface topographies design using different technologies and in distinct length scale.

2.3.2 Design of topography

In the case of amorphous rough structures, surface roughness is an important parameter to regulate the wetting behavior. As discussed, both Wenzel and Cassie–Baxter theories indicated that a rough surface is essential to impart hydrophobic characteristic to the surface. In the following section, we will introduce the different methods that have been reported to prepare hierarchical surface topographies with distinct topographical scale length to achieve different levels of liquid wettability (Figure 2-2b).

Lithography

Lithography refers to processing of surfaces of materials via etching and laser radiation and it can be used to introduce roughness on different substrates.[43] This method generally begins using the regular micro-structured substrate as the template and then pressing the polymer onto the template. After curing the polymer with the imprinted substrate is released and the micro- or nanostructure is obtained. It is worth mentioning that the lithography method is an important strategy to prepare complex and homogeneous micro scale structure.

The most basic utilization of lithography is to construct micro-pillar arrays on the substrate. This traditional 'top-down' method can reduce the contact fraction between solid and liquid, further increasing the hydrophobicity of the surface according to Cassie's equation. Numerous scientists have investigated on the relationship between roughness and superhydrophobicity by utilizing micro-pillar array system.[44] For example, Butt and co-workers[45] constructed the micro-pillar array surfaces, and regulated the dimension of micropillar and distance between adjacent micropillars. They found that by simultaneously decreasing the asperity size and spacing the solid-air-liquid interface became more stable allowing for a higher impalement pressure without affecting the apparent contact angle. Except for the basic cubic-like micropillar, the nanopatterns with different morphology could further reduce the solid-liquid contact fraction and generate unique physical behavior. As reported by Song et al.[46] and Liu et al.[47] the utilization of lithography could create special conical pillars, and such topography could reduce the contact time and the droplet will bounce on surface displaying a 'pancake' profile. They believed that pancake shaped water profile was the result of the rectification of capillary energy stored in the penetrated liquid transferring into an upward motion that lifted the drop from the surface.

Lithography can be utilized to design more complex and unique surface topography, like over-hang and reentrant structure. Liu et al.[48] introduced a double re-entrant 'T' shape topography and these microstructures consisted of a top surface containing vertical overhangs at the sides. The liquid could wet the top surface and continue down to the vertical overhang stopping at the lowermost point of the vertical overhang, generating the superomniphobicity without the need to coat the surface with hydrophobic materials.

Electrospinning

Electrospinning is a novel and well-known technology to generate nano or micro-nano topographies that is widely used in the field of fabric, membrane, separation and packaging.[49] This method involves subjecting a polymer solution or melt in a high voltage electric field, where the charged polymer droplets are transformed into a jet stream. As the solution is ejected from the nozzle, the solvent evaporates, and a non-woven fabric-like fiber membrane is formed. It can effectively produce homogeneous and continuous micro or nanofiber driven by the effect of electric field to construct irregular nano or micro topography. In the following section, we will introduce the various strategies that researchers utilized for topography regulation toward the field of superhydrophobic modification.

First, controlling the concentration of polymeric precursor solution will directly influence the topography of the prepared film. As reported by Jiang et al.[50], a concentrated polystyrene solution in DMF (25wt%) would generate a network structure composed of numerous randomly oriented nanofiber. A dilute precursor solution (5wt%) would generate microparticles with diameter ranging from 2 to 7 μm due to the constringence and collapse of the fine droplets during solidification upon the evaporation of solvent. If the substrate was prepared from a 7 wt% PS/DMF precursor solution, the prepared film would comprise of microsphere and nanofiber distributed densely over the whole substrate. Each microparticles is interlinked with nanofibers and the randomly distributed nanofibers constitute a 3D network that enhance the structural stability. Kang and co-workers[51] examined the wettability and topography of electrospun fibers produced from PS solution in various solvents. They concluded that in contrast to chloroform and tetrahydrofuran, PS in DMF generated a protuberant secondary structure on the nanofiber surface with a higher roughness and hydrophobicity. Recently, Zhou et al.[52] reported a facile one-step electrospinning method to

prepare a superhydrophobic membrane. They dissolved poly(vinylidene fluoride-co-hexafluoropropylene) (PVDF-HFP) in a high-boiling-point solvent, i.e., N-methyl-2-pyrrolidone (NMP), and control the injection rate to construct a series of bead-on-string nanofiber network. At different injection rates, the formed microsphere possessed distinct sizes, structures and morphologies, endowing the membrane with different topography and hydrophobicity.

In addition to the modulation of precursor solution, the regulation of electrospinning method is also an attractive approach to generate complex surface topography. As developed by Woo and co-workers[53], the co-axis electrospinning could generate homogeneous nanofibers with core-sheath structure and enhanced wetting resistance. The poly(vinylidene fluoride-co-hexafluoropropylene) (PH) core offered a high structure stability and PH/silica aerogel (SiA) at the outer surface of nanofiber could provide enhanced surface roughness and hydrophobicity. Combining these two factors, the formed nanofiber membrane with 3D-hierarchical structure displayed promising potential for long-term application in membrane distillation.

A post treatment of membrane prepared from electrospinning is also a good strategy to produce complex topography. Zeng et al.[54] prepared a 3D graphene fiber by carbonizing electrospun polyacrylonitrile fibers in NH_3 and followed by in situ growth of the radially oriented graphene sheets (GSs) via the thermal CVD process. They claimed that the carbonization process in NH_3 would produce numerous pores and streaks on the nanofibers, and the vertical hydrophobic GSs produced from the thermal chemical vapor deposition process (CVD) resulted in the nanoscale roughness. Additionally, the low temperature sintering method is also a useful method to prepare hierarchical nano, micro-topography. Zou and co-workers[55] use polytetrafluoroethylene /poly(ethylene oxide)/SiO_2(PTFE/PEO/SiO2) emulsion as a precursor solution to fabricate a double roughness membrane via the combination of electrospinning and low temperature sintering. They believe that during sintering process, PEO would decompose, and the micro/nano cavities were formed in the fibers, while the molten PTFE would diffuse, flow and fill the micro/nano cavities forming PTFE/SiO2 fibers with enhanced roughness and hydrophobicity.

Chemical fabrication

Chemical fabrication is one of the easiest preparation methods for topography engineering. By varying the reaction protocols, solvent type, and temperature, materials of various morphology

could be prepared to construct more complex micro and nano surface topography. The chemical deposition method is an effective approach to generate hierarchical structure in various substrates. For example, Li's research group[56] reported on a facile template free electro-deposition method to produce copper micro-cone arrays on various substrates. This approach could be further extended to develop hierarchical micro-nano-cone array using secondary deposition process (like Ni and Ag), to prepare double length scale rough topography.[57, 58] Utilizing the replacement reaction, Cao et al.[59] deposited a layer of flower-like Ag micro clusters on the surface of copper mesh and the cluster is composed of numerous nano-sized ginkgo-leaf-like lamellas. This type of nano and micro hierarchical structure dramatically enhanced the surface roughness, which is necessary for preparing the superwetting surface. Xu et al.[60] fabricated a micro-nano dendritic topography via a vacuum thermal evaporation and chemical deposition process. The vacuum deposition process would form a homogeneous copper film of 100 nm thickness on a steel mesh. The chemical deposition process using $AgNO_3$ solution would gradually oxidize the Cu to Cu_2O as confirmed by X-ray diffraction (XRD) and the silver recrystallized into the dendrite morphology generating a double length scale roughness.

The chemical etching is also a surface roughening technology for generating nano-, micro topography, which is widely adopted in the preparation of metallic substrate. Qu et al.[61] used nitric and sulfuric acids as etching agents to prepare rough topography with numerous cavities and island structures on the surface of steel/copper alloy. They demonstrated that these unequal morphologies were attributed to the distinct etching rate on the alloy surface due to the heterogeneous distribution of metals in the alloy. Besides the acid etching, alkaline solutions are also widely used as etching agent. Lei and his research group[62] immersed fresh copper film into dilute ammonia solution (0.03M) for etching over a 36h period. After reaction, a large number of $Cu(OH)_2$ needles would form on the surface perpendicular to the substrate. Surprisingly, the lateral surface of the needles was also sculptured with nanogrooves in the longitudinal direction and each needle possessed 4 to 8 grooves on its surface. They believed that this unique topography might be attributed to the hydrogen bond interactions between the copper hydroxide nanoribbons that were stacked along the axial direction, forming bundled structures that grew into the nanogrooves.

Another convenient and effective method to construct complex topography is the wet chemistry method, such as hydrothermal and sol-gel method. Yu et al.[63] reported a complex core/shell

nanowire array structure on nickel foam via the hydrothermal reaction between $Co(NO_3)_2 \cdot 6H_2O$, NH_4F and $CO(NH_2)_2$. Besides, Liu and co-workers[64] designed a ZnO@SiO_2 nanorod array on cotton fiber, that displayed a strong water repellency and UV-blocking characteristics. The generation of the hierarchical topography comprises three steps: (1) deposition of ZnO seed on cotton fibers via dip-coating, (2) hydrothermal reaction to construct ZnO nanorod array, (3) a layer-by-layer deposition of SiO_2 to increase the nanoroughness of the surface. Seeger's research group[65] designed a robust hierarchical structure by combining micro glass bead, silicone nanofilaments and TiO_2 nanoparticles. To prepare such well-organized topography, three major steps are required. Initially, the microscale (75 μm) glass beads were deposited on the low-density polyethylene (LDPE) substrate and partially embedded into the matrix by medium temperature heating. Utilizing the droplet-assisted growth and shaping (DAGS) method, a homogeneous silicone nanofilaments (SNF) was coated on the surface of LDPE substrate and glass beads. Then, the TiO_2 nanoparticles were decorated on the SNF surface via a mild hydrothermal reaction of TiF_4. They concluded that the micro-scale structure (glass beads) would enhance the mechanical strength and stability of the surface topography and the nanoroughness from the SNF and TiO_2 nanoparticles would decrease the solid-liquid contact fraction and increase the hydrophobicity. The combination of inorganic nanoparticles and organic polymer is an alternative approach to improve the mechanical property of hierarchical structure. Xu et al.[66] grafted γ-Aminopropyltriethoxysilane (APS) on the surface of silica nanoparticles, forming a well dispersed paste-like or semisolid gels. The dispersed sols were utilized to construct the micro-nano porous structure on glass substrate due to the agglomeration of silica nano particles from the dip-coating process. It is worth mentioning that the coating of APS could increase mechanical strength of topography and increase the surface transmittance. Recently, Li et al[56] reported a convenient and practical "glue+powder" method for the construction of hierarchical microstructure and superhydrophobic surface. In this work, a thin layer of diluted and uncured commercialized polydimethylsiloxane (PDMS) is firstly deposited on solid surface and acted as glue for powder fixing. Then two types of powders can be utilized for topography construction, the nanoparticles which radius much smaller than the thickness of PDMS layer or the microparticles with a lager diameter. They found that the smaller particles tend to aggregate and form the microscale clusters on the surface which stuck by the cured PDMS. In the meantime, the increased roughness and encapsulated PDMS will facilitate the surface water

repellent property. Differently, due to the large diameter of microparticles, the PDMS will only migrate and partially decorate particles' surface, retaining the initial surface microroughness. It is also worth to mention that the intrinsic wettability of particles has little relationship to the final superhydrophobicity of solid surface, expanding the application fields and functionalities of superhydrophobic surface.

Template method

The template method refers to the use of suitable polymers to pattern the surface with micro- and nanostructures. The template can be from natural plant source, inorganic or organic substance with a special regular structure, such as porous alumina and colloidal microspheres. Once the original template is inversed, the copy layer can be obtained by dissolving the template. Thus, it is a convenient and cheap way to construct nano, micro or micro-nano hierarchical topographies.

The lotus leaf is a well-known superhydrophobic system that researchers have prepared micro-nano hierarchical topography by mimicking its surface structure. Ji and co-workers[67] reported for the first time the use of liquid poly(dimethylsiloxane) (PDMS) to mould fresh lotus leaf yielding a negative template after solidification. Then a monolayer of trimethylchlorosilane (TMCS) and a second PDMS replication was performed. The hierarchical micro, nano topography would be transferred to the artificial PDMS surface with high precision. Due to the water evaporation during the templating process, shrinkage of papillae structures occurred resulting in a variation of surface topography. Furstner et al.[68] utilized the polyether (PE) to replicate the surface of lotus leaves with a similar micro-topography without nano crystalloids.

There are many reported studies on the development of micro-nano surface topography via the replication of different biological templates. For example, the mimicking of Salvinia molesta leaf with complex egg-beater topography endowed the surface with a special air-retaining capability under water.[69] The duplication of topography from gecko feet produced surfaces with superydrophobicity and ultra-high adhesive force, both in dry and wet conditions.[70] By utilizing rice leaves as template, micro-papillae array with anisotropic distribution on the surface was prepared and it possessed directional water transportation capability.[71] In addition, the wings of butterfly (Morpho aega) possess unique topography, comprising a large number of quadrate scales, of length of 150 mm and width of 70 mm to form a periodic hierarchial surface. Interestingly, by

replicating this unique surface structure, the droplet would transport in one direction while pinned on the surface in reverse direction.[72]

The inorganic materials can also be used as template for constructing nano- and micro topography. For example, anodic aluminum oxide (AAO) membrane has a high-density porous structure, and is good candidate for constructing nanotube or nanopore topography. For instance, Liu et al.[73] used porous alumina (AAO) as a template to prepare nanofibrous membranes via extrusion of polyacrylonitrile (PANI) and polyvinyl alcohol (PVA). Also, Lee et al.[74] used AAO and textured aluminum sheets as replicating templates. The molten polystyrene (PS) was used as a substrate in the templating process. After cooling to the room temperature, the template (aluminum-based materials) was removed by immersing in $HgCl_2$ solution. In this way, it is convenient to produce the PS nanofiber array with large surface area. Another popular inorganic template is porous candle soot. Deng et al.[75] deposited a layer of black candle soot on a glass consisted of carbon particles of diameter of 30 to 40 nm, that displayed a loose, fractal-like network. Then the chemical vapor deposition process was conducted to coat a silica shell on the soot particles. After high temperature calcinating, the carbon core was combusted while the silica shell maintained the roughness and topography.

2.4 Superhydrophilic treatment

In 1996, the term "superhydrophilic surface" was first coined, in a manner akin to the superhydrophobic surface. Specifically, researchers led by Fujishima defined a surface with superhydrophilicity as one that exhibits a static contact angle lower than 5° when in contact with a water droplet.[76] Later studies suggested that a superhydrophilic surface must achieve a static contact angle of less than 3°, or that a water droplet should completely spread and form a water film on a rough surface with $r > 1$. However, the definition of superhydrophilicity is still subjected to debate, as roughness is not always necessary to produce film-forming surfaces for water.[77]

In technological applications, there are two distinct types of superhydrophilicity that are frequently discussed. The first is super-adsorbing surfaces, which draw inspiration from natural plant structures such as Sphagnum or peat moss. These porous, sponge-like structures are capable of absorbing more than 20 times their dry weight. The hair-like microstructures of these plants contribute to their superhydrophilic properties, which aid in the uptake of water and nutrients. For such porous

structures, the appropriate definition of superhydrophilicity is related to the adsorption time. Some researchers suggested that the adsorption-based superhydrophilic surfaces should minimize the spreading time to less than 0.5 seconds.[78] The Cassie-Baxter wetting mechanism for adsorbing-based superhydrophilic structures exhibits subtle differences when compare to their superhydrophobic counterparts. Owing to their highly interconnected structure, strong capillary forces facilitate the penetration of water into the structure. As a result, the Cassie-Baxter equation must be modified to account for these effects (Eq. 2-9):

$$\cos\theta = \varphi_s(\cos\theta_1 - 1) + 1 \qquad (2\text{-}9)$$

where θ is the apparent contact angle, θ_1 is the intrinsic contact angle and φ_s is the porosity. The relationship between the surface porosity and apparent contact angle for highly hydrophilic surfaces is evident from Eq. (2-9). In Figure 2-3, it can be observed that when the intrinsic contact angle is below 20°, surface wettability is minimally affected by porosity. In this case, achieving superhydrophilicity requires only a low porosity. On the contrary, when intrinsic contact angles are greater than 20°, porosity significantly impacts the measured contact angle. To attain superhydrophilicity in such scenarios, a high porosity (φ > 90%) is required, particularly when intrinsic contact angles exceed 40°.[79] However, in a porous system, the surface will fully adsorb the droplet when the volume of the pores exceeds the droplet.

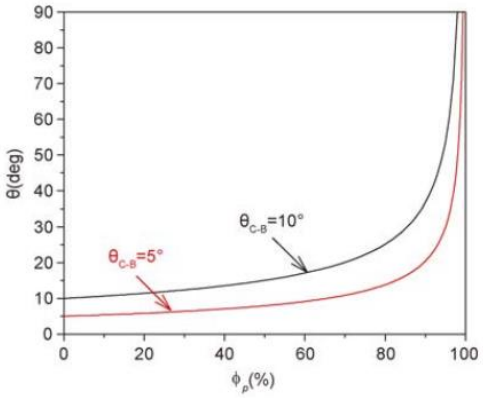

Figure 2-3. Relationship between the minimum porosity and the intrinsic contact angle necessary to achieve superhydrophilicity on porous surfaces.[79]

The second type of superhydrophilicity is characterized by the rapid and complete spreading of water on a solid surface, forming a thin liquid film that eliminates light scattering instead of

adsorbing the light. To achieve this type of superhydrophilicity, the apparent contact angle limitation is not the only considering factor. The spreading time and surface roughness also need to meet the specific criteria. As for the superhydrophobic surface, researchers have proposed that a surface with sufficient roughness ($r > 1$), fast spreading time (<0.3s), and a contact angle less than 3° can be classified as a spreading-based superhydrophilic surface. When characterizing the dynamic spreading behaviors of superhydrophilic surfaces, the Wenzel equation was found to be suitable since it accounts for the complete penetration of water droplets into the rough surface structure. Due to the hydrophilic nature of the surface, capillary forces are generated, resulting in both advancing and pinning forces acting on the top of the rough structure when in contact with water. The advancing force encourages the water to spread out across the surface, while the pinning forces restrict the spreading. At this point, the roughness of the nanostructure becomes crucial, as only when it surpasses a superspreading criterion does it enable the droplet to overcome the pinning forces and continue spreading, as illustrated in Figure 2-4.[78]

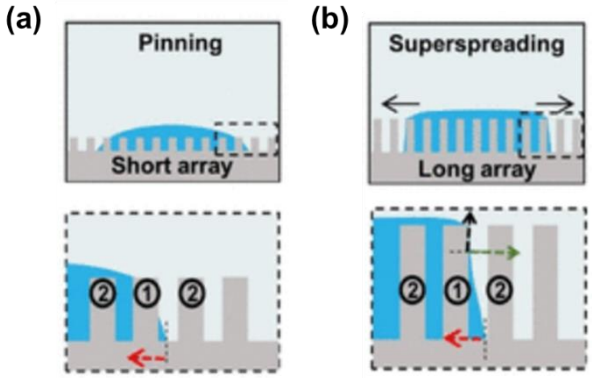

Figure 2-4. Effect of surface roughness on water spreading. (a) The liquid spreading process will be pinned on a short array. (b) Only when the length of a nanofiber or the roughness of the nanostructured surface is larger than a critical value will the superspreading occur.[14]

Many techniques have been used to prepare a superhydrophilic surface by combining the structural modification and surface chemistry functionalization that is very similar to the superhydrophobic surface construction as discussed in section 2.3. However, the superhydrophilic modification is achieved by grafting functional groups with high water affinity, such as hydroxyl (-OH), amidogen ($-NH_2$) and carboxyl (-COOH) groups. A range of methods can be employed to introduce high-

energy functional groups onto a surface, such as UV irradiation, plasma etching, and chemical modification. For instance, UV light can induce the formation of hydroxyl groups on the surface by generating highly active free radicals, regardless of the type or morphology of the substrate.[80] Similarly, plasma etching can break and reform chemical bonds on the solid surface, resulting in the formation of hydroxyl groups through energy and ion bombardment using a plasma source.[81] However, these physical fabrication methods have several limitations that hinder their large-scale applications. For instance, the highly active free radicals generated during UV irradiation can induce unintended side reactions, altering the surface's structure and morphology. Additionally, the complex equipment and energy requirements of these methods increase the cost of such hydrophilic modification processes, thereby limiting their extensive utilization. The chemical modification offers an efficient and easy approach to construct stable high-energy functional groups. Such as the silane coupling agent and sulfhydryl modifier based on chemical grafting and the widely accept RCA (Robertson-Cockrell-Anderson) redox reaction used in the semiconductor industry.[82] These modification methods could not only accurately tune the surface hydrophilicity in temperature and pressure windows, the additional functional groups could also be introduced onto the surface during the surface grafting, endowing the surface with special properties, such the antimicrobial property, anti-fouling property, biocompatibility. Thus, based on the types and properties of substrates, suitable modification methods should be chosen for surface hydrophilicity construction.

The surface topography construction is another important factor to achieve the surface superhydrophilicity, while it has a little difference when fabricating super-adsorbing and spreading surfaces, which focuses on the creation of a porous substrate to increase the capillary force or to increase the roughness. Except the aforementioned methods, like electrospinning, sol-gel, hard/soft templates, the porous and microchannel construction is also a consideration to achieve superhydrophilicity. Inspired from animals' corneas which have a super-spreading time of less than 839 ms, the superspreading phenomenon is induced by the double-scale micro/nano structure, where periodical polygonal nanofiber array microdomains are separated by microchannels.[83] The nanofiber arrays induce in-/out-of-plane nanocapillary forces, which improve the surface hydrophilicity, while the microchannels control the flow and significantly accelerate the superspreading process. Similarly, Ma and co-worker[84] reported that the spreading capability was controlled by the trade-off between the capillary pressure and the viscous resistance generated by

the length scale of the structure feature. They designed the special inter-connected “V groove” copper nanowires on surface, where the hydrophilic characteristic and uniform distribution of Cu provided sufficient capillary pressure. The V-groove with sufficient height and depth were the liquid film transport microchannels that reduced the viscus resistance and increasing the wicking efficiency.

2.5 The superwettable surface

The rational and precise design of surface chemistry and topography could endow the surface with unique water manipulation capability, like distinct adhesion or responsiveness. The various regulation methods and special capabilities extend the the practical application of superwettable surfaces. In the following section, we will detailly describe the mechanism and fabrication method for these special superwettable surfaces and on the utilization of environment and energy applications.

2.5.1 Tunable adhesion of superhydrophobic surface

Recent studies on Lotus leaves and Rose petal revealed that a superhydrophobic surface with both a large CA could exhibit significantly different water adhesion characteristics.[85] Although both surfaces are covered with micro wax protrusion, these two kinds of extreme super-antiwetting situations in nature, ‘Lotus leaf’ and ‘rose petal’, indicate the interaction force between liquid droplet and the solid surface. For Lotus leaf like superhydrophobic surface, the droplet sliding off the surface with ultra-low tilt angle and the adhesion force is extremely low. On the contrary, the droplet will be pinned on the sticky rose petal superhydrophobic surface, exhibiting high adhesive force. Recently, the controllable adhesive superhydrophobic surface has attracted increasing interest since their representative wetting phenomenon and promising application, such as the none-loss microdroplet transportation in microfluidic devices.[86] Previous research demonstrated that the synergistic effect of surface chemical components and structural topography plays a crucial role in tuning the liquid adhesion on the special functionalized surface. In this section, we will describe several examples on the modification of surface functional groups and the construction of nanostructure for designing superhydrophobic surface with tunable adhesion.

Morphology control

By mimicking the mechanism of gecko feet with ultra-high surface adhesion, Jin et al.[87] utilized a porous anode aluminum oxide nanotube as sacrificial template and deposited a hydrophobic polystyrene (PS) layer. The prepared PS nanotubes layer exhibited large water contact angle (CA) and CA hysteresis. The droplet would adhere to the surface and the interaction force between liquid and surface approached 59.8 μN. The author claimed that this remarkable adhesion is mainly derived from the intimate interaction between the PS tubes and water droplets. According to the mechanism of gecko feet, the high density of PS nanotubes would generate a high Van der Waal's force, leading to the strong adhesion between PS layers and liquid droplets. Notably, the adhesive force increased to 75.2 μN when the density of PS layers approached $7.44x10^6$ nanotubes mm^{-2}, demonstrating the tunable adhesion property of the surperhydrophobic surface. Accordingly, to better understanding the mechanism between tunable adhesion and topography construction, Lai et al.[88] designed three types of superhydrophobic TiO_2 nanostructured substrates as shown in Figure 2-5a, which consisted of nanopore array (NPA), nanotube array (NTA) and nanovesuvianite structure (NVA). Interestingly, three structures displayed various wetting properties caused by the controllable porosities that effectively adjusted the air-pockets below the water droplets within the porous structure. The NPA and NCA exhibited the highest and tunable adhesive force respectively due to the negative capillary force generated by the sealed-airpocket structure. Based on their open air-pockets model, the droplet would hardly stick on the NVA, displaying the 'Lotus leaf' superhydrophobicity. The experiment results indicated that the surface adhesive force could be adjusted by controlling the solid-liquid contact and fraction of air pockets within nanostructure system.

Recently, Kim et, al.[89] prepared two types of structured surfaces with open-pore zinc oxide nanowires (SH-ZnO) and sealed-pore anodic aluminum oxide nanochannels (SH-AAO). After depositing a monolayer of octadecyltrichlorosilane (OTS) on the outer surface, the two surfaces displayed high contact angle and water repellency (Figure 2-5b). The water droplets adhered to the SH-AAO surface when the substrate was inverted at 180°, and the adhesion properties would impact the dynamic behavior of droplets in contact with the superhydrophobic surface. As shown in Figure 3B, the water jet would splash and bounce off the SH-AAO surface while maintaining contact with the SH-AAO surface without rebounding, indicating that the potential capability of sticky superhydrophobic surface to handle large quantities of water. Another successful example on the topography control of surface adhesive force was reported by Naito and coworkers[90]. They used

the commercially available methods to construct a layer of porous ZnO tetrapod acicular skeletons and polydimethylsiloxane (PDMS) was uniformly dispersed as adhesive and hydrophobic modification agent. By controlling the preparation method (dip-coating or spin-coating) and fabrication time, four types of superhydrophobic surfaces mimicking gecko, petal, and lotus were constructed with different roughness factor and length of roughness, while keeping the same chemical composites (Figure 2-5c). The key findings are: (1) Single nanosized roughness would lead to the gecko effect superhydrophobicity, and the adhesion is velocity-sensitive and could be utilized to handle high-speed droplets and need strong adhesion, (2) Both existence of nano and micro-sized rough hierarchical structure would reduce the adhesion and transform the wetting state from Petal to Lotus state (from high adhesion to low adhesion).

Besides the tube-like morphology, the surface constructed by hierarchical particles will also exhibit superhydrophobicity with switchable sticky characteristics due to their over-hang structure. Chen et al.[91] presented a superhydrophobic surface constructed by all-polymer particles, which can adjust the wetting property from highly adhesive to self-cleanable. In their protocol, the hollow reactor particles were first prepared via a sacrificial hard SiO_2 template method. To achieve the multi-scale hierarchical structure, nanocomplex was synthesized by 1,4-conjugated addition reaction between dipentaerythritol penta-/hexa-acrylate (5Acl), octadecylamine (OTCA) and polyethylenimine ethylenediamine (BPEI) in tetrahydrofuran (THF). By controlling the reaction time and ratio between the reactor and nanocomplex, the nanosized roughness can be finely adjusted from oversized to undersized. As a result, only the suitable dense and size of nanoparticles, appropriate hierarchical structure with the Lotus-leaf superhydrophobicity satisfying the requirement of air-pocket layer thickness and solid-liquid contact fraction. In addition, both the oversized or undersized nanoparticle would produce the adhesive effect and achieve the Cassie impregnating wetting state (rose-petal like superhydrophobic surface) in the absence of nanocomplex on the surface. Besides, Xu et al.[92] reported a solution precursor plasma spray (SPPS) technique to design superhydrophobic ytterbium oxide (Yb_2O_3) coating. The surface was distributed with micro-sized clusters with inter-cluster gaps. For each single cluster, the nanosized Yb_2O_3 particles and slats were randomly coated, forming the nano-sized roughness structure. Due to the presence of double-scale hierarchical structure, the resulting surface possessed a high static CA (162°) and extremely low roll-off angle (5°). Interestingly, the adhesive force gradually increased with the number of plasma

scans and the surface lost its superhydrophobicity after 9 scans. It is believed that the increase in the adhesion was attributed to the smoother topographies and higher solid-liquid area fraction. Tan et al.[93] used a facile, template-free 3D-shrinking method to generate a "rose-petal" like graphene micropapillae superhydrophobic surface. The hydrophilic oxygen containing groups (-OH and -COOH) on surface promotes the chemical adhesion to the water droplets due to hydrogen bonding. The adhesive force of superhydrophobic surface depended on the number, or the arrangement of the papillae arrays. Additionally, this superhydrophobic surface could attach to different substrates, like tweezers or gloves, acting as a physical barrier and soft microdroplet manipulator for toxic chemical reaction (**Figure 2-5D**). It is worth mentioning that the hexagon array could generate ultra large adhesive force of up to 129.4 μN that is capable of capturing a maximum liquid volume of 22 μL while maintaining the superhydrophobicity (The CA about 170˚). This finding offers a new inspiration for the design of 3D superhydrophobic surface with tunable adhesion.

Control of Chemical composition

The chemical composition is also a critical parameter to manipulate the surface wettability and adhesive force. For superhydrophobic surface with high roughness, the heterogeneous chemical composition, such as the chemical state of surface functional groups would generate external solid-liquid interaction, thereby increasing the surface adhesive force.

One example was reported by Lai and co-workers,[94] who prepared a high roughness TiO_2 layer with sponge like morphology. After modification with 1H,1H,2H,2H-perfluorooctyltriethoxysilane (PTES), the droplet placed on the surface exhibited a perfect sphere shape and could easily roll off the surface due to the Lotus-leaf superhydrophobicity. However, if the surface was modified with a mixture of PTES and trace amounts of nitrocellulose, the dynamics of water droplet on surface could resist the gravitational forces when the sample was tilted vertically (90°) or even turned upside down (180°) due to the strong adhesion. The morphology and topography estimated by SEM and AFM indicated that the surface morphology did not change except for the variation of chemical composition. They characterized the surface free energy variation after the modification with PTES-NC mixture, concluded that the high adhesion was caused by two factors: (i) the functionalized NC on surface would disrupt the densely packed hydrophobic PTES structure, leading to a lower static contact angle, (ii) the hydrophilic nitro groups in the NC molecule would generate hydrogen bonds

with water molecule, increasing the solid-liquid interaction and surface adhesive force.

Recently, Jana et al.[95] reported a superhydrophobic surface prepared with biodegradable polymer that displayed chemical activity and tunable adhesion. In this study, the chitosan nanoparticles were first prepared by the de-solvation method and grafted with dipentaerythritol pentaacrylate (5Acl). The resulting particles were further modified by exposing them to two types of functional groups, amine and acrylate groups. Interestingly, if the surface proceeded with a post-treatment with octadecylamine (ODA), the acrylate groups on surface would be grafted with long hydrocarbon chain, showing a strong hydrophobicity. However, the residue amine groups from the chitosan particle endowed the surface with pH sensitivity, where the droplets would form a spherical shape on the surface at pH greater than 3 and spread out at pH lower than 3. This is attributed to the protonated amine groups in acidic condition, which perturbs the chemical environment (low surface free energy) that is necessary for preparing water repellent surface caused by in the loss of air-pockets trapped in rough structures. Besides, the surface would display superhydrophobic with high adhesion when the amine groups are substituted by decanoyl chloride (DC) via nucleophilic addition, since the hydrophilic acrylate groups induce strong chemical activity and generate strong interaction force with the water droplet. Additionally, the surface would simultaneously exhibit low adhesion and superhydrophobicity when the nanoparticles were reacted with DC and ODA mixtures. Both the acrylate and amine groups would be replaced by hydrophobic hydrocarbon chains, resulting in the 'lotus-leaf' superhydrophobicity.

The tuning of intrinsic chemical structure can also adjust the wetting property and behavior of the surface (Figure 2-5e). Li et, al.[96] designed a new type of sticky superhydrophobic surface by forming numerous bundle-like cerium oxides (CeO_2) nanotubes on the outer surface. The wetting experiment showed that the water CA of the prepared CeO_2 surface could reach up to 157˚, indicating strong water repellency and superhydrophobicity. Notably, the surface could generate strong adhesive force to the liquid and the critical weight for hanging droplet is as high as 20 mg when the film was tilted at 90˚. The authors believed that the superhydrophobicity was caused by the preferentially exposed hydrophobic (111) crystal plane of CeO_2 and the tube-like micro-nano hierarchical topography. Meanwhile, the air-pockets sealed the open-pore CeO_2 nanotubes under the water droplets generating negative Laplace pressure and produced a strong capillary force and a sticky effect. Interestingly, the adhesive force of CeO_2 superhydrophobic surface would increase

after UV irradiation as shown in Figure 3C due to the lower oxygen concentration and the defective Ce^{3+} in the structure. The peroxide intermediates dissociated under UV irradiation of the CeO_2 film converting Ce^{3+} to Ce^{4+}, which increased the amounts of hydroxyl groups on the surface as confirmed by XPS analysis. Consequently, the enhanced hydrogen bond interaction between additional hydroxyl groups and liquid droplet would increase the adhesion with little effect on the static CA. Besides, the adhesion returned to its original state after high temperature calcination (450˚C) since the replacement of oxygen atoms at oxygen vacancies (hydroxyl groups), indicating the tunable adhesion property.

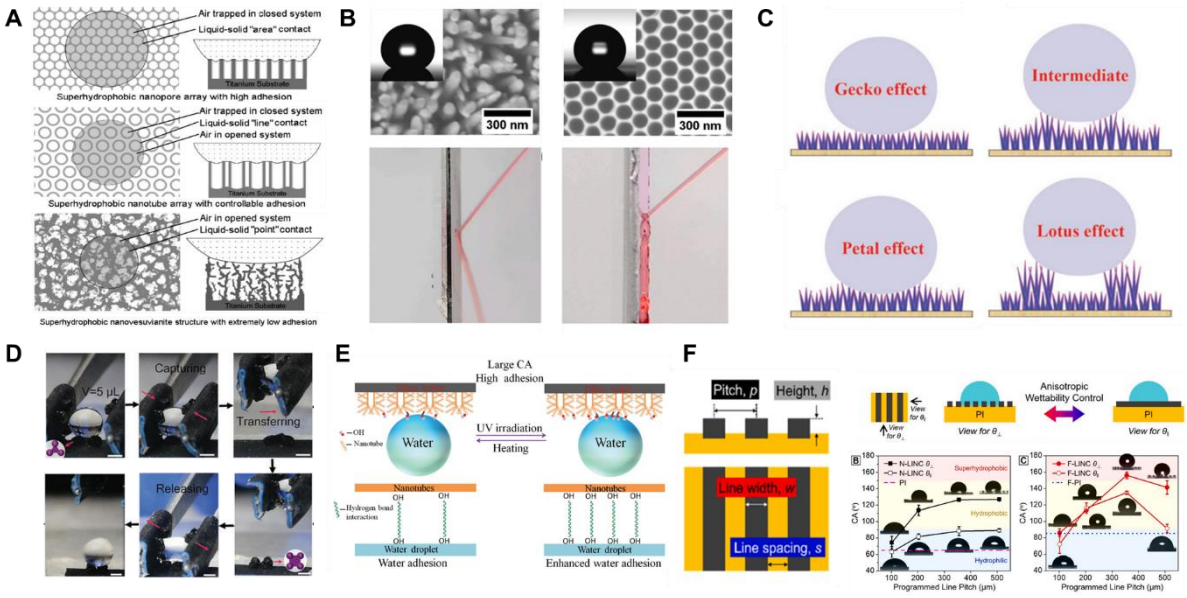

Figure 2-5. The examples of superhydrophobic surfaces with tuable adhesive force. (a) Schematic illustration of three types of superhydrophobic nanostructure models with high water adhesion, controllable water adhesion and low water adhesion, respectively. [88] (b) The static contact angle and SEM images of SH-ZnO and SH-AAO (top two images), respectively, and their water contacting behavior difference. [89]. (c) schematics of water droplets sitting on superhydrophobic surface with different wetting state. [90]. (d) Controlling the maximum liquid capacity and adhesive force of papillae arrays by regulating the arrangement of the papillae (left) and the snapshots show the transfer process of one droplet from triangle array (N=3) to square array (N=4) via microdroplet-manipulation tweezers (right). [93] (e) Schematic illustration for regulation of water adhesion over the film of CeO_2 nanotubes. [96]. (f) Schematic diagrams of LINC micropatterns showing geometric parameter (left) and Anisotropic wetting behavior of

heteroatom-doped LINC micropatterns (right). [97]

External force control

The in-situ or post treatment by external processes, such as laser etching and machinal pressing, can be used to generate superhydrophobic surfaces with tunable adhesion. For example, Nam et al.[97] prepared a fluorinated graphene superhydrophobic surface by post laser etching treatment. The surface displayed strong adhesion between the water droplet and textured surfaces clearly illustrating the synergistic effect between surface chemistry and topographic regulation. Two well-ordered laser-induced nanocarbon (LINC) patterned surfaces with nitrogen doping (N-LINC) and fluorine doping (F-LINC) were constructed on flexible polymer films with adjustable line width and pitch distance as shown in Figure 4F. According to the observation of CA from different viewing direction (parallel CA ($\theta\parallel$) and perpendicular CA ($\theta\perp$)) to the direction of the lines in Figure 2-5f), an important findings is that the structure strongly influence the apparent CA in some surfaces. For N-LICN surface, all the $\theta\parallel$ were lower than $\theta\perp$ in different programmed line pitch distance (p) since the Wenzel wetting state of the droplet could easily spread in the parallel direction compared to the perpendicular direction of surface, leading to a reduction in the apparent CA. The fluorinated surface modification could significantly increase the CA at the same pitch distance. Besides, the superhydrophobicity was achieved when the line pitch was increased to 355 μm and the trapped air pockets beneath the droplet were clearly evident. Interestingly, the surface was sticky to the water droplet and this adhesive force can decrease by bending the flexible sample to inject more air into the micropattern arrays, enabling the release of water droplets. This study provides a scalable structural engineering and surface chemistry modification protocol for manufacturing flexible devices with tunable surface wetting and adhesion. In addition, Mazaltarim et al.[98] proposed a facile and versatile two-step etching method to prepare adaptive superhydrophobic surfaces with tunable adhesion. A mechanical induced fracturing step would significantly reduce the solid-liquid contact and the chemical etching process produced numerous nanosized bumps and protrusions on the surface that increased the nanorougness of the surface. Notably, the surface adhesion can be tuned by altering the surface chemistry with a fluorosilane reagent, achieving a wide range of adhesive force control. Besides, air-pressure is also a convenient way to control the surface morphology and structure. For example, Li et al.[99] reported a facile and scalable pressure-control method for constructing superhydrophobic surfaces with adjustable adhesion. The polytetrafluoroethylene (PTFE) microparticles with uniform size and morphology were first

dispersed in fluorinated epoxy resin solution. By controlling the air pressure during the spraying process, the modified PTFE particles would self-assemble into a hierarchical topography with different roughness. The lower working pressure would generate a relatively smoother surface and the droplet would partially penetrate the microstructure, causing a Cassie-impregnating superhydrophobic state and an increase in the surface adhesion. On the other hand, the hydrophobic particles would agglomerate into larger protrusion forming a rougher structure, endowing the surface with a lower adhesion and the Cassie superhydrophobic wetting state.

The utilization of shape memory polymer (SMP) can achieve an in-situ control of topology and structure, resulting in a tunable wetting behavior. Chen et al.[100] described a shape memory polymer (SMP) superhydrophobic surface with directional adhesion control. By mimicking the surface structure of lotus leaf, this study designed the micro array structure and with numerous nanopits on the pillar tips. The wetting experiment showed that the structured surface has a high static contact angle as high as 151˚ and a low sliding angle (24˚) in different directions, indicating the surface possessed a superhydrophobic isotropy in both static and dynamic wettability. Interestingly, the surface can be constructed with microscale groove (about 260 μm) by pressing with a template at a temperature of materials exceeding the glass transition temperature, T_g. The pressed micropillars exhibited uniform deformation and orientation while those unpressed micropillars maintained the original morphology (rice-leaf like structure). The surface displayed a superhydrophobic anisotropic wetting behavior, where both the sliding angle and static CA measured perpendicular to the groove was higher than in the parallel direction. Further, the wetting behavior can restore to the initial state after heating the surface higher beyond T_g and such transition can be repeated several times without any deterioration in the behavior. The author claimed that the special and different wetting behaviors of two surfaces were attributed to the external energy barrier arising from the topography. This strategy to manipulate the dynamic wetting behavior based on the morphology control of SMP materials can be extended to other SMP materials that respond to other forces. Bai et al[101] also reported the superhydrophobic surface from laser-induced shape memory polymers (SMP) with switchable adhesion forces. The mechanical stress would alter the morphology of the micro arrays from vertical standing to bending state, and alter the wetting state from Cassie to water-impregnating Cassie state that displays high sticky force. Besides, the surface would recover its original wettability and morphology after thermal annealing. Inspired by gecko's

feet with tunable adhesion, Zhang et al.[102] design a layer of hydrophobic micro-PU pillars array on shape memory polymer (SMP) substrate, which displayed superhydrophobicity and switchable adhesion to both water and solid. The surface free energy could be regulated via the oxygen plasma treatment at different times and the value of γ_s varied between 24.6 to 52.1 mN m^{-1}. Besides, the SMP allows the surface reversibly to transform from curved and uncurved shapes at temperatures above the glass transition point (T_g). For the curved shape, the number of pillars is not in the same plane and only very few pillars are in contact with the target surface and the total adhesive force would increase in uncurved shape due to the higher contact area, offering an ON/OFF adhesion control.

2.5.2 Hydrophilic/superhydrophobic Hybrid surface

Recently, a single and uniform superhydrophobic surface is not sufficient in a wide variety of applications. The hybrid superhydrophobic surfaces that combined distinct wettability properties (hydrophilic or hydrophobic) on the same surface were developed to meet the complex and specific requirements of real applications. In this section, we will discuss the hybrid hydrophilic/ superhydrophobic surfaces from two perspectives: (1) surface patterning that are divided into homogeneous patterned surface and heterogeneous structured surface in accordance with the pattern of wettability, (2) surface functionalization that focuses on spatial control of chemical or morphological structures in specific locations on the surface.

Surface patterning

A variety of methods can be used to fabricate or tune the chemistry and morphology of surfaces to produce various wettability characteristics. First, we will present some of the methods used to prepare surfaces with patterned structures.

Homogeneous patterned surfaces

Lithography encompasses many different types of surface patterning methods, and it is useful for generating superhydrophobic surfaces where the shape and pattern of the structures are well-defined. One of the common methods is photolithography, which can be sub-divided into various categories depending on the radiation source: UV[103], X-ray[104], and e-beam[105]. Chen et al.[106]

demonstrated that the controlled growth of conducting poly-pyrrole polymer microstructures can be realized on superhydrophobic micropillar-structured silicon templates by a direct laser writing method combined with electrochemical polymerization (Figure 2-6a). Gurumukhi et al.[107] described a biphilic surface to study the dynamic defrosting, where the surface fabricated by a microstructured superhydrophobic CuO surface and laser ablation to introduce hydrophilic characteristics to the surface. Lo et al.[108] proposed a three-dimensional (3D) hybrid surface to enhance the condensation at high subcooling temperatures. The 3D hybrid surface consisted of superhydrophobic (SHB) nanowire arrays and hydrophilic microchannels, constructed via the patterning of the photoresist on the Si substrate followed by deep reactive-ion etching of the microchannels (Figure 2-6a). Besides, nanoimprint lithography (NIL) is one of the modern techniques for pattern replication.[43] In this method, pattern replication is induced using heat and pressure. Leitgeb et al.[109] demonstrated the fast (>10 m/min) and continuous fabrication of multilength scale structures by roll-to-roll UV-nanoimprint lithography on a 250 mm wide web (Figure 2-6b). Moreover, template-based methods are very suitable to prepare regular surface morphology. Oh et al.[110] developed highly scalable, simple, and nondestructive NIL using a dissolvable thermoplastic resin as the template with surface nanofeatures of ∼100 nm in height, replicating from cicada wings.

Heterogeneous structured surface

Many approaches have been developed to prepare surfaces with heterogeneous topography, including phase separation, crystal growth, assembly of particles, and etching. Rough surfaces can be formed by the phase separation of a multi-component mixture, and one of the common routes is sol-gel method.[111, 112] Besides, hierarchical structure can be generated by crystal growth, while the crystallisation parameters, such as rate of cooling and solvent evaporation or addition can be altered to manipulate the size and shape of crystals. Liu et al.[113] designed a hydrophilic/superhydrophobic patterned surfaces through a dynamic control on the growth of zeolitic imidazolate framework (ZIF) micro- and nanocrystals on soy protein, followed by the selective modification of stearic acid on the ZIF micro-particles. Colloidal particles can form close-packed assemblies on surfaces by either spin-coating, dip-coating or reverse-dip coating process. In addition, etching methods utilised plasma and ion etching or laser ablation, are also suitable methods

to prepare rough surfaces.[114]

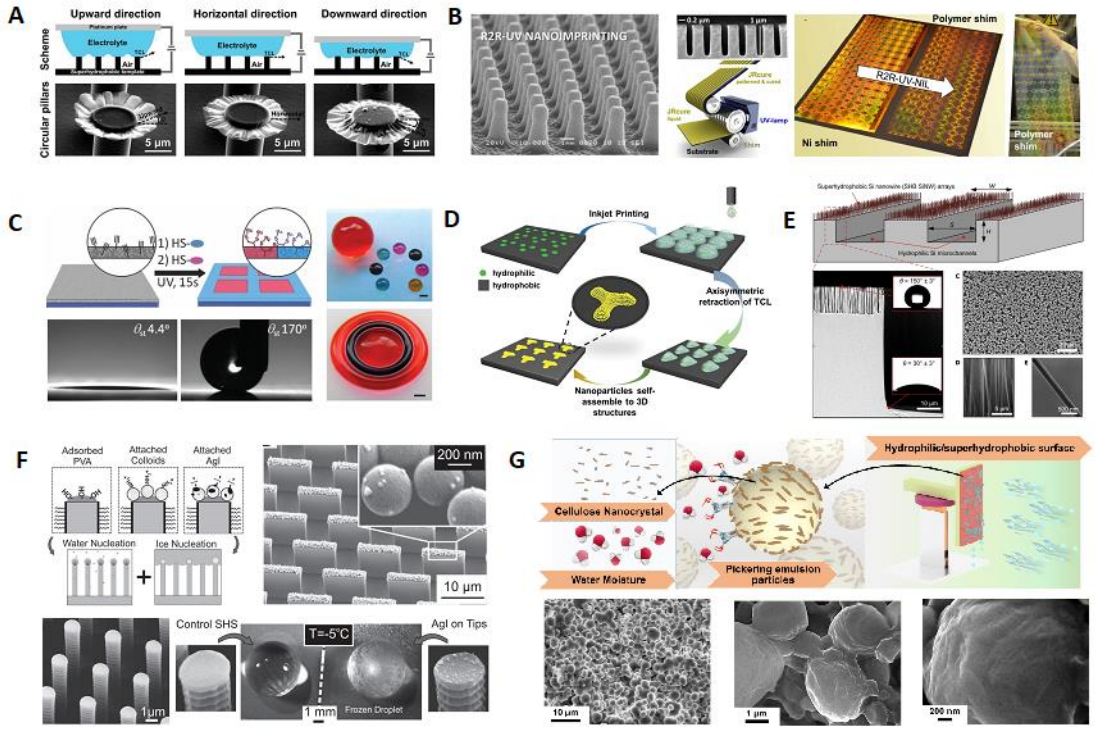

Figure 2-6. The examples of patterned superhydrophobic/superhydrophilic surface. (a) Illustration of patterned microsuckers on Superhydrophobic micropillar structured templates. [106] (b) Scheme of roll-to-roll UV-nanoimprint lithography on a plastic films. [109] (c) Schematic illustration of superhydrophobic-superhydrophilic micropatterns using thiol-yne “click” chemistry. [33] (d) Schematic illustration of 3D ink-jet printing. [115], (e) Illustration of 3D hybrid surface consisted of superhydrophobic (SHB) nanowire arrays and hydrophilic microchannels for the enhancement on the condensation. [108] (f) Tip depositions method on superhydrophobic surface (SHS) and droplet freezing experiment on SHS surface with AgI tips. [108] (g) Schematic illustration of fog harvesting on superhydrophobic surface with tunable hydrophilicity and the dynamic droplets behaviors observation.[116]

Surface functionalization

The creation of surfaces with a combination of distinct wetting properties via the modification of patterned structures are key processes to produce hybrid superhydrophobic surfaces. The combination of photomask and hydrophobic modification (UV-induced modification and surface

grafting, chemical vapor modification) can be easily implemented to achieve large-scale production of hybrid hydrophilic/superhydrophobic surfaces. For example, a surface exposed to UV light irradiation[117] or UV/ozone (UVO) irradiation[118] are used to generate superhydrophilic domains. Moreover, surface modification methods based on UV-initiated free radical polymerization and surface grafting have been used to prepare desired superhydrophilic/superhydrophobic domains.[119] As an alternative approach to prepare superhydrophilic–superhydrophobic patterned surfaces, photoinitiated click reactions have also been actively investigated for producing patterned surfaces due to their excellent spatial and temporal control over photochemical processes. Feng et al.[33] developed an extremely fast (<15 s), initiator-free surface modification method that is compatible with aqueous conditions for producing superhydrophobic-superhydrophilic micropatterns using thiol-yne "click" chemistry (Figure 2-6c). An alkyne functionalized porous poly(2-hydroxyethyl methacrylate-co-ethylene dimethacrylate) (HEMA-EDMA) surface could be transformed into either a superhydrophobic or superhydrophilic surface under 260 nm UV irradiation, depending on whether a hydrophobic or hydrophilic thiol was used. Since the thiol-yne reaction could be performed at room temperature in water, this method could produce surfaces patterned with peptides as well as a variety of reactive functional groups containing a terminal thiol (e.g. OH, NH_2, or COOH).[120] Neto et al.[121] fabricated superhydrophobic-hydrophilic micropatterns platforms using this thiol-yne photo-click reaction for producing microdroplets of controlled size and geometry. Li et al.[122] introduced a UV-induced disulfide formation and reduction reaction for surface functionalization and dynamic photopatterning, which permits the light induced attachment, exchange, and detachment of surface functional groups. Du et al.[123] developed a new strategy for preparing reparable superhydrophobic surface with hidden reactivity (SuSHiR) using photodynamic properties of disulfides. This method allows the use of diverse end functionalities (reactive or nonreactive, hydrophobic, or hydrophilic), while maintaining the same reactive disulfides "hidden" in the middle of the functional surface-grafted chains. Bai et al.[124] designed surfaces with star-shaped wettability patterns via selective illumination of UV light to integrate water-collecting strategies of both desert beetles and spider silk, where applying photocatalytic decomposition of the hydrophobic heptadecafluorodecyl-trimethoxysilane monolayer on superhydrophilic TiO_2 surface with photomask.

Additionally, selectively deposit and align the nanomaterials based on the interactions between the solvent and the patterned surface, is a facial approach to endow surfaces with patterns of contrasting wettability. Zhang et al.[125] introduced a facile inkjet printing strategy for creating well-defined, superhydrophilic micropatterns on a superhydrophobic surface based on the use of a piezoelectric-based inkjet printer to dispense picolitre drops of dopamine solution directly onto the superhydrophobic surface. Compared with the uniform superhydrophilic and superhydrophobic surfaces, the micropatterned superhydrophobic surfaces prepared by the inkjet printing methods exhibited enhanced water collection efficiency. Wu et al.[115] demonstrated a new approach to fabricate controllable 3D microstructures from a droplet on a hydrophilic pinning point patterned substrate via ink-jet printing. Poly(styrene-methyl methacrylate-acrylic acid) nanoparticles solution was used to perform the hydrophilic pattern (Figure 2-6d).

Meanwhile, many novel approaches have been developed to fabricate hybrid superhydrophobic surfaces. Mishchenko et al.[126] reported a bottom-up method to control the condensation and freezing of microscopic droplets on topographical surfaces, depositing hydrophilic polymers (polyvinyl alcohol) and silver iodide nanoparticles on the tips of superhydrophobic pillars. This type of approach can serve as a platform for systematically analyzing micrometer-scale condensation and freezing phenomena (Figure 2-6f). Wang et al.[116] presented a unique superhydrophobic surface with tunable nano-scale hydrophilicity via a self-assembled process, and it possessed outstanding fog harvesting performance. The hybrid surface was constructed via the assembly of structured Pickering emulsions, comprising of hydrophilic cellulose nanocrystals decorating on the surface of hydrophobic paraffin microspheres, and no complex post-modification was necessary. The emulsion templated surface engineering described here not only offers a convenient approach to tailor the hydrophilic nanodomain density, but it also imparted superhydrophobicity to the fog-harvesting surface via topography design (Figure 2-6g).

2.4.3 Smart superhydrophobic/superhydrophilic surface

With the application of superhydrophilic and superhydrophobic surfaces into different fields, such as chemical, agriculture and biomedical sectors, the dynamic environment requires the adaptiveness of surfaces to the surrounding environment. However, the characteristics of these superwettable surface remain unchange once the structure has been constructed, which limits their further

development and wider applications. A new generation of smart superhydrophobic/superhydrophilic surface should be capable of responding to external stimuli, such as optical radiation, temperature, pH, and external force that changes their intrinsic wetting properties for flexible and specific application.

Smart superhydrophobic surfaces with responsive characteristics have attracted growing interest, where switchable and programmable wettability properties could be manipulated by external stimuli. The following sections will describe different responsive materials used to prepare stimuli-responsive superwettable surfaces. In this section, we will introduce various responsive superwettable surfaces (photo-responsive superwettable surfaces, thermo-responsive surfaces, pH-responsive surfaces and other stimuli-responsive surfaces) covering the fabrication methods, modification materials and applications.

Photo-Responsive Superwetting Surfaces

Among the different external stimuli, light is one of most convenient one to reversibly change the geometric and electronic structures of photo-responsive molecular materials in solutions, crystals, and gels. It provides a facial way to achieve non-contact control of surface wettability due to the benefit of light sensitive trigger of the surface to achieve precise control of tunable direction, illumination area, and irradiation intensity. The change in the wettability mechanism of these photo-responsive materials is consistent with the mechanism of photocatalysis, i.e., electrons and holes photogenerated by light irradiation and absorption by water molecules.

The typical photo-responsive systems include inorganic oxides (TiO_2) and organic compounds, such as azobenzene, malachite green and spiropyran. As early as 2000, Ichimura et al.[127] reported that the motion of liquids could be manipulated reversibly by light when a substrate surface wass modified with a photoisomerizable azobenzene monolayer. The light-driven motion of liquids was achieved by an appropriate choice of photoreactive molecules tethered to an outermost surface and fluid substances. Following this concept, many organic materials have been explored, such as azobenzene, which could form cis and trans isomers under ultraviolet and visible irradiation respectively. Kwon et al.[128] demonstrated a dye-sensitized TiO_2 surface fabricated using straightforward dip-coating method can be engineered to have its wettability state optically modulated by exposure to visible light. Utilizing this photo-induced wetting of their dye-sensitized

TiO_2 surface, they demonstrated the light-guided manipulation of liquid droplet motion along the surface. This phenomenon could be applied to the demulsification of surfactant-stabilized brine-in-oil emulsion via interfacial coalescence of brine droplets under visible light illumination. Yuan et al.[129] report the synthesis and fabrication of a two-dimensional crystalline trisilyl metal–organic framework (TSiMOF) together with the classical photoresponsive hexamethyltrisilane groups on the surface. Irradiated by UV light under air in minutes the fluorescence of the TSiMOF was simultaneously activated resulting in the intriguing surface transformation from superhydrophobic to hydrophilic, which could be applied on Quick Response (QR) codes or logo (Figure 2-7a).

Thermo-responsive Superwetting Surfaces

Temperature-responsive polymers have been widely studied, such as poly(N-isopropylacrylamide) (PNIPAAm), polycaprolactone (PCL) and poly-oligo(ethylene glycol) methacrylate (POEGMA) , and these polymer chains often exhibit a conformation change in response to external stimuli. Jiang et al.[130] deposited a poly(N-isopropylacrylamide) (PNIPAAm) thin film surface-initiated atom-transfer radical polymerization from a smooth silicon substrate (Figure 2-7b). The surface possessed a hydrophilic state with a CA of 63.5° at the temperature of 25 °C, and the surface became hydrophobic with a CA of 93.2° at 40 °C. In addition, rapid reversibility and excellent stability of thermally switching were observed by Fu et al.[131] for PNIPAAm-grafted porous anodic aluminum oxide (AAO) membranes. Atomic force microscopy (AFM) on the surface revealed dramatic changes in the surface nanostructure above and below the lower critical solution temperature. Additionally, the thermo-responsive characteristics could be used in different applications, such as anti-adhesive surfaces[132, 133] (Figure 2-7c), smart devices[134], water harvesting[135] and purification[136].

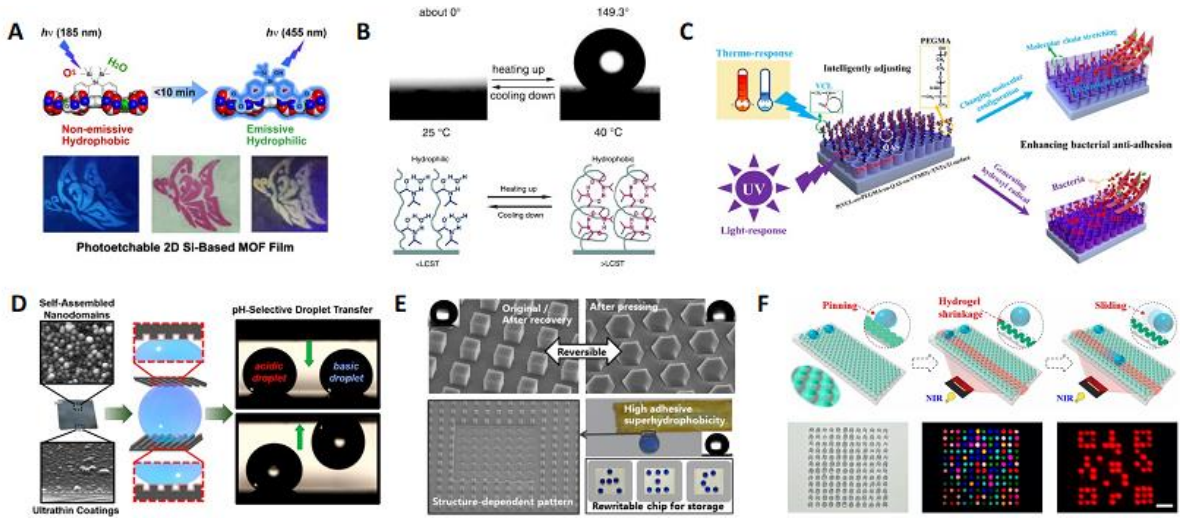

Figure 2-7. The examples of smart superwettable surface with tunable superhydrophobicity and superhydrophilicity. (a) Illustration of photoresponsive 2D Si-based MOF film.[129] (b) Scheme of thermos-responsive poly(N-isopropylacrylamide) (PNIPAAm) thin film. [109] (c) Schematic illustration of the procedure for the preparation of the smart bacterially anti-adhesive composite surface with thermo and light-responsive strategies. [132] (d) Schematic illustration of pH-responsive superhydrophobic surface with droplet transfer capability. [137] (e) Illustration of a superhydrophobic with shape memory structure. [138] (f) Schematic illustration of bioinspired programmable wettability arrays for droplets manipulation, [139]

Reversible and Tunable pH-Responsive Wetting Surfaces

Furthermore, the environment of superwettability surface is also a key consideration in many systems, and pH-responsive surfaces have attracted increasing attention as they could be applied to many applications, such as drug delivery, separation, and biosensors. There are many organic compounds that possess the sensitive pH responsive property, such as poly(tert-butyl acrylate)(PtBA), poly(2-(dimethylamino)ethyl methacrylate) (PDMAEMA), polyvinylpyrrolidon (PVP), 2-(11-mercaptoundecanamido)benzoic acid (MUABA) and many others. Cao et al.[140] fabricated a bioinspired metal-intermetallic laminated composite surfaces with responsive wettability, where titanium and copper foils were diffusion bonded to prepare the MIL composites. The accurate control of the microscale structure was easily realized by etching, while the influence of the microscale structure on the WCAs in the parallel and vertical directions was investigated. Wang et al.[141] reported on an eco-friendly nano-starch-based superhydrophobic coating by

combining SNPs with poly(dimethylsiloxane). An anthocyanin-rich extract was innovatively loaded into the SNPs to endow the coating with pH responsiveness, generating a waterproof pH-sensing colorimetric coating for food freshness monitoring. Brito et al.[137] developed an all-aqueous layer-by-layer (LbL) deposition of polyelectrolytes to prepare specific hydrophobic coatings, and the surfaces had the capability to sense environmental pH, which can be used in droplet-based microfluidics applications and water collection/harvesting (Figure 2-7d).

Multi-responsive Superwetting Surfaces

As described previously, many smart surfaces capable of switching between superhydrophilicity and superhydrophobicity have been widely reported by grafting of responsive materials and surface topography control. However, majority of them can only respond to one external stimuli, which largely restrict their potential application in practical environment. Thus, the multi-responsive superwetting surfaces are strongly required to meet the requirement of future applications. Jiang and coworkers[142] described a dual-responsive rough surface coated with polypeptide that displayed switching between superhydrophilic and superhydrophobic states. Besides, a series of intelligent surfaces with self-regulated characteristics that are responsive to the dynamic environment, such as mechanical, pressure, magnetic, have been developed. Liu et al.[143] designed a multifunctional smart surface based on the hierarchical structure of graphene and TiO_2 nanofilm with dual bioinspired roughness, integrating the advantages of both biomimicry and stimuli-responsiveness. The surface exhibited tunable wetting, adhesion, and directional water transport properties, which provided a general protocol for applications such as moisture management, microfluidic control, self-cleaning, and water/oil separation. Huang et al.[144] designed a magnetically transformable surface that could reversibly switch between superhydrophobic and slippery states. From the on-demand switching of the liquid-repellent state, the transformable surface could be used for adaptive liquid repellency and programmable fog harvesting and transport. Additionally, Lv et al.[138] reported on a superhydrophobic surface produced from epoxybased shape memory polymer (SMP) with particular shape memory hierarchical micro/nanostructure and the application in rewritable droplet-based functional chip (Figure 2-7e). Sun et al.[139] presented a surface with programmable wettability arrays for droplets manipulation, which was constructed using a coaxial capillary microfluidics to emulsify and packed graphene oxide (GO) hybrid N-

isopropylacrylamide (NIPAM) hydrogel solution into silica nanoparticles-dispersed ethoxylated trimethylolpropane triacrylate (ETPTA) phase. Owing to the outstanding photothermal energy transformation property of the GO, the encapsulated hydrophilic hydrogel arrays could shrink back into the holes to expose their hydrophobic surface with near-infrared (NIR) irradiation; which imparts the composite film with remotely switchable surface droplet adhesion status (Figure 2-7f).

Integrated superwettable surface for various applications.

This special water manipulating capability of superwettable surface can be integrated into other systems with added functionality that incorporates both superwettability and other special properties. For example, the passive daytime radiative cooling system (PDRC) offer an effective and sustainable strategy to cool the object by combining radiation heat through mid-infrared wavelengths and reflection of solar energy. However, in practical application, various PDRC materials were easily contaminated by dust accumulation or become wet by rain or fog, and this will severely influence the sunlight reflectance performance. As a result, Wang et al.[145] designed a superhydrophobic PDRC composites film via a solvent exchange method, consisting of ethylene-propylene-diene copolymer (EPDM) and hydrophobic SiO_2 nanoparticles. The SiO_2 nanoparticle (25 nm) would aggregate into micronized cluster and distributed into the pores formed by the self-assembled EPDM polymer. Due to the reduced surface free energy and increased roughness, the EPDM/SiO_2 composites film possessed a high static contact angle (162˚) and low sliding angle (1.2˚), endowing the surface with anti-contamination property. The durability experiment demonstrated that the system could retain its original performance even after UV illumination, sandpaper abrasion and 70 times of finger touch test. Also, superhydrophobic surface with Cassie wetting state can also be utilized as fabrication substrate to synthesize free-standing materials membrane or film due to the water repellent property. For example, Chen et al.[146, 147] reported an electrochemical printing method on superhydrophobic micropillar-structured substrates and successfully synthesized the free-standing metal organic framework (MOF) and microcavity-patterned polymer film, respectively. They demonstrated that the obtained material film can be easily peeled from substrate and transferred without adhesion. Besides, the topography and roughness of thin material film can also be tuned via controlling of the geometrical parameters of micropillar arrays.

The superwettabile materials can also participate in interface engineering involving phase and thermal transition reactions. Zhang et al.[148] reported a strategy to transform hydrophilic MXene to superhydrophobic MXene for application in photothermal membrane desalination (MD). In their study, the superhydrophobic interface engineering could address several drawbacks in traditional MD system (Figure 2-8a), such as; (1) Conventional MD materials that are usually adopted consisted of commercial polyvinylidene fluoride membrane (C-PVDF). They were hydrophobic while the Wenzel wetting behavior would generate a direct contact between hypersaline water and materials leading to the contaminating and fouling of membrane surface, (2) Due to the direct interaction between bulk feed water and the membrane surface, it required continuous and large amounts of energy to maintain the temperature gradient (T) between the feed water and cooling water to generate the driving force of water-to-vapor transient. They prepared a polydimethylsiloxane (PDMS) decorated MXene layer on PVDF via electrospinning, and the coating layer (PM-PVDF) could resolve the challenges in mass and energy transfer. Firstly, the superhydrophobicity of PM-PVDF could convert the wetting behavior from Wenzel state to Cassie's state. Therefore, the feed water would suspend on the rough structure of membrane and generate a boundary slippage and stable shear-free water-air interface line during desalination. The introduction of MXene materials could endow the surface with unique solar harvesting capability, enabling a self-heating sustainable surface that could replenish the heat-loss on the side of feed water during the continuous desalination process. Thus, the introduction of superhydrophobic PDMS/MXene coating layer could simultaneously address problems in mass and energy transfer, thereby achieving a high desalination efficiency.

In addition, the utilization of superwettable surface in some systems could directionally improve the output performance of the system. One such example is from the droplet-based electricity generator (DEG) reported by Kim and co-workers.[149] They designed the Lotus-leaf like ethylene propylene (FEP) superhydrophobic film with low adhesive force as the dielectric layer in the DEG system. Due to the non-wetted property of the superhydrophobic layer, a wide operational droplet volume range could be utilized to convert the kinetic energy of the microdroplets, including raindrop, dew and precipitation, to electrical output (even 6L microdroplet bouncing could generate the electrical output). Besides, the Cassie's wetting state could improve the droplet spreading after impact, which further boost the electrical performance of the DEG system. In practical application, the

superhydrophobicity can endow the DEG system with self-cleaning property, sustaining the electrical performance in outdoor environment. Furthermore, the pH-responsive electrical output could be used as the acidity alert of falling droplet, indicating the versatile potential applications in the future. Similarly, Ma et al.[150] also design a superhydrophobic magnetoelectric generator (SPEG), which can effectively harvest the dispersed hydropower like raindrop or fog droplets. In their study, the superhydrophobic layer in SPEG system could prevent the accumulation of water. When droplets falling from the top layer, the splashing water could not enter the gap of the SPEG or accumulated on the surface due to the water repellency force of the superhydrophobic layer. However, the splashing water would gradually fill the gap between the top layer and the magnetic materials layer. Then the accumulated water would act as a "cushion" to absorb the impact of the falling water droplets with the magnetic pillars acting as tiny springs, diminishing the gap change between the top coil and bottom magnet. Consequently, the overall electrical output would decrease due to the smaller magnetic flux. Taking a step further, Ma et al.[151] modified the magnetoelectric hybrids system (MS) by replacing the linkage with glycerin droplets (the traditional linkage was normal tiny springs) between the conductive coil and magnetic powders/Ecoflex base. Due to the superhydrophobic property of the coating layer on both sides, the glycerin droplets partially penetrate the magnetic materials to fix the position while it would be compressed then recovered when the raindrops impacted the MS system. This reversible compression/recovery process would change the distance between coil and magnetic base, altering the magnetic flux and the electricity produced. Besides, due to the high-sensitivity of the glycerin-based linkage, it could harvest electricity multiple times when the raindrops fell on the top layer. In addition, the patterned superhydrophobic plate can also be utilized for fog harvesting to produce water droplets. By combining the fog harvesting and MS system together ss shown in Figure 2-8b, it could simultaneously achieve the electricity generation and water collection, exploiting new systems toward sustainable resource utilization. Combining the superhydrophobicity and hygroscopic properties in a single platform, Yoon et al.[105] developed a wet-style superhydrophobic film that simultaneously exhibited anti-fogging, self-cleaning and anti-reflecting properties (Figure 2-8c). This special superhydrophobic could be separated into two components, the top low-surface-energy micropillar arrays composed of perfluoropolyether (PTFE) and underlying polymeric reservoir assembled by chitosan (CHI) and carboxymethyl cellulose (CMC). As results, the top micropillar

region could support the water droplets in Cassie-Baxter state displaying the superhydrophobic and self-cleaning properties. On the other hand, when the film was exposed to a temperature difference, the water molecules would condense on the underlying polymer-silica nanocomposite instead of forming the fog on outer surface, thus the surface would remain optically clear during condensation.

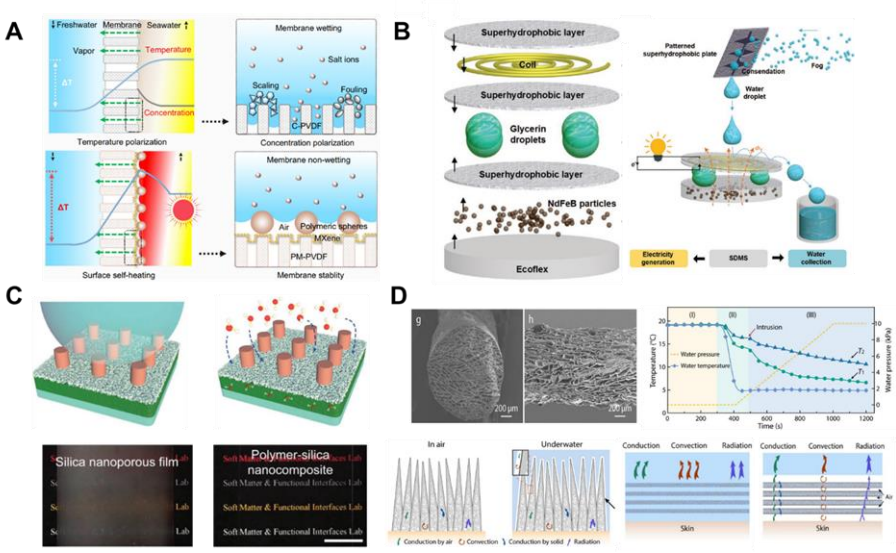

Figure 2-8. The various application of superwettable surfce in real-world applications. (a) The schematic illustration of conventional membrane distillation (MD) process with thermal inefficiency and membrane wetting issues using conventional C-PVDF (upper image) and optimized PMD process with localized surface self-heating and superhydrophobic-dependent membrane stability endowed by PM-PVDF membrane (bottom image). [145] (b) A superhydrophobic droplet-based magnetoelectric system (SDMS) shows the mechanical–electrical conversion capability by generating electricity from falling water drops (left image) and the simultaneous electricity generation and water collection from flowing fog (right image). [151] (c) Schematic illustration of the wet-style superhydrophobic antifogging coating consisting of the top low-surface-energy micropillar region and the bottom polymer–silica nanocomposite region (upper two images), the anti-fogging performance of wet-style superhydrphobic surface and silica nanororous film (the bottom two images). [105] (d) SEM images showing the hollow core and aligned shell of a porous fiber. The thermal insulating performance and schematic illustration of the thermal insulating mechanism of hydrophilic textile, superhydrophobic porous textile in air and underwater, respectively.[152]

The surface superwettability can also be utilized in food related applications. By utilizing the pH sensitivity of responsive superhydrophobic/superhydrophilic surface, Wang et al.[141] developed an eco-friendly nano-starch-based superhydrophobic coating achieved by combining starch nanoparticles (SNP) and poly(dimethylsiloxane) (PDMS) for food freshness monitoring. The non-toxic and pH-sensitive anthocyanins were immobilized on the hydrophilic SNP and a layer of PDMS coating could effectively increase the hydrophobicity of the systems, overcoming the contamination limit during practical application. The color of the surface would change purple to blue and pink when it came into contact with droplets of different pHs, associating with the deprotonation and protonation of the hydroxyl groups in the B ring of the quinoidal base. At practical application, this superwettable materials could be coated on aquatic products, allowing the monitoring of the food freshness during storage and transportation by monitoring the variation of the color on the package. In addition to the monitoring of food freshness, the superhydrophobic film could also be endowed with bactericidal and anti-fouling activity in food packaging. A multifunctional sustainable superhydrophobic surface was developed by combining Ag nanoparticles, carnauba wax and polydimethylsiloxane (PDMS).[153] The three deposition steps endowed the surface with high roughness, which could repel various liquids, including milk, cola, coffee and ice tea. In addition, the Ag nanoparticles deposited on the surface could effectively kill bacteria via oxidation and the release of Ag^+ ions. Besides, the surface enhanced Raman scattering (SERS) activity from the Ag nanoparticles could also be utilized to detect harmful chemicals (such as rhodamine B in sausage) or other molecules of interest. It is worth noting that the maximum leaching of Ag ion occurred in acidic conditions, which is above the safety limit, and within the neutral and basic conditions, the amount of Ag leached was within the acceptable limit (50 ppb) set by European regulations required for materials in contact with food products. Therefore, the superhydrophobic Ag@Wax@PDMS-Paper is considered safe in food packaging applications, at least within a short storage time (7 days).

Keeping warm in various harsh environment is crucial for both human and other mammal's health, and it ensure the possibility to expand activity range and explore unknown regions. By mimicking the polar bears which can maintain its body temperature at around 37°C in extremely cold regions, Shao et al.[152] developed a special superhydrophobic textile with multiscale porous structure via a freeze-spinning method. In air, the porous structure could effectively capture the air inside the

cores and the filled air could reduce the heat transfer since the air has much smaller thermal conductivity than solid surface. When surface expose to water, the superhydrophobic porous textile captures air between fibers and on the rough fiber surface that prevented severe heat loss through convection. The strategy of combining superhydrophobicity and porous structure paves the way for the thermoregulating textiles in thermal insulation both in air and underwater (Figure 2-8d). Superhydrophobic surface with additional fire-extinguishing and adhesive properties could be used for preparing advanced adhesive fire-retardant polymeric coatings for many flammable substrates. Ma et al.[154] designed an advanced water-based polymeric coating that are highly adhesive and fire-retardant. In detail, by mimicking the mechanism of tree frogs exhibiting strong adhesion to various surfaces, they synthesized waterborne poly(VS-co-HEA) copolymers via a facile radical copolymerization of hydroxyethyl acrylate (HEA) and sodium vinylsulfonate (VS). In this material, the abundant hydroxyl groups in HEA possessed a strong interface adhesion through interfacial hydrogen bonding and the sodium sulfonate groups in VS provided flame retardancy. After hydrophobic treatment, the surface displayed strong water repellency that reduced the coating moisture sensitivity. As a result, the integration of three properties, superhydrophobicity, thermal insulation and adhesion offer the materials in many promising applications in building, electrical devices, and transportation. Also reported by Wang et al., the introduction of superhydrophobicity into MXene/silver nanowire/melamine hybrid sponge could largely increase the material stability and water repellency, helping the functionalized system work in complex practical environment.[155]

Chapter 3. Tunable adhesion superhydrophobic surface based on wax-in-water Pickering emulsion

3.1 Introduction

The wettability of solid surface is a very important property that is dominated by both the chemical composition and topography of the surface. Among the diverse superwetting surface, superhydrophobic surface, with a water contact angle (CA) greater than 150° has attracted increasing interest in both fundamental research and practical application over the last few decades. Recent studies on Lotus leaves and Rose petal revealed that a superhydrophobic surface with both a large CA displayed significantly different water adhesion characteristics.[156] Although both surfaces were covered with micro wax protrusion, the Lotus leaves displayed weak adhesion with a small sliding angle of about 2° while the water droplet pinned on the rose petal. This demonstrates that the size and topography of protrusions will have a large impact on the surface wetting behavior.[157]

Typically, the superhydrophobic coating is fabricated using poly- or perfluoroalkyl agents since fluorocarbon possesses low water affinity, exceeding that of carbon black.[158] However, the use of fluorinated compounds has raised serious environmental concerns regarding their potential toxicity to human life and the persistence of such compounds. Therefore, it is highly desirable to design processes for formulating superhydrophobic coating materials without the need of using hazardous materials.

Superhydrophobic coating materials prepared by emulsion particles can be a suitable method as they are scalable and the particle size can be easily controlled.[159] However, due to the large surface area and high interfacial energy of dispersed droplets, emulsions are thermodynamic unstable system without the use of surfactants. Thus, Pickering emulsion that is stabilized by solid particles offers a practical method to design and prepare superhydrophobic surfaces. The Pickering emulsion is more stable, efficient, and sustainable when compared to surfactant stabilized emulsions. In recent years, many types of solid particles have been used to stabilize Pickering emulsion, such as SiO_2[160], metal microparticles[161], polysaccharide[162] and cellulose nanocrystal (CNC).[163] Among them, CNC is considered as an excellent emulsifier due to its outstanding mechanical

strength, biocompatibility, and low cost. Additionally, the abundant hydroxyl groups on the surface of CNC offer many avenues for modification and functionalization.[164]

The motivation of this research is to utilize CNC and modified CNC stabilized wax-in-water Pickering emulsion to prepare sustainable superhydrophobic surface with tunable adhesive property. CNC and cationic modified CNC stabilized Pickering emulsions were first prepared using water and molten wax at moderate temperature (60 to 80 ºC). These Pickering emulsions serve as building blocks to prepare superhydrophobic surface by spray coating onto a substrate. By studying the water adhesion behavior of different superhydrophobic surfaces, we will determine and examine the relationship between the surface topography prepared with various Pickering emulsion systems and water adhesive forces.

The overall objective of this study is to explore and exploit the use of pristine and cationic modified CNC (CNC-GTMAC) to prepare wax-in-water Pickering emulsion with controllable particles size, which was then spray coated onto a substrate (glass, wood or ceramic) to form a superhydrophobic surface. In order to prepare the superhydrophobic surface with controllable adhesive force, we prepared surfaces using mono-dispersed emulsion particles and mixture of emulsion particles of varying sizes. To achieve this goal, four related tasks have been identified and described below:

- Modification of CNC-GTMAC as a cationic Pickering emulsion stabilizer.
- Formation of pristine CNC and CNC-GTMAC stabilized wax-in-water emulsion.
- Prepare superhydrophobic surface with single size and mixed size emulsion particles.
- Characterize the hydrophobicity capability and water adhesive force of different superhydrophobic surfaces

3.2 Materials and method

Cellulose nanocrystal (CNC) was provided by Celluforce Inc. The chemicals used in this study are analytical grades, purchased from Sigma–Aldrich, and used as received.

Preparation of CNC-GTMAC

The surface modification of CNC with glycidyltrimethylammonium chloride (GTMAC) proceeded via the nucleophilic addition of alkali-activated cellulose hydroxyl groups to the epoxy moiety of

GTMAC. 11 g of NaOH (aq) was added to 150 mL of 5wt% CNC solution to achieve a concentration of 7% w/v NaOH. After 30 minutes of mixing at room temperature, 5 mL of GTMAC was added and the mixture containing 10 ml, 15 ml and 20 ml of 5 wt% CNC maintained for 5 hours at 65 °C to prepare cationic CNC of different surface charge densities. The reaction mixture was diluted 5-fold with water and dialyzed using a cellulose dialysis membrane (molecular weight cut-off of 12 000–14 000 Da from Spectrum Labs) against purified water for 15 days. The resulting suspension of glycidyltrimethylammonium chloride cellulose nanocrystals (CNC-GTMAC) at approximately 1% w/w, was sonicated and filtered under vacuum and then concentrated by evaporation at reduced pressure and at room temperature.

Time-evolution of interfacial tension change of wax and water

The water/wax interfacial tension were measured using the DCAT-11, Dataphysics equipped with a TV 70 liquid temperature control unit. The liquid dosing unit LDU 25 was equipped to control the dosing of liquid into the measuring cell.

Wax-in-water Pickering Emulsions

The wax-in-water w/o Pickering emulsions were prepared by sonicating the molten paraffin wax in the aqueous solution containing the CNC-GTMAC (GCPE) and pristine CNC (PCPE) respectively. In order to control the size of emulsion particles, various CNC concentrations ranging from 0.1 to 4 wt% were investigated. The ratio of oil to water was set at a ratio of 2:8.

Particle size distribution

The size of the emulsions was measured using the PSA 1190 particle sizer from Anton Pear. To avoid the agglomeration of particles, the Pickering emulsion was sonicated and then introduced to the measuring cell.

Optical microscopy

Photomicrographs of the wax-in-water emulsions were recorded using a polarized light microscope (Nikon Polarizing Micro-scope Eclipse LV100POL with Nikon DS Camera control unit DS-U2).

Preparation of superhydrophobic surface with single size emulsion particles.

The prepared CNC stabilized Pickering emulsions (20 wt%) were diluted to 5 wt% using Mill-Q water and the emulsion was spray-coated onto a vertically placed clean glass substrates using a spray-coater with a nozzle diameter of 0.35 mm at a pressure of 30 psi. The coated glass substrate was left to dry prior to further analysis.

Preparation of superhydrophobic surface with mixed size emulsion particles.

The mixed size Pickering emulsions were prepared by adding CNC-GTMAC stabilized emulsion (GCPE) to pristine CNC stabilized system (CPE). In order to examine the influence of the changes in emulsion size on the surface roughness, we prepared 5 types of mixed size emulsion particles based on the weighted ratio of GCPE to CPE of 7:1, 3:1, 1:1, 1:3, 1:7. Then the prepared emulsion mixtures were sprayed onto glass substrate using the same process described previously.

Contact angle measurements of different types of superhydrophobic surface

The water static contact angle measurements were performed using a sessile drop system in ambient environment at room temperature. The liquid was dispensed with a micro-needle (New Era Pump Systems Inc.) through a syringe pump as a spherical droplet of volume 5 μl. Measurements were conducted in ambient environment at room temperature 5 secs after the droplet was dispensed onto the surface. The contact angle was measured by fitting the profile using a LabVIEW program.

Zeta Potential

Electrophoretic mobilities of the unfunctionalized CNC and CNC-GTMAC were measured using the Nanosizer ZS, Malvern, UK. Mobility values were converted to zeta potentials using the Smoluchowski equation (3-1, 3-2 and 3-3) and the reported values are an average of 20 measurements.[165]

$$\frac{\partial g(x,t)}{\partial t} = L(x)g(x,t) \qquad (3\text{-}1)$$

where

$$L(x) = -\frac{\partial}{\partial x}[a(x) - D\frac{\partial}{\partial x}] \qquad (3\text{-}2)$$

and

$$a(x) = -\frac{1}{\xi}\frac{\partial U(x)}{\partial x},) \quad (3\text{-}3)$$

U(x) is the potential energy of the ligand. ξ is the friction coefficient, and $D=k_bT/\xi$ is the diffusion coefficient.

Fourier transforms infrared (FT-IR) spectroscopy

FT-IR spectroscopy measurements on the original CNC and CNC-GTMAC were performed using a Bruker Tensor 27 FTIR spectrometer. This was used to confirm the modification of CNC-GTMAC, when the spectrum was compared with the pristine CNC. Samples were freeze-dried and pressed into potassium bromide (KBr) pellets.

TEM Imaging

The size and morphology of the nanoparticles were evaluated using a transmission electron microscope (TEM). A droplet of the sample solution was placed on a carbon coated copper grid, and left for 10 min, after which the excess liquid was removed using a small piece of filter paper and left to dry overnight before TEM analysis.

Adhesive force analysis

The adhesive force of the prepared single size superhydrophobic surface and mixed size superhydrophobic were characterized using a high precision electronic balance of the DataPhysics system.

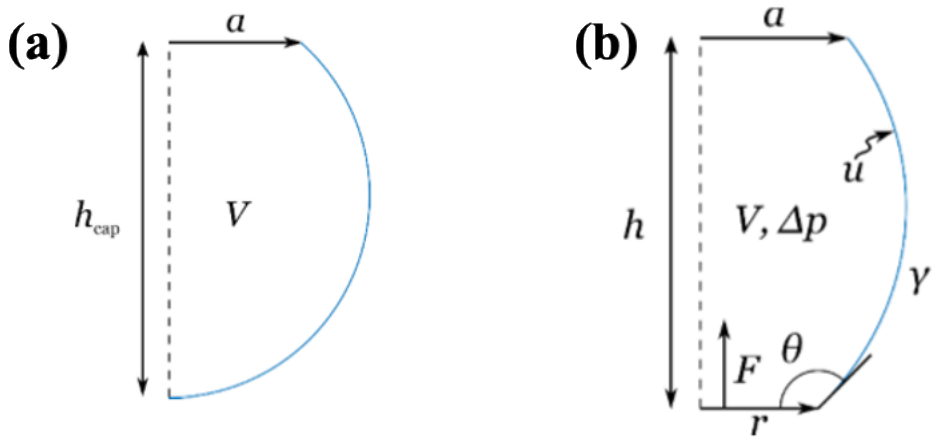

Figure 3-1. Schematic illustration of droplet geometry for water adhesive force analysis.

In this method, the 4 μL droplet was dispensed from a nozzle to the substrate, and the changes in force measurements as the droplet made contact by force and Laplace pressure maintained the spherical shape of the droplet. Based on this, we used a droplet volume of 4 μL (Figure 3-1). After calculating the geometry of droplet prior to and after touching the superhydrophobic surface, we achieved a radius of nozzle, *a* of 0.5 mm, and the radius of droplet was 0.955 mm and height from the nozzle to the substrate, h_{cap}=1.782 mm. When we controlled and set the advance distance to h_{adv}=0.01 mm after the droplet made contact with the superhydrophobic surface, the height change for the droplet decreased from h=1.782mm to h=1.772 mm. Because the height difference was very small compared to the diameter of droplet (0.01 mm versus 1.782 mm), we noted that the shape of the spherical droplet did not change. The sagging pressure corresponding to the highest pressure experienced by the superhydrophobic surface resulted in the Cassie state. Normally, the sagging pressure is of the order of $P_{sag} \approx \gamma / r$, where r is the distance between the droplet surface and the substrate. Here, we approximated γ to be about 0.03 N/m and r was approximately 2-3 microns, thus the P_{sag} for our superhydrophobic surface was equal to 10 kPa.

Surface force mapping

In the single adhesive force testing, the diameter of contact area of the substrate was about 0.2x0.2 mm. Therefore, we could conduct a line scan over an area of 20x10 mm to determine the pull-off forces when the droplet interacted with the surface. The changes in the wetting characteristics corresponded to the variations in the structural color due to subtle structural differences of the aggregation structure of the wax/CNC droplets on the surface.

3.3 Result and discussion

3.3.1 The modification of cellulose nanocrystal (CNC)

The surface cationization of CNC was conducted by the nucleophilic addition of alkali-activated cellulose hydroxyl groups to the epoxy moiety of GTMAC. According to the Figure 3-2a, a sufficient amount of a base (NaOH) was added to activate the hydroxyl groups on the surface of CNC, which also hydrolyzed the surface sulfate ester groups. Under these conditions, some of the

surface sulfate ester groups were removed without disrupting the crystal morphology. After extensive dialysis and sonication, a stable aqueous dispersion of CNC-GTMAC was obtained.

The different amounts of GTMAC were firstly examined to find the optimal modification conditions. The grafting of GTMAC (5mL) could significantly change the surface zeta potential of CNC due to positive charged $–NH_4^+$ groups on GTMAC. As evident from Figure 3-2b, 10 mL GTMAC would alter the surface charge of CNC from negative to potisive and 20mL GTMAC would increase the surface charge of CNC from -44mV to +32 mV. It worth highlighting that the mild modification (5 mL and 10 mL) would lead to the aggregation of colloidal particles due to the electrical neutrality, reflected by the broader and asymmetric peak in zeta potential measurements. This phenomenal can also be demonstrated by the hydration diameter of CNC-GTMAC tested at different zeta potentials. As shown in Figure 3-2d, the higher zeta potential either positive or negative charge (-44 or +32 mV) exhibited a lower hydration diameter. However, the flocculation would occur in CNC-GTMAC solution when zeta potential approaching to 0 mV, demonstrating the role of high surface charge in stabilizing the colloidal system. The zeta potential remained constant when the volume of GTMAC added exceeded 20 mL, confirming that the further increase in the GTMAC did not contribute to the grafting of more cationic groups on the CNCs. The FT-IR spectroscopy was also used to confirm the successful functionalization of cationic groups on the CNC surface. As shown in Figure 3-2b, the typical peak of trimethyl group at $1480cm^{-1}$ is associated to the quaternary ammonium substituent in GTMAC, whereas the strong band at 2985 cm^{-1} asymmetrical and symmetrical CH_2 stretches are from the long alkyl chain of stearyltrimethylammonium chloride.[166] These results confirmed the successful grafting of GTMAC onto the surface of CNC. After modification (Figure 3-2f and 3-2g), the average length of cellulose nanocrystals as determined by TEM and AFM images was approximately 200 nm, and the CNC-GTMAC was well-dispersed in water (Figure 3-2e). This demonstrated that the modification of cationic group did not influence the size or shape of the nanoparticles.

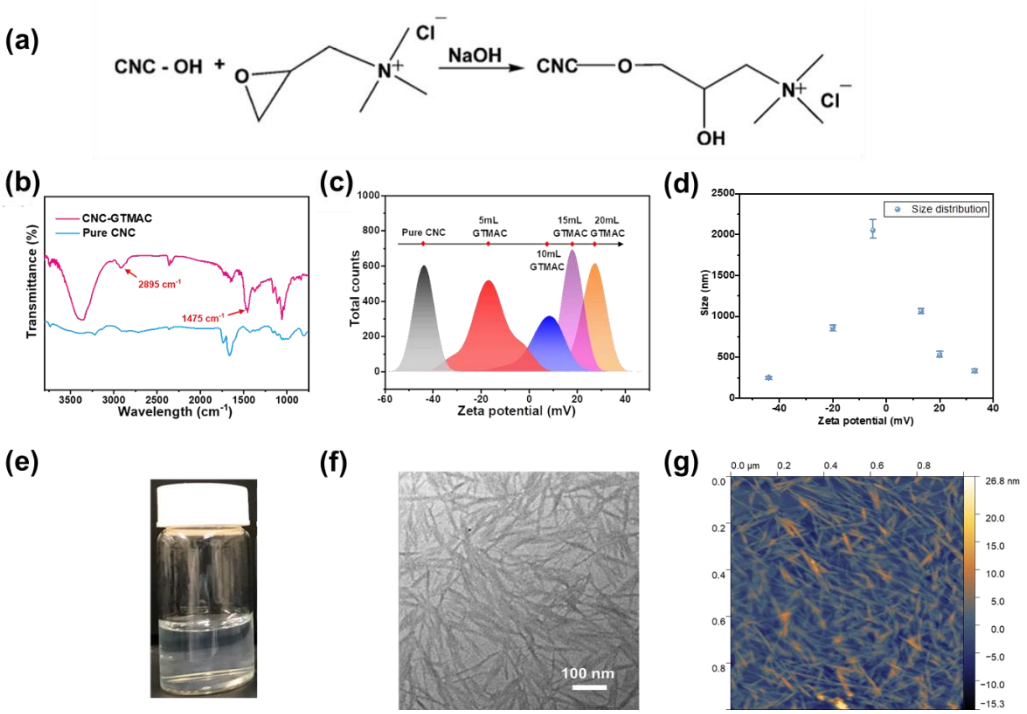

Figure 3-2. (a) Schematic illustration of surface modification of CNC with GTMAC. (b) The FT-IR spectra of pure CNC and CNC-GTMAC. (c) The zeta potentials of CNC and cationic modified CNC-GTMAC. (d) the hydration diameter of CNC-GTMAC in different zeta potential. (e) Vial containing 0.5%w/w CNC-GTMAC in water and (f) Corresponding TEM image and (g) AFM image of the dispersion. The scale bar is 100 nm.

3.3.2 Time-evolution of interfacial tension change

The interfacial tension variation is a key parameter to evaluate whether the colloidal particle could generate a robust interface and form stable Pickering emulsion. Thus, the interfacial tension of oil and water and interfacial kinetic of CNC and CNC-GTMAC jamming, adsorption at the interface of wax/water was first investigated by the DCAT-11 tensiometer. The pristine CNC was well-dispersed in the water phase due to its high negative charges and abundant hydroxyl groups on its surface. However, as shown in Figure 3-3(a) the interfacial tension of oil/CNC dispersion possessed an equilibrium value of about 34.8 mN m^{-1}, which was close to the pure wax/water system (38.5 mN m^{-1}). This demonstrated that the high intrinsic negatively charged CNC did not partitioned at the oil/water interface, hence they were not interfacially active and would not form stable Pickering emulsion. However, the cationic modified CNC significantly reduced the interfacial tension of oil and water, approaching 27.1 mN m^{-1} with a small addition of 0.1wt% CNC-GTMAC to the solution.

With the increasing concentration of CNC-GTMAC in water, a further reduction of interfacial tension was observed (23.2 mN m^{-1} in 0.5wt% CNC-GTMAC), indicating increasing amounts of CNC-GTMAC was partitioned to the oil/water layer. Additionally, as shown in the photo image (Figure 3-3a right), the CNC-GTMAC that aggregated at the interface would induce a long-range electrostatic interaction with the CNC-GTMACs in the bulk solution (since CNC-GTMACs are zwitterionic possessing positive and negative charges). Hence the equilibrium interfacial coverage would increase and from Figure 3-3a, we observed that the interfacial tension of oil/water decreased to 15.5 mN m^{-1}. These results indicated that the assembly of CNC-GTMAC at the interface could be manipulated by concentration, which is critical to the stability of Pickering emulsions. To further prove the adsorption and coverage of CNC-GTMAC arranged at the oil-water interface, the buckling experiment was conducted with the assistant of poly(styrene-*r*-vinylpyridine) (PSV). The aqueous CNC-GTMAC solution with different concentrations (wt%) were prepared and sonicated for 5 min before use to ensure the uniform dispersion. An artificial interface was constructed by injecting the CNC-GTMAC droplet into the melt wax dispersed with PSV co-polymer. This co-polymer could be well-dispersed in the oil (melt wax) and formed stable hydrogen-bond with CNC-GTMAC in solution, trapping the particles organized at the interface. The assembly process of CNC-GTMAC at the interface could be monitored by the interfacial variation with time during the equilibration of a pendent water droplet in oil. At the equilibrium condition, the volume of pendent droplet was reduced by withdrawing the fluid using a syringe. Subsequently, the interfacial area would decrease and the buckling phenomena would occur due to the light scattering effect of nanosized CNC trapped at the interface as shown in Figure 3-3b. It is worth to highlight that although the co-polymer was essential to reduce the interfacial tension (Figure 3-3c), the absence of CNC-GTMAC (only PSV in oil) could not generate such phenomena. This is because the buckling effect derived from the formation of robust elastic film assembled by closely packed CNC-GTMAC could withstand the massive shrinkage of the droplet.

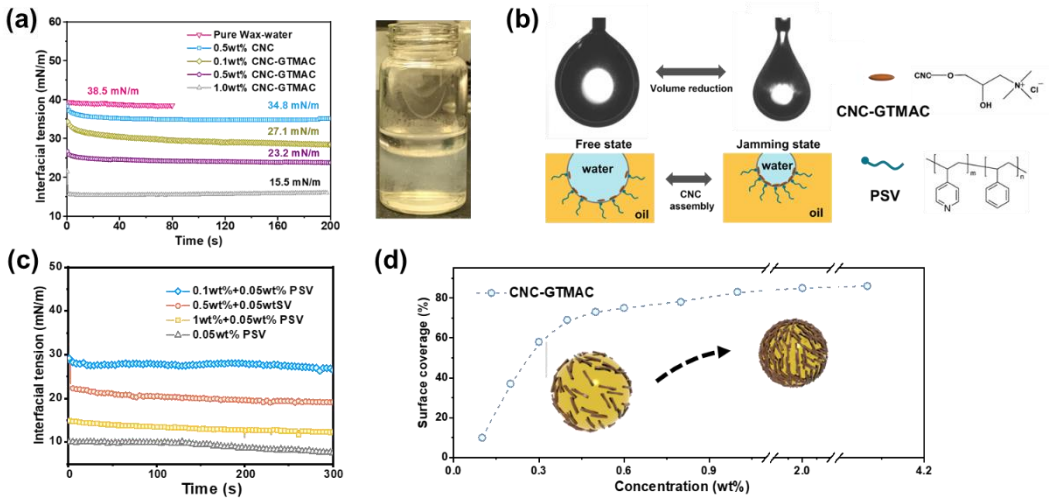

Figure 3-3. (a) The time-evolution interfacial tension change of pure wax-water, pristine CNC and CNC-GTMAC with different concentration by using Wilhelmy plate method. The figure on the right depicts a vial containing a 0.5% w/w solution of CNC-GTMAC in water, where the dispersed CNC-GTMAC particles automatically migrate to the oil-water interface. (b) The CNC-GTMAC stabilized oil/water interface and the buckling effect during volume decrease. (c) The oil/water interfacial variation at different concentration of CNC-GTMAC by using pendant drop method. (d) the hydration diameter of CNC-GTMAC in different zeta potential.

Thus, the "buckling point" (the light scattering effect occurred) provided a simple method to measure the coverage of CNC-GTMAC assemble at the interface. At the initial stage, the CNC-GTMAC was uniformly dispersed at the interface (free state) and gradually moved closer to each other when the volume of droplet was reduced. Finally, the buckling effect occurred when the CNC-GTMACs were closely packed together (termed as jamming state, S_J), and the surface coverage (C) of CNC-GTMAC could be calculated from Eq. (3-4):

$$C \approx \frac{S_J}{S_f} \qquad (3\text{-}4)$$

where S_f refers to the surface area of droplet in free state and S_J is the surface area of droplet in jammed state. The surface coverages of CNC-GTMAC at different concentrations were determined and shown in Figure 3-3d. At very low concentration (0.1wt%), only small numbers of CNC-GTMAC particles were partitioned at the interface, resulting in a low surface coverage of about

≈10%. The surface coverage would dramatically increase to ≈70% when concentration of CNC-GTMAC was increased to 0.5 wt%. However, due to the geometrical effect of the rod-like morphology of CNC-GTMAC, they could not closely pack together to achieve a 100% surface coverage. The value would become flat when concentration exceeded 1 wt%, where the maximum surface coverage was about 80% even at a concentrated CNC-GTMAC of about 4 wt%.

3.3.3 Wax-in-water Pickering emulsion

In this study, 0.5 wt% CNC-GTMAC and pure CNC were used to stabilize wax-in-water Pickering emulsion. In order to obtain stable emulsions of uniform particle size distribution, they were subjected to 3 minutes of sonication. The prepared emulsions were store at 25°C and used within 3 days for further testing. To evaluate the stability of the prepared Pickering emulsions, different concentrations (0.1-4 wt%) of CNC-GTMAC and pure CNC were dispersed in the water phase to prepare oil/water Pickering emulsions. As illustrated in Figure 3-4, all the concentrations of CNC-GTMAC were effective in stabilizing the emulsions. Notably, lower concentrations of CNC-GTMAC (0.1-0.3 wt%) successfully stabilized the interface and formed Pickering emulsions. However, due to lower surface coverage, the CNC-GTMAC assembled at the interface was unable to completely separate the particles. Consequently, the oil particles (discontinuous phase) in contact with each other aggregated due to Brownian movement and Ostwald ripening, leading to a wide and uneven particle size distribution. Further, The Pickering emulsion stabilized with 0.5 wt% CNC-GTMAC exhibited a particle size range of approximately 8 µm (±2 µm), suggesting the successful

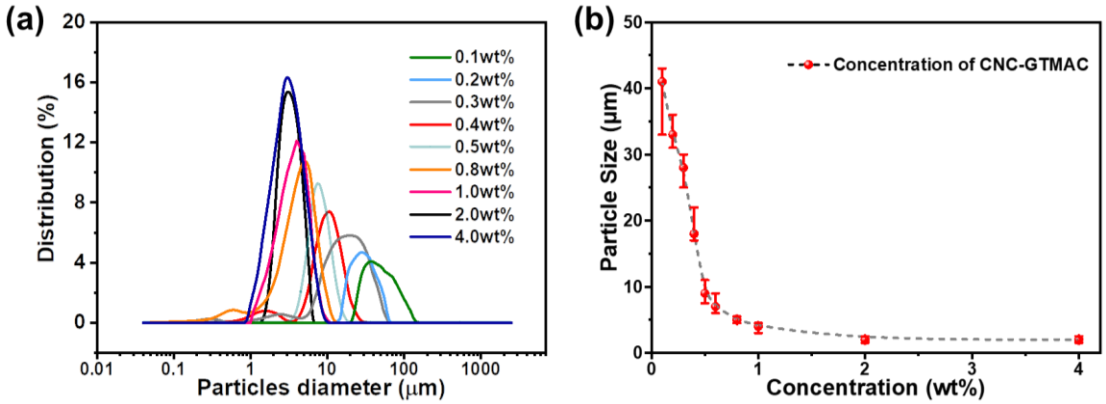

Figure 3-4. (a) and (b) The emulsion particle size changes via the variation of CNC-GTMAC concentration.

formation of a stable emulsion system facilitated by cationic CNC-GTMAC. Notably, increasing the concentration of CNC-GTMAC beyond 0.5 wt% resulted in emulsion systems with narrower particle size distributions, providing evidence that higher surface coverage promoted the formation of a more stable interface.

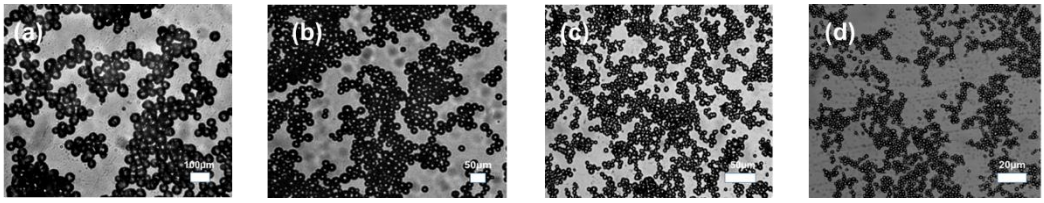

Figure 3-5. The microscopic images of Pickering emulsions particles when the concentration of CNC-GTMAC is (a) 0.2wt%, (b) 0.4wt, (c) 0.5wt% and (d) 2wt%.

At a CNC-GTMAC concentration of 0.1 wt%, the particle size was approximately 44 μm, which could be attributed to the low surface coverage of the modified CNC on the surface of wax particles, as illustrated in Figure 3-3d and Figure 3-5. However, due to the extremely low coverage of CNC-GTMAC at the oil/water interface, the emulsion system was unstable resulting in a broad size distribution. The size of the emulsion particles decreased significantly with increasing CNC-GTMAC concentration, indicating that the diameter of emulsion droplets was impacted by the amounts of CNC-GTMAC in stabilizing the interface as indicated by the interfacial surface coverage data (Figure 3-3d). The emulsion droplets attained a size of approximately 2 μm at a concentration greater than 2wt%, where the oil-water interface was saturated by the CNC-GTMAC particles. The fluorescence optical microscopic image also confirmed that the CNC-GTMAC was trapped at the water/oil interface. As shown in Figure 3-6a and b, the Calcofluor stained CNC-GTMAC distributed mainly at outer shell and oil phase stained with Nile red showed a strong signal in the inner phase. This core-shell structure revealed by the fluorescent optical microscopy demonstrated the CNC-GTMAC (0.2wt% and 0.5wt%) were well distributed at the interface, separating the oil droplets and preventing coalescence. Pure CNC was not an effective emulsifier at concentration lower than 1% as the high density of negative charges on its surface inhibited the partitioning of the CNC to the interface. After the o/w Pickering emulsion was prepared, the interfacial energy did not decrease significantly, thus the oil droplets would agglomerate to minimize

their free energy. Thus, coalescence between the oil droplets occurred and the Pickering emulsion became unstable. When the concentration of pure CNC exceeded 1 wt%, stable Pickering emulsion was produced due to the higher CNC concentration, whose counter-ions shielded the electrostatic repulsion.

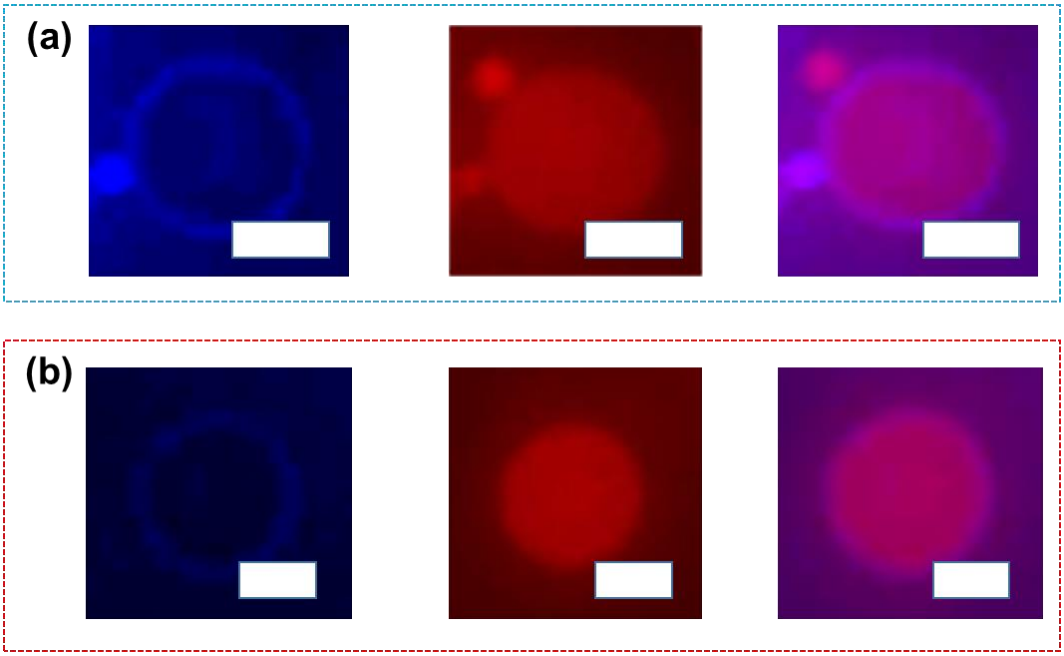

Figure 3-6. The core-shell CNC-GTMAC stabilized Pickering emulsion particle, (a) 0.2wt% and (b) 0.5wt%, observed by fluorescent optical microscopy. The scale bar, (a) 10μm and (b) 5μm.

3.3.4 Construction of superhydrophobic surface

The preparation of the superhydrophobic surface is shown schematically in Figure 3-7. The Pickering emulsion was first diluted with water to reduce the concentration from 20% to 5%, and it was then spray coated onto a vertical glass substrate using a spray-coater with a 0.35 mm nozzle at a pressure of 30 psi. The distance between the spray gun and glass plate was kept at about 15 cm and the spraying time for one surface was about 5 s and the coating process was repeated 3 times. The coated glass substrate was then left to dry before it was further analyzed in order to correlate the superhydrophobic surface with the size of Pickering emulsions prepared from different CNC-GTMAC concentrations. The nomenclature of these systems is as follows: the CNC-GTMAC stabilized Pickering emulsion (PE) was denoted as CGPE and CGPE-33 corresponds to the PE with an average size of about 33 μm. For instance, as can be seen in size distribution Figure 3-8c, the 0.2,

0.4, 0.5 and 2 wt% CNC-GTMAC stabilized Pickering emulsion were designated as CGPE-33, CGPE-18, CGPE-8 and CGPE-2, respectively.

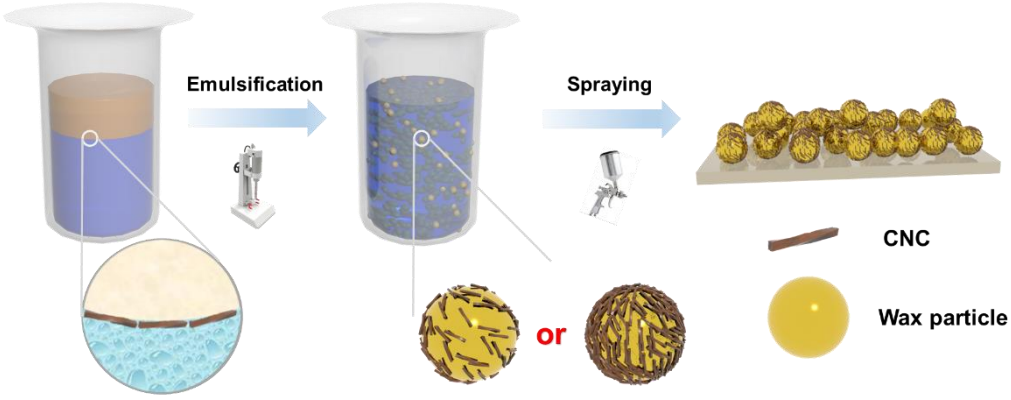

Figure 3-7. Schematic illustration of superhydrophobic surface prepared from wax-in-water Pickering emulsions.

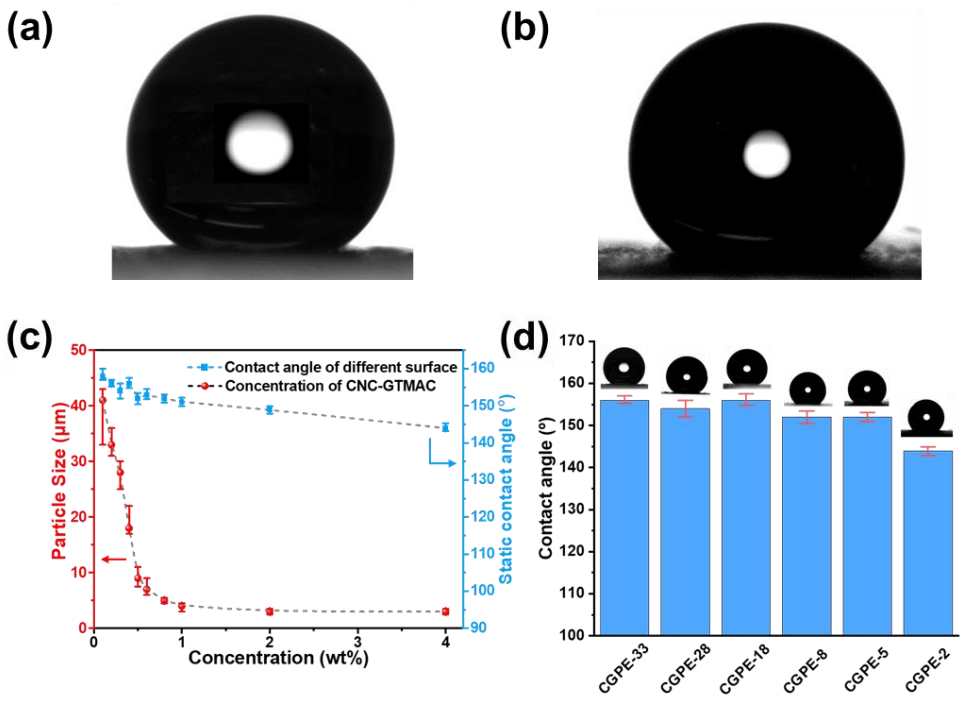

Figure 3-8. The static contact angle of water-repellent surface coated with emulsion particles of (a) 33μm and (b) 2μm. (c), (d) The size distribution of emulsion particles and corresponding static contact angle of different superhydrophobic surface.

Figure 3-8 (a) shows the effect of the size of the emulsion droplets (prepared using varying concentrations of modified CNC) on the contact angles of the superhydrophobic surfaces. Most of

the surfaces displayed strong water repellency and the contact angles were between 144° to 156°. The surface prepared using the 33 μm emulsion particle possessed the highest contact angle of 156° (Figure 3-8a and b), which is attributed to the larger particle size trapping more air between the protrusion formed during the drying process. However, the superhydrophobicity of surface gradually decreased as the particle size became smaller. As evident from Figure 3-8 (c) and (d), the contact angle was about 144° for a particle size of about 2 μm. The smaller particle diameter yielded a lower separation distance between each protrusion, which reduced the hydrophobicity of the surface. In addition, the packing density of smaller emulsion particles at the surface would be higher, and due to the hydrophilic characteristics of CNC-GTMAC, the water would spread over this surface and penetrate into the interstitial air-pockets. Conversely, larger emulsion particles possessed lower surface coverage and larger distance between protrusion that reduced the contact area between the droplets and the surfaces thereby producing a higher static contact angle. The characterization and demonstration of the significant effect of surface morphology and topography on the prepared superhydrophobic surfaces were conducted using scanning electron microscopy (SEM). Figure 3-9a illustrates the morphology of surface CGPE-2, revealing a reduced roughness and a limited number of protrusions or bumps on the surface. This characteristic leads to a reduced presence of air cushions within the structure. Besides, the densely packed arrangement of small particles contributed to a smoother topography, ultimately resulting in a higher apparent contact angle and reduced superhydrophobicity according to the Cassie equation. The surface CGPE-5 composed of larger particles possessed a higher apparent contact angle of about 153°. This stronger hydrophobicity could be attributed to their looser structure capable of entrapping more air inside the structure, consequently reducing the solid-liquid contact area and improving the surface superhydrophobicity. Moreover, when the surface was prepared using the largest particles (i.e., CGPE-33), the resulting topography became significantly rougher, as evidenced by the increased height of protrusions shown in Figure 3-9b. This increased roughness enabled the surface to more effectively resist water penetration and exhibited the highest apparent contact angle among the prepared surfaces.

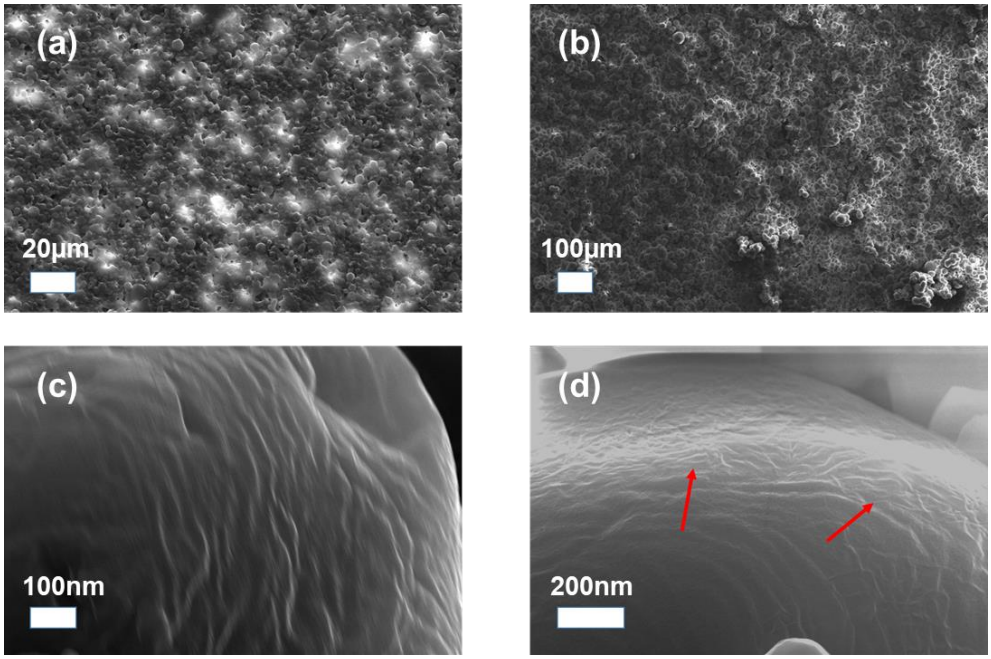

Figure 3-9. The SEM images of (a) CGPE-2 and (b) CGPE-33, respectively. The zoom-in SEM images of (c) CGPE-2 and (d) CGPE-33 and the clear observation of rapped CNC at their surface (The red arrow).

The adhesive force testing protocol was conducted using a highly sensitive microelectromechanical balance system. As shown in Figure 3-10a, a platinum ring (droplet holder in diagram) hanging with a test droplet connected to the balance that records the adhesive force as the stage was being raised to the droplet. As illustrated in Figure 3-10b, a software controlled the motion of the solid substrate as it was raised towards the liquid droplet (**1**. Advancing process inset Figure 3-10b and c) at a constant speed until it contacted the liquid droplet (**2**. Touching process). On touching the liquid droplet, the software-controlled protocol moved forward a short distance then reversed the direction of the substrate and moved away from the liquid droplet, and the adhesion forces during this process was recorded (**3**. Removing). Finally, the liquid droplet became detached from the substrate as indicated in **4.** Separating process in Figure 3-10b.

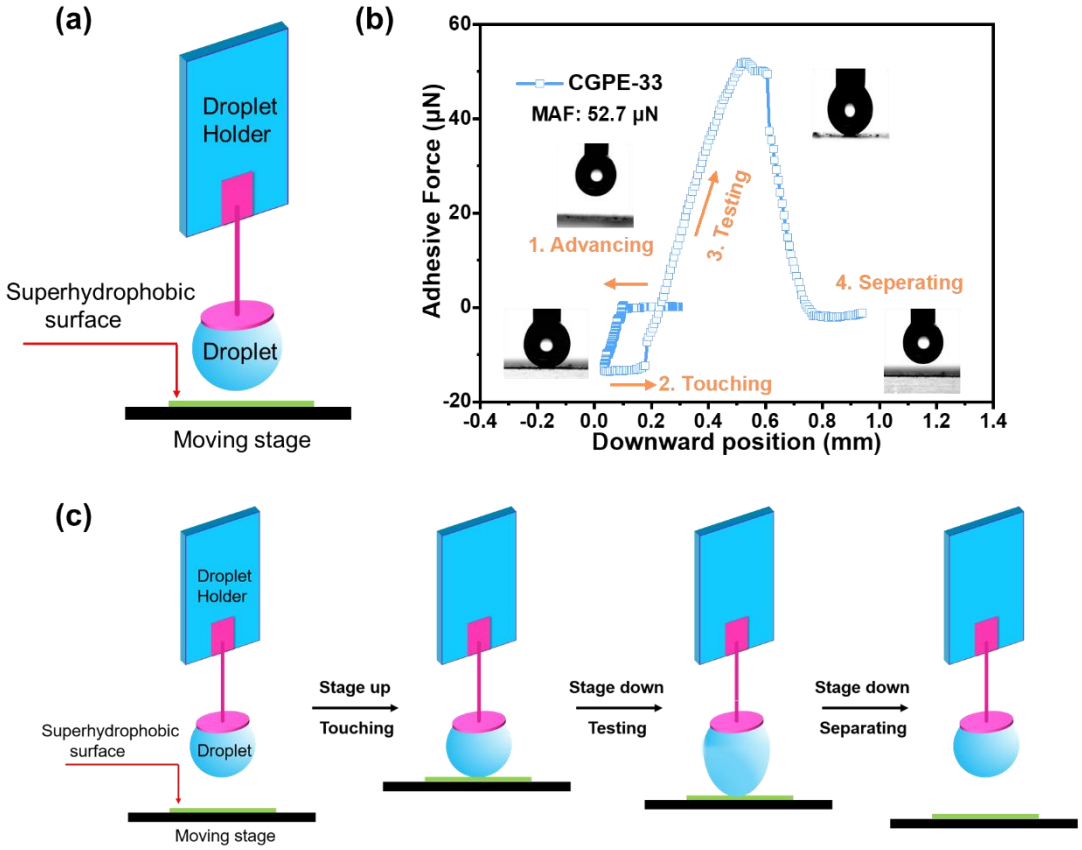

Figure 3-10. (a) The diagram of droplet holder for testing water adhesive force. (b) The graphical illustration of adhesive force measurement protocol for the surface prepared with CGPE-33. (c) Schematic illustration of testing process of surface adhesive force.

The superhydrophobic surface prepared with the largest particle size, CGPE-43, displayed the smallest adhesive force (47.7 μN). The adhesion increased as the emulsion particles were reduced, which is identical to the trend observed for the static contact angle. The adhesive force was observed to increase from 52.7 μN for CGPE-33 to ~110 μN at a particle size of about 2μm which corresponds to CGPE-2.

Despite the superhydrophobicity observed in most of these surfaces (CGPE-5, 8, 18, 28, and CGPE-33), as well as the highly hydrophobic character of CGPE-2, there was a substantial difference in the measured adhesion forces. The adhesion forces displayed a wide variation, ranging from 47.7 μN to 79 μN for the superhydrophobic surfaces and 110 μN for the highly hydrophobic surface. The variation in adhesive force could be attributed to the differences in surface topography and the resulting wetting states induced by the size of particles. The superhydrophobic surface constructed

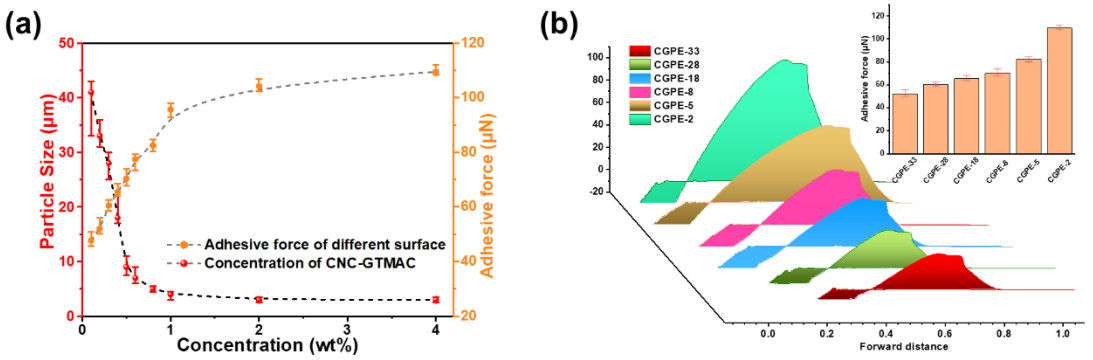

Figure 3-11. (a) The adhesive force profiles (as a function of droplet separation and substrate) for (low to high concentration from front to back in the graph). (b) The relationship between adhesive force and emulsion particle sizes.

using large emulsion particle could potentially form the Cassie wetting state, indicating that the droplets became suspended on the protrusion. However, if the dimension of protrusion, the size of emulsion particle was relatively small, the droplet could penetrate into the air cushion and touched the substrate forming the Wenzel wetting state. As shown in Figure 3-12a, when the droplet contacted the micro-size protrusions on the surface, it would form a concave liquid surface above the air pocket. Thus, the height of protrusion and thickness of the air pocket determined the wetting state of superhydrophobic surface. For example, the bottom surface of the liquid would not touch the substrate if the surface was produced using large particles such that the liquid was not in contact with the substrate. In contrast, when the surface was constructed using smaller emulsion particles, the liquid did not suspend between the particles due to their smaller protrusions (Figure 3-12b). Instead, the liquid was in contact with the substrate, causing it to infiltrate into superhydrophobic surface, and this wetting state is known as Wenzel's wetting state. As a result, the adhesive force of CGPE-33 and CGPE-28 possessed a relatively low adhesive force of about 52.7 μN and 60.5 μN respectively due to the Cassie wetting state. The surface of CGPE-2 displayed higher adhesive forces of about 110 μN respectively due to the Wenzel wetting state. The confocal laser microscopy was utilized to demonstrate the wetting state of different surfaces.

.

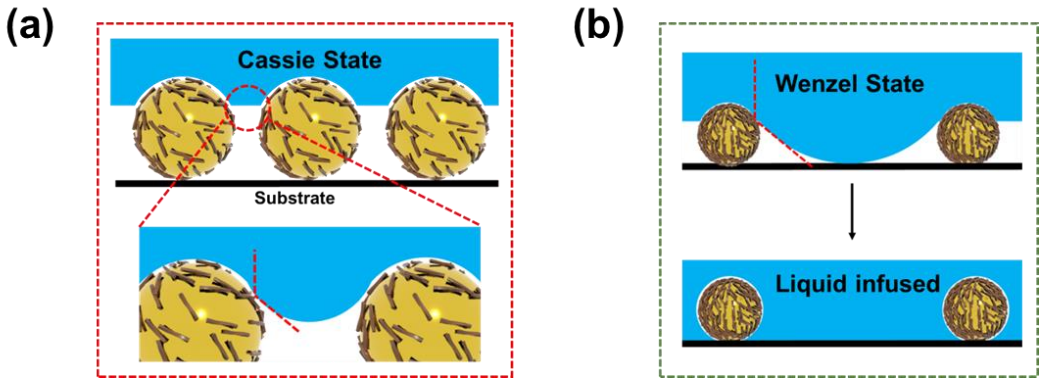

Figure 3-12. The schematic illustration of adhesive force generation for emulsion particles with different sizes. (a) The Cassie wetting state. (b) The Wenzel wetting state.

In order to clearly observe the liquid-solid contact line, the emulsion particles were initially stained with Calcofluor white before the superhydrophobic surface preparation and the droplet was stained with a low concentration Rhodamine B (0.01wt%). The low concentration of Rhodamine B did not impact the surface properties of water, and the surface tension remained around 72 mN/m². During the experimental procedure, a 5 μL droplet stained with Rhodamine B was carefully placed on the target superhydrophobic surface, and the fluorescence signal was collected by a laser to generate an image. The characterization of the solid-liquid contact line was achieved using the "z-stack" technique, enabling the acquisition of multiple images at different focal planes along the vertical (Z-axis) direction. These images were subsequently overlapped and reconstructed to form a 3D representation. In Figure 3-13, the green dots and red dots corresponded to the water signal and paraffin wax particle, respectively. For the highly hydrophobic CGPE-2 surface, Figure 3-13c clearly shows the gaps between the emulsion particles as in contact with the droplet. However, after stabilized for 30s, these gaps were filled with water, as confirmed by the laser confocal microscopy image in Figure 3-13d, demonstrating the Wenzel wetting state of the surface.

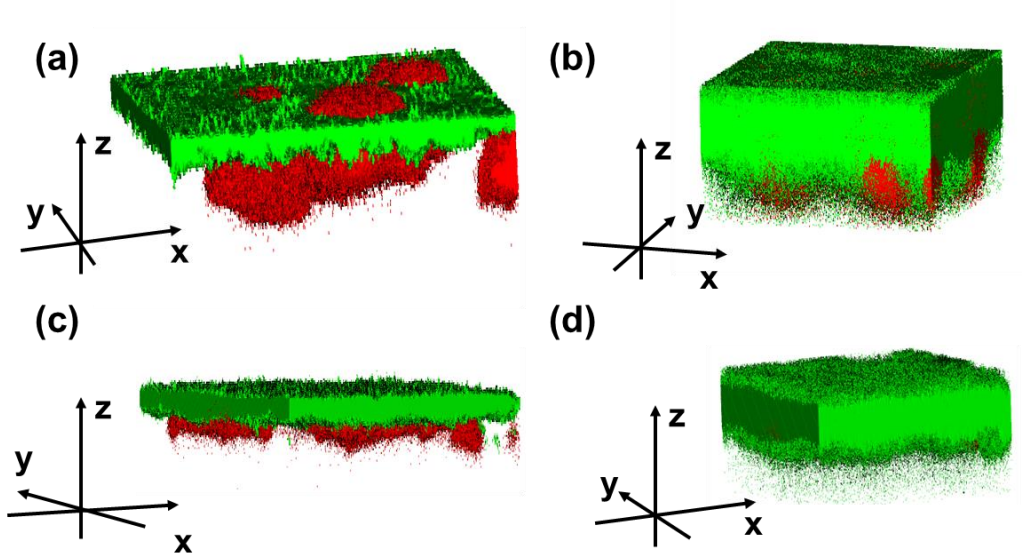

Figure 3-13. (a) The laser confocal microscopy images of three phase contact line when CGPE-5 was in contact with droplet and (c) the three phase contact line after stabilized with 30s. (b) The laser confocal microscopy images of three phase contact line when CGPE-2 was in contact with droplet and (d) the three phase contact line after stabilized with 30s.

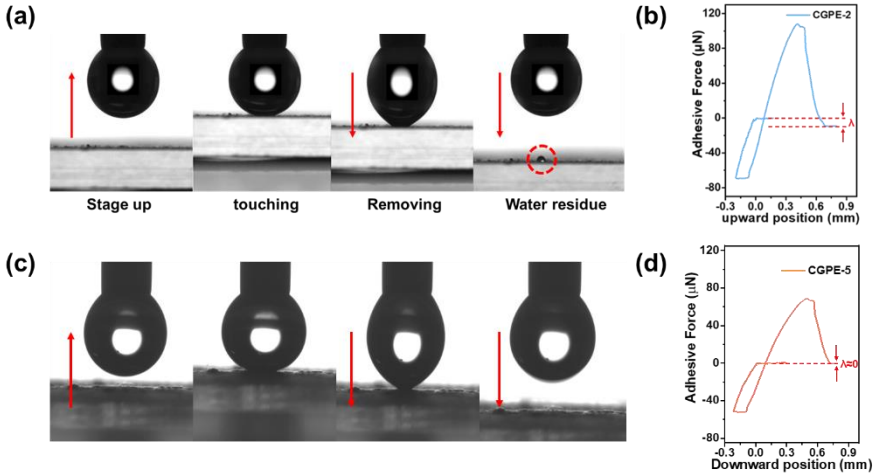

Figure 3-14. (a) The adhesion behavior of CGPE-2 when contacted by a 5 μL liquid droplet. (b) The adhesive force characterization of CGPE-2. (c) The adhesion behavior of CGPE-5 when contacted by a 5 μL liquid droplet. (d) The adhesive force characterization of CGPE-5.

Such an investigation was also conducted on the CGPE-5 surface. As depicted in Figure 3-13a and b, water only partially penetrated the porous structure but remained suspended between the particles, resulting in medium adhesion forces and partially wetted Cassie-state superhydrophobicity. The digital image further illustrates the infusion of water into the air pocket on the CGPE-2 surface,

whereas no penetration occurred on the superhydrophobic CGPE-5 surface. Figure 3-14a captures the moment when a liquid droplet was detached from the substrate prepared with CGPE-2, revealing a small residue of the droplet on the surface. The adhesion measurement also demonstrated the Wenzel wetting state. As the droplet became detached from the surface, the adhesive force detected by electromechanical balance did not return to zero and a height difference, h, appeared before and at the end of the test (Figure 3-14b). As a consequence, the droplet was stretched and dissociated during testing, forming a tiny droplet on the surface, as indicated by force balance system. However, the adhesion behavior of CGPE-5 was not caused by the Wenzel wetting state. As shown in Figure 3-14c, even though the droplet was deformed due to the adhesion, no water residue remained on the surface after testing, confirming that the water droplets were completely removed from the superhydrophobic surface. Also, the value of adhesion for droplet in Figure 3-14d was consistent before and after recording, demonstrating the droplet was entirely separated from superhydrophobic surface.

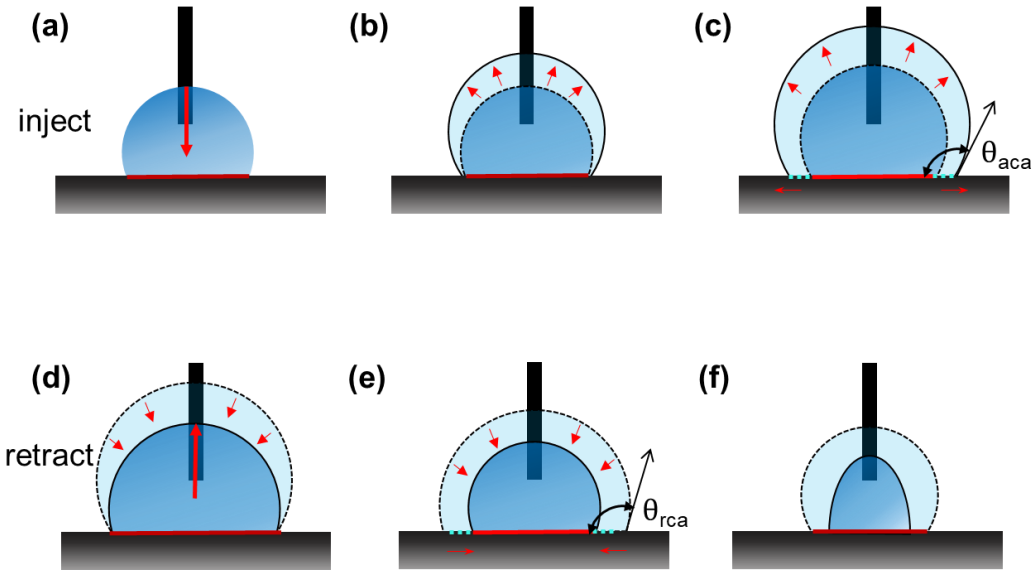

Figure 3-15. Different stages of advancing contact angle (ACA) and receding contact angle (RCA) measurement.

In addition to the topography effect discussed earlier, the presence of CNC-GTMAC on the surface also plays a role in the adhesion of the droplet due to its intrinsic hydrophilic properties. To evaluate the impact of hydrophilic CNC-GTMAC on the superhydrophobic CGPE surface, contact angle

hysteresis testing was employed, providing a valuable method to measure the movement of the three-phase contact line during droplet advancement and receding on the surface. In Figure 3-15, an initial 2 μL droplet was deposited, and water was subsequently added before the measurement began. At this stage, the advancing contact angle (ACA) was not achieved, as the droplet shape underwent changes while the baseline (highlighted with a black line) remained stable. Once the ACA was attained, the baseline steadily advanced with the addition of water, resulting in an increase in droplet volume from 3 to 10 μL during the video recording. For the receding contact angle (RCA) measurements, water was initially removed from a starting droplet before the video recording commenced. Similar to the ACA stage, the RCA was not achieved immediately, with the droplet shape changing while the baseline remained stable. After reaching the RCA, the baseline progressively receded when the droplet volume was reduced from 10 to 3 μL while capturing a video. Droplets smaller than 3 μL became distorted by the needle, compromising the reliability of the data obtained. As evident from Figure 3-16, CGPE-33 displayed a large advancing contact angle (ACA) of approximately 158° and a corresponding receding contact angle (RCA) of about 148°, indicating a relatively low contact angle hysteresis of 10°. However, as the surface coverage of CNC-GTMAC was increased to approximately 40, 60, 70, and 75% for CGPE-28, CGPE-18, CGPE-8, and CGPE-5, respectively, the ACAs were minimally affected while the RCAs decreased significantly. This resulted in an increase in contact angle hysteresis, from 13° for CGPE-28 to 25° for CGPE-5. The sliding angle testing aligned well with the observed trend in the contact angle hysteresis. The underlying reason could be explained as follows: during ACA measurements, the hydrophilic nanostructures on the outer surface of the micro-particles was wetted by water, forming bridges between neighboring pillars and increasing the solid-liquid contact area resulting in a strong adhesion force. When the droplet's contact line began to retract from the neighboring pillars, a substantial energy barrier has to be overcome for surfaces with a high density of hydrophilic domains. In other words, the nonwetting state over the large micro-grooves enhanced the advancing contact angle, while water impregnation on the nano-grooves delayed the receding contact angle. Notably, the hydrophilic nanodomains on the outer surface of the pillars reduced the receding contact angle, resulting in a pronounced hysteresis.

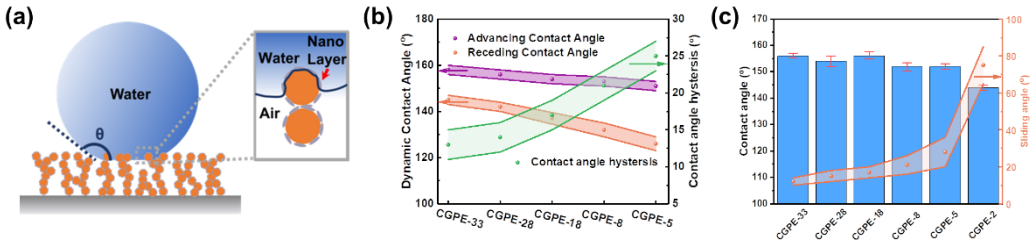

Figure 3-16. (a) Schematic of a sessile liquid drop on a hydrophilic/superhydrophobic surface made of highly porous aggregates of microspheres. The schematic illustrates the definition of the static contact angle. The term "edge" is used to distinguish the formation of three-phase contact line (TPCL) between nanostructure and microstructure. (b) The advancing contact angles, receding contact angles and contact angle hysteresis of different surfaces. (c) The static contact angles and sliding angles of different surfaces.

Although the single size emulsion particles are sufficient to prepare superhydrophobic surface with a high static contact angle, we noted that the water droplet would slightly pin onto the surface. This could be attributed to the single size emulsion particles forming a homogeneous liquid-solid contact points, where the partially intruded water would be sealed into the micro-protrusion leading to a high capillary force with a large contact angle hysteresis. However, for extremely low contact angle hysteresis surfaces, such as lotus leaf with hydrophobic wax pillars, multiple contact points and hierarchical structure were present on the rough surface that inhibited the intrusion of water into the micro-gaps within the microstructure. In other words, the micron-sized papillae on the surface could suspend the droplet, forming a high static contact angle and superhydrophobicity. The second-scale-sized wax pillars on the papillae offered more contact points on each papilla, which reduced the solid-liquid contacts and increased the number of air pockets and height of protrusion. Since air is a hydrophobic medium, the entrapped air pockets contributed to the enhanced water repellency, and a reduction in the adhesive force and sliding angle.

To verify this hypothesis, we prepared superhydrophobic surfaces containing mixtures of wax emulsions of two different size i.e. CGPE-33 (33 µm) and CPE-2 (2 µm) as CNC emulsified CPE-2 possessed negative charges and would interact with positively charged CGPE-33 emulsion. As shown in Table 1-1, this surface was designed as ME (mixed emulsion surface) and ME-7-1 refers to the ratio of CGPE-33: CPE-2 of 7:1.

Table 1-1. The construction of low adhesive force superhydrophobic surface by mixing CGPE-33 and CPE-2

CGPE-33	CPE-2	
8	0	ME-8-0
7	1	ME-7-1
3	1	ME-3-1
1	3	ME-1-3
1	1	ME-1-1
0	8	ME-0-8

As shown in Figure 3-17, the adhesive force of the superhydrophobic surface decreased rapidly when a small amount of CPE-2 was added to the CGPE-33, where ME-7-1 only displayed an adhesive force of about 50.5μN, indicating that the introduction of secondary roughness could significantly reduce the adhesive force. Further, if CPE-2 was added to the system up to a ratio of 1:1, the surface ME-1-1 displayed an ultra-low adhesive force of only 5.7μN (Figure 3-17b and 3-17c). For this substrate, liquid droplet would immediately roll off the surface under gravitational force without any hysteresis when a small tilt angle was applied (less than 5° in Figure 3-18a and b). As shown in Figure 3-18c, a water droplet with 1 mm in radius at a velocity of 1m/s impacted the surface prepared with ME-1-1 emulsion, and it did not penetrate the air pocket of the coated layer. The drop's kinetic energy of the liquid droplet was converted to vibrational energy, allowing the drop to rebound before it underwent damped oscillations and finally rested on the surface in the Cassie state. In addition, when a droplet touched with the ME-1-1 surface shown in Figure 3-18d, the surface could easily be separated confirming the low adhesive force of ME-1-1 surface.

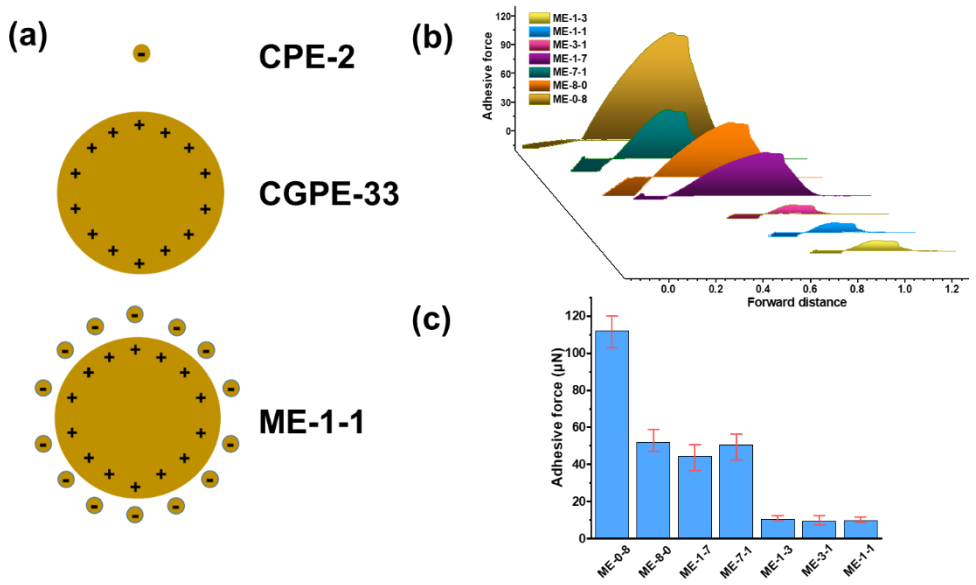

Figure 3-17. (a) Schematic diagram of CPE-2 with negative charge attracted by positive charged CGPE-33. (b) Adhesive force profiles of ME-1-3, ME-1-1, ME-3-1, ME-1-7, ME-7-1, ME-8-0 and ME-0-8. (c)The value of different mixing superhydrophobic surface).

The mechanism is as follows; when we added the CPE-2 into CGPE-33, the CPE-2 would electrostatically absorb on the surface of CGPE-33. Thus, the CGPE-33 with larger dimension served as the rough structure, which could support the droplet and prevent it from penetrating the air pocket. The smaller CPE-2 on the CGPE-33 surface formed smaller protrusion at the solid-liquid interface, thereby increasing the number of air pockets and reducing the fraction of contact area. Consequently, the 'lotus leaf' like structure could be achieved and the surface of ME-1-1 possessed an ultra-low adhesive force and self-cleaning characteristics. However, if we continued to increase the fraction of CPE-2 up to a ratio of ME-1-7, there are more negative CPE-2 particles bound to CGPE-33 droplets and the gap between the CPE-2 particles became smaller than ME-1-1 resulting in an increase in the contact area between the solid surface and water resulting in an increase of the adhesive force from 5.7 to 44.6 μN. However, if fewer CPE-2 particles were introduced to CGPE-33, the contacting area between solid and liquid was reduced, since the CPE-2 particles could not support the liquid due to the larger distance between them causing the liquid curve surface to intrude into the air cushion, thereby increasing the droplet adhesive force.

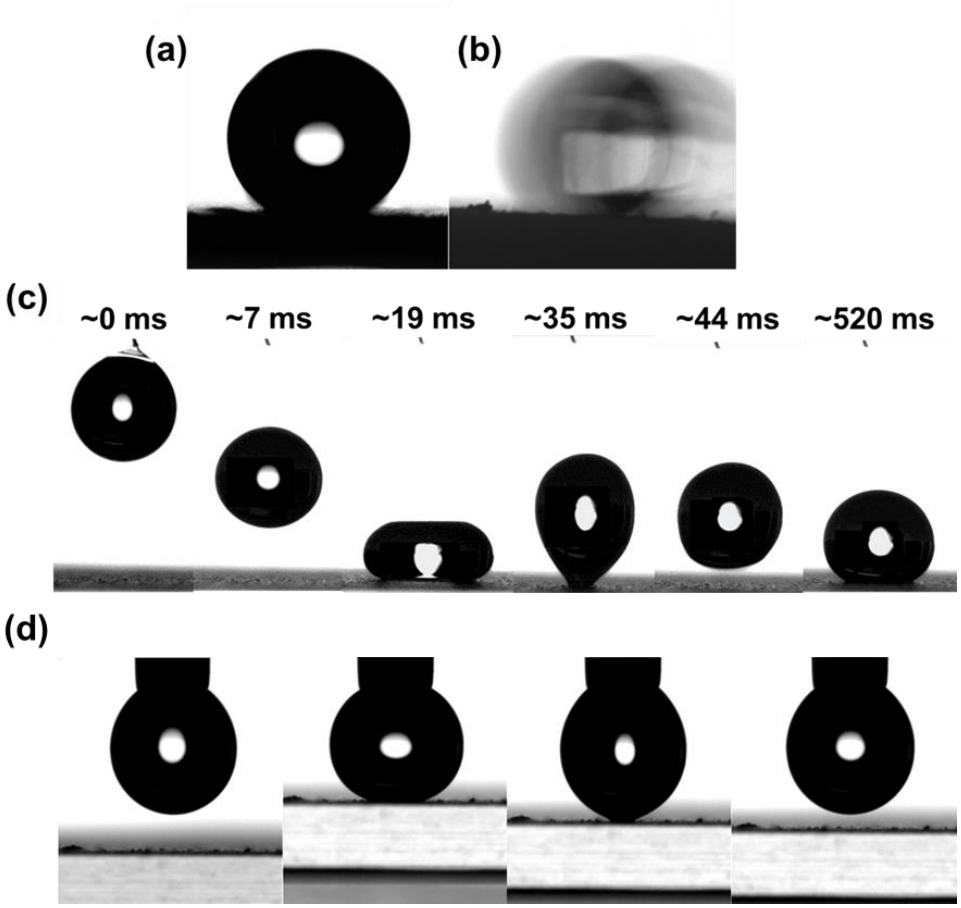

Figure 3-18. (a) Static contact angle of superhydrophobic surface prepared using ME-1-1 and (b) droplet sliding off the surface as the substrate was tilted. (c) Dynamics of a 5μL falling water droplet on the ME-1-1 surface. (d) The adhesion behavior of ME-1-1 when contacted by a 5 μL liquid droplet.

3.3.5 Mapping of the surface adhesive force

To precisely measure the adhesive force of our superhydrophobic surface, a mapping of the force distribution on the surface was conducted. In natural and most engineered superhydrophobic surfaces, the irregular and anisotropic microstructures would affect the wetting phenomena on the surface. Additionally, the uneven surface would strongly influence the accuracy of the wettability test and analysis. In developing this methodology, the apparatus used comprises of a precision electronic balance and a x-y stage that allowed us to scan the adhesive force over a pre-determined surface.

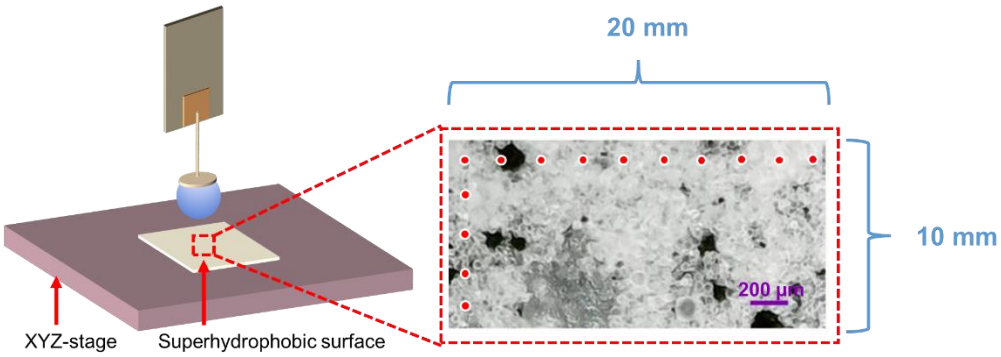

Figure 3-19. The microscopic images and corresponding illustration of force scan maps (The scale bar is 200 µm, the red color indicates the high adhesive force and blue color shows low adhesive force).

The forward speed of our superhydrophobic surface was set to 5 µm/s and the retraction speed was set to 10 µm/s. This was to ensure that for each probing step, the droplet would be in equilibrium. We then scanned an area of 20x10 mm with 200 µm spacing between each measurement point. After determining the pull-off force, the adhesive force scan mapping was recorded and analyzed as recorded in Figure 3-19 together with the corresponding microscopic image. The wetting variations corresponded to variations in the structural colour which were due to the subtle structural differences of the emulsion particles. Therefore, we could obtain precise adhesive force characterization of the surface even though the structure was uneven. Although the spraying method would generate the irregular uneven porosity, the surface force mapping demonstrated that the different superhydrophobic surfaces (CGPE-5, CGPE-8, CGPE-18, CGPE-28, CGPE-33 and ME-1-1) exhibited a homogeneous adhesive force over an area of 20x10 mm revealed by the force mapping shown in Figure 3-20. This homogeneity could be attributed to the fact that the main variations in contact angle and adhesive force associated with the microstructure were primarily influenced by the differences in emulsion particles. These particle variations resulted in distinct solid-liquid contact lines that contributed to the observed variations in wetting state.

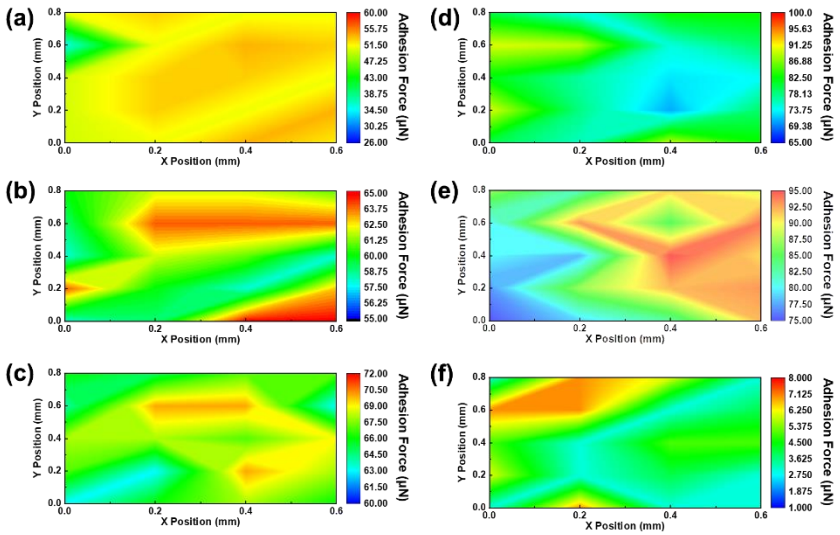

Figure 3-20. The adhesive force mapping of (a) CGPE-33, (b) CGPE-29, (c) CGPE-18, (d) CGPE-8, (e) CGPE-5 and (f) ME-1-1.

3.3.6 Non-loss micro droplet transportation

As a result of the switchable adhesion behavior, the ME surface prepared by mixing different size emulsion particles could be used for the non-loss micro droplet transportation. As shown in Figure 3-21, a liquid droplet with 6μL was placed on a low adhesion superhydrophobic surface. Next, the surface was raised until it touched the high adhesion superhydrophobic surface. Because of the large vertical adhesive force, the droplet could be collected by high adhesion superhydrophobic surface. Finally, the water droplet was transported to a hydrophilic surface without any loss during the transportation process.

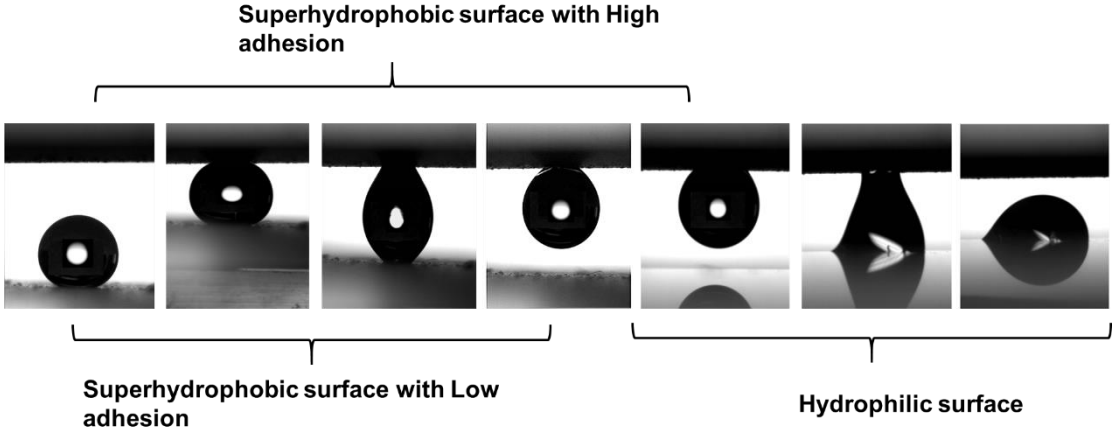

Figure 3-21. Transportation of a water droplet from superhydrophobic surface with low adhesion

to a hydrophilic surface using a superhydrophobic surface with high adhesion.

3.4 Conclusions

In this study, we investigated the utilization of CNC functionalized with positively charged functional groups as an emulsifier for preparing wax-in-water Pickering emulsions. The size, surface charge, and morphology of the CNC-GTMAC particles were characterized after the functionalization process. Besides, the interfacial properties of the wax-water interface, including interfacial tension and surface coverage, were evaluated. It was found that higher concentrations of CNC-GTMAC led to a reduction in interfacial tension and an increase in surface coverage, with coverage reaching up to 80% when the CNC-GTMAC content exceeded 2%.

The prepared Pickering emulsions, containing CNC-GTMAC particles of different sizes, were utilized to construct superhydrophobic surfaces with tunable adhesive forces towards water droplets. Through various techniques such as contact angle, contact angle hysteresis, and sliding angle measurements, we successfully demonstrated the construction of these surfaces with adjustable adhesive properties, ranging from extremely low adhesion (5.7 μN) to high adhesion (79 μN). The variation in emulsion particle size played a crucial role in determining the surface topography, as well as the solid-liquid contact lines and contact areas. Scanning electron microscopy (SEM) was employed to observe the distinctive surface topographies, while laser confocal microscopy provided valuable insights into the superhydrophobicity and three-phase contact lines of the surfaces. Additionally, two-dimensional adhesive force measurements further confirmed the homogeneity of the surface, ensuring consistent adhesive behavior across the sample. Finally, as a demonstration of the potential applications of these special superhydrophobic surfaces, we utilized a non-loss micro droplet transportation method, showcasing one of the future directions for these surfaces. These findings highlight the ability to tailor the adhesive properties of superhydrophobic surfaces through the manipulation of emulsion particle size, opening up possibilities for various applications where controlled adhesion to water droplets is desired.

Chapter 4. Unusual under liquid dual superlyophobic surface

4.1 Introduction

Surfaces with special wetting behaviors have attracted significant attention due to their wide range of applications.[7, 167] Examples include the Lotus leaf-inspired superhydrophobic surfaces that possess self-cleaning properties, amphiphilic clam shells capable of recovering oil spills from water due to their oleophilic nature, and superhydrophilic membranes inspired by fish scales that selectively separate oil from oil/water mixtures by exhibiting underwater oleophobicity.[168-170]

In addition to single-function surfaces, there is an increasing interest in smart surfaces that can dynamically respond to external stimuli such as light[171], CO_2[172], temperature[173], pH[174], and many other external stimuli. These surfaces offer the potential for versatile and controllable wetting behavior. More recently, a new and intriguing type of surface, known as "under liquid superlyophobic surface," was reported.[175] These surfaces can exhibit simultaneous superoleophobicity underwater and superhydrophobicity under oil. However, the preparation of under liquid dual superlyophobic materials remains a challenge, as it relies heavily on complex re-entrant topography and special surface energy materials.[176] The underlying mechanisms for designing under liquid super-lyophobic surfaces are still unclear, particularly from the perspective of surface energy.[177] Therefore, significant challenges remain in achieving under liquid superlyophobicity without relying on lyophobic materials and intricate re-entrant structures.[5, 178] Further research is needed to explore novel approaches and understand the fundamental principles governing the design and fabrication of such surfaces.

For a given surface, achieving under liquid dual superlyophobicity (underwater superoleophobicity and underoil superhydrophobicity) is not thermodynamically favorable. As depicted in Figure 4-1, surfaces with high free energy, such as normal hydrophilic surfaces like metals or ceramics, exhibit a stronger affinity to water than oil.[179] Consequently, when oil comes into contact with such a hydrophilic surface, it is displaced by water droplets, resulting in a low contact angle between water and oil ($\theta_{w/o}$). On the other hand, when the hydrophilic surface is immersed in water, the oil droplet cannot displace the water trapped on the surface, leading to a high contact angle between water and oil.[180] Conversely, surfaces with low surface energy, such as systems consisting of fluorinated chains, alkanes, or organosilicon materials, exhibit a stronger affinity for oil.[181] As a result, these

surfaces display a low contact angle between oil and water ($\theta_{o/w}$) and a high contact angle between water and oil (Figure 4-1). Therefore, only one state (either superoleophobic or superhydrophobic) may be thermodynamically stable for a given surface.

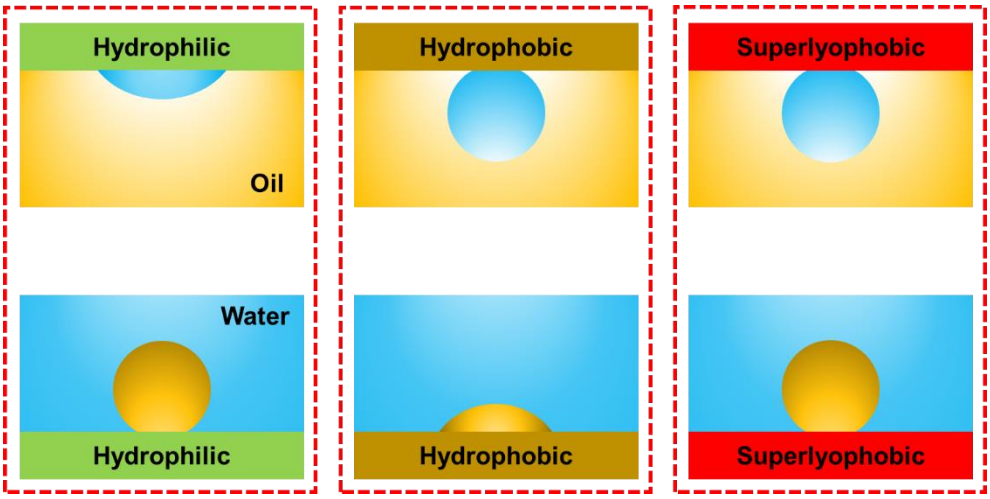

Figure 4-1. The wetting behavior of hydrophilic, hydrophobic and super-lyophobic surface under dual liquid (water and oil).

However, under liquid superlyophobicity can be achieved by manipulating the surface into a metastable state. This concept has been extensively studied in solid-liquid-air systems.[182-184] By employing a metastable state in a solid-oil-water system, a Cassie-type composite can be produced. In other words, the droplet (either oil or water) becomes suspended on the composite interface between the solid and the infused liquid (either water or oil). To generate such a surface, two criteria need to be satisfied: (1) the surface must possess both hydrophobic and hydrophilic components to be compatible with water and oil that ensures that the surface can trap a water or oil film; (2) the configured surface free energy should support a stable oil-water interface when a secondary liquid is introduced.[185] To achieve this, we will combine the superhydrophilic cellulose nanofiber (CNF) and superhydrophobic ODA modified lycopodium sporopollenin extine shell (ODA.SES). The hydrophobicity of the overall system is strongly dependent on the proportion of the two components, in other words, the hybrid membrane (CNF-ODA.SES) would become more hydrophobic when higher percentage of ODA.SES is introduced. Conversely, the membrane would exhibit stronger affinity to water when higher contents of superhydrophilic CNF is introduced to the system. Based on the composition of CNF and ODA.SES, the free energy of hybrid membrane could be precisely tuned and determined via a sessile drop method. Besides, the prepared membrane exhibited strong

mechanical properties when small contents of CNF is incorporated into system. Meanwhile, the densely packed CNF and uniformly distributed ODA.SES offer a vacuum-controlled filtration system to separate the oil-water mixture from oil/water emulsions.

4.2 Materials and method

Materials

Lycopodium clavatum pollen (Flinn Scientific Canada Inc.), phosphoric acid, acetone, ethanol purchased from Sigma-Aldrich were used as received. The cellulose nanofibers (CNF) were prepared from cotton pulp via TEMPO oxidation. All chemicals were used without additional purification, unless stated otherwise. Milli-Q water (resistivity of 18.2 MΩ cm) was used to prepare the aqueous dispersions.

Particle size distribution

The size of the lycopodium pollen particle was measured using the PSA 1190 particle sizer from Anton Pear. To prevent the agglomeration of the particles, the pollen particle was sonicated and introduced into the measuring cell.

Optical microscopy

Photomicrographs of the pollen particles were recorded using a polarized light microscope (Nikon Polarizing Micro-scope Eclipse LV100POL with Nikon DS Camera control unit DS-U2). This was used to characterize the morphology of lycopodium pollen particles and confirm the extraction of pollen shell.

Fourier transforms infrared (FT-IR) spectroscopy

FT-IR spectroscopic measurements on the pollen particles, cellulose nanofiber (CNF) and ODA.SES were performed using a Bruker Tensor 27 FTIR spectrometer. This was used to confirm the modification of lycopodium pollen, and the spectrum was compared with pristine pollen. Samples were freeze-dried and pressed into potassium bromide (KBr) pellets.

TEM Imaging

The size and morphology of the nanoparticles were evaluated using a transmission electron microscope (TEM, Philips, CM10). A droplet of the sample solution was placed on a carbon coated copper grid, and left for 10 min, after which the excess liquid was removed using a small piece of filter paper and left to dry overnight before the TEM analysis.

SEM imaging

The morphology and electrode surface were characterized by scanning electron microscopy (Zeiss Ultra-Plus FESEMs) together with the energy-dispersive X-ray spectroscopy for identifying the elemental composition of samples.

Contact angle analysis

The water static contact angle measurements were performed using a sessile drop system in ambient environment at room temperature. The liquid was dispensed as a spherical droplet of volume 5 µl using a micro-needle (New Era Pump Systems Inc.) and a syringe pump. Measurements were conducted in ambient environment at room temperature 5 secs after the droplet was dispensed to the surface. The contact angle was measured by fitting the profile using a DCAT-15 and Labview program.

Preparation of monodispersed lycopodium pollen particles.

Natural Lycopodium clavatum pollen grains were defatted to remove lips and intine materials yielding indestructible, ultra-tough, defatted pollen microcapsules. For this purpose, Lycopodium clavatum pollen granules (50 g) were refluxed in acetone (300 mL) for 3 h in a round-bottom flask under magnetic stirring (50°C, 350 rpm). The defatted pollen grains were recovered via vacuum filtration for intine materials extraction. This process involves pollen shell extraction and subsequent incubation in an alkaline medium, where the defatted pollen was treated with 10 wt vol%$^{-1}$ potassium hydroxide (KOH) at 80°C and stirred for 2 h to remove its internal cytoplasmic content. KOH-treated spores were next subjected to acidolysis by stirring in 200 mL of 85% (w w^{-1}) phosphoric acid (H_3PO_4) at 60 °C for 3h.[186] After the acid treatment, the spore solution was cooled, and washed extensively with water, acetone and ethanol, and filtered. Finally, H_3PO_4-treated

spores were dried at 60 °C for 24 h in an oven, and the weight of the final dried spores was measured. Spore samples after each chemical treatment step were recovered for analysis. All the spores were stored at room temperature before their use in further experimentations.

Preparation of superhydrophobic ODA.SES particles

Three different concentrations (1, 5 and 10 wt%) of octadecylamine (ODA in alcohol) solutions were prepared separately by vigorous stirring the mixture for 30 mins until the solutions became transparent. Then the ODA solutions were added sequentially into the three separately dispersed SES suspensions and kept stirring the mixtures for another 1 h. Next, glutaraldehyde solutions (12.5 wt%, diluted in water) were added slowly to the SES solutions under continuous stirring for 4 h at 55°C to complete the reaction between the two reactants. After that, the solutions were vacuum filtered and washed with sufficient water followed by large amount methanol to remove unreacted ODA and glutaraldehyde from the SES surface. Subsequently, the products were thoroughly air and oven dried and labelled as ODA.SES-1, ODA.SES-5 and ODA.SES-10 based on the ODA concentrations for further analysis.

Preparation of Cellulose nanofiber using the TEMPO oxidization method from pulp.

The cellulose nanofiber (CNF) was prepared by the TEMPO method from the cotton pulp.[187] In this process, 100 g cotton pulps were dispersed in 9000 mL of deionized water. TEMPO (2,2,6,6-Tetramethylpiperidine-1-oxyl) at a concentration of 0.1 mM/g of fiber and sodium bromide at a concentration of 1 mM/g of fiber were dissolved in deionized water and mixed with the fiber suspension at a consistency of 1% pulp. The pH of the slurry was adjusted to 10 by adding a 0.5 M NaOH solution. After 5 mins of mixing at 500 rpm, the TEMPO-mediated oxidation process was initiated by adding a solution of NaClO (sodium hypochlorite) dropwise to the slurry. The concentration of NaClO ranged from 4 to 12 mM/g of fiber. Throughout the reaction, the pH was maintained at 10.5 by adding 0.5 M NaOH. The reaction proceeded at 500 rpm and 23°C until no further consumption of NaOH was observed. Following the addition of NaClO, the reaction continued at pH 10.5 (maintained by adding 0.5 M NaOH) for 4 h. Once the reaction was complete, the TEMPO-oxidized pulp was thoroughly washed with approximately 8 L of deionized water to remove any residual chemicals. The washing process involved filtration, and the resulting CNF was

stored at 4°C until further use in subsequent experiments and the concentration of prepared CNF suspension is about 10 wt%.

The preparation of superlyophobic CNF-SES-ODA surfaces

To prepare the superhydrophobic ODA.SES particles, they were initially dispersed in ethanol at various concentrations and sonicated to obtain a uniform solution. The CNF suspension was then added to the ODA.SES system. The weight ratio between CNF and ODA.SES was controlled to achieve the desired superlyophobic properties. For example, 100 mg of ODA.SES was firstly dispersed in 100 mL ethanol. Then, 1 mL of TEMPO-oxidized superhydrophilic CNF suspension (10 wt%) was added to the ODA.SES suspension, resulting in a precursor solution with a weight ratio of 1:1 between the two components. This precursor solution was denoted as CNF-ODA.SES-0.5, indicating that the weight percentage of CNF in the solid hybrid system is 50%. By varying the volume of CNF added to the ODA.SES solution, different CNF-ODA.SES precursor solutions could be prepared, ranging from CNF-ODA.SES-0.05 to CNF-ODA.SES-0.95. Finally, the different membranes composed of superhydrophilic CNF and superhydrophobic ODA.SES were prepared using a simple vacuum-assisted filtration method. The precursor solution was poured onto a filter membrane, and the vacuum pressure was applied to facilitate the filtration process, resulting in the formation of the membrane.

4.3 Result and discussion

4.3.1 The modification of superhydrophobic ODA.SES particles

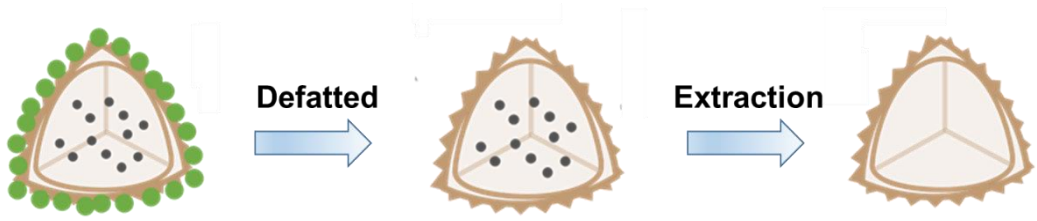

Figure 4-2. The Schematic of transforming Lycopodium clavatum pollen into a hollow Lycopodium sporopollenin extine shell following the defatted and extraction process.

Pollens, as vital components of plant reproduction, possess a dual defense system comprising the

intine and extine layers. The intine, rich in cellulose, provides internal protection for the delicate components of the pollen grains.[188] On the other hand, the extine consisting primarily of sporopollenin served as a robust and chemically stable shield, safeguarding the essential reproductive material within the pollen grain and ensuring the survival and successful propagation of plant species.[189] Besides, the extine exhibited remarkable variations in morphology among different pollen species, enhancing their adaptivity and facilitating plant reproduction in diverse and challenging environments.

Among various pollen particles, lycopodium pollen deserved attention due to its unique 3D architectures and honeycomb-like morphology. This microscale roughness amplified the surface area and influenced the wetting behavior of the pollen particles. Specifically, the wettability of the particles increased when the particle surface was hydrophilic, while the particle exhibited higher hydrophobicity when the surface was hydrophobic. To fully exploit the special morphology and functionality of the lycopodium pollen, the extine was extracted via a chemical extraction process as illustrated in Figure 4-2 (detailed experimental procedures are provided in the Materials and Methods section). Briefly, the natural lycopodium pollen particles were coated with a wax layer, that effectively protected them from being wetted. To obtain monodispersed pollen particles, a defatting process was conducted using acetone and ethyl ether. This process could effectively remove the hydrophobic wax materials, exposing the honeycomb-like morphology of the pollen particles. Subsequently, a simple one-pot KOH treatment was employed to remove the inner protein-based reproductive materials, resulting in the isolation of pure sporopollenin extine shell particles. The extraction process and the morphological changes were visualized with a scanning electron microscope (SEM) and digital microscope, as depicted in Figure 4-3. Initially, the pollen particles exhibited an unclear boundary with an approximate size of 30 μm. SEM image in Figure 4-3a revealed the pollen particle coated with wax, making it challenging to observe the porous structure. However, after the washing steps, the outer shell structure of the pollen became apparent, showcasing its three-dimensional architecture and porous topography (Figure 4-3b). Finally, following the KOH treatment, distinct and well-defined lycopodium sporopollenin extine shell (SES) particles with a hollow structure were obtained, as depicted in Figure 4-3c.

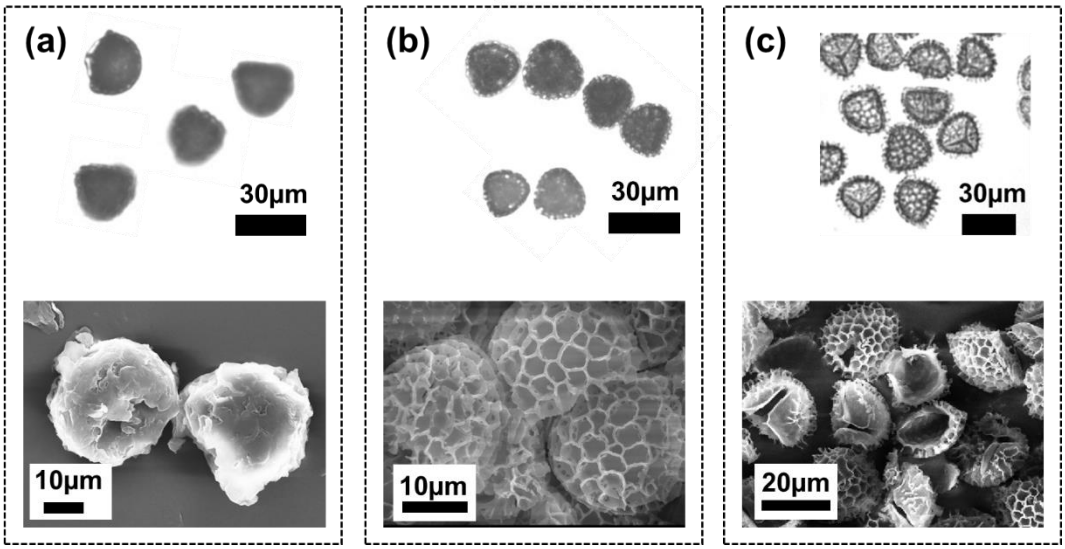

Figure 4-3. The digital microscopic images and scanning electron microscopic (SEM) images of (a) nature pollens, (b) defatted pollens and (c) extracted lycopodium sporopollenin extine shell (SES) particles.

The hydrophobic modification of the surface of SES was conducted via a simple coupling reaction with octadecylamine (ODA) and glutaraldehyde (GA). In this process, the hydroxyl groups (-OH) on the surface of SES would initially form the hemiacetal linkage with GA. Subsequently, the amino groups of octadecylamine (ODA) reacted with the aldehyde groups present on the GA through the formation of a Schiff base. This reaction allowed for the immobilization of ODA on the SES, exposing long alkane chain on the upper sides of SES and increasing the hydrophobicity of SES particles. Three different ratios of SES and ODA were investigated to achieve a balance of SES particles' superhydrophobicity and exposed morphology (Experimental are given in the Materials and method section, section 4.2). Specifically, The FT-IR spectrum analysis revealed significant changes in the surface functional groups of the modified samples (Figure 4-4). The pure SES exhibited a broad peak in the range of 3150 to 3620 cm^{-1}, corresponding to the absorption band of hydroxyl groups (-OH) involved in intermolecular and intramolecular hydrogen bonding.[190] Following the modification process, all three samples (ODA.SES-1, ODA.SES-5, and ODA.SES-10) displayed new peaks around 1460 cm^{-1} and 2840 to 3000 cm^{-1}, which could be attributed to the stretching and deformation of the carbon-hydrogen (-C-H) functional groups.[191] Additionally, a

new peak around 1640 cm^{-1} indicated the formation of the carbon-nitrogen (-C=N-) group, indicating the successful coupling reaction between GA, ODA, and SES particles.[192] The X-ray photoelectron spectroscopy (XPS) results further supported the variation of surface functional groups. The surface atomic composition data revealed a significant reduction in the oxygen (O) content, from 49.52% for pure SES to 25.21%, 15.29%, and 8.06% for ODA.SES-1, ODA.SES-5, and ODA.SES-10, respectively. The reduction in O content corresponded to the higher concentrations of ODA in the modification process, indicating the grafting of more alkane chains onto the SES surface altering the atomic ratio between carbon (C) and oxygen (O). High-resolution C 1s spectra shown in Figure 4-4b revealed a significant reduction in the peak height corresponding to C-O and carboxylate (-C-O-) at 286.2 eV and 287.9 eV, respectively.[193] In contrast, the height of the C-C peak increased substantially, indicating a higher contents of long carbon chains typically derived from the ODA backbone. These spectral changes provided strong evidence on the successful modification of the SES particles with ODA and the subsequent alteration of their surface chemistry and composition.

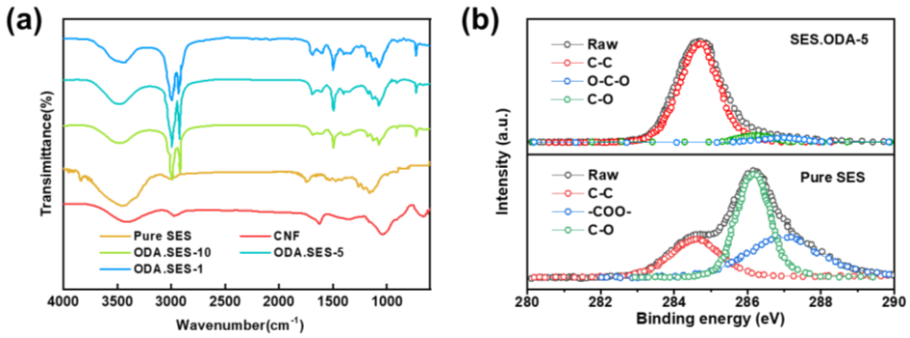

Figure 4-4. (a) The FT-IR spectrum of CNF, Pure SES and SES modified with different contents of ODA. (b) The high resolution XPS spectrum of Pure SES and SES.ODA-5.

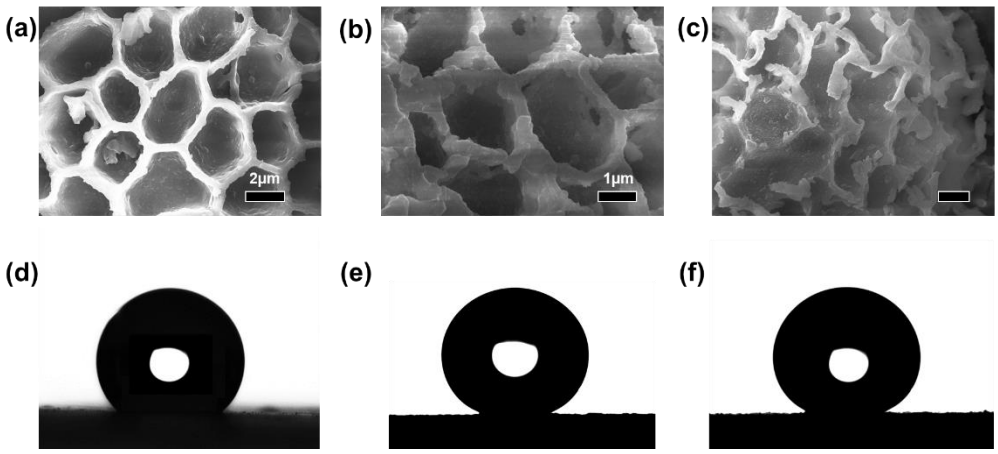

Figure 4-5. The detail morphology of three different ODA.SES particles, including (a) SES.ODA-1, (b) SES.ODA-5 and (c) SES.ODA-10. And the corresponding static contact angle of three different particles (d), (e) and (f).

The concentration of ODA used for the modification would have a significant impact on the hydrophobicity and topography of the ODA.SES particles. Figure 4-5 presents the SEM images illustrating the morphology variation of SES particles modified with different ODA contents. When the ODA content was very low, the morphology of SES particles remained largely unchanged, with clear edges and a hollow structure after modification. However, as the ODA content was increased, the topography of SES particles changed significantly. In Figure 4-5b, the micro-bridges between the pores of SES particles became denser and thicker, while the overall pore morphology remained relatively unaffected. In contrast, when the ODA concentration reached 10 wt%, the pores of SES particles became saturated with ODA and GA, resulting in a denser outer surface and blurred boundaries, which led to a significant reduction in the surface roughness.

The variation in the topography had a direct impact on the static contact angle of the ODA.SES particles. Three types of ODA.SES particles (ODA.SES-1, ODA.SES-5, and ODA.SES-10) were characterized by their static contact angles to evaluate their hydrophobicity. ODA.SES surfaces were constructed by filtering the ODA.SES ethanol solution into a membrane. As shown in Figure 4-5c, ODA.SES-1 displayed the lowest contact angle, which could be attributed to its lower content of hydrophobic materials (Low ODA and GA grafting ratio). However, higher ODA contents increased the water repellency of the surface, as demonstrated by the contact angles in Figure 4-5d.

ODA.SES-5 displayed an increased contact angle from 135° to 158°, indicating higher superhydrophobicity with a higher level of ODA grafting. However, when the ODA concentration was increase further, the reduction in the surface topography of ODA.SES-10 particles led to a lower static contact angle that reduced to 151° (Figure 4-5e).

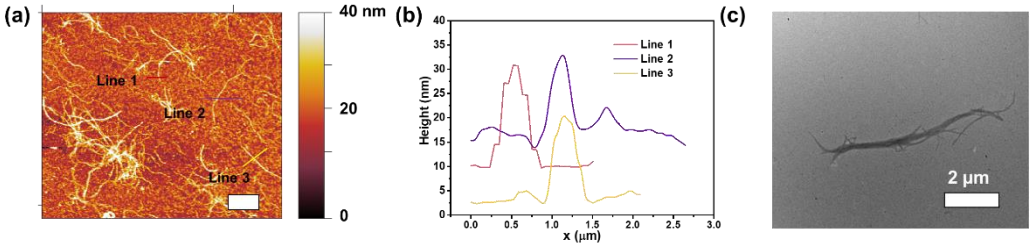

Figure 4-6. The (a) AFM image and (b) the characterization of height of prepared CNF. (c) The TEM image of CNF made from cotton fiber by TEMPO oxidization method.

The CNF made from cotton pulp via the TEMPO oxidization method was characterized to confirm the functional groups and morphology. As shown in Figure 4-4a, the peak at around 1050 cm^{-1} and 1650 cm^{-1} are attributed to the C-C-O glycosidic stretching bond and -COO carboxyl stretching bond respectively, indicating that the TEMPO oxidization process altered the surface functional groups and generated new -COOH groups on the surface.[194] The AFM image was utilized to measure the diameter of CNF. Using the interaction force between AFM tip and surface of the materials, and different testing modes, the characterized height of CNF was utilized to evaluate the diameter of the CNF. Together with the TEM image (Figure 4-6c), the diameter of prepared CNF was estimated to about 20 nm and the length single CNF was around 2-5 μm.

4.3.2 Preparation of CNF-ODA.SES membrane and corresponding wetting behavior in air

The CNF-ODA.SES membranes were fabricated using a vacuum-assisted filtration method, and the ODA.SES-5 particles were used to fabricate the superlyophobic surface due to their combined excellent superhydrophobicity and hierarchical topography. The experimental procedure is illustrated in Figure 4-7. First, 100 mg of ODA.SES was dispersed in 100 mL of ethanol and thoroughly sonicated to achieve a well-dispersed suspension. Subsequently, CNF-ODA.SES-n membranes with varying weight percentages of CNF relative to ODA.SES were prepared for further

characterization (refer to the Materials and Methods section for detailed experimental protocols). In this formulation, n represents the weight percent of CNF with respect to the total weight of ODA.SES used. For example, by adding 0.1 mL of TEMPO-oxidized superhydrophilic CNF suspension (10 wt%) to the ODA.SES ethanol suspension, a precursor solution with a weight ratio of 1:10 between the two components was obtained. Consequently, the CNF-ODA.SES-0.1 membrane was prepared.

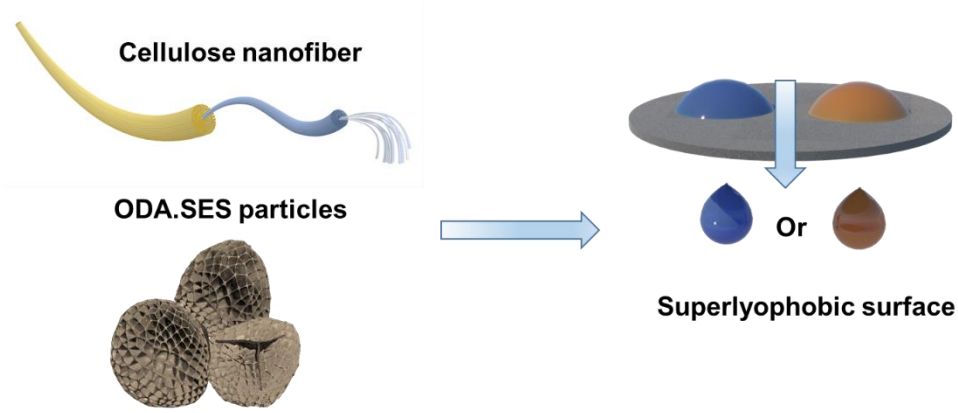

Figure 4-7. Illustration of the preparation of CNF-ODA.SES superlyophobic surface for oil/water separation.

The water contact angle in air was initially measured to determine the wettability of the membrane. As illustrated in Figure 4-5e, the membrane formed by aggregating 100% ODA.SES particles through vacuum filtration exhibited excellent water repellency due to the synergistic effect of the rough structure and hydrophobic coating. However, when a small amount of CNF was introduced, the static contact angle decreased, indicating a highly hydrophobic surface for the CNF-ODA.SES-0.1 membrane with a contact angle of approximately 134°. As the amount of CNF in the system was increased, the static contact angle further decreased. For example, the CNF-ODA.SES-0.2 membrane exhibited a static contact angle of around 117° due to the higher content of superhydrophilic CNF in the system. For the CNF-ODA.SES-0.3 membrane, the static contact angle decreased further to 85°, indicating a transition from hydrophobic to hydrophilic characteristic. The SEM morphology in Figure 4-8 also confirmed the variation in the wettability. In the CNF-ODA.SES-0.1 membrane, the outer surface comprised mainly of ODA.SES particles, which generated numerous air cushions within the structure that prevented the penetration of the droplet.

A similar topography was observed in the CNF-ODA.SES-0.2 and CNF-ODA.SES-0.3 membranes (Figure 4-8e and f), where uniformly distributed ODA.SES particles served as the basic units and established the hierarchical topography where a certain amount of CNF was interspersed between the particles. The CNF fibers formed bundles and aggregates, wrapping around the surface of ODA.SES particles through hydrogen bond interactions that resulted in the formation of an interconnected three-dimensional structure that significantly enhanced the mechanical properties of the membrane.

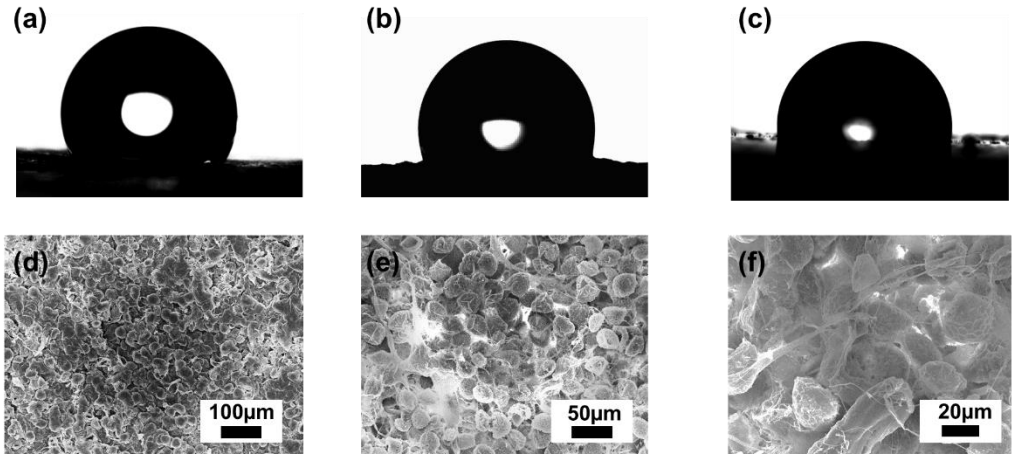

Figure 4-8. The static contact angle of (a) CNF-ODA.SES-0.1, (b) CNF-ODA.SES-0.2 and (c) CNF-ODA.SES-0.3, and the corresponding SEM images of three membrane shown in (d), (e), and (f) respectively.

Further increase in the CNF contents in the membrane formulation led to a loss of water repellency. For CNF-ODA.SES-0.4, the droplet initially placed on the membrane surface exhibited a hydrophilic contact angle of around 81°. Over time, the droplet gradually penetrated into the porous structure, resulting in a contact angle of 76° after 60s of stabilization. Finally, the droplet yielded a contact angle of approximately 3° after 245 s of stabilization (Figure 4-9a).

For CNF-ODA.SES-0.5 with a higher CNF content, the membrane possessed stronger hydrophilicity in air. The initial static contact angle was lower at around 62° but the droplet penetrated into the porous structure after 35s of stabilization (Figure 4-9b). This indicated that the higher content of CNF on the outer surface increased the surface capillary force, resulting in a rapid wetting process, and the SEM images (Figure 4-10) supported this hypothesis. With a higher CNF

content, the ODA.SES particles were partially or fully covered by CNF, exposing a larger amount of hydrophilic CNF on the membrane surface (Figure 4-10a and b), which accounted for the lower initial static contact angle. Additionally, the higher content of superhydrophilic CNF provided a pathway for the water diffusion, facilitating water transport inside the membrane. As a result, CNF-ODA.SES-0.5 was more prone to droplet spreading achieving a faster water spreading state compared to CNF-ODA.SES-0.4.

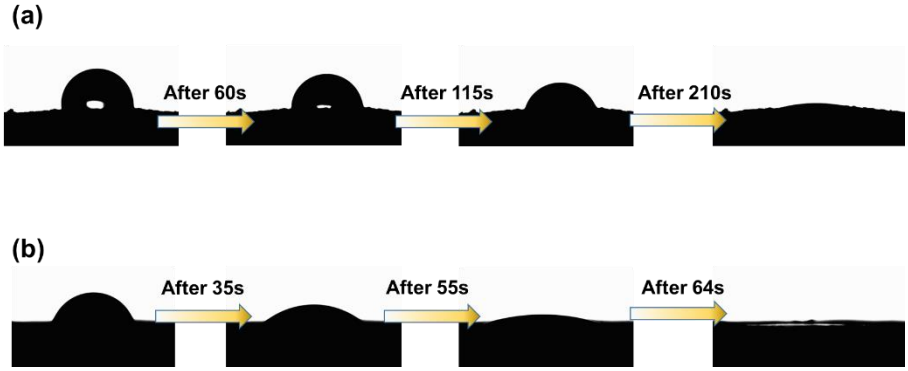

Figure 4-9. The contact angle measurements in air for the (a) CNF-ODA.SES-0.4 membrane and (b) CNF-ODA.SES-0.5 membrane.

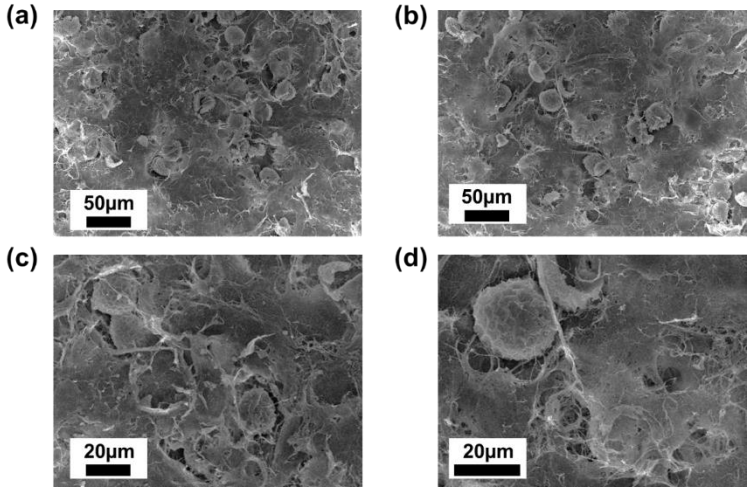

Figure 4-10. The SEM images of (a) CNF-ODA.SES-0.4 and (b) CNF-ODA.SES-0.5, and the corresponding zoom-in image (c) and (d), respectively.

The excessive presence of CNF in the membranes, such as CNF-ODA.SES-0.6, -0.7, -0.8, and -0.9, resulted in the emergence of superhydrophilic properties. In these membranes, when a droplet was

placed on the surface, it would be adsorbed without displaying an apparent contact angle. The presence of an adequate amount of hydrophilic CNF introduced a high surface free energy to the membrane, facilitating the interaction between the membrane and the droplet. Furthermore, the nano-sized CNF with its large surface area increased the solid-liquid contact area, promoting spreading of the water inside the channels formed by the CNF. This enhanced the contact area and facilitated water transport that contributed to the overall superhydrophilicity of the membrane.

4.3.3 The wetting behaviour of CNF-ODA.SES membrane under oil and water

The oil contact angle under water was measured for a series of CNF-ODA.SES membranes to evaluate the water affinity of the hybrid system in the presence of oil. In the experiment, the membrane was first immersed in a water environment, and then an oil droplet (hexane) was placed on the surface of the membrane. The oil contact angle was conducted to evaluate the wettability of membrane. The results showed that the CNF-ODA.SES-0.9 membrane exhibited perfect underwater oil repellency. As shown in Figure 4-11b, a 5 μL hexane droplet was fully repelled by the membrane, and the oil static contact angle under water was determined to be about 160˚, indicating superoleophobic behavior underwater. This phenomenon was attributed to the strong water affinity and superhydrophilicity (in air) of the CNF-ODA.SES-0.9 membrane. The membrane exhibited a strong interaction with water molecules under water, causing the water to be trapped inside the rough structure of the membrane, which formed a uniform "water protection layer" on the outer surface of the membrane, preventing the penetration of the hexane droplet into the structure as illustrated in Figure 4-11c. Similarly, the CNF-ODA.SES-0.8 and -0.7 membranes also exhibited superoleophobic behavior underwater, with the hexane droplets being fully repelled achieving high static contact angles of approximately 158˚ and 155˚, respectively. When the CNF-ODA.SES-0.4 surface was employed, a notable reduction in the oil contact angle was observed, measuring approximately 118˚ (Figure 4-11d). The diminished oil repellency could be ascribed to the reduced surface free energy resulting from the higher concentrations of hydrophobic ODA.SES particles Importantly, these hydrophobic particles exhibited enhanced water repellency in specific areas, resulting in the aggregation of oil molecules in these favored regions. In other words, the intricate interplay between the hydrophobic ODA.SES particles and oil molecules on the CNF-ODA.SES-0.4 surface illustrated the nuanced wetting behavior of the system. Despite the surface maintaining

an overall underwater oleophobic nature, the localized oil affinity counteracted the inherent oil-repellent characteristics yielding a partially oil-wetted state as illustrated in Figure 4-11e.

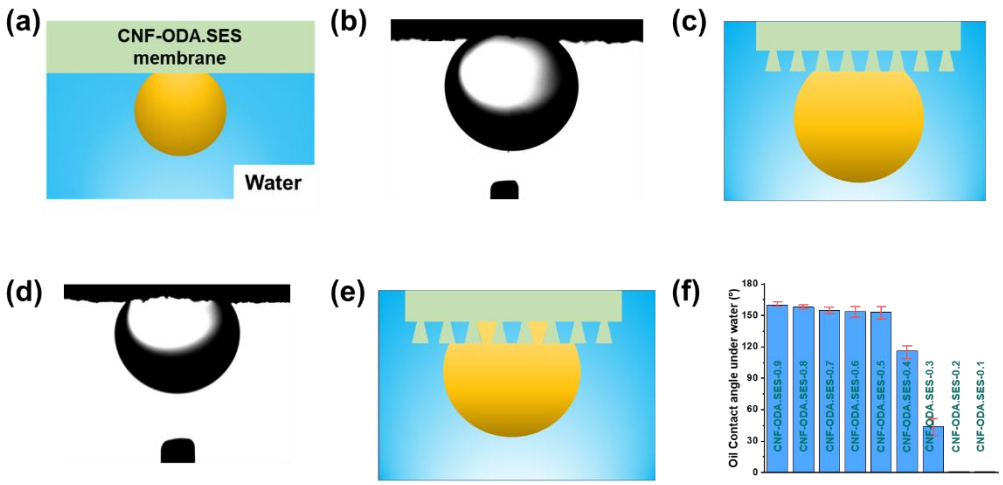

Figure 4-11. (a) Illustration of oil static contact angle measurement underwater. (b) The hexane contact angle on CNF-ODA.SES-0.9 surface under water. (c) Illustration of superoleophobic state underwater. (d) The hexane contact angle on CNF-ODA.SES-0.4 surface under water. (e) Illustration of partially oil wetted state underwater. (f) The hexane contact angle measurement of various CNF-ODA.SES membranes under water.

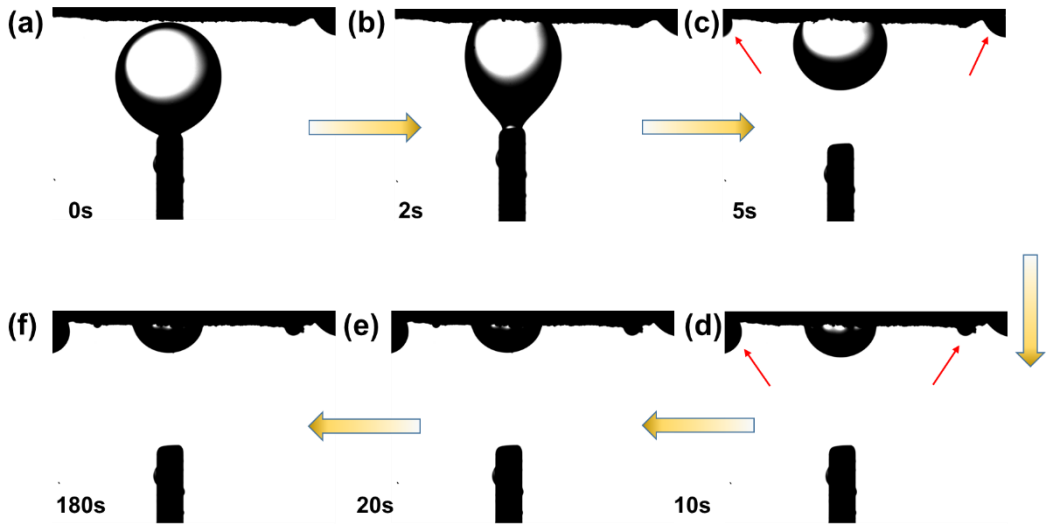

Figure 4-12. Time-dependent variation of under water hexane contact angle on CNF-ODA.SES-0.2.

The augmentation of hydrophobic ODA.SES content within the hybrid system contributed a more pronounced hydrophobic-hydrophobic interaction that resulted in a reduction in the hexane contact angle under water, as depicted in Figure 4-11f (From superoleophobic 155˚ for CNF- ODA.SES-0.7 to the 116˚ for CNF-ODA.SES-0.4). Specifically, the utilization of the CNF-ODA.SES-0.3 membrane led to a considerable reduction in the hexane contact angle, reaching about 48˚ since the CNF-ODA.SES-0.3 exhibited inherent hydrophobicity in air, leading to the entrapment of air within its rough structure. When the surface came into contact with a hexane droplet, the trapped air was displaced by the infiltrating oil as illustrated in Figure 4-12, where the hexane droplet firmly adhered to the CNF-ODA.SES-0.3 surface and penetrated the rough structure. After a brief 5s interval, the previously trapped air was displaced and replaced by the infiltrated hexane. Notably, the surface bubbles formed by the air displacement are indicated by the red arrow in Figure 4-12c and d. Ultimately, after a stabilization period of 180 seconds, the oil contact angle stabilized at approximately 48˚, signifying the achievement of a thermodynamically stable state at the surface (Figure 4-12f). Due to the pronounced hydrophobic nature of the CNF-ODA.SES-0.2 and -0.1 membranes, a substantial volume of air was trapped within their textured structure when submerged in water. Concurrently, numerous oleophilic regions on the surface exhibited a strong affinity for oil, facilitating the rapid oil penetration upon contact with hexane. This phenomenon is vividly illustrated in Figure 4-13, where water readily permitted the ingression of hexane into the intricate textured surface, effectively displacing the trapped air within a short duration of 510 ms.

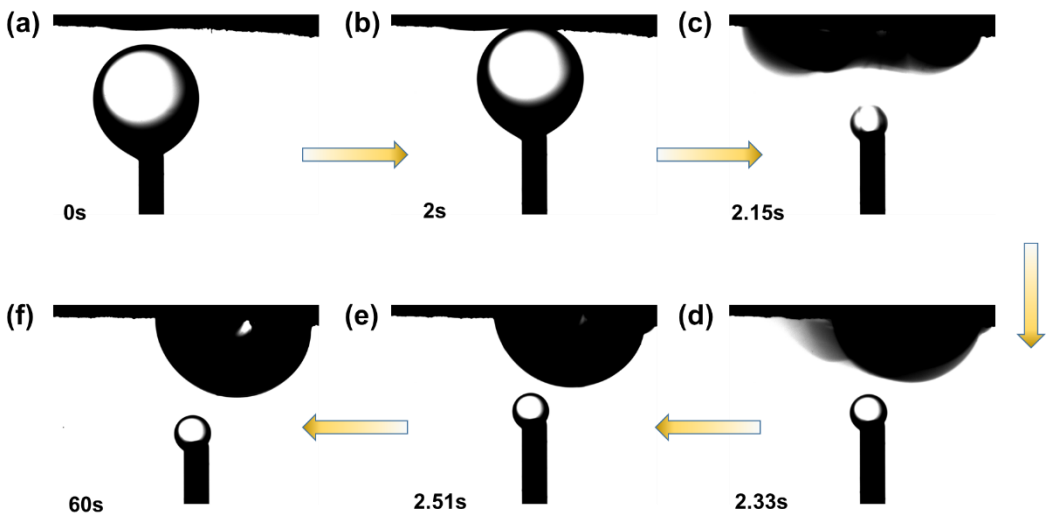

Figure 4-13. Time-dependent variation of under water hexane contact angle on CNF-ODA.SES-

0.2.

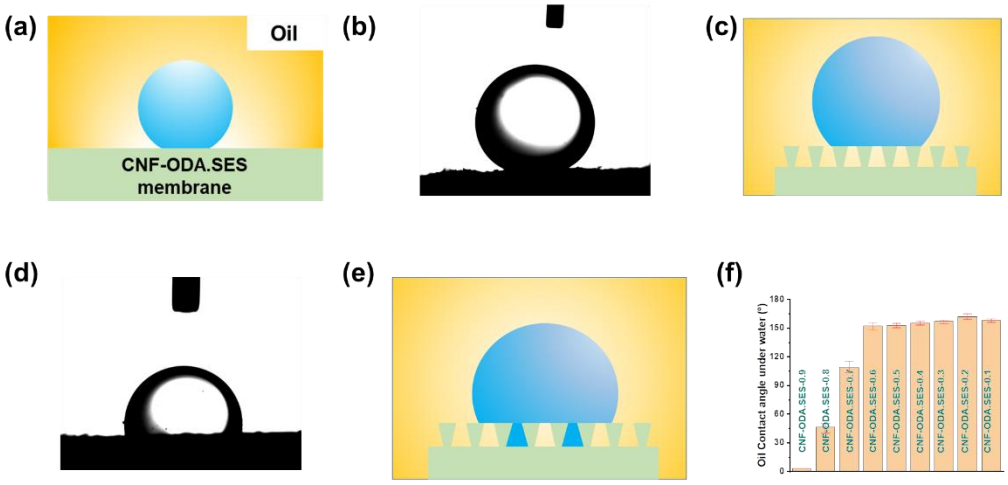

Figure 4-14. (a) Illustration of water static contact angle measurement underoil. (b) The hexane contact angle on CNF-ODA.SES-0.2 surface under water. (c) Illustration of superoleophobic state underwater. (d) The hexane contact angle on CNF-ODA.SES-0.7 surface under water. (e) Illustration of partially oil wetted state underwater. (f) The hexane contact angle measurement of various CNF-ODA.SES membranes under water.

The water affinity of the surface was also assessed by measuring the water contact angle under hexane, yielding contrasting results compared to the oil contact angle under water. Remarkably, the highly hydrophobic CNF-ODA.SES-0.2 membrane displayed exceptional water repellency when immersed in hexane, as depicted in Figure 4-14b. This behavior can be attributed to the hierarchical structure of the hydrophobic ODA.SES, which facilitated the formation of an "oil cushion" on the surface, leading to a Cassie-type wetting state. Conversely, membranes with higher hydrophilicity demonstrated reduced water contact angles under hexane, such as the CNF-ODA.SES-0.7 membrane, which exhibited a contact angle of only 109˚. Further increase in the hydrophilicity resulted in a contact angle reduction to 43˚ for CNF-ODA.SES-0.8 and complete wetting with a contact angle of 0˚ for CNF-ODA.SES-0.9 (Figure 4-14f). This behavior could be attributed to the surfaces having high free energy, thereby exhibiting a stronger affinity for water over oil. Consequently, the solid-water-oil three-phase contact line was disrupted, leading to the replacement

of trapped hexane by water (Figure 4-14e).

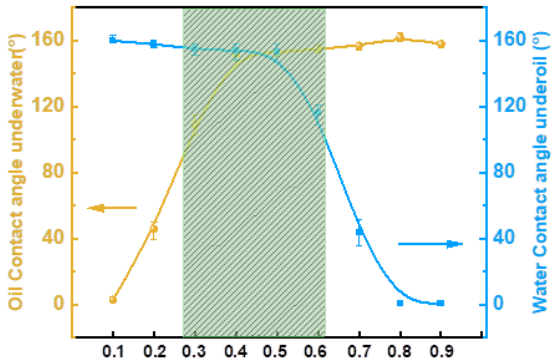

Figure 4-15. The under liquid wetting behavior of series of CNF-ODA.SES (from CNF-ODA.SES-0.1 to CNF-ODA.SES-0.9) surface in the hexane-water system.

As illustrated in Figure 4-15, the CNF-ODA.SES-0.3, -0.4, -0.5, and -0.6 surfaces displayed high underliquid lyophobicity, demonstrating the resistance to wetting by water under hexane and hexane under water. Notably, the CNF-ODA.SES-0.4 and -0.5 surfaces could achieve superlyophobic behavior under both liquids. To provide further validation of this unique wetting state, sliding angle and adhesion experiments were conducted. In Figure 4-16a and c, inclined surfaces with a 15˚ tilt were prepared, upon which water or hexane droplets were carefully placed, and their subsequent behavior was recorded using an ultrafast camera. As depicted in Figure 4-16b and d, the CNF-ODA.SES-0.5 surface possessed a thin liquid "protection layer" that effectively reduced the contact area between the surface and the secondary droplet. Consequently, secondary droplets of either water or hexane could slide down effortlessly on the slightly inclined surface. Adhesion measurements were also performed on the CNF-ODA.SES-0.5 surface, as illustrated in Figure 4-17. A water droplet was introduced to the surface and subsequently withdrawn after stabilization. Evidently, the droplet detached rapidly from the surface without any pinning or residual liquid. These observations corroborated unequivocally with the Cassie-favorable superlyophobic state of the CNF-ODA.SES-0.5 surface, wherein the droplet rested on a separate liquid film with a minimized contact area with the surface. This special wetting behavior arose from the controlled ratio of superhydrophobic ODA.SES particles and superhydrophilic CNF that generated the appropriate surface free energy and attraction forces for both the water and oil. Consequently, the oil-water-solid three-phase contact line achieved a metastable state, where the structure trapped the

water or oil within the rough structure, forming a stable “liquid cushion” that promoted the Cassie-superlyophobic state.

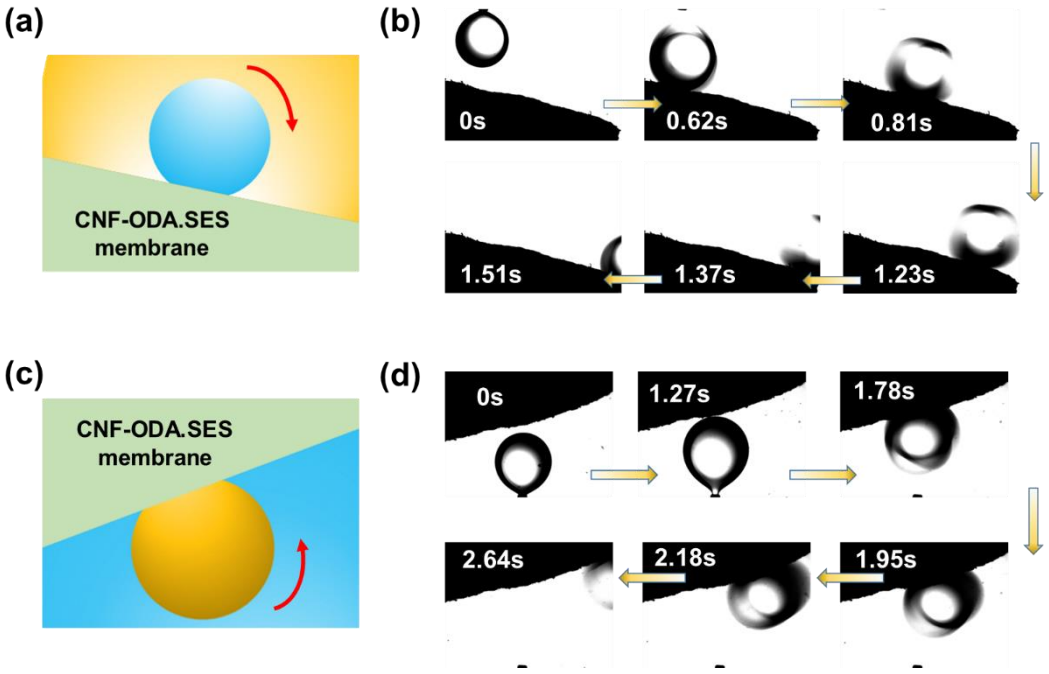

Figure 4-16. Illustration of sliding angle measurements of (a) water droplet under hexane environment and (c) hexane droplet under water environment. (b) and (d) The digital images showed that both water droplet or oil droplet could easily move away from the CNF-ODA.SES-0.5 surface with a slightly inclined degree in oil-water system.

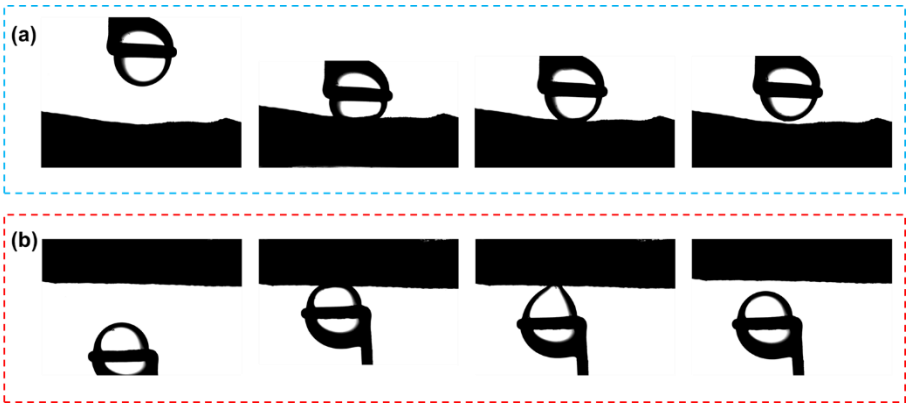

Figure 4-17. Adhesion measurement of CNF-ODA.SES-0.5 surface. The image shows a controlled experiment where either (a) a water droplet or (b) hexane was brought into contact with the CNF-ODA.SES-0.5 surface and exhibited no pinning effect under hexane or water, respectively.

4.3.4 The surface free energy induced under liquid superlyophobicity

The mechanical model analysis as depicted in Figure 4-18, was conducted to investigate whether CNF-ODA.SES membranes could maintain a stable solid-water-oil three-phase contact and achieve a superlyophobic state. The model analysis involved prewetting the membranes with oil, leading to the formation of a stable oil-solid interface. The total interfacial energy of the system (E_{oil}) in this configuration (config. 1 in Figure 4-18) corresponds to the sum of the surface tension of the oil (γ_o) and the interfacial tension between the solid surface and the oil (γ_{so}). Similarly, when the membranes were placed in a water environment, the total interfacial energy (E_{water}) in this configuration (config. 3 in Figure 4-18) corresponds to the sum of the surface tension of water (γ_w) and the interfacial tension between water and the surface (γ_{sw}). It is important to note that $E_{water/oil}$ represents the interfacial energy generated when the oil-infused rough structure was replaced by a newly placed water phase, resulting in a water-infused structure. The equation incorporated the roughness factor, which accounts for the actual and projected areas of the surfaces. Laser confocal microscopy was employed to determine the roughness factor, and the results are presented in Table 4-1.

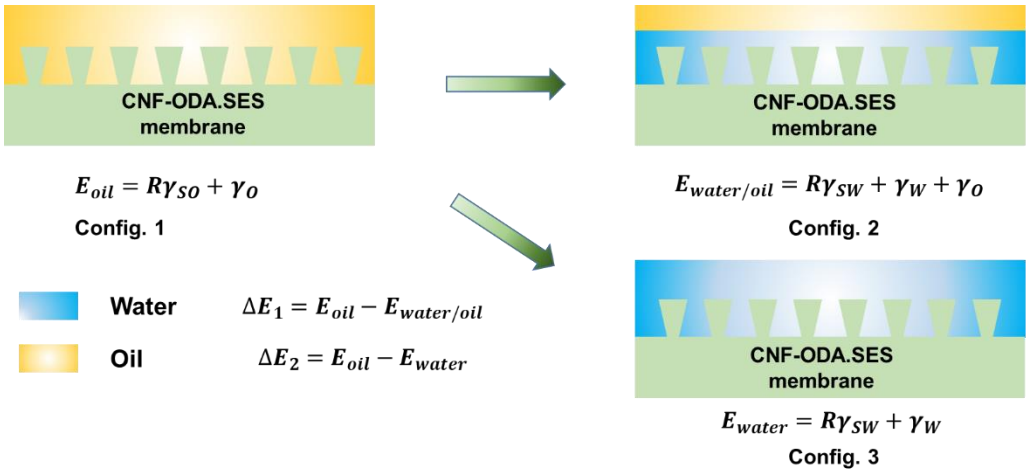

Figure 4-18. Thermodynamic wetting models analysis of the CNF-ODA.SES membrane under liquid.

Table 4-1. Total interfacial energy calculation on various CNF-ODA.SES membranes.

surfaces	liquid A	liquid B	R (μm)	γA (mJ/N)	γB (mJ/N)	γAB (mJ/N)	θA (°)	θB (°)	ΔE_2(mJ/m²) =E_A-E_B	ΔE_1(mJ/m²) =E_A-E_{AB}	Stable Film? Theoretical	Stable Film? Experimental
CNF-ODA.SES-0.2	water	hexane	3.95	72.4	17.9	41.8	117	65	138.1	234.3	N	N
	hexane	water	3.95	17.9	72.4	41.8	65	117	-66.8	-79.5	Y	Y
CNF-ODA.SES-0.3	water	hexane	3.58	72.4	17.9	41.8	85	50	-23.1	73.1	Y/N	N
	hexane	water	3.58	17.9	72.4	41.8	50	85	-60.4	-73.1	Y	Y
CNF-ODA.SES-0.35	water	hexane	3.25	72.4	17.9	41.8	83	32	-21.1	75.1	Y/N	DL
	hexane	water	3.25	17.9	72.4	41.8	32	83	-62.4	-75.2	Y	DL
CNF-ODA.SES-0.4	water	hexane	2.91	72.4	17.9	41.8	81	15	-24.4	71.9	Y/N	DL
	hexane	water	2.91	17.9	72.4	41.8	15	81	-59.1	-71.8	Y	DL
CNF-ODA.SES-0.45	water	hexane	2.88	72.4	17.9	41.8	73	12	-52.9	43.3	Y/N	DL
	hexane	water	2.88	17.9	72.4	41.8	12	73	-30.6	-43.3	Y	DL
CNF-ODA.SES-0.5	water	hexane	2.76	72.4	17.9	41.8	62	10	-86.9	9.3	Y/N	DL
	hexane	water	2.76	17.9	72.4	41.8	10	62	3.3	-9.3	Y/N	DL
CNF-ODA.SES-0.55	water	hexane	2.13	72.4	17.9	41.8	55	5	-92.2	4.1	Y/N	DL
	hexane	water	2.13	17.9	72.4	41.8	5	55	8.6	-4.2	Y/N	DL
CNF-ODA.SES-0.6	water	hexane	1.85	72.4	17.9	41.8	31	1.3	-123.5	-27. 5	Y	Y
	hexane	water	1.85	17.9	72.4	41.8	1.3	31	39.9	27.2	N	N
CNF-ODA.SES-0.7	water	hexane	1.43	72.4	17.9	41.8	2.1	0	-119.6	-23.4	Y	Y
	hexane	water	1.43	17.9	72.4	41.8	0	2.1	36.1	23.4	N	N

Based on energy considerations, if the membrane is preferentially wetted by water, it indicates that the energy state of E_{oil} is higher than that of $E_{water/oil}$ and E_{water}. In other words, ΔE_1 and ΔE_2 are greater than 0. Conversely, if the surface exhibits a stronger affinity for oil, ΔE_1 and ΔE_2 are less than 0, resulting in the formation of a stable solid-oil-water interface. When ΔE_1 and ΔE_2 have opposite signs, it suggests that the infused liquid may or may not be displaced by newly placed liquid. Combining these considerations with Young's equation, the expressions for ΔE_1 and ΔE_2 can be derived as followed[195]:

$$\Delta E_1 = R(-\gamma_o cos\theta_O + \gamma_w cos\theta_w) - \gamma_{ow} \quad (4\text{-}1)$$

$$\Delta E_2 = R(-\gamma_o cos\theta_O + \gamma_w cos\theta_w) + \gamma_o - \gamma_w \quad (4\text{-}2)$$

The calculation results are presented in Table 4-1, where liquid A and liquid B could be either water or hexane. This table allows for the evaluation of whether the surface can achieve a stabilized oil-water-solid three-phase contact under both water and oil environments. The surface of CNF-

ODA.SES-0.2 was found not to be able to attain a superlyophobic state, as indicated by both theoretical model analysis and experimental observations. As shown in Table 4-1, when the surface was prewetted by water, ΔE_2 exhibited a positive value, indicating that the interfacial energy of the water-membrane system was larger than the oil-membrane system. Additionally, ΔE_1 was also calculated to be positive, suggesting that the replacement of oil with water in the CNF-ODA.SES-0.2 structure was not energetically favorable. Similarly, when the model was prewetted with oil (the exchange of liquid A and B), both ΔE_2 and ΔE_1 exhibited negative values. This indicated that the oil-infused membrane was in a low energy state, and the conformational transformation to a water-infused state was hindered by an energy barrier that was identical to the experiment results, and the membrane could only achieve an under oil superhydrophobic state. Similar analyses were performed for CNF-ODA.SES-0.6 and CNF-ODA.SES-0.7 surfaces. The results indicated that these surfaces were more likely to be wetted by water rather than hexane. This conclusion was supported by the lower energy state observed in the water-infused models, which aligned with the experimental findings demonstrating that these two surfaces could achieve a superoleophobic state under oil. Except for the stable oil-solid composite interface in oil prewetted mode which could be calculated from CNF-ODA.SES-0.3, -0.35, -0.4 and -0.45 membranes (both ΔE_2 and ΔE_1 smaller than 0), the ΔE_2 and ΔE_1 were opposite in sign for water-solid surface. This could be attributed to the overall system being in a metastable state and two opposing thermodynamic states could appear on the same surface (The ΔE_2 indicates that the interfacial energy of water infused surface is lower than the hexane filled surface while ΔE_1 suggest that the infused water can be substituted by hexane without energy barrier). The final experimental results revealed that the CNF-ODA.SES-0.35, 0.4, -0.45, -0.5 and 0.55 could combine the underoil superhydrophobicity and underwater superoleophobicity, achieving the metastable oil-water-solid interface and superlyophobic wetting state.

To further evaluate the relationship between the under liquid superlyophobic property and the surface wettability behavior of different combinations of superhydrophilic CNF and superhydrophobic ODA.SES, surface free energy measurements was conducted to assess the inter-molecular attraction forces at the interface. The surface free energy could be divided into the polar (γ_s^p) and dispersive components (γ_s^d) that could be estimated based on the contact angle data of two liquid (water and methylene iodide) and they could be fitted to the Owens, Wendt, Rabel and Kaelble (OWRK) method (Eq.4-3) as shown below.[196]

$$1+\cos\theta = 2\sqrt{\gamma_s^d}\left(\frac{\sqrt{\gamma_l^d}}{\gamma_{lv}}\right)+2\sqrt{\gamma_s^p}\left(\frac{\sqrt{\gamma_l^p}}{\gamma_{lv}}\right) \quad (4\text{-}3)$$

where θ referred to the contact angle of liquids, γ_{lv} refers to the free energies of the liquid and solid against their saturated vapor, γ_l^d and γ_l^p refer to the free energy of liquid, where the superscripts p and d, are the polar and dispersion force components respectively. and γ_{lv}, γ_l^d and γ_l^p are documented in many references for different liquids. Here two types of liquid, water and methylene iodide, were utilized for the evaluation of surface free energy. As shown in Table 4-2, both the contact angle of water and methylene iodide decreased with the higher contents of superhydrophilic CNF in composites. It is worth noting that while CNF-ODA.SES-0.3, -0.35, and -0.4 displayed similar water contact angles in air, the contribution of γ_l^d to the surface free energy became more stable when the CNF content was 0.35 (CNF-ODA.SES-0.35 and -0.4). compared to CNF-ODA.SES-0.55, CNF-ODA.SES-0.6 and -0.7 demonstrated a significant increase in γ_l^p. This could be attributed to the differences in the intermolecular forces between the surface and the liquid. Water primarily generates hydrogen bonding and dipole-dipole interactions with the surface, while methylene iodide relies on the dispersion force generated by the nonpolar chains in the hydrophobic groups on the surface (such as $-CH_2-$). Consequently, the decrease in the hydrophobic groups after CNF-ODA.SES-0.35 would lead to a smaller increase in the dispersion force, whereas the dipole-dipole force was greatly enhanced after CNF-ODA.SES-0.6. Combining with the thermal dynamically analysis and experiment results, we determined that a surface free energy (ranging from 56 mJ m^{-2} to 40 mJ m^{-2}) was capable of establishing a stable oil-water-solid interface and achieving a metastable superlyophobic state. Moreover, the superlyophobicity was also confirmed that can be worked not only on hexane-water system, but also in other oil-water systems. As shown in Table 4-3 and Figure 4-19, other four types of oil with different physical properties were selected for the measurements. The CNF-ODA.SES-0.5 membrane could maintain a stable oil-water-solid interface under water environment or under different oil systems, achieving both the water repellency under oil and water repellency under oil.

Table 4-2. Components of Surface Energy for various CNF-ODA.SES membranes

Surface	Contact angle (°)		Surface free energy (mJ m^{-2})		
	Water	Methylene iodide	γ_s^d	γ_s^p	γ_s
CNF-ODA.SES-0.2	117	83	16.2	0.1	16.6
CNF-ODA.SES-0,3	85	57	24.0	4.5	28.5
CNF-ODA.SES-0.35	83	43	35.5	4.8	40.3
CNF-ODA.SES-0.4	81	36	38.9	3.3	42.2
CNF-ODA.SES-0.45	73	30	40.2	5.9	43.6
CNF-ODA.SES-0.5	62	25	40.1	11.2	51.3
CNF-ODA.SES-0.55	55	18	42.1	14.6	56.7
CNF-ODA.SES-0.6	37	3	41.1	24.7	65.8
CNF-ODA.SES-0.7	2	1	38.7	37.4	76.1

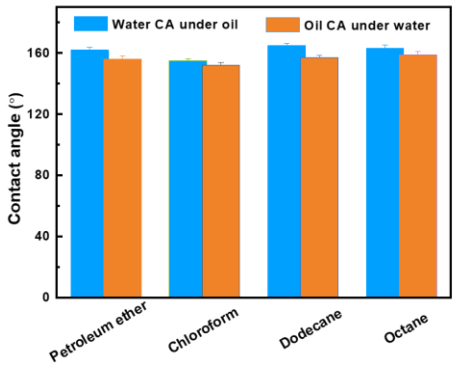

Figure 4-19. The Dual superlyophobic properties of the CNF-ODA.SES-0.5 in different oil water system. The blue columns indicate the water contact angle under different oil and brown columns represent the oil contact angle under water.

Table 4-3. Physical properties of four tested oils.

Oil	Petroleum ether	Chloroform	Dodecane	Ocatne
Density (g/mL)	0.64	1.49	0.75	0.7
Surface tension (mN/m)	18.4	19.1	25.4	21.6
Interfacial tension (mN/m)	38.6	22	41.2	43.1

4.3.5 Water-in-Oil and Oil-in-Water Emulsion Separation

The achievement of under-liquid superlyophobicity in CNF-ODA.SES membranes enabled their application in the separation of oil/water emulsions. Hexane-in-water and water-in-hexane emulsions, stabilized with 4 mg ml^{-1} Cetyltrimethylammonium bromide (CTAB), were prepared for evaluation, with volume ratios of 1:100 or 100:1. Digital and microscopic images in Figure 4-20 revealed the presence of numerous emulsion droplets in both the oil-in-water and water-in-oil emulsion solutions before filtration. However, when subjected to a constant and low vacuum (0.03 MPa) assisted filtration process using the CNF-ODA.SES-0.5 membrane, both emulsions were effectively filtered. The final fluxes of the emulsions permeating through the CNF-ODA.SES-0.5 membrane were determined to be approximately 14750 L m^{-1} h^{-2} bar^{-1} for hexane-in-water emulsion and 17000 L m^{-1} h^{-2} bar^{-1} for water-in-hexane emulsion, calculated based on the effective area (45 mm) of the substrate and the pressure difference (~0.03 MPa). Additionally, stability testing was performed by passing 100 mL of the emulsion through the membrane and subsequently washing the membrane with 15 mL of ethanol before drying in air. Figure 4-21 confirms that the flux did not significantly decrease with increasing cycle number, even up to 20 cycles, indicating excellent separation capability and stability of the membrane.

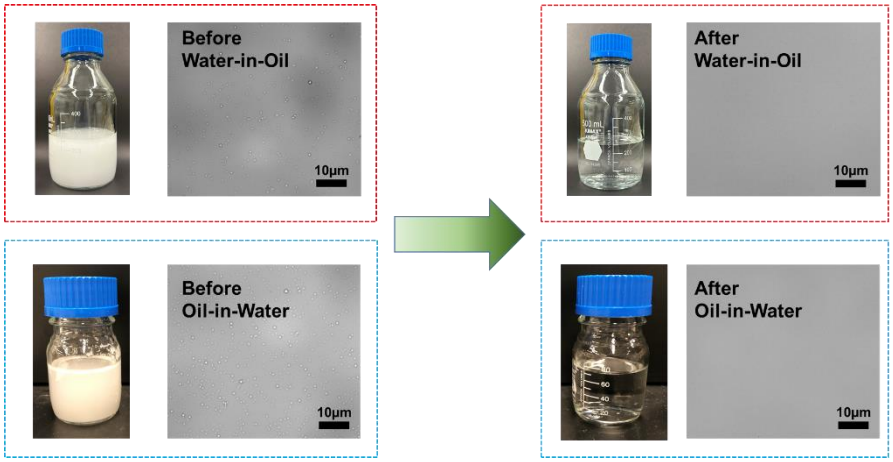

Figure 4-20. The potential application of CNF-ODA.SES-0.5 membrane for the water-in-oil and oil-in-water emulsion separation and their optical images of feed emulsion and filtrate.

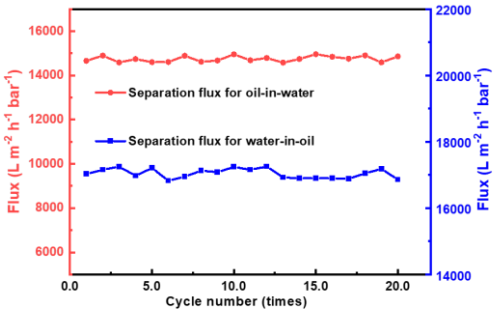

Figure 4-21. The stability measurement of separation flux of CNF-ODA.SES-0.5 for the water-in-hexane and hexane-in-water emulsion.

4.4 Conclusions

In this study, we have developed a facile method for creating under-liquid dual superlyophobic membranes which could bring unique applications in various field involving multiphase fluids. The key components used in this approach were defatted and KOH-treated Lycopodium clavatum pollen and cellulose nanofibers (CNF) derived from cotton fibers. The hierarchical 3D topography of the treated pollen provided essential rough structure, which could create superhydrophobicity in air by grafting hydrophobic materials onto its surface. The CNF, on the other hand, introduced surface hydrophilicity and facilitated the construction of compact membranes due to the presence of hydroxyl and carboxyl groups. By combining superhydrophilic CNF and superhydrophobic ODA.SES particles, we were able to tune the wettability and surface free energy of the composite

membranes over a wide range, from highly hydrophobic to superhydrophilic in air. Morphological and contact angle analyses revealed that increasing the CNF content enhanced the water affinity of the system both in air, water, and oil environments. Besides, the hierarchical structure provided by the superhydrophobic ODA.SES particles effectively trapped water or oil for creating “liquid cushion” for superlyophobicity, depending on the environment. The model analysis energy analysis and experiments demonstrated that the propel surface free energy (56 mJ m^{-2} to 40 mJ m^{-2}) tuning would let the surface maintain a meta-stable oil-water-solid interface, letting the overall system is favorable to these two contradictory wetting states (noted as under water superoleophobicity and under oil superhydrophobicity in this part). Also, a simple emulsion separation experiment demonstrates the importance of this kind of underliquid superlyophobic surface for the future multiphase fluid applications such as soild-oil-water systems, such as the oil recovery, particle phase transfer and liquid–liquid interface assembly.

Chapter 5. Highly hydrophilic and oppositely charged cellulose nanocrystal intercalating GO membranes for ions transport and osmotic energy harvesting

5.1 Introduction

With the ever-growing energy demands and environmental concerns of fossil fuel, researchers are seeking abundant, sustainable and inexpensive energy sources to meet these challenges.[197] The osmotic power, also known as 'blue energy', is generated when two fluidic systems of different salinity are combined, and it offers promise as a renewable and clean energy source.[198, 199] Among various devices and methods, the reverse electrodialysis (RED) offers a promising strategy to harvest 'blue' osmotic energy from the direct conversion of salinity gradient to electric current via ion-selective membrane.[200, 201] In nature, many living creatures display capability of converting osmotic pressure into the electrical potential, for example the electric eels that generate voltages greater than 600 V via the potassium channels embedded in the electrocyte cells.[202] However, commercial ion-exchange membranes for RED system suffer from low selectivity, inadequate mass transportation, high energy barrier, and thus, is not an economically viable power density source.[203] Thus, the harvesting of salinity energy can be achieved by utilizing nanofluidic channel due to its special ion transportation phenomena.[204-206]

In contrast to conventional one-dimensional (1D) nanochannel that requires precise control of geometry and high-density pores, many 2D materials were incorporated into nanofluidic channels to produce highly efficient and large-scale RED membrane.[207, 208] With the assembly of 2D materials, the ion transports within the parallel lamellar sheets of less than 1 nm, is spatially confined in the direction of interstitial path of the 2D nanosheets.[209] When the channel dimension is close to the Debye screening length, the surface charge controls the ion transport process and the surface functionalities of the channels offer superior ion selectivity, ion rectification, ion gating and ion permeability.[210-212] The bottom-up assembling of pristine nanosheets yields membranes that possess good ion selectivity.[213, 214] However, 2D nanochannel formed by stacking suffers from low mechanical strength, as well as undesirable swelling in water, which strongly impact the durability of the lamellar membranes.[215] Recently, a strategy of using pristine exfoliated layered materials intercalated with other charged materials, like nanofiber, offers a new opportunity to

increase the long-term cycling and electrochemical performance of osmotic energy devices.[216] The guest materials generate a space charge zone, when combined with surface and space charge in the interstitial channels generates higher ion flux and power density. For example, silk[217], Kevlar[218] and cellulose nanofibers[219] used in intercalated 2D channels improve ion transport dynamics. Nevertheless, soft fibers with a micron length scale will twist and entangle together in the fiber axis direction that leads to a higher internal resistance and lower ion selectivity compared to pristine membrane.[220] Therefore, to achieve a nanocomposite channel with a balance of high osmotic performance and mechanical strength, a state-of-art intercalated 2D channel system with rational structure design needs to be developed.[221]

Cellulose nanocrystal (CNC) derived from nature sources is one of the abundant renewable biopolymers with highly ordered and anisotropic structure.[222] Its crystalline 1D rod-like nanostructure is composed of densely packed hydrogen-bonded parallel chains consisting of repeating anhydro-D-glucopyranose units.[223] CNC possesses high tensile strength (7500 MPa) and Young's modulus (around 150 GPa), comparable to commercial Kevlar fiber.[9] Besides, their dimension, width of 3-5 nm and length of 100-200 nm reduces entanglement and disruption of the linkage in the 2D channel that maintains the π-π stacking of the nanosheets.[224] More interestingly, the distribution of three hydroxyl groups on the monomeric glucose unit allow for the ease of chemical modification. With post-hydrolysis reaction, the surface of CNC could be modified with cationic (amino) or anionic groups (carboxyl and thiol), that facilitate the generation of space charge zone for interlayer channel that enhances the ion flux of the system.[225]

Herein, we report on a 1D/2D composite membrane consisting of negatively or positively charged CNCs intercalated with graphene oxide sheets to form a nano-fluidic reverse dialysis (RED) system for high performance sustainable osmotic energy harvesting. The introduction of robust structural unit of CNC imparts excellent structure stability and mechanical strength to the composite membranes. Benefitting from the high charge density of CNC, it could form a high space charge inside the nanochannel that generates a faster ion transport while maintaining ion selectivity. Due to the special geometry and architecture of the intercalated CNC, it could expand the interlayer spacing of the nanochannel allowing for a higher electrolyte flux. Additionally, the intercalating of CNC reduces steric effect during ion transport as reflected by the reduced transmembrane energy barrier (from 38.8 kJ mol^{-1} for pure GO to 26.33 kJ mol^{-1} for PCNC/pGO and 26.89 kJ mol^{-1} for

NCNC/GO). All these beneficial properties resulted in a high osmotic power generation of up to 4.73 W m^{-2} at room temperature under a controlled salt gradient (50 folds) in KCl electrolyte solution. This osmotic energy conversion corresponds to an electricity generation of 10.92 W m^{-2} at 337 K, which exceeds the critical standard for commercialization (5 W m^{-2}). Additionally, the tandem oppositely charged CNC/GO pair produced high voltages of up to 1.8 V when 10 units were connected in series, indicating the commercial viability of the composite membranes. These results suggest that the geometry and the charge density of intercalating compounds in 2D nanochannel play a crucial role in modulating the ion diffusion process by controlling the ion transport velocity, internal resistance and electrolyte flux. Our findings offer new insights and a strategy on the development of a nano-channel based ion transport membrane produced from the assembly of 1D and 2D nanomaterials.

5.2 Materials and method

Chemicals and materials

Cellulose nanocrystal was provided by Celluforce, Inc. PEI (polyethylenimine), PDDA (polydiallyl dimethyl ammonium) solution, 20% in water), CMC (Sodium carboxymethyl cellulose), TEMPO (2,2,6,6-Tetramethylpiperidine 1-oxyl, 2,2,6,6-Tetramethyl-1-piperidinyloxy, 98%), NaOH (Sodium hydroxide), KCl (Potassium Chloride) and epoxy embedding medium were analytically pure and purchased from Sigma-Aldrich. Inc. Natural flake graphite was purchased from Alfa Aesar.

Preparation of GO and pGO

The negatively charged GO was synthesized according to the Tour's improved Hummers method[226]. The concentration of the obtained GO solution was ~0.4 mg mL^{-1}. The positively charged pGO nanosheets were prepared by the dropwise addition of PDDA aqueous solution (5 mL, 1 wt%) to the colloidal solution of pristine GO (30 mL, 0.4 mg mL^{-1}). Then the mixture was magnetically stirred for 24 h. The solution was then centrifuged at 3500 rpm for 1 h. Subsequently, the obtained sediment was washed four times using Milli-Q water at 3500 rpm for 1 h. The obtained sediment was re-dispersed in Milli-Q water and sonicated for 5 mins yielding the positively charged pGO nanosheets.

Preparation of NCNC and PCNC

The NCNC was prepared using a TEMPO based oxidation method.[227] In detail, 400 mL of DI water was added to 2 g of CNC. After vigorous mixing, sonication was applied for 15 mins, TEMPO (59 mg) and NaBr (0.65 g) were added to the CNC suspension and stirred for 30 mins at room temperature. The pH of the solution was then adjusted to 10 using 0.5 M NaOH. The oxidation was initiated with the addition of 15 % NaOCl solution (14.2 mL) to the CNC suspension over a period of 30 mins. The pH of the solution was kept at 10 for 4 h, and left to stir overnight. Finally, 22 mL of methanol was added to stop the reaction. The obtained NCNC solution was centrifuged and washed four times using Milli-Q water. The final NCNC was collected after high-speed centrifugation. The PCNC was prepared according to the procedure reported in previous paper.[228] In detail, NCNC was re-dispersed in water (1%, 5 ml) and mixed with PEI solution (2%, 10 ml) for 1h. During stirring, the pH was reduced to 1.5 to increase the ionic interaction between NCNC and PEI. After that, the PEI-functionalized NCNC (PCNC) was collected via high-speed centrifugation and washed four times using Milli-Q water to remove unbound PEI chains. Finally, the PCNC was successfully prepared and collected by centrifuging at 10000 rpm.

Preparation of NCNC/GO, PCNC/pGO, NeCNC/GO, NeCNC/pGO, CMC/GO and CMC/pGO membrane

The NCNC was dispersed in Milli-Q water, then sonicated for 20 mins to yield a NCNC suspension at 0.6 mg/ml. GO was dispersed and sonicated in Milli-Q water to obtain a suspension at 1 mg/mL. Then 1ml NCNC suspension was mixed with GO solution (10 ml) and the NCNC/GO membrane was prepared by filtration of the solution through the AAO (anode aluminum oxide, 200 nm pore size) substrate using vacuum assisted filtration. PCNC/pGO, NeCNC/GO, NeCNC/pGO, CMC/GO and CMC/pGO membrane was prepared using a similar procedure except the suspension constituents were changed during mixing.

Electrical measurements

To test the ion transport behavior of the membranes, the prepared ion transport membranes were cut into the small pieces (10 mm x 5 mm) and soaked in water for 24 h to ensure that the nanochannels were fully open. After that, the precut membranes were installed into the epoxy resin and solidified

at 60℃ for 2 h. Two sides of epoxy plates were carefully trimmed to ensure all the 2D channel were exposed. Then the epoxy plate was fixed between two chambers of electrochemical cell (Figure 3b). Ag/AgCl electrodes were used to measure the I-V (current-voltage) profiles. I-V curves and ion conductivity were recorded using a Keithley 2450 source meter. The range of the sweeping voltage was -0.4 V to +0.4 V, with a step voltage of 0.05 V. The open-circuit voltage (U_{OC}) and short-circuit current (I_{SC}) were determined from the intercepts on the voltage and current axes of the I-V curves, respectively. For the ChCNC/GO, NeCNC/GO, CMC/GO and pure GO pair based RED devices, the oppositely charged nanochannel membranes were clamped into the three-chamber electrochemical cell (Figure 4a). The effective testing area of the nanochannel based RED devices were about 0.2 mm^2.

Other characterization

The surface chemical groups of different membranes were characterized with the Bruker VERTEX 33 units over the wavenumber range of 400-4000 cm^{-1}. The zeta potentials and ion conductivity in solution were measured using zeta potential analyzer (Nanosizer ZS, UK). The surface topography was characterized via scanning electron micrography (SEM, Hitachi SU8010) observations and energy dispersive X-ray spectroscopy (EDS) analysis. The mechanical characterization of the composite membrane was conducted on a tensile-compressive tester (M5-2) with a loading rate of 1 mm/min. The membrane samples were cut into strips with a width of 2 mm and length of 8 mm. The Young's modulus can be calculated by the slope of the linear region of the stress–strain curves and the toughness were determined by the area under the stress–strain curves. The reported tensile strength, modulus, and toughness were the averages of three samples.

5.3 Result and discussion

5.3.1 Synthesis of oppositely charged CNC/GO membranes

Figure 5.1a illustrates the fabrication process of negatively charged (NCNC/GO) and positively charged (PCNC/pGO) nanofluidic reverse dialysis membranes (NF-RED) for high performance osmotic energy harvesting. Using the vacuum assisted assembly process, the 2,2,6,6-tetramethylpiperidine-1-oxyl-radical-mediated (TEMPO) oxidized cellulose nanocrystal (NCNC) and polyethylenimine (PEI) modified positively charged PCNC were interlocked and intercalated

with graphene oxide (GO) and polydiallyl dimethyl ammonium (PDDA) modified graphene oxide (pGO) membranes respectively. Following a mild thermal reduction process to enhance the stability in water against swelling, a pair of oppositely charged membranes (ChCNC/GO pair) were embedded in epoxy glue and placed in a three-compartment electrochemical reservoir containing high and low concentrations KCl solutions. The cations prefer to migrate through the negatively charged NCNC/GO membrane toward one side (From high concentration to low concentration, HC to LC), while the anions will be transported by PCNC/pGO toward the other side (also HC to LC). Thus, this two-way selective ion transmembrane movement leads to the potential difference between the electrodes that generates power to the external source.

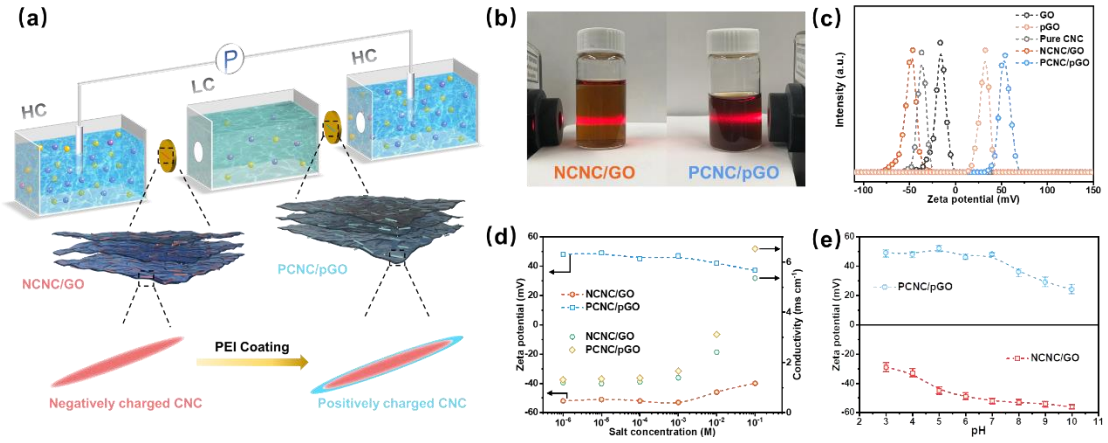

Figure 5-1. (a) Schematic depiction of oppositely charged NCNC/GO and PCNC/pGO nanofluidic energy harvesting device. (b) NCNC/GO and PCNC/pGO solution with typical Tyndall effect, indicating the excellent dispersibility of colloidal particles. (c) The zeta-potential of different colloidal particle solutions. (d) The zeta-potential and conductivity (G) as a function of the salt concentration in colloidal solution. (e) The zeta-potential variation with changes in pH.

The TEMPO oxidized NCNC was a 203±10 nm in length with an average diameter of 8±2 nm, as observed by the transmission electron microscope (TEM) and atomic force microscope (AFM), (Figure 5-2). The PCNC was prepared by coating a 'primer' layer of cationic PEI at pH=1 to introduce positive surface and space charge to the channel system[228]. The multi-angle static laser scattering (SLS) system was used to determine and confirm the dimensions of PCNC. As shown in Figure 5-2, after PEI modification, the length of PCNC increases from 203 to 251 nm and diameter

from 8 to 10 nm. The GO suspension was prepared using the improved Hummer's method[226] (see 'method section') and the mean size of the as-prepared nanosheet was around ~730 nm with predominantly 1.1 nm thick monolayer as confirmed by AFM measurement shown in Figure 5-2c.[229] During the exfoliation, various functional groups, such as oxide (-O-), carboxyl (-COOH) and hydroxyl (-OH), would be terminated on the surface of GO.[230] Polydiallyl dimethyl ammonium (PDDA) was used to convert the type of charge on GO surface according to the electrostatic attraction and π-π stacking.[231] After modification, the zeta-potential of GO was shifted from -24mV to positive +33mv (Figure 1c), indicating the successful loading of PDDA layer on the surface of pristine nanosheets.

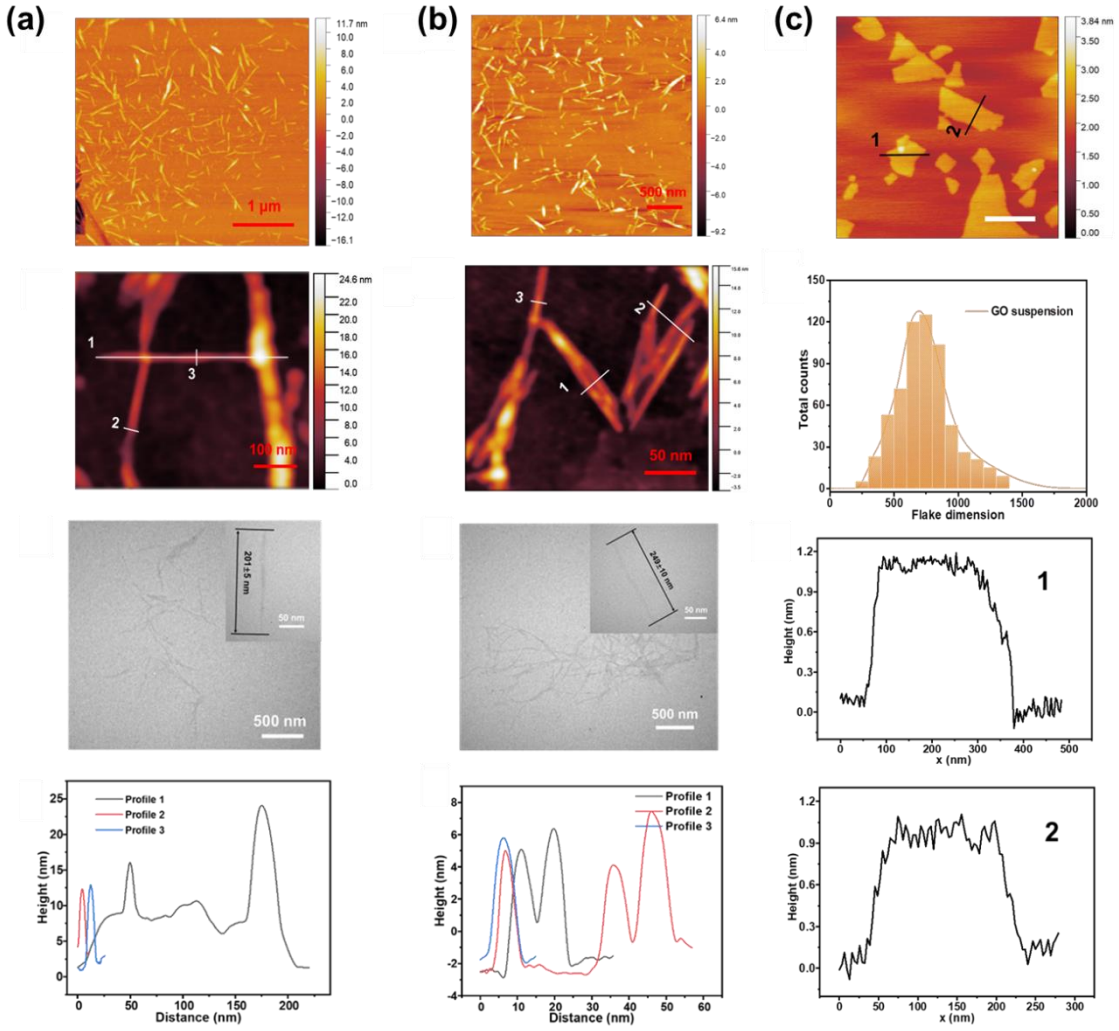

Figure 5-2. (a) Typical AFM image of NCNC distributed on substrate. The TEM image of NCNC and the inset image show the dimension of single distributed NCNC. The high-resolution AFM

image of NCNC and height profile of different position on the image: (Profile 1) The longitudinal section of NCNC; (Profile 2 and Profile 3). The cross section of NCNC. (b) Typical AFM image of PCNC distributed on substrate. The TEM image of PCNC and the inset image shows the dimension of a single distributed PCNC. The high-resolution AFM image of PCNC and height profile of different position on the image: (Profile 1, Profile 2 and Profile 3). The cross section of NCNC. (c) Characterization of GO nanosheets. Particle size distribution of exfoliated GO suspension (scale bar: 300nm). AFM height image of graphene oxide. Cross-section profile of different position on the AFM height image (1) and (2).

The NCNC and GO as well as PCNC and pGO formed stable suspensions with strong Tyndall's effect in deionized water (denoted as NCNC/GO and PCNC/pGO separately), demonstrating the good dispersibility of the colloidal system. The chemical response of NCNC/GO and PCNC/pGO to pH as well as supporting electrolyte are shown in Figure 5-1d and 1e, respectively. The zeta-potential decreased slightly with the addition of electrolyte due to the salt effect towards the colloidal particles. Figure 5-1d shows the two distinct behaviors of the relative conductance (G) of NCNC/GO and PCNC/pGO, where the measured G became independent of ionic concentrations at concentration less than 0.01M since the ion transport was fully controlled by surface charge. The two types of suspension maintained the same charge polarity over the pH range of 3-10, with the zeta potential of -20 mV for NCNC/GO or greater than +20 mV for PCNC/pGO as shown in Figure 5-1e.

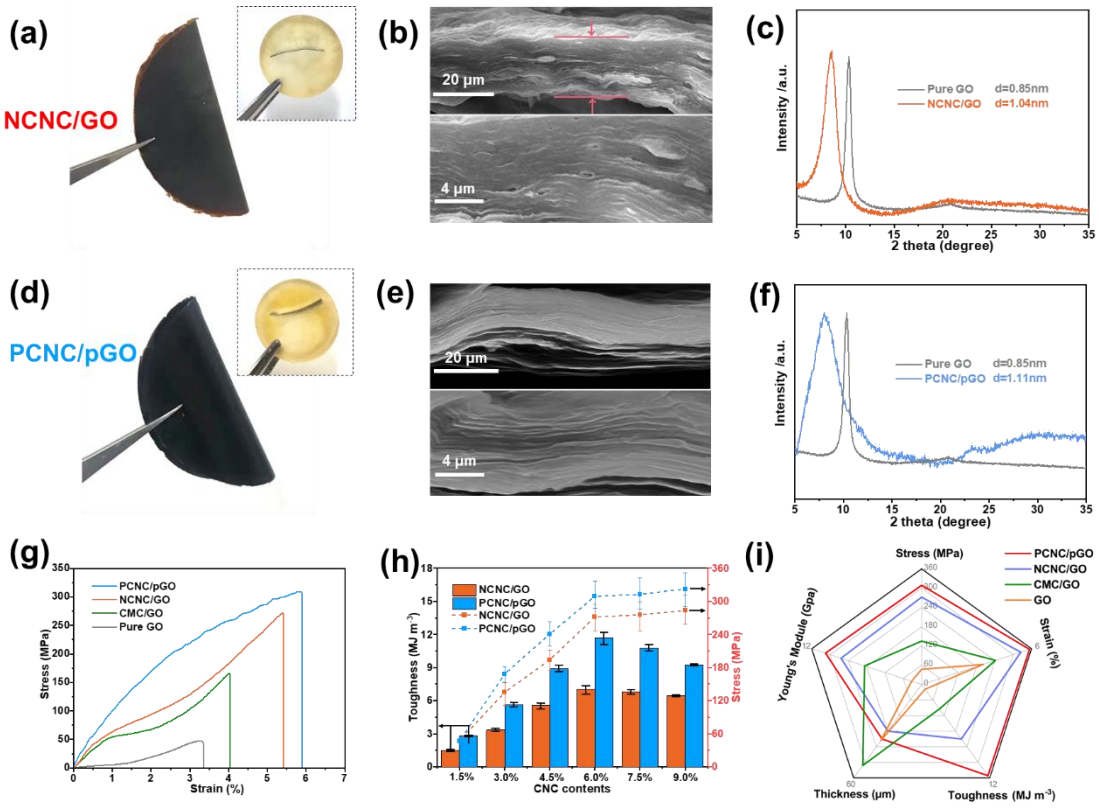

Figure 5-3. (a), (d) Photographs of self-standing and flexible NCNC/GO and PCNC/pGO membranes, respectively. (b), (e) Cross-section SEM characterizations of NCNC/GO and PCNC/pGO membranes. The thickness of the membranes was about 20 μm. (c), (f) XRD patterns of NCNC/GO and PCNC/pGO membranes. (g) Tensile stress-strain curve of the NCNC/GO, PCNC/pGO, CMC/GO and pure GO membranes. (h) The ultimate strength and toughness of NCNC/GO and PCNC/pGO composite membranes with different CNC contents. (i) Comparison of mechanical performance in terms of stress, strain, Young's modulus, thickness and toughness.

The membranes denoted as NCNC/GO and PCNC/pGO were prepared via a simple vacuum filtration of the colloidal suspensions. Both dark brown membranes were highly flexible and freestanding (Figure 5-3a and d), with the typical lamellar morphology which could be observed from the cross-sectional scanning electron microscopic images (SEM) (Figure 5-3b and e). As shown in Figure 5-3c and f, both the X-ray diffraction spectra (XRD) of NCNC/GO and PCNC/pGO exhibited sharp diffraction peaks, demonstrating the laminated long-range ordered structure. The calculated interlayer spacing of NCNC/GO and PCNC/pGO were 1.04 nm and 1.11 nm according to the XRD peaks (2θ=8.47° and 7.94°, respectively). Considering the thickness of a single graphene

layer (0.43nm), the effective channel size for ion transport was about 0.61 nm for NCNC/GO and 0.68 nm for PCNC/pGO, which was large enough for small hydrated ions to diffuse through the channel.[232]

5.3.2 Structure characteristic and mechanical viability of the oppositely charged membrane

The Fourier transform infrared (FT-IR) was utilized to characterize the chemical structure of the membranes (Figure 5-4a). Compared to pure CNC, the sharp peak at 1730 cm^{-1} for NCNC/GO indicated that the negatively charged carboxyl groups (-COOH) were present on the CNC and GO surfaces. Additionally, new peaks of PCNC/pGO at 1616 cm^{-1} and 1470 cm^{-1} corresponding to the amide I group ($-NH_2$) and quaternary ammonium associated to the PEI grafted on CNC and PDDA adsorbed on GO respectively, confirming the successful modification of the membrane surface.[233] The mechanical performance of the composite membranes possessed sufficient strength for practical applications. First, the stress-strain tests were conducted to evaluate the tensile property of various samples. As shown in Figure 5-3g, the mixing of NCNC and PCNC with GO induced a distinct enhancement in both the strength and strain. For the optimized NCNC/GO and PCNC/pGO membranes with CNC content of about 6%, the ultimate strength was 272 MPa and 309 MPa respectively, which were significantly higher than stacked GO film (i.e. about 47 MPa) and natural nacre (i.e. about 135 MPa). The elastic moduli of NCNC/GO and PCNC/pGO also exhibited considerable value, which were about 8.8±0.2 GPa and 10.5±0.6 GPa, respectively. In order to further understand the mechanical property of CNC/GO membrane, the sodium carboxymethyl cellulose (CMC)/GO composite film was prepared, where the CMC/GO displayed higher tensile strength than pure GO membrane but lower than the CNC/GO membranes. Besides, the stiffness of CMC/GO (3.2 MJ m^{-3}) was about 3.9 MJ m^{-3} and 11.5 MJ m^{-3}, which were lower than NCNC/GO and PCNC/pGO (Figure 5-3i), respectively. To better understand the mechanism of high mechanical strength brought by introduced CNC, further interface interactions between CNC and GO were discussed. As shown in Figure 5-4b, the few stacked pristine GO layers possessed a relatively smooth topography and the root-mean-square (rms) was about 0.34±0.05 nm determined from AFM. Thus, the adjacent GO nanosheets could interact via weak attractive force (e.g., hydrophobic-hydrophobic interaction, π-π interaction forces), resulting in the poor mechanical strength.[234] The CMC (carboxymethyl Cellulose) with similar chemical structure as NCNC (TEMPO oxidized CNC)

shown in Figure 5-4c possessed carboxyl groups that generated strong attractive force with the GO sheets via hydrogen bonding between the oxygenated groups, overcoming the electrostatic repulsion, and functioned as physical crosslinkers for the GO sheets.[235] Thus, both CMC/GO and NCNC/GO exhibited higher mechanical strength than pure GO membrane. Due to the special geometry of NCNC (stiff nanorod) trapped on the GO surface (Figure 5-4c and 4d), it induced the formation of artificial wrinkles on the GO layer and the rms would increase to 4.5±0.21 nm. The CNC-induced wrinkles on the GO basal planes were analogous to the nano-asperities on the surfaces of aragonite tablets as shown in Figure 5-4e, which was beneficial in forming interlocked interfaces between the graphene sheets that increased the frictional resistance.[236] Besides, the interaction between the adjacent GO nanosheets was reinforced by the addition of NCNC since the NCNC bridged the neighboring GO nanosheets via additional hydrogen bonds, which was confirmed by the morphologies of the fractured regions (Figure 5-4f).[237] Therefore, the improved mechanical strength was attributed to the highly wrinkled topology of the GO sheets tailored by the addition of NCNC. For PCNC/pGO membrane, the PDDA was first coated on the surface of GO nanosheet that increased the surface zeta-potential from -24 to +33 mV inducing the electrostatic repulsion between the composites. Therefore, the reason for the higher mechanical of the PCNC/pGO was identical to the NCNC/GO system since the surface topology of composite was identical (Figure 5-4c and d).

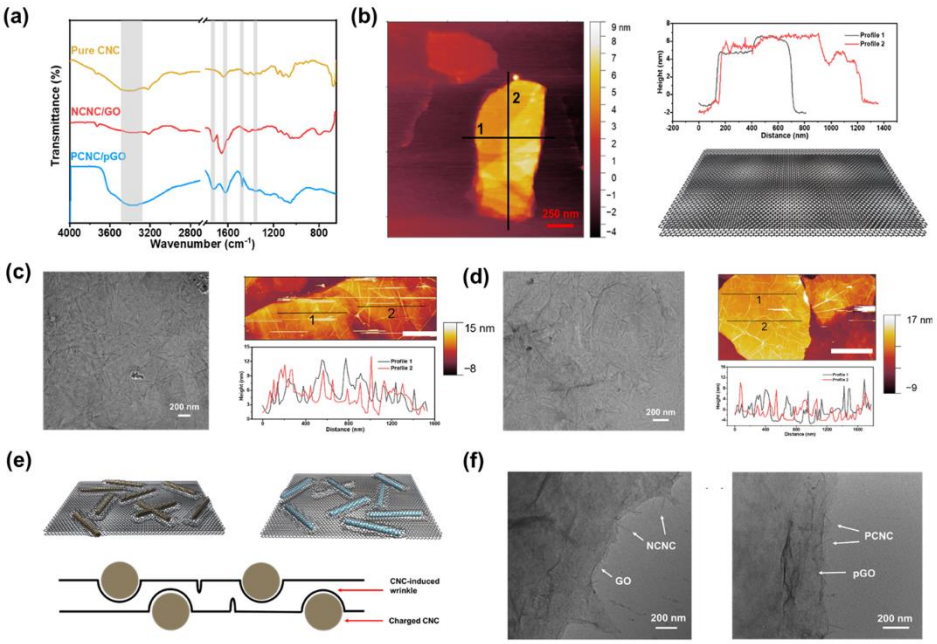

Figure 5-4. (a) Fourier transform infrared spectrum acquired from Pure CNC, NCNC/GO and PCNC/pGO membrane, in which the characteristic peaks were marked to represent the functional groups. (b) The AFM image, height profile and the schematic structure of the several layers of stacked GO nanosheet. (c) The TEM image and AFM image NCNC wrapped on the surface of GO. The height profile shows the covering of NCNC that induces the formation of artificial wrinkles on GO (The scale bar is 1μm). (d) The TEM and AFM image of PCNC wrapped on the surface of pGO. The height profile shows the covering of PCNC that induces the formation of additional artificial wrinkles on pGO (The scale bar is 1μm). (e) The schematic structure of the NCNC/GO and PCNC/pGO, and schematic illustration of the wrinkles when NCNC and PCNC is trapped in GO basal planes. (f) TEM images of the fractured regions with wavy cracks, pulled sheets, and bridged NCNC and PCNC.

5.3.3 Charge governed ion transport property

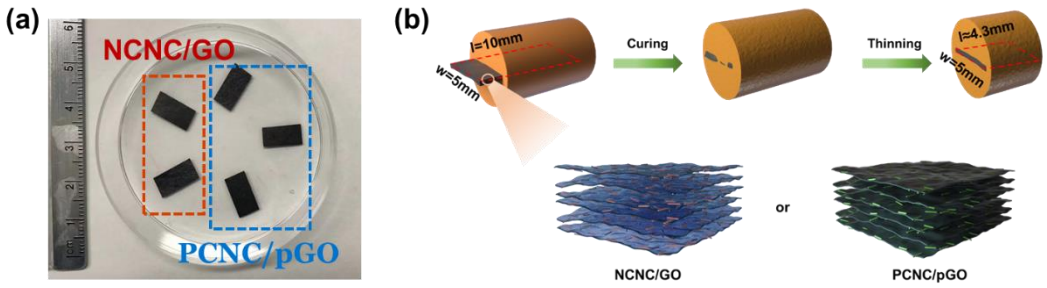

Figure 5-5. (a) Small rectangular strips for nanofluidic testing. The red framework contains the NCNC/GO membranes and the blue framework represents PCNC/pGO membranes. (b) Schematic illustration for the encapsulation of the 2D membrane (NCNC/GO andPCNC/pGO) into the epoxy resin.

The oppositely charged 2D CNC nanofluidic membranes were cut into small rectangular strips of dimension of 10 mm x 5 mm (Figure 5-5a). After soaking in water for 10 hours, the NCNC/GO and PCNC/pGO strips were fixated to the epoxy resin mold (The preparation process can be seen in Figure 5-5b) consisting of plastic plates (inset of Figure 5-3a and Figure 5-3d) and clamped between two electrochemical testing chambers as shown in Figure 5-6b for evaluation. The transmembrane

ionic diffusion characteristic of oppositely charged NCNC/GO and PCNC/pGO with a thickness of about 20 µm (Figure 5-7a, b, c and d) were evaluated by measuring the current-voltage (I-V) profiles. As shown in Figure 5-6a and c, for the KCl electrolyte concentration ranging from 1M to 0.01M, both the I-V curves of NCNC/GO and PCNC/pGO followed a linear ohmic behavior with negligible ionic rectifying phenomenon, confirming the microstructure symmetry and the charge-controlled ion transport of the composite membranes. However, when the salt concentration was below 10^{-3}M, the ionic conductance of two nanofluidic membranes deviated from the bulk value and became independent of the electrolyte concentration, confirming the surface charge-controlled ions transport (Figure 5-7e). In general, at low salt concentration, the thickness of electric double layer (EDL) increased and overlapped the whole nanochannel. Thus, the NCNC/GO nanofluidic membrane with negative charge would allow the cation to pass through and repelled the anion. Similarly, for PCNC/pGO, the nanofluidic channel would concentrate the anions while the cations were excluded. As a result, the overall ionic conductance of nanofluidic channel was determined by the ionic concentration inside the nanofluidic channel, which was further evaluated by the charge density of NCNC/GO and PCNC/pGO membranes.

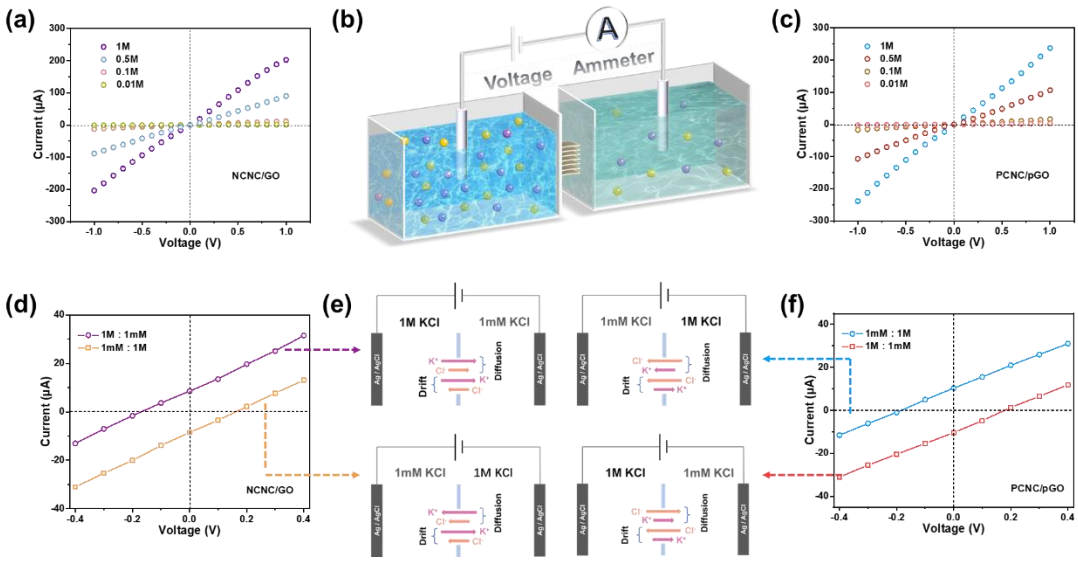

Figure 5-6. (a), (c) Current-Voltage (I-V) curves of NCNC/GO and PCNC/pGO at different electrolyte concentrations. (b) Schematic illustration of ion transport testing. (d), (f) Measurement of Current-Voltage (I-V) curves for NCNC/GO and PCNC/pGO membranes recorded in 1000-fold KCl concentration gradient. The low concentration side was set to 1 mM. (e) Schematic

illustration of the ion transport testing setup under a concentration gradient. The diffusion current is consistent with the net flow from high to low concentration.

Next, the selective ion transport process could be verified by the chemical potential gradient using asymmetric KCl electrolyte solution. With the concentration difference, the chemical potential gradient would be converted into a net diffusion current, which was detected as ions diffused at a higher rate (Figure 5-6e). Notably, the negatively charged NCNC/GO preferred to transport cation (i.e. K^+) from high to low concentration, generating the diffusion current (I_{diff}) and voltage (V_{diff}). The absolute values of I_{diff} and V_{diff} were determined from the intercept on the current axis (I_{sc}, short-circuit current) and the voltage axis (V_{oc}, open-circuit voltage) after the extraction of redox potential on the electrode (The calculation details are shown in Figure 5-8 and Table 1). As shown in Figure 5-6d and f, when the concentration difference was 1000 folds, the calculated diffusion voltage V_{diff} of NCNC/GO and PCNC/pGO were about 123 mV and -136 mV respectively. In addition, under a reverse concentration gradient, the similar absolute values of the intercepts for NCNC/GO and PCNC/pGO on the X/Y axes suggested that the membranes' structure were symmetrical, and no preferential ion diffusion direction was observed. To further explore the ion selectivity and energy conversion efficiency, a series of concentration gradients were applied to determine the V_{diff} change (Figure 5-8 and Table 1). According to Equations (5-1) and (5-2)[238]:

$$V_{diff} = (2t_+ - 1)\frac{RT}{F}\ln(\frac{a_{high}}{a_{low}}) \quad (5\text{-}1)$$

$$\eta_{max} = \frac{1}{2}(2t_+ - 1)^2 \quad (5\text{-}2)$$

where the t_+ and t_- are the transference numbers for cations and anions respectively. R, T, F, and a are the universal gas constant, absolute temperature, Faraday constant and activities of electrolyte, respectively. Under the concentration gradient difference of 10-105, the cationic transference number (t_+) of NCNC/GO approached 0.89 with more than 29% energy conversion efficiency. For PCNC/pGO, the t_- ($1-t_+$) approached 0.91 and a higher energy conversion efficiency was obtained (35%). This high ion selectivity for NCNC/GO and PCNC/pGO membranes improved the energy conversion process since the electric energy was generated only by the preferential ionic transport.

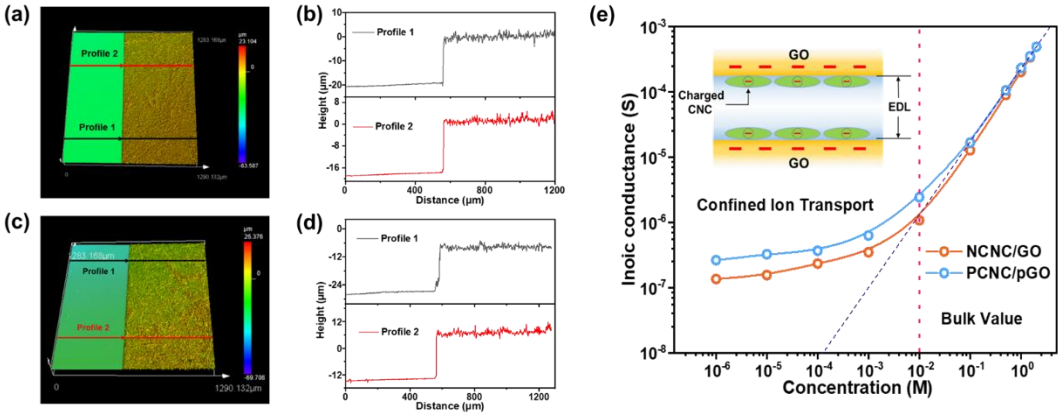

Figure 5-7. Surface profile image of the section of (a) NCNC/GO and (c) PCNC/pGO membrane and (c), (d) the corresponding height profile. (e) Ionic conductance variation versus salt concentration of the NCNC/GO and PCNC/pGO.

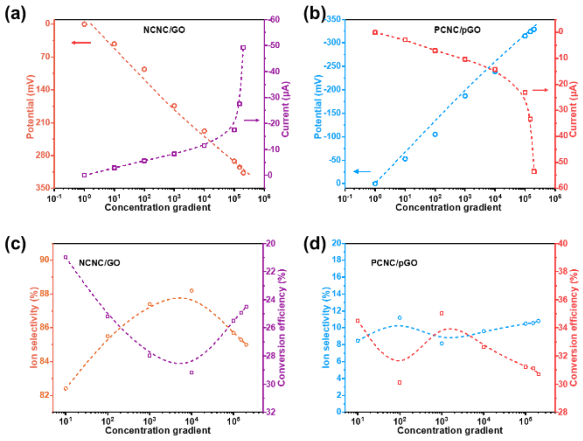

Figure 5-8. (a), (b) Open-circuit potential and short-circuit current variations with the concentration gradient difference. (c), (d) Ion selectivity (t+) and conversion efficiency.

The selective ion transport behavior was further confirmed from the energy dispersive X-ray spectroscopy (EDS) mapping on the cross-section of the membranes. The NCNC/GO and PCNC/pGO membranes were immersed in 0.05 mM KCl for 1 hour to saturate the membrane with the electrolyte. It was then washed with Milli-Q water to remove excess ions on the membrane surface. As evident from Figure S17, the higher content of K^+ was observed for the NCNC/GO membrane, indicating its cationic selectivity, while the Cl^- content were evident in the PCNC/pGO,

confirming its anion selectivity.

Table 5-1. Measured open-circuit potential, redox potential and diffusion potential for NCNC/GO and PCNC/pGO, respectively.

Concentration gradient (M/M)		**$10^{-5}/10^{-4}$**	**$10^{-5}/10^{-3}$**	**$10^{-5}/10^{-2}$**	**$10^{-5}/10^{-1}$**	**$10^{-5}/1$**
	E_{redox} (mV)	7	21	51	65	97
NCNC/GO	$E_{Diffusion}$ (mV)	35	75	123	163	195
	V_{oc} (mV)	42	96	174	228	292

Concentration gradient (M/M)		**$10^{-5}/10^{-4}$**	**$10^{-5}/10^{-3}$**	**$10^{-5}/10^{-2}$**	**$10^{-5}/10^{-1}$**	**$10^{-5}/1$**
	E_{redox} (mV)	-8	-22	-51	-64	-101
PCNC/pGO	$E_{Diffusion}$ (mV)	-45	-83	-136	-175	-214
	V_{oc} (mV)	-53	-105	-187	-239	-315

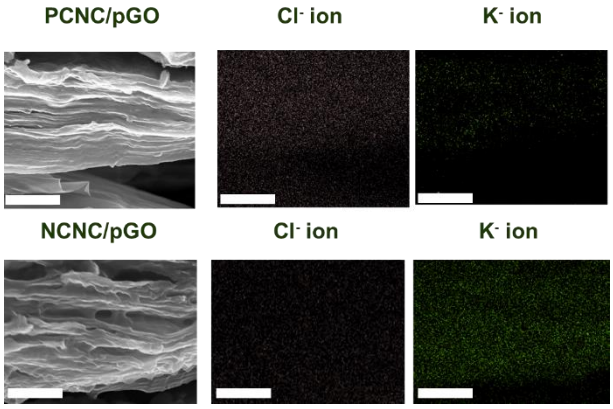

Figure 5-9. Element mapping of prepared PCNC/pGO and NCNC/GO. For PCNC/pGO

membrane, showing the binding of chloride ions, and repulsion of potassium ions. On the contrary, the potassium ions are condensed in NCNC/GO membrane, showing the anion selectivity. The scale bar is 2μm.

Osmotic energy conversion performance

The generated osmotic electric power was evaluated by connecting the system to an external load resistance (R_L). In detail, a pair of cationic selective NCNC/GO and anionic selective PCNC/pGO denoted as charged ChCNC/GO pair, was coupled in series in a three-compartment electrochemical cell filled alternatingly with concentrated (HC) and diluted ionic solutions (LC). In this device (Figure 5-10a), under the two-way transmembrane chemical gradient, the cation (i.e. K^+) preferred to travel through the NCNC/GO toward the anode raising the electrode potential, whereas the anion (i.e. Cl^-) preferentially migrated across PCNC/pGO toward the cathode and lower the electrode potential. This two-way ion separation process generated a large potential difference and ion flux between the two electrodes producing an electrical power output to the external R_L.

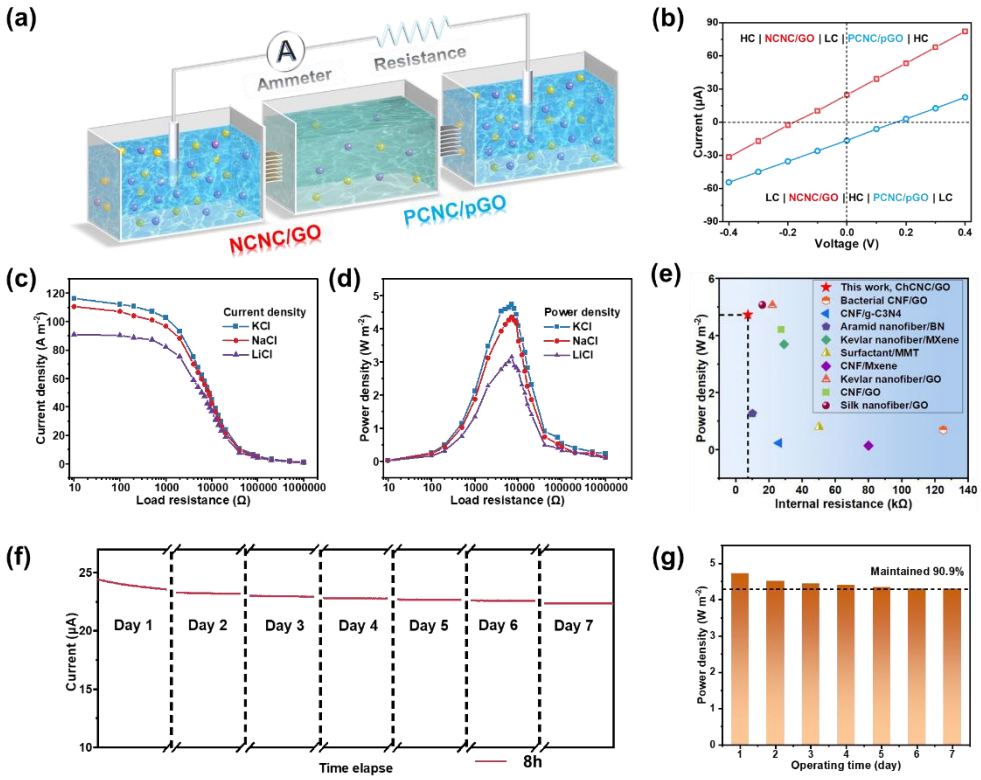

Figure 5-10. (a) The nanofluidic reverse electrodialysis of the combination of oppositely charged ChCNC/GO (NCNC/GO and PCNC/pGO composites membrane) pair. (b) I-V responses for

single-unit nanofluidic reverse eletrodialysis device measured under two configurations methods, High concentration (HC) in the central or low concentration (LC) in the central compartment. (c) Current density and (d) output power of ChCNC/GO based RED system as function of load resistance under the placement of different electrolyte solution (KCl, NaCl and LiCl) in the central cell. (e) Comparison of the power density and internal resistance with the reported intercalated 2D nanofluidic membranes. (f) Short-circuit current and (g) output power density of ChCNC/GO pair membrane for continuous 7 days.

Firstly, two combination methods of electrolyte arrangements were assembled to evaluate the overall electrochemical performance. From the I-V curve in Figure 5-10b, the obtained membrane potential approached 176 mV and measured current was about 24 μA under 50-fold concentration difference for Method 1, where the HC in the central compartment and two side compartments were filled with LC electrolyte. However, with the LC in the central compartment and HC in the two side compartments (Method 2), the measured potential showed similar potential of about 168 mV but with a lower current of about 16μA. The maximum power density was calculated from the equation: $P_{max}=U_{oc}\times I_{sc}/4$ and the results showed that Method 1 produced a power that was 37% higher than Method 2. Thus, subsequent testing was conduct using the set up in Method 1.

As discussed above, the osmotic power was directed to an external circuit with different resistance, R_L. When R_L was increased, the real-time current decreased accordingly, and the output power density could be calculated from the relationship, $P_{out}=I^2\times R_L$. As shown in Figure 5-10c and Figure 5-10d, the maximum power output achieved 4.73 W m^{-2} for R_L of 7000 Ω, which was extremely close to the internal resistance of the composites of about 7213 Ω. The internal resistance of ChCNC/GO membrane pair was among the lowest ever reported for 2D nanofluidic membrane, which was crucial for developing large-scale nanofluidic osmotic energy harvesting devices (Figure 5-10e and Table 2). Besides, the permselectivity (α) and energy conversion efficiency (η) were calculated from Equation (5-3) to (5-5) [239].

$$V_{thea} = N\frac{RT}{F}\ln(\frac{a_{high}}{a_{low}}) \ , \tag{5-3}$$

$$\alpha = \frac{V_{mea}}{V_{thea}}\times 100\% \tag{5-4}$$

$$\eta_{max}=\frac{\alpha^2}{2} \tag{5-5}$$

where V_{mea} corresponds to the measured membrane potential, V_{thea} is the theoretical potential calculated from Nernst equation, N is the number of membranes used in the osmotic system. Due to the high ion flux and low internal ionic resistance, the obtained permselectivity was 88% and the energy conversion efficiency of ChCNC/GO pair was as high as 37%, which was superior compared to recent reported nanofluidic membrane. In addition, the long-term stability strongly influenced the real-world application of CNC/GO pair in osmotic power harvesting. As shown in Figure 5-10f and g, the ChCNC/GO pair membrane only lost 9.1% of its origin performance over 7 days of continuous testing, confirming that the membranes were stable and could generate continuous power output. On the contrary, as shown in Figure 5-11, the current of prepared GO pair membrane (GO and pGO membranes) will fast decrease and even lose its electrochemical performance since the decomposition of nanochannels in prolonged stability testing. It could be attributed that the epoxy glue could partially increase the structural stability due to the physical confine effect that reduced the swelling of the GO membrane during testing. However, the robustness and mechanical strength of 2D membranes comprised not only of the overall membrane but also the stability of the nanochannel and surface charge layer. As shown in Figure 5-11, the epoxy encapsulated GO nanochannel membrane could maintain the electrochemical performance in the first two days of testing. However, during the long-time testing, the continuous diffusion of ions inside the nanochannel would lead to the inevitable slips of GO nanosheets due to the weak interaction between adjacent nanosheet. Consequently, the 2D nanochannel of GO membrane became unstable and decomposed after long-time use, losing their ion separation capability. However, the introduction of ChCNC into GO system would enhance the stability of the nanochannel to counteract the interfacial stress, which prevented the decomposition of the nanochannels [240]. As a result, the prepared 2D ChCNC/GO membrane could maintain their electrochemical performance during stability assessment (7 days continuous testing).

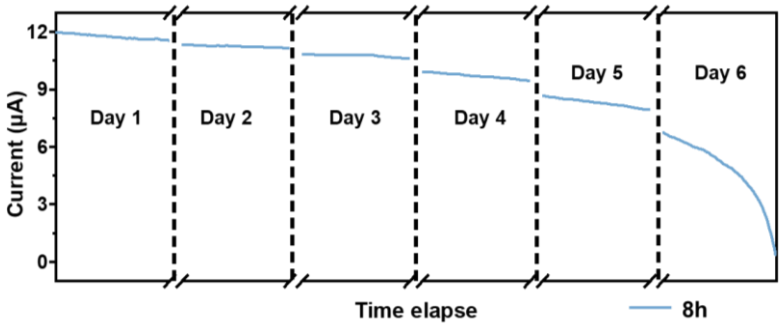

Figure 5-11. Short-circuit current testing for epoxy resin confined GO membrane pair for continuous 7 days.

5.3.4 The mechanism of high-power generation of composites membrane.

The intercalated negatively charged NCNC and positively charged PCNC not only enhanced the mechanical property of nanofluidic membrane, but their special geometry and charged surface functional groups enhanced the osmotic power generation performance of the composite membranes. The intercalating agent of charged NCNC and PCNC enlarged the interlayer spacing leading to faster ion transport and higher transmembrane flux. In solution, the charged NCNC and PCNC in confined channel produced a space charge zone, offering the extra space charge to fill the electric double layer (EDL). When combined with the surface charge of GO and pGO, the EDL confined in the enlarged 2D nanochannel would completely overlap, which optimized the energy conversion process. As calculated in Figure 5-12, In order to quantify the charge density contributed by the CNCs, the surface charge densities of different samples were calculated from the Zeta potential measurements, where the surface zeta potential (ξ) was determined from the Malvern Zetasizer Nano ZS90 together with the surface zeta potential cell. Then the surface charge density was calculated using Equation (5-6) [241]:

$$\sigma_{surface} = \frac{\varepsilon\varepsilon_0\xi}{\lambda_D} \tag{5-6}$$

where ε, and ε_0 are the dielectric constant, the permittivity of a vacuum, respectively. And the Debye length (λ_D) can be obtained according to Eqation (5-7) [237]:

$$\lambda_D = \sqrt{\frac{\varepsilon\varepsilon_0 RT}{2n_{bulk}z^2F^2}} \tag{5-7}$$

where n_{bulk}, and z were the concentration of solution, the valence number, respectively. F, T, and R represented the Faraday's constant, the absolute temperature, and the universal gas constant,

respectively. Based on the surface zeta potential of GO, NCNC/GO, pGO and PCNC/pGO, the surface charge density GO and pGO was about -3.2 and 3.6 mC/m^2, respectively. After the introduction of guest materials, the additional space charge form NCNC and PCNC improves the surface charge density of 2D membranes up to -5.7 and 6.1 mC/m^2, respectively. As a result, the coexistence of surface charge and space charge would maintain the permselectivity and increase ion flux during ion transport inside the composite membranes, enhancing energy conversion efficiency.

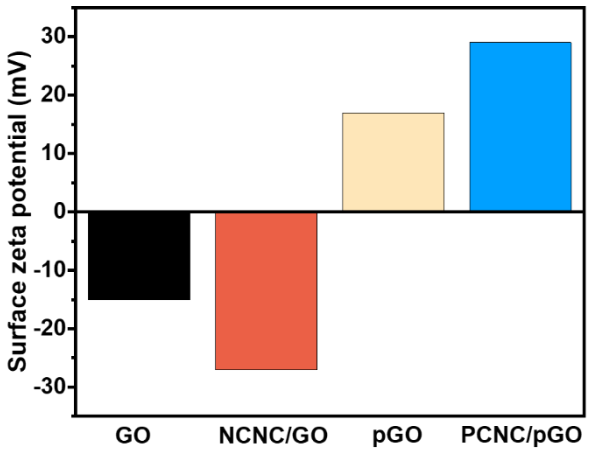

Figure 5-12. The surface zeta potential of four different types of membrane.

To gain more insight on how the charged CNC improved the osmotic power generation, pure GO pair (GO and pGO membranes) was fabricated for comparison. As shown in Figure 5-13b and c, the power output of pure GO pair achieved only ~1.8 W m^{-2}, which was significantly lower than the ChCNC/GO system, demonstrating that the intercalated NCNC and PCNC played critical roles in boosting the osmotic power performance. Further, the pristine CNC was treated with NaOH for six hours to remove negative sulfate groups on the surface, rendering the CNC with a low surface zeta-potential of -2.5 mV (NeCNC). Accordingly, the neutral charged NeCNC was used to fabricate NeCNC/GO and NeCNC/pGO nanofluidic membrane (NeCNC/GO pair), and the power density of NeCNC/GO system reached 3.0 W m^{-2}, which was higher than pure GO membranes (1.8 W m^{-2}) but lower than ChCNC/GO membranes (4.73 W m^{-2}).

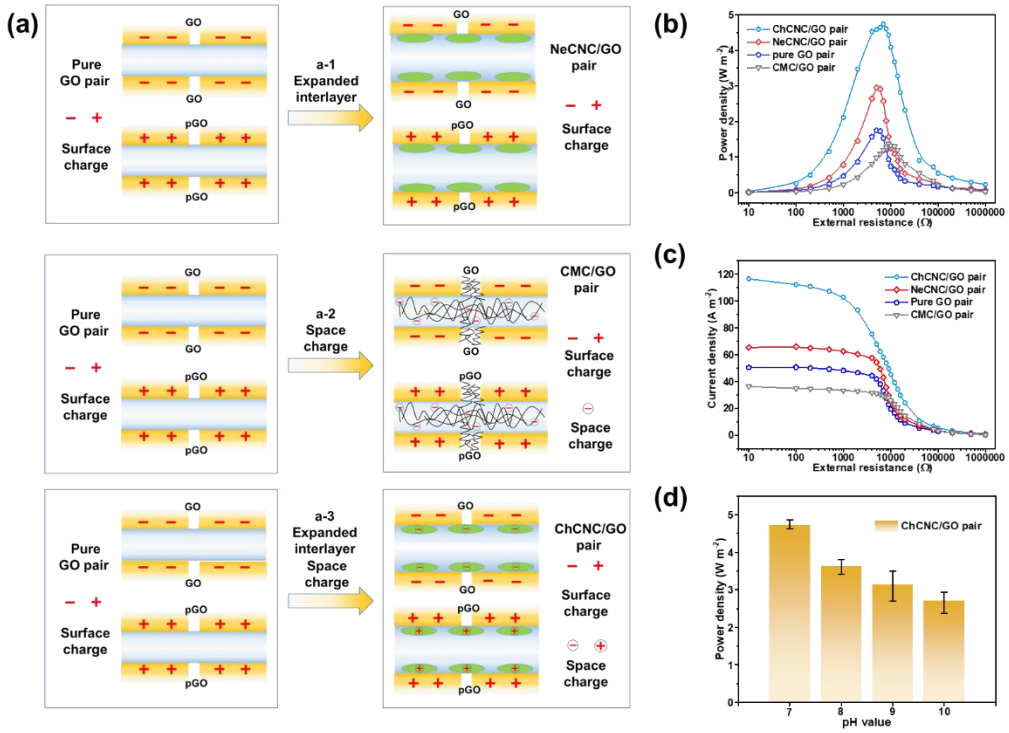

Figure 5-13. (a) Schematic illustration of the mechanisms of different intercalating agents for the improvement of performance. (a-1), adding neutral charged NeCNC to the GO system. (a-2), adding CMC to the GO system. (a-3), introduction of oppositely charged ChCNC to the GO system. (b) and (c) The electrochemical performance variation for ChCNC/GO, NeCNC/GO, CMC/GO and pure GO system. (d) Dependence of output power density on the electrolyte pH.

This trend could be attributed to the expansion of nanochannel by the intercalated NeCNC in GO nanosheet as shown in Figure 5-13(a-1). Since the increase of the interlayer space caused by intercalated NeCNC, the internal resistance of 2D nanochannel would be greatly reduced allowing for a faster ion transport that led to a higher osmotic current. Contrast experiment was also performed with the composite membrane using CMC as the intercalating agent, which was a water-soluble analogue of CNC. The maximum current density of this membrane only achieved 36 A m^{-2} with an inferior power density of about 1.3 W m^{-2}. This result could be attributed to two factors: (i) the adverse effect of space charge and (ii) high system internal resistance. As shown in Figure 5(a-2), the CMC being a negatively charged polymer would screen the positive surface charge of pGO. Thus, the overall charge of CMC/pGO pair would be reduced, resulting in a lower performance of the power density. Besides, previous studies have demonstrated that the maximum power density

occurred when R_L was equaled to the internal resistance of RED system, which mainly derived from nanofluidic membranes.[211] Therefore, the CMC/GO pair possessed a much higher internal resistance than other nanofluidic membrane as shown in Figure 5-13b. As shown by the AFM image of CMC/GO in Figure 5-14, due to the water solubility and highly hydrophilic characteristic of CMC, the CMC would be densely packed on the GO surface, narrowing the size of the nanochannels. Besides, the entanglement and agglomeration of CMC chains would block the nanochannel between the GO sheets and disrupt the bridging of the GO nanosheets. Thus, the resulting steric hindrance would restrict the movement of ions inside the nanochannel, leading to a higher internal resistance.

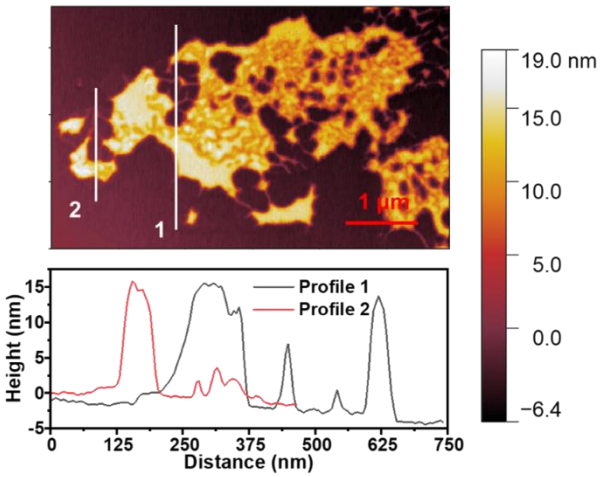

Figure 5-14. The AFM image of CMC/GO and the corresponding profile.

The contribution of space charge from PCNC could be demonstrated by changing the pH of the electrolyte. When the pH of electrolyte in the PCNC/GO compartment was increased from 7 to10, abundant positively charged NH_3^+ groups on PCNC surface would be deprotonated to NH_2, resulting a lower charge density in the confined nanochannel and a lower output power density reflected in Figure 5-13d. The horizontally stacked charged CNC/GO membrane pair (H-ChCNC/GO, ion diffusion direction perpendicular to the 2D membrane) were prepared to compare the performance of the system prepared using the same fabrication condition as ChCNC/GO. Accordingly, these two types of CNC intercalated 2D GO membranes (H-ChCNC/GO and ChCNC/GO) possessed identical interlayer spacing and chemical composition but different ion transport modes across the membrane (Figure 5-15a, b and c). The stacked ChCNC/GO membranes were separated with the interlayer spacing (d) about 1.08 nm (the average value of NCNC/GO and PCNC/pGO) and considering the

thickness of single graphene layer (a=0.43 nm), the empty space for hydrate ion transport was estimated from δ=(d-a) =0.65 nm. For the as-prepared ChCNC/GO membrane (Figure 5-15a), the passing path for ions was parallel to the 2D membrane and most of ions were capable to travel straight through a single nanochannel inside the ChCNC/GO membrane. Thus, the full distance of single nanocapillary was similar to the geometrical length of 2D nanomembrane (l≈4.3 mm). In sharp contrast, for the ions travelling inside the nanochannel of H-ChCNC/GO (5-15b), most of them had to travel via the zig-zag trajectories and pass though the gap between the adjacent GO layers. Therefore, the length of ion transport involves the thickness of prepared H-ChCNC/GO (h≈20μm) with amounts of turns (h/d) involving a capillary length w (750 nm, the average size of GO membrane measured from nanosizer. Hence, the full transmembrane length of H-ChCNC/GO membrane for ion passing was calculated from l=w*h/d=13.89 mm which was almost three times larger than ChCNC/GO membrane. As a result, during the ions crossing the nanochannel, the tortuous geometric structures and prolonged ion passage in H-ChCNC/GO membrane generated high impedance, resulting a lower ion transport velocity. Besides, the H-ChCNC/GO membrane pair exposed the basal plane to the electrolyte solution and the ion could only enter the nanochannel through the gaps or pores of the stacked 2D nanosheets. In sharp contrast, the ChCNC/GO exposed much higher effective surface area for ion to enter due to the parallel ion diffusion direction, leading to a better electrochemical performance. The effective testing area of ChCNC/GO and H-ChCNC/GO pairs were 0.2 mm^2 and 0.04 mm^2, respectively. As shown in Figure 5-15d and e, both the current density and output power density of H-ChCNC/GO were significantly inferior to the ChCNC/GO due to two reasons, the prolonged ion transport paths inside the channel and insufficient pores on membrane for the diffusion of the ions.[242]

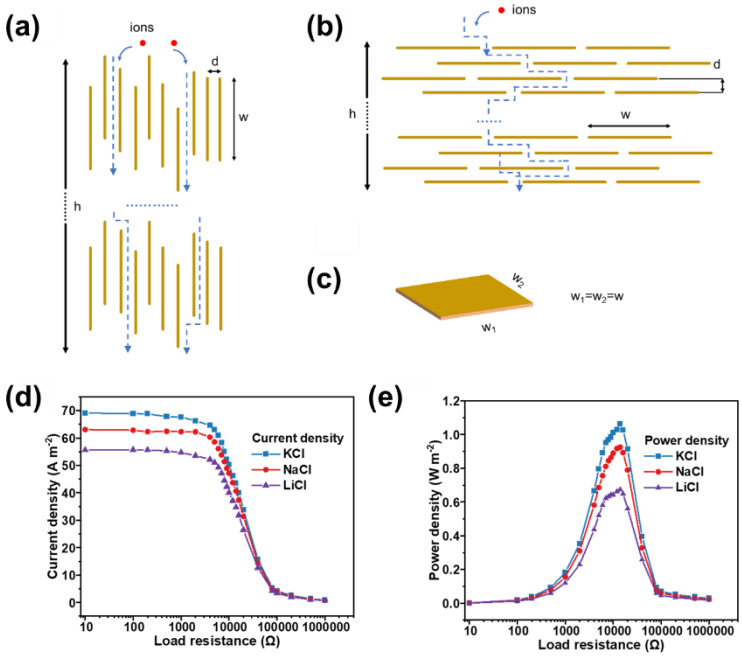

Figure 5-15. Schematic illustration of the ion transport pathway for (a) vertically stacked ChCNC/GO membrane (ion diffusion direction parallel to the 2D membrane) and (b) horizontally stacked ChCNC/GO (ion diffusion direction perpendicular to the 2D membrane) membrane. (c) the dimension of single ChCNC/GO membrane for the estimation of ion transport length. The (d) current density and (e) output power density of the H-ChCNC/GO as functions of load resistance under the placement of different electrolyte solution (KCl, NaCl and LiCl) in the central cell.

Besides, the electrochemical performance ChCNC/GO membrane pairs with different contents of ChCNC were also be investigated. When the contents of intercalated ChCNC was low (below 3%), the space charge generated by ChCNC was not adequate to construct the EDLs with expanded nanochannels. In sharp contrary, the superfluous of ChCNC (Higher than 10%, Figure 5-16) into the 2D nanochannel will increase the cover density on GO and cause the increase of physical hinderance, lowering the output power density. When the content of ChCNC added to GO system was between 4.5% ~ 9%, the generated power density reached an optimal of around 4.7 W m^{-2} (±2%) caused by the balance between enhanced charge and physical hindrance effect.

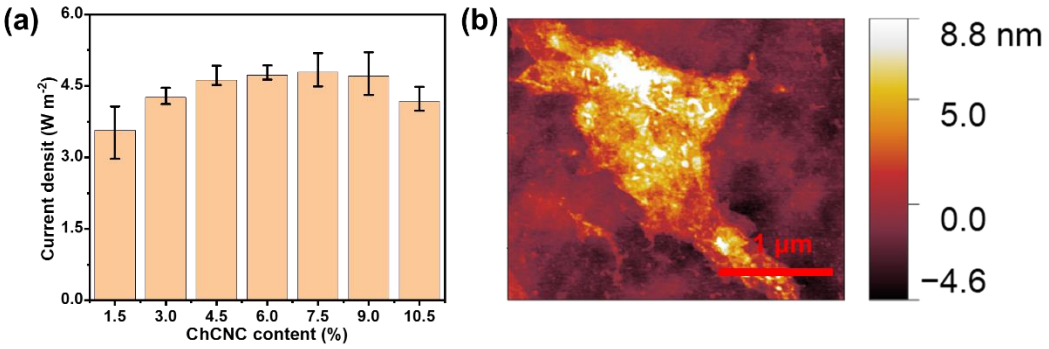

Figure 5-16. (a) Influence of the weight content of ChCNC on the output power density. Error bars represent s.d. (b) The AFM image of densely coated (10.5% weight content) NCNC on GO surface.

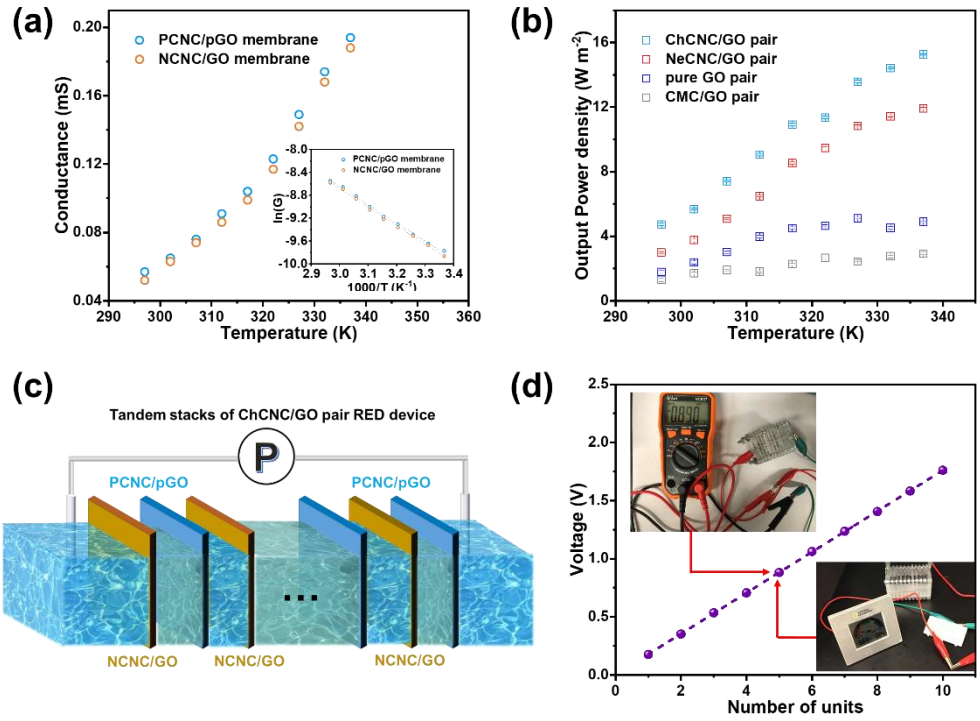

Figure 5-17. (a) Ionic conductance as a function of temperature. The inset shows the Arrhenius-type plot of the ion conductance versus temperatures. (b) The maximum output power density as a function of temperature in 50-fold KCl concentration gradient. (c) Schematic illustration of the tandem stacks of ChCNC/GO pair RED device. (d) The output voltage of 10 units. The inset image shows the voltage of 5 connected RED units and power a 0.8V thermo/hygro clock.

To gain further investigation on the power generation and membrane resistance arising from the intercalating agents (such as charged NCNC and PCNC, neutral NeCNC and CMC polymer), the thermal dependence of the conductance was investigated. In Figure 6a, when the temperature was increased from 298 to 337K, the ionic conductance of NCNC/GO and PCNC/pGO exhibited a linear dependence and followed the Arrhenius behavior (inset Figure 5-17a). This phenomenon could also be observed for other nanochannel membranes as shown in Figure 5-18a.

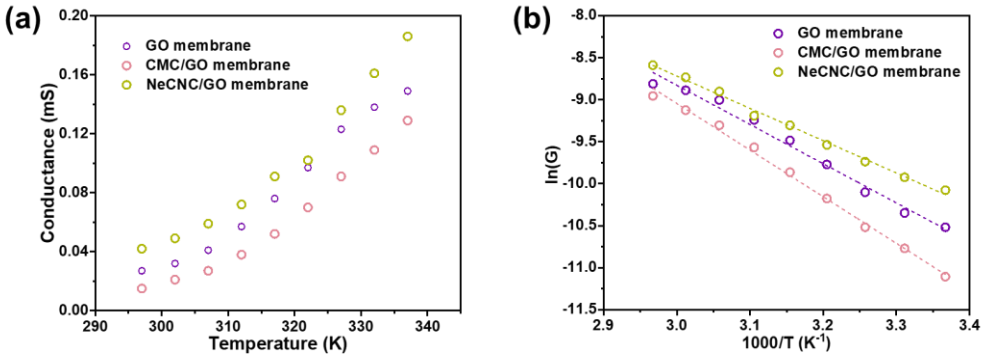

Figure 5-18. (a) Ionic conductance variation with temperatures. (b) The Arrhenius-type plot of the conductance as a function of temperature.

According to the thermal-conductance analysis, the ion transport energy barrier in the nanochannel membrane is described by Equation (5-8)[243]

$$G = G_0 e^{\frac{-E_a}{RT}} \quad (5\text{-}8)$$

where G is the ionic conductance, G_0 the constant, R, T the gas constant and temperature, respectively. The ion movement energy barrier E_a was determined from the slope of the inset in Figure 5-17a and Figure 5-18. The calculated results indicated that the energy barrier of K^+ transported in pure GO membrane was 38.8 kJ mol^{-1}, which was comparable to the reportable value[244]. When NeCNC was introduced to the GO nanosheets, the energy barrier decreased to 31.9 kJ mol^{-1}, which could be attributed to the screened physical steric hindrance factor caused by the expanded interlayer spacing. However, the NCNC/GO and PCNC/pGO membrane systems possessed E_a of 26.89 kJ mol^{-1} and 26.33 kJ mol^{-1} respectively due to the lower internal resistance

and space charge offered by charged CNC, which were favorable for the fast ion transport and energy conversion efficiency. In the case of CMC/GO membrane, the energy barrier was as high as 46.13 kJ mol^{-1}, suggesting that the entangled and aggregated CMC polymer chain in the nanochannel would lead to the significant blocking effect. This steric hindrance would even shield the enhancing effect of charge factor produce by the CMC.

The power conversion efficiency variations were also measured in different working temperatures. As demonstrated in previous studies[245], the increased fluid temperature would reduce the liquid viscosity (η) and enhance the ionic mobility (μ) in a confined space as shown by Equation (5-9) and (10)[219]:

$$\mu(T) = \frac{q|z_i|}{6\pi r_i \eta(T)} \tag{5-9}$$

$$\eta(T) = T^{1.5} \times 10^{(0.159(\frac{1000}{T})^3 - 1.323(\frac{1000}{T})^2 + 4.587(\frac{1000}{T}) - 5.261)} \tag{5-10}$$

where T is the temperature of fluids, r_i and z_i are the radius and valence of the ion that transport in confined space. When the temperature was increased, these two factors (η and μ) synergistically governed the ion transport process and enhanced the power generation. As expected, the testing power generation of the nanochannel pairs showed strong temperature dependence, the ChCNC/GO and NeCNC/GO pair achieved 10.92 W m^{-2} and 8.53 W m^{-2} at 337K (Figure 6b), respectively. However, it was important to note that the pure GO and CMC/GO pair showed non-linear temperature dependency. The power density showed an increasing trend below 317K, but the value fluctuated at the higher temperature region, where such a variation might be associated with ion clogging occurring in confined nanochannel due to bubble nucleation on the wrinkled pure GO surface and entangled CMC polymer chain.[245, 246] Accordingly, the nanochannel would be gradually filled with nano-gas bubble at high temperature, which hindered the transport of electrolyte resulting in the poor electrochemical performance. However, this thermal response performance was very promising in practical application since the amount of low-grade thermal energy from industrial waste can be utilized to further boost the performance of osmotic power generation.

The tandem ChCNC/GO pair RED devices stacks could produce high voltage when they were connected in series as shown in Figure 5-17c. In this study, the output voltage showed a linear dependence of 176 mV per unit cell producing 0.89V when 5 ChCNC/GO pair RED devices were

connected in series, and it could power a thermo/hygro clock (inset of Figure 5-17d). The output voltage could generate 1.8 V when 10 ChCNC/GO pair REDs were connected together twith a 50-fold KCl salinity gradient solution (Figure 5-17d). The output voltage can even reach 1.8 V when 10 ChCNC/GO pair REDs were connected together under 50-fold KCl salinity gradient solution (Figure 5-17d), demonstrating the possibility of ChCNC/GO pair based RED devices, making the osmotic blue energy a promising alternative.

5.4 Conclusion

In summary, the oppositely charged 2D CNC intercalated GO membranes were constructed via a facile vacuum-assisted assembly process to harvest osmotic energy from nature. The introduction of small amount (6%wt) of 1D CNC nanorod into GO lamellar could significantly enhance the structural and mechanical stability, achieving a high ultimate strength up to 272 and 309 MPa for NCNC/GO and PCNC/pGO, respectively, thus satisfying the requirements for practical application. Additionally, due to the special geometry and morphology of CNC nanorod, it could also expand the interlayer spacing of 2D nanosheet for faster ion transport without generating extra transmembrane resistance and physical hinderance. Due to the chemical flexibility of CNC, its surface charge could be easily tuned with either negative or positive by modifying it with charged polymer. The NCNC and PCNC with high charge density could introduce space charge inside the 2D nanochannel. Combined with the surface charge of GO and pGO, they could synergistically improve the energy conversion performance. In this study, the composite membranes of ChCNC/GO produced a power density of 4.73 W m-2 under 50-fold salinity gradient, which was very close to the standard commercialization benchmark (5 W m^{-2}). The performance could be further increased to 10.92 W m^{-2} in power density by utilizing thermal treatment (337K), outperforming conventional RED systems. Our results advanced the understanding of ion transport in the intercalated GO nanofluidic membrane and this material design strategy offers a promising approach to develop 2D membrane-based osmotic power generator.

Chapter 6. Superhydrophilic and aligned CNF array for selective ion transport and salinity energy harvesting

6.1 Introduction

Fluidic conduction membranes with charged nanosized channel walls have gained significant attention and have been widely utilized in various applications, such as desalination[247], ion/molecule separation[210], and ionic regulation[248]. These membranes, particularly ion-selective membranes, hold great potential for harnessing "blue energy" and addressing the increasing energy demands of modern society.[249, 250] Traditional nanofluidic membranes, such as two-dimensional (2D) nanochannels, offer precise control over channel size and diameter. However, their scalability, low porosity for ion transport, and high cost pose challenges for further real-world applications.[251] One-dimensional (1D) nanochannels, on the other hand, have emerged as a promising type of ion-selective membrane for osmotic power harvesting.[252] They possess a geometry that is particularly conducive to ion transport and exhibit a higher density of nanochannels, allowing for increased ion flux and theoretical power output. However, synthesizing and constructing 1D membranes has been a major hurdle.[253] Additionally, lower ionic conductivity and mechanical strength have limited the application of 1D nanochannels. Silicon-based materials, for example, can be fabricated into aligned 1D nanoscale channels using lithography or templating, but they lack surface charge and suffer from performance degradation when subjected to bending or folding.[254] Nanoporous polymer membranes, while easy to fabricate, are not sustainable, and their three-dimensional tortuous nanoporous structure and low charge capacity restrict their use in selective ion transport and osmotic energy harvesting.[255] Therefore, the development of high-performance ion-selective membranes relies heavily on advancing fabrication methods and sustainable raw materials capable of constructing nanochannels with suitable geometry and charge capacity.

Cellulose, the most abundant and biodegradable polymer in the world, offers an attractive solution.[222] Its basic chain consists of repeating D-glucose units that can be functionalized with charged groups to increase the charge capacity of the system. In this study, we present a straightforward "bottom-up" method for fabricating aligned cellulose nanofiber membranes with high charge capacity. The abundant negatively charged functional groups on the membrane's surface

enable exceptional ion selectivity for cations, including both monovalent and divalent ions. Moreover, due to its high ion selectivity, the fabricated membrane exhibits remarkable performance in osmotic energy harvesting, achieving a high power output of approximately 3.95W m^{-2}, surpassing previous cellulose-based nanochannel membranes reported in literature.

6.2 Materials and method

Materials

The cellulose nanofibers (CNF) were prepared from cotton pulp via TEMPO oxidation. Urea, concentrated sulfuric acid, and epichlorohydrin (EPI) were purchased from Sigma Chemical (Canada). All chemicals were used without additional purification, unless stated otherwise. The cotton linter pulp was used after complete drying under vacuum at 60 °C and without further purification. Milli-Q water (resistivity of 18.2 MΩ cm) was used to prepare the aqueous dispersions.

Fourier transforms infrared (FT-IR) spectroscopy

FT-IR spectroscopic measurements on the pollen particles, cellulose nanofiber (CNF) and ODA.SES were performed using a Bruker Tensor 27 FTIR spectrometer. This was used to confirm the modification of lycopodium pollen, when the spectrum was compared with the pristine pollen. Samples were freeze-dried and pressed into potassium bromide (KBr) pellets.

AFM imaging

AFM images were recorded on a Cypher S (Asylum Research) using a silicon nitride probe (RTESP-300, BRUKER) with a tip radius of 2 nm, a spring constant of 40 N/m and a high resonance frequency of 300 kHz. All imaging results were analyzed using the AFM accessory software (Gwyddion).

TEM Imaging

The size and morphology of the nanoparticles were evaluated using a transmission electron microscope (TEM). A droplet of the sample solution was placed on a carbon coated copper grid, and left for 10 min, after which the excess liquid was removed using a small piece of filter paper and left to dry overnight before TEM analysis.

SEM imaging

The morphology and electrode surface were characterized by scanning electron microscopy (Zeiss Ultra-Plus FESEMs) and in combination with energy-dispersive X-ray spectroscopy for identifying the elemental composition of samples.

Raman spectroscopy

Raman spectroscopy was conducted on LabRam HR800 confocal Raman microscope (HORIBA JobinYvon) with ×50 and x20 objective (excitation at 532 nm).

Confocol microscopy

The measured confocal (Zeiss LSM 510 Meta Laser Scanning Confocal Microscope (CLSM) image was shaped into a 3D image using ZEN 2009 analysis. The observation magnification was 40x/1.3 Water DIC, and an immersion objective lens was used, with the immersion medium being water.

Rheology testing

The rheological properties of the concentrated suspension were characterized in a Malvern Kinexus ultra^{+} rheometer with the cylindrical measuring system and a solvent trap to prevent water evaporation.

Zeta potential testing

Zeta potential (ζ) of the dispersed suspension was measured using a Zetasizer Nano S90 (Malvern Instrument) without adjusting the ionic strength. The ζ value was calculated from the electrophoretic mobility using the Henry equation and Huckel approximation.

Contact angle analysis

The water static contact angle measurements were performed using a sessile drop system in ambient environment at room temperature. The liquid was dispensed with a micro-needle (New Era Pump Systems Inc.) with a syringe pump as a spherical droplet of volume 5 µl. Measurements were conducted in ambient environment at room temperature 5 secs after the

droplet was dispensed onto the surface. The contact angle was measured by fitting the profile using a DCAT-15 and Labview program.

Electrical measurements

A cellulose membrane was embedded into polydimethylsiloxane elastomer with two wells carved on either side to serve as reservoirs for the electrolyte solution. The cellulose nanofluidic membrane was immersed in electrolyte for at least 1 day before measurements were performed. Two homemade Ag/AgCl electrodes were inserted into the reservoirs. BioLogic from Science Instrument was used to record the current signal while providing the voltage source at a scanning rate of 10 mV s−1.

6.3 Results and discussion

6.3.1 The construction of align distributed CNF membrane

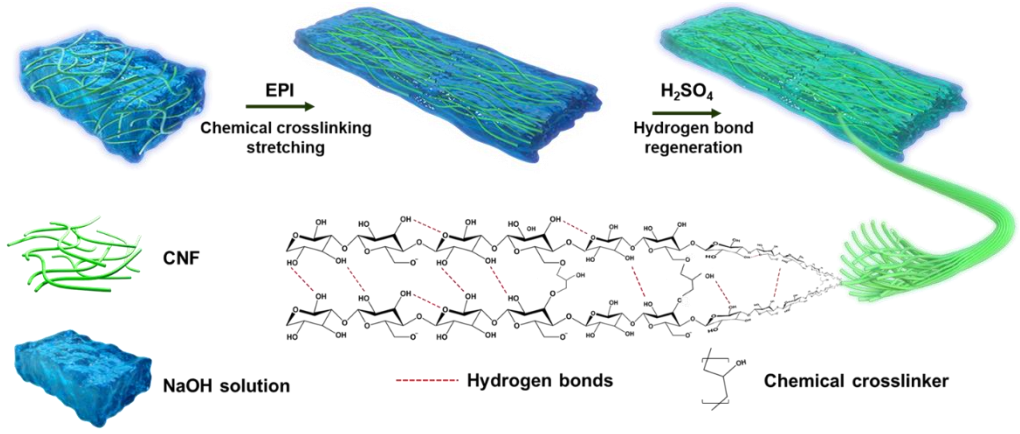

Figure 6-1. Schematic image of the bottom-up approach for fabricating aligned distributed CNF.

Figure 6-1 illustrates the fabrication process of the anisotropic cellulose film through a dual cross-linking strategy followed by a structural re-organization process. Initially, cellulose nanofibers (CNFs) were obtained via the TEMPO-oxidization method as discussed in Chapter 4. Subsequently, the TEMPO-oxidized CNFs were dispersed into a NaOH-Urea system at a low temperature of -4°C. The reduced hydrogen bond strength at low temperatures allowed for the incorporation of urea molecules into the gaps between cellulose chains.[256] Then the amino and carbonyl groups of urea acted as both hydrogen bond donors and acceptors, competing with existing hydrogen bonds within the cellulosic chains and consequently disrupted the closely packed cellulose chains. Under alkaline

conditions, epichlorohydrin (EPI) will react with the hydroxyl groups (-OH) through the open-ring reaction, resulting in the chemical cross-linking of the cellulose chains and the formation of a gel-like structure.[257] Subsequently, this chemically cross-linked gel was stretched and manipulated to induce a temporary alignment of the cellulose nanofibers via stretching. Following this, the gel was immersed in an aqueous H_2SO_4 solution, leading to the removal of urea and NaOH from the cellulose chains and facilitating the re-establishment of hydrogen bonds between neighboring cellulose chains. This step permanently fixed the aligned and distributed structure within the gel. Finally, the water within the gel was evaporated using an air-drying process, resulting in the successful fabrication of the double cross-linked, aligned and distributed CNF membrane, designated as A-CNF.

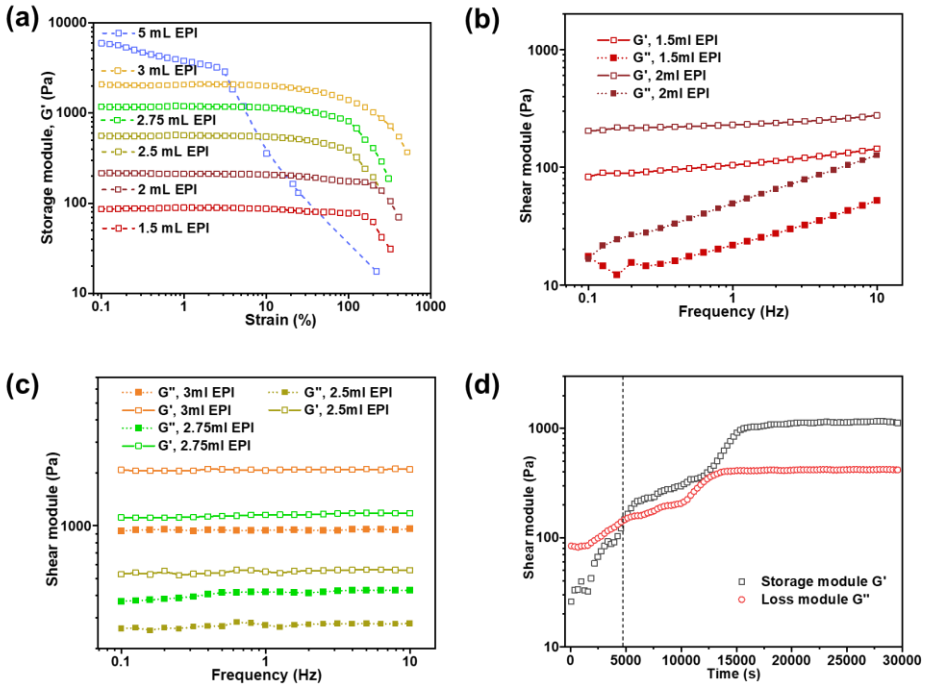

Figure 6-2. (a) Storage (G′) and loss (G″) modulus as a function of time during the cross-linking of the hydrogel precursor solution (6 wt% cellulose with 2.75 mL EPI) at -12 °C. (b) and (c) The amplitude sweep of diverse sample with different contents of EPI. (d) single-frequency measurements of gelation progress with 2.75 ml EPI crosslinker.

In the initial investigation, different amounts of EPI were used in the pre-solutions to examine the role of covalent bonds and determine the optimal stretching conditions prior to the re-establishment of the hydrogen bonds. The amplitude sweep in Figure 6-2b shows that higher EPI content increased

the concentration of covalent bonds in the hydrogel structure, resulting in a gel with higher toughness but increased fragility. For instance, when using 3 mL of EPI, the hydrogel exhibited a high storage modulus of approximately 6000 Pa, but its structure disintegrated easily, leading to a significant reduction in the storage modulus after a 3% strain. Conversely, lower EPI content indicated a relatively lower concentration of covalent bonds in the gel system, making it softer and larger linear viscoelastic region (LVR) as shown in Figure 6-2a. The frequency sweep measurements were also conducted in the LVR region to further characterize the rheological properties of the five samples. As shown in Figure 6-2b and c, all EPI crosslinked systems behaved like gels, with the phase angle independent of frequency. However, it is worth mentioning that at very low EPI concentrations, the loss modulus exhibited an increasing trend, indicating that an inadequate concentration of covalent bonds in cross-link structure resulted in a gel system with higher viscosity and stickiness, which was detrimental to the subsequent stretching process. On the other hand, the storage and loss moduli in the other three EPI contents remained constant over a wide range of frequencies confirming that the effective covalent bonds endowed the gel with sufficient elastic properties. This means the material could rapidly respond to stress, effectively storing and recovering stress energy without significant energy dissipation or viscous behavior.

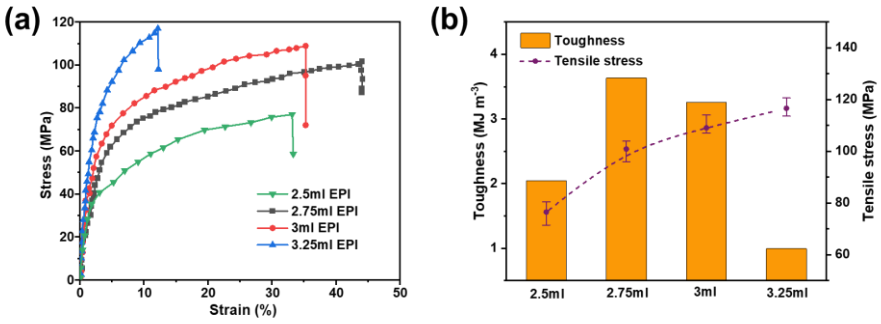

Figure 6-3. (a) The mechanical properties of membrane after structural re-organization in acid solution and dried in air. (b) The ruptured stress and toughness of the different membranes prepared by different contents of EPI.

In seeking for an optimal formulation that achieved a balance between the mechanical properties and the surface functional group content of the nanochannel membranes, a stress-strain analysis was conducted on four different types of membranes. These membranes were prepared using varying

volumes of EPI (epoxypropylisopropanol) cross-linker before the hydrogen bond generation process. Figure 6-3a and b illustrate that the tensile strength of the membranes increased significantly with increasing concentrations of EPI in the system. This could be attributed to the formation of more covalent cross-links points, which enhanced the overall strength of the membrane. However, an excessive amount of chemical bonds could result in a reduction in the number of flexible and reversible physical bonds. This was observed in the membrane prepared with 3.25 ml of EPI, as shown in Figure 6-3a, where the membrane exhibited less tolerance to strain. Comparatively, the membrane prepared with 3 ml of EPI displayed a slightly higher tensile stress than the one prepared with 2.75 ml EPI. However, it is important to consider that a higher content of physical bonds in the 2.75 ml EPI formulation led to a significantly higher toughness in the membrane. Additionally, the covalent cross-linking process consumed a substantial portion of the surface functional groups for crosslinking purposes. Therefore, the 2.75 ml EPI cross-linker formulation was deemed more suitable for applications involving ionic transport. Additionally, the gelation process was monitored using single-frequency measurements to study its time dependence characteristics. Figure 6-2d reveals that the cross-linking process occurred approximately 30 minutes after the addition of 2.75 mL EPI to the CNF-NaOH-Urea solution, resulting in an increase in both the storage modulus (G') and loss modulus (G"). Subsequently, the gelation process reached a plateau after 4.2 hours, as indicated by the stable storage and loss moduli curves. This demonstrated that the gelation process was indeed time-dependent, and the addition of EPI contributed to enhanced structural stability and elasticity. Furthermore, it is noteworthy that the storage modulus exhibited a significantly faster rate of increase compared to the loss modulus, and the crossover point (indicated by the black dashed line in Figure 6-2a) is considered the critical gelation point. This phenomenon could be attributed to the etherification process between cellulose and EPI leading to the formation of more covalent bonds. Consequently, the material exhibited an elastic-solid behavior, rather the predominant viscous behavior, demonstrating a heightened ability to withstand stress while maintaining its shape and mechanical properties.

6.3.2 The properties of A-CNF membrane

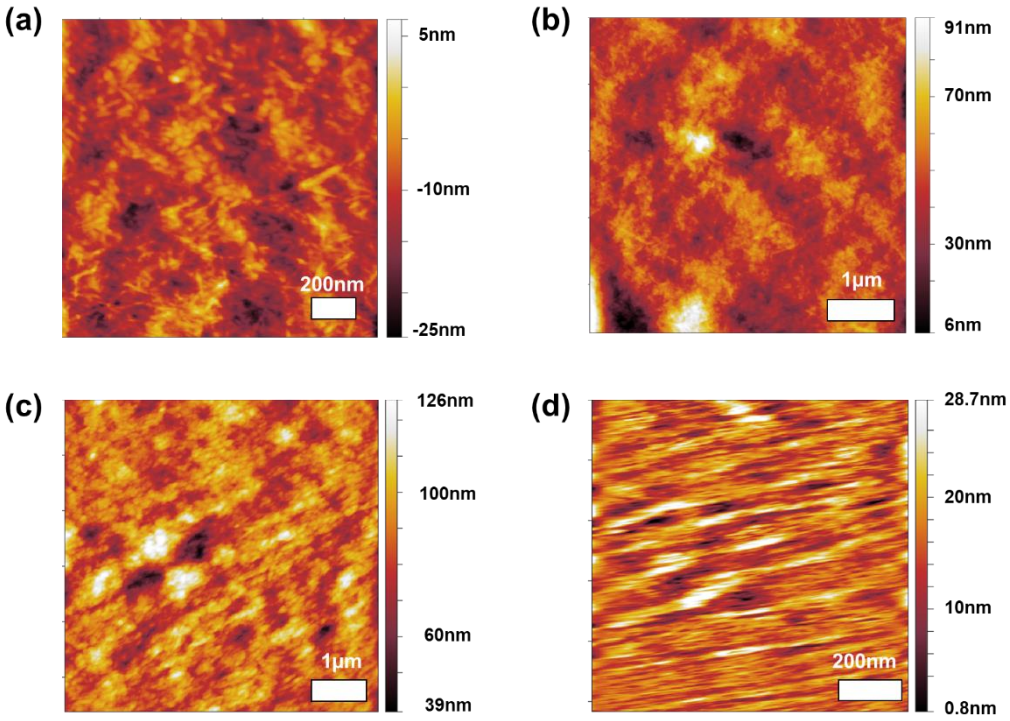

Figure 6-4. The AFM images of the surface of the anisotropic cellulose films with various prestretching strains, including 40%, 80%, 120%, and 160% respectively.

The restoration of hydrogen bonds was conducted in an H_2SO_4 solution, which provided the gel with sufficient physical cross-link points, where the A-CNF (Align distributed CNF) membranes could be produced after drying in air. The morphology of the A-CNF membranes was investigated using AFM and SEM methods. Figure 6-4 illustrates the different deformed A-CNF membranes at various tensile strains (ε) of 40%, 80%, 120%, and 160%, respectively. At a 40% pre-stretching strain, the A-CNF membrane did not display aligned nanostructure along the stretching direction and the isotropic distributed CNFs were observed on the surface of membrane. However, at 80% strain, a slightly oriented structure was observed, and when the strain was increased to 120%, the CNF became more aligned, resulting in a tendency to assemble and stack together, forming a compact nanostructure. When the strain was further increased to 160%, a dense and highly aligned structure was obtained, accompanied by a significant reduction in the surface roughness due to the well-oriented nanostructure. The SEM images further demonstrated the highly anisotropic properties of the A-CNF membrane. As shown in Figure 6-5a, three different cross-section analyses were conducted to verify the presence of the highly aligned structure. The magnified SEM image in

Figure 6-5b illustrates that the surface of the A-CNF membrane (xy plane) exhibited very low

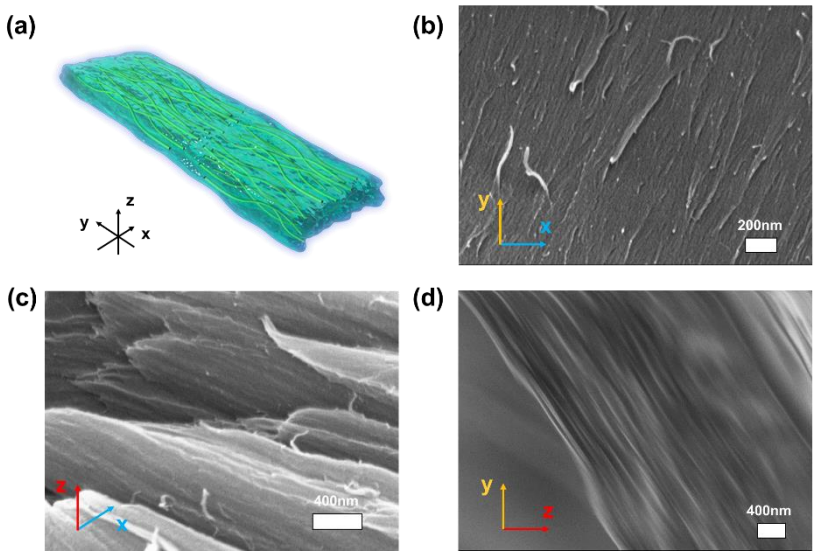

Figure 6-5. The SEM images of anisotropic TEMPO oxidized CNF membranes. (a) the illustration of observed A-CNF membrane from (b) xy plane, (c) xz plane and (d) yz plane.

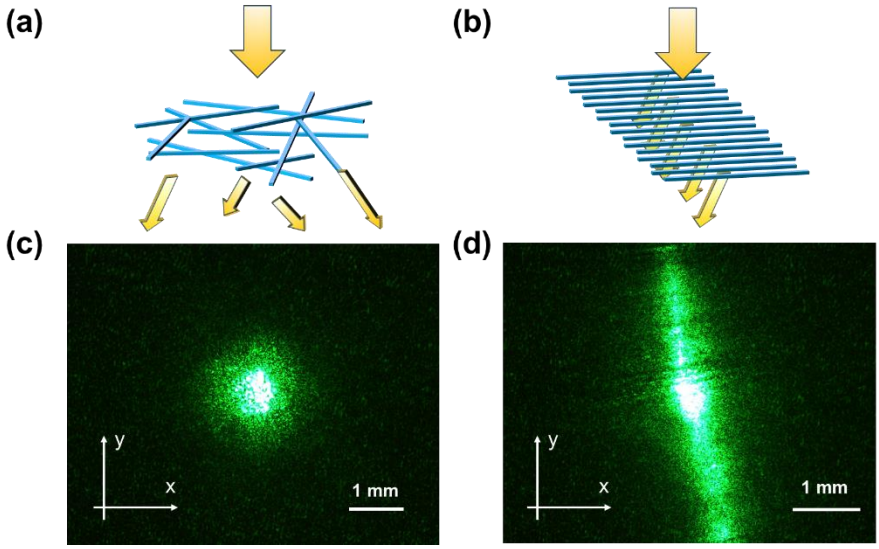

Figure 6-6. Characterization of tunable optical properties of the A-CNF membrane. Illustrations and optimal images showing the light scattering effect of the A-CNF membrane without stretching (0% strain) (a) and (c), as well as with 160% strain (b) and (d), respectively.

surface roughness, with densely packed TEMPO-oxidized CNFs that formed an interlocked and well-ordered topography. The cross-section images along the pre-stretching yz direction (Figure 6-5c) and the perpendicular xz direction (Figure 6-5d) also demonstrated the tightly assembled and

highly aligned CNF structure, with reduced topographical defects. This aligned structure could enhance the mechanical properties of both the membrane and the formed nanochannels between the CNF fibers, contributing to the improved performance. The highly aligned arrangement of the A-CNF membrane induced a light anisotropic scattering effect, which further confirmed the membrane's alignment on a macroscopic length scale. In this experiment, a single-mode laser with an emission wavelength of 532 nm (Thorlabs, Inc.) was used, and its beam was first collimated to an approximate spot size of 200 μm before being perpendicularly illuminated the samples. In the case of the CNF membrane without pre-stretching (0% strain), the highly isotropic distribution of CNF resulted in the divergence of light propagation in both the x and y directions. The generated light spot followed a standard Gaussian distribution, with the full width at half maximum (FWHM) of the transmitted light spot remaining the same in both the x and y directions. On the other hand, for the highly pre-stretched A-CNF membrane (160% strain), the light intensity diverged primarily in the y direction, which is perpendicular to the alignment of CNF in the x direction. This difference in light scattering behavior clearly demonstrated the high level of uniformity and alignment in the fabrication of the A-CNF membrane, even at the millimeter scale.[258] These results confirmed the effectiveness of our "bottom-up" method in producing highly ordered and uniformly distributed membranes with aligned structures.

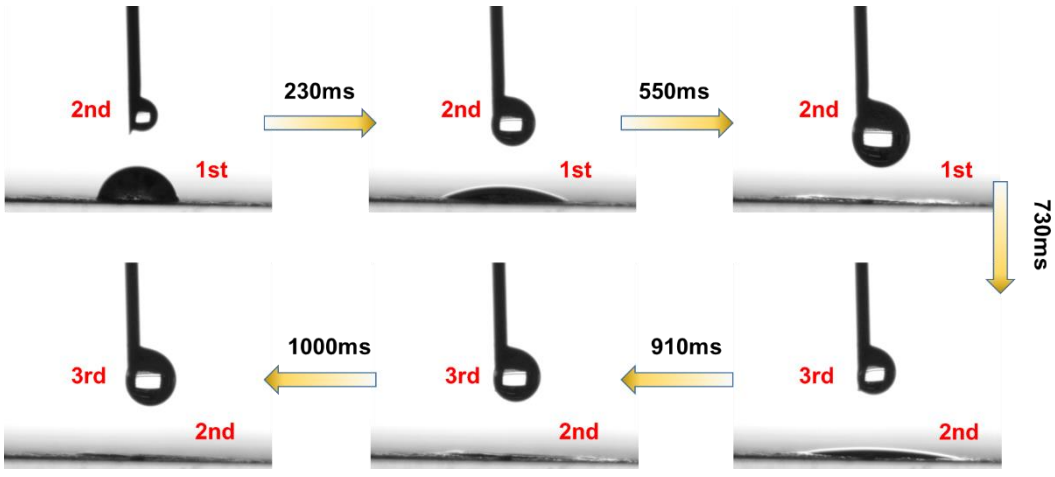

Figure 6-7. The superhydrophilic characteristics of A-CNF membrane.

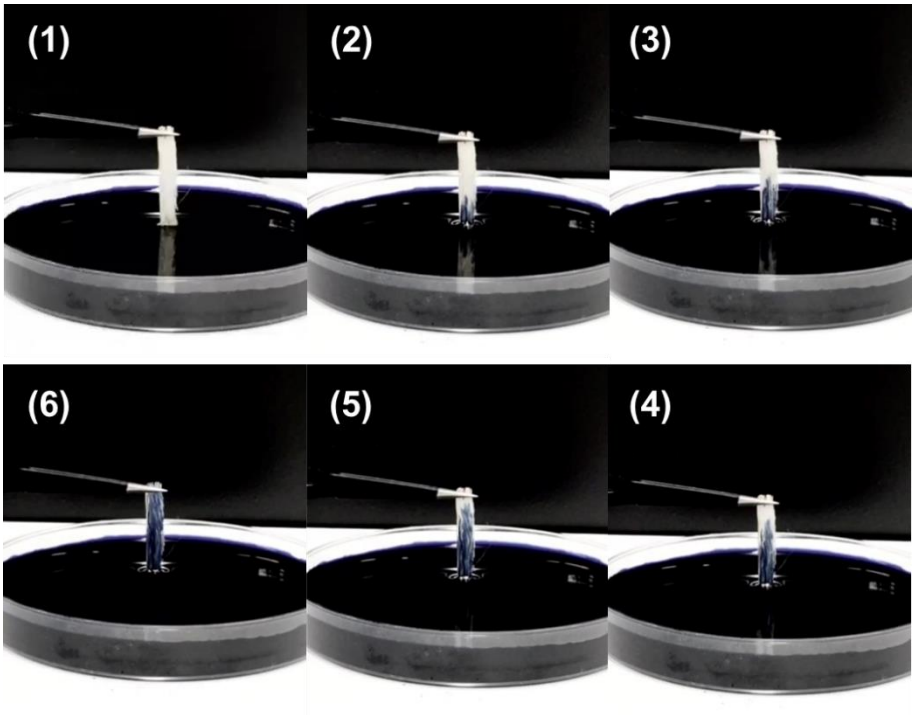

Figure 6-8. Superhydrophilic A-CNF membrane demonstrating directional fluidic transport against the gravity.

The A-CNF membrane exhibited remarkable superhydrophilic characteristics and possessed strong water transport capabilities. In Figure 6-7, it is evident that the first drop of water deposited on the A-CNF membrane's surface was rapidly adsorbed, spreading out within a mere 550 ms. Subsequently, when a second drop (depicted in Figure 6-7 as the 2nd water droplet) was placed on the surface, it spread even faster, being completely transported within nanochannels in just 270 ms. This exceptional water transport efficiency could be primarily attributed to the anisotropic nature and superhydrophilic properties of the A-CNF membrane. Furthermore, this high efficiency in fluidic transport enables the membrane to possess strong water uptake capabilities against gravity. As illustrated in Figure 6-8, one end of a sample measuring 5 cm in length (aligned with the channel direction), 5 mm in width, and 2 mm in thickness was immersed into an colored ink solution to examine the liquid uptake. The liquid rapidly ascended and flowed along the A-CNF channel direction. The appearance of color of approximately 2.5 cm above the liquid level (indicated as (4) in Figure 6-8) occurred within 5 seconds, indicating a higher transport velocity of approximately 5 mm/s. This velocity is approximately 10 times higher than that of isotropic cellulose-based membranes. The complete saturation of the membrane took approximately 15 seconds, suggesting

a water transport velocity of around 3.3 mm/s.

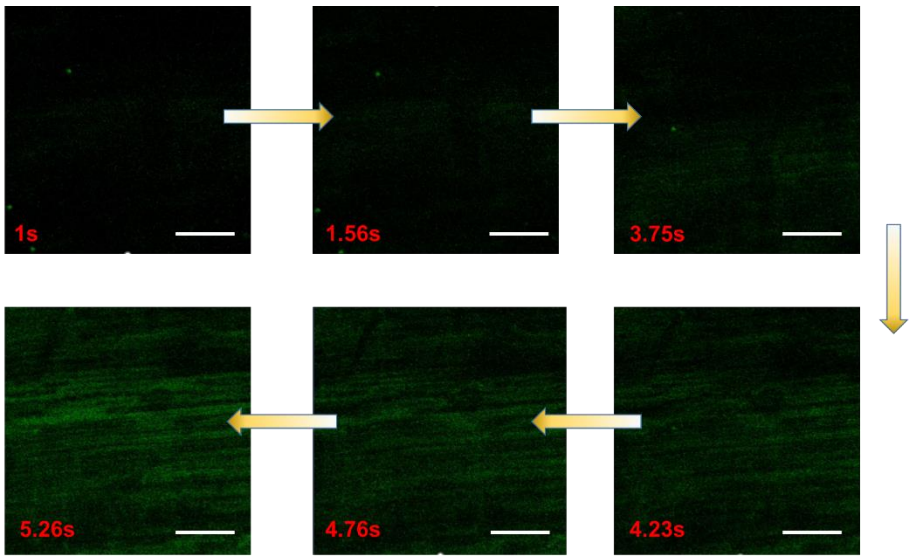

Figure 6-9. The water transport behavior inside the nanochannel of A-CNF observed by the time-dependent laser confocal microscopy images. The scale bar is 100μm

In addition to the aforementioned observations, we employed confocal microscopy to further investigate the rapid water transport performance of the nanochannels within the A-CNF membrane. Following the methodology outlined in Chapter 3, we introduced a low-concentration Rhodamine B dye (0.01 wt%) into the water, which allowed us to visualize the water transport without altering its physicochemical properties. By placing a droplet at one end of the A-CNF membrane, we monitored the stained water being transported from one end to the other. Using time-series confocal laser microscopy, we monitored the middle section of the A-CNF membrane and captured the water transport signals. As depicted in Figure 6-9, the colored water gradually filled the nanochannels within the membrane and moved along the direction of the A-CNF membrane. Furthermore, the water transport traces clearly indicated the presence of aligned and distributed nanochannels within the A-CNF membrane. This significant water transport capability stems from the superhydrophilic characteristics of the A-CNF membrane and the strong capillary force generated along the nanochannel direction due to the aligned distribution of CNF.

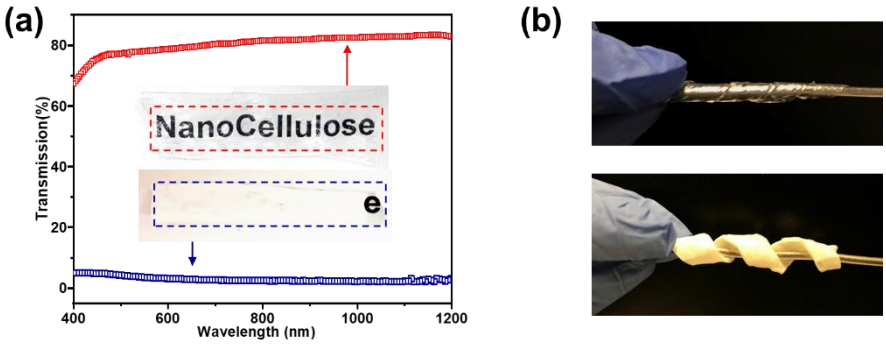

Figure 6-10. (a) The transmittance of the dry and wet A-CNF membrane. (b) Photos of wet and dried A-CNF membrane wrapped around a rod.

The dried A-CNF membranes displayed a white appearance due to the nanosized configuration of CNF. However, upon complete water adsorption, the membranes undergo a transformative change, achieving a broad band transmittance exceeding 68%. This transformation permitted for the previously hidden text beneath the A-CNF membrane to become visible as illustrated in the inset of Figure 6-10a. The transparency of the wet A-CNF membrane demonstrated its potential for applications requiring optical changes at different water uptake levels. In addition to their optical properties, both the dry and wet A-CNF membranes possessed remarkable flexibility, as demonstrated in Figure 6-10b. The membranes could be wrapped around a rod without cracking, water extrusion, or structural breakage. This exceptional flexibility highlighted the superior mechanical stability of the A-CNF membrane and the integrity of its internal nanochannels, which were attributed to the double cross-linked structure. The membranes' ability to withstand deformation without compromising their structural integrity further demonstrated their suitability for a wide range of applications.

6.3.3 The ion transport behavior of A-CNF membrane

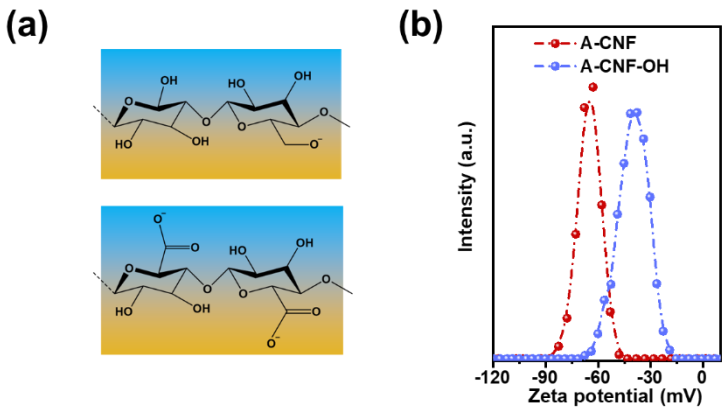

Figure 6-11. (a) Illustration of the differences in surface functional groups between hydroxylated A-CNF-OH and carboxylated A-CNF. (b) The zeta potential of A-CNF and A-CNF-OH under neutral pH at a concentration of approximately 0.1%.

The anisotropic characteristics of A-CNF, along with its well-oriented and designed internal nanochannels, contributed to its outstanding water transport capability and potential for fast ion transport. The mild TEMPO oxidation process introduced carboxyl functional groups to the surface of CNF, which could dissociate into negatively charged carboxylates, resulting in higher surface charge capacity compared to pristine CNF. Figure 6-11a illustrates the higher surface charge capacity of carboxylate-functionalized A-CNF (-62 mV) compared to A-CNF-OH (-37 mV), indicating an enhanced charge capacity of the system.

To evaluate the ion conductance of the membranes, a home-made electrochemical measurement chamber described in Figure 5-6 in Chapter 5 was used. A piece of A-CNF membrane was mounted between two reservoirs containing KCl as the electrolyte. Before testing, the A-CNF membrane was soaked in water for 24 hours to ensure that the nanochannels were opened. The ionic conductance in KCl solution was measured for A-CNF, A-CNF-OH, and an isotropic cellulose membrane, as shown in Figure 6-12a. When the electrolyte concentration was greater than 1 mM, the ion transport followed omnic behavior in all three samples, with the ionic conductance decreasing with electrolyte concentration. However, the ionic conductance of A-CNF and A-CNF-OH membranes approached a plateau when the electrolyte concentration decreased to below 10^{-3} M, which was orders of

magnitude higher than that of the isotropic cellulose membrane. This behavior could be attributed to the nanoconfined effect, where the electrostatic double layer (EDL) covered the entire nanochannel, and the surface charge dominated the ion transport behavior. A-CNF achieved a very high ionic conductance of approximately 2.35 mS cm^{-2}, compared to 1.38 mS cm^{-2} for A-CNF-OH, demonstrating the effectiveness of negatively charged carboxylate functional groups for ion transport. To further demonstrate this, the surface charge capacity of membrane was evaluated via the surface zeta potential (ζ) as shown in Eq. (6-1),[259]

$$\sigma = \frac{\varepsilon\,\varepsilon_0 \zeta}{\lambda_d} \tag{6-1}$$

where σ is the surface charge capacity, ε and ε_o refers to the dielectric constant and the permittivity of vacuum, respectively. The λ_d is the Debye length in electrolyte. The surface charge capacity of A-CNF was calculated to be approximately -4.73 mC m^{-2}, which is higher than the surface charge capacity of A-CNF-OH, which is approximately -3.28 mC m^{-2}. Additionally, the ionic conductance in different concentrations of KCl solution (c) was fitted using equation 6-2 to estimate the theoretical size of the nanochannels.[260]

$$\kappa = Ze(\mu_{cation} + \mu_{-})CN_A + 2\sigma\mu_{cation}h \tag{6-2}$$

where Z is the cation valence, μ_{cation} and μ_{-} refer to the cation and anion mobility, C represents the ion concentration in electrolyte, N_A is the Avogadro's number and h is the estimated diameter of channel in nanofluidic system. At low concentration, the first term of bulk behavior in Eq. (6-2) was negligible and only related to the net surface charge σ and the cation mobility inside the nanochannel. The dash line in Figure 6-12a, obtained from equation 6-2, fitted well to the experimental data, and the theoretical diameter of the A-CNF nanochannels was estimated to be about 2.15 nm, which agreed with the high-resolution AFM image shown in Figure 6-12c. A-CNF-OH exhibited a relatively smaller diameter of nanochannels, which might be attributed to the lower charge capacity and the smaller expansion of -OH functional groups in the nanochannels. Furthermore, another A-CNF sample prepared via freeze-drying instead of air-drying was also examined (referred to as A-CNF-FD). As shown in Figure 6-12b, the freeze-dried A-CNF-FD exhibited a similar charge capacity to A-CNF but a significantly lower ionic conductivity plateau. The fit of the A-CNF-FD membrane conductivity results indicated a channel diameter of approximately 13.38 nm, which was almost 7 times larger than that of the air-dried A-CNF

membrane.

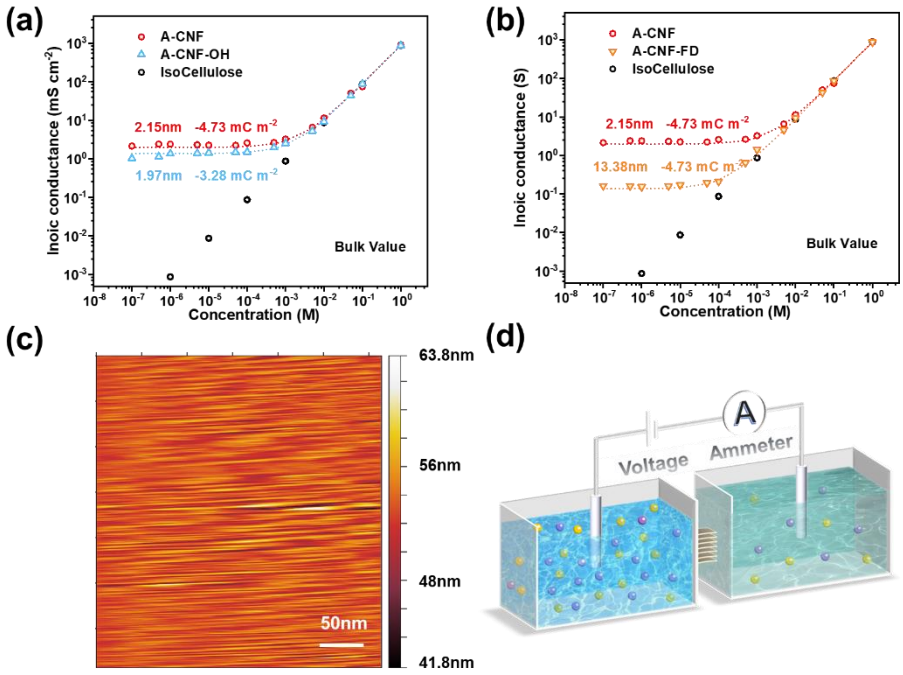

Figure 6-12. Ion conductance measurement in KCl electrolyte for the membrane between (a) A-CNF and A-CNF-OH, and (b) A-CNF and A-CNF-Freeze dried samples, respectively. (c) High resolution AFM image of anisotropic CNF membranes. (d) Home-made electrochemical cell for I-V testing.

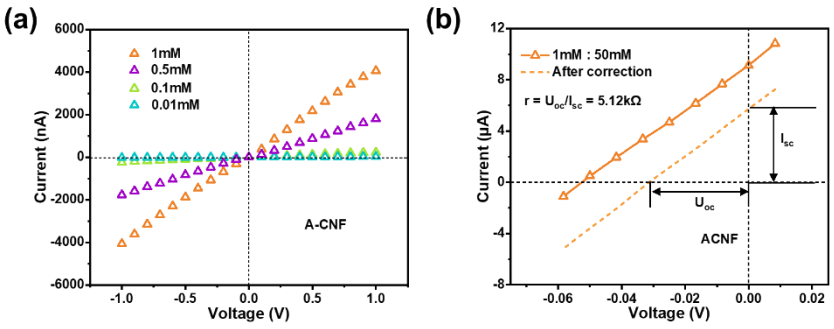

Figure 6-13. The current-voltage (I-V) curves of A-CNF membrane in KCl electrolyte at different concentrations. (b) Measurement of current-voltage (I-V) curve for A-CNF membrane recorded in 50-fold salinity gradient. The low concentration side was set to 1 mM.

The ion transport measurements were conducted to evaluate the nanofluidic performance of the A-

CNF membrane. In Figure 6-13, the I-V curves of A-CNF at different concentrations ranging from 1 mM to 0.001 mM demonstrated that all the curves followed the omnic behavior, where the current is proportional to the voltage applied across the membrane. No rectifying or polarization behavior was observed at different electrolyte concentrations, indicating the symmetry, regularity, and homogeneity of the nanochannel structure and the surface charge-controlled ion transport behavior. Selective ion transport behavior was then evaluated under a 50-fold salt concentration gradient between two electrochemical reservoirs (1 mM and 50 mM). In this measurement, the cation (K^+ in this case) automatically travelled through the membrane from the high concentration to the low concentration side due to osmosis forces, and the generated electricity was harvested by electrodes. The unequal chloride concentration led to the redox reaction on the electrode, resulting in a higher open-circuit voltage (U_{oc}) and short-circuit current (I_{sc}). By subtracting a blank test using a non-selective Polyethersulfone (PES) membrane, the U_{oc} was determined to be 30 mV and I_{sc} was approximately 5.85 μA. These values indicated an extremely low internal resistance of about 5.12 kΩ, which confirmed the superior ion transport capability of the A-CNF membrane in the presence of an ion concentration gradient.

Table 6-1. The electrophoretic mobility of different type of ion and the relative mobility compared to K^+.

Type of Ion	Electrophoretic Mobility [10^{-4} (cm s^{-1})/(V cm^{-1})]	Relative mobility
K^+	7.62	1
Li^+	4.01	0.53
Na^+	5.19	0.68
Ca^+	6.17	0.81
Mg^+	5.50	0.72
Cl^-	7.92	1.04

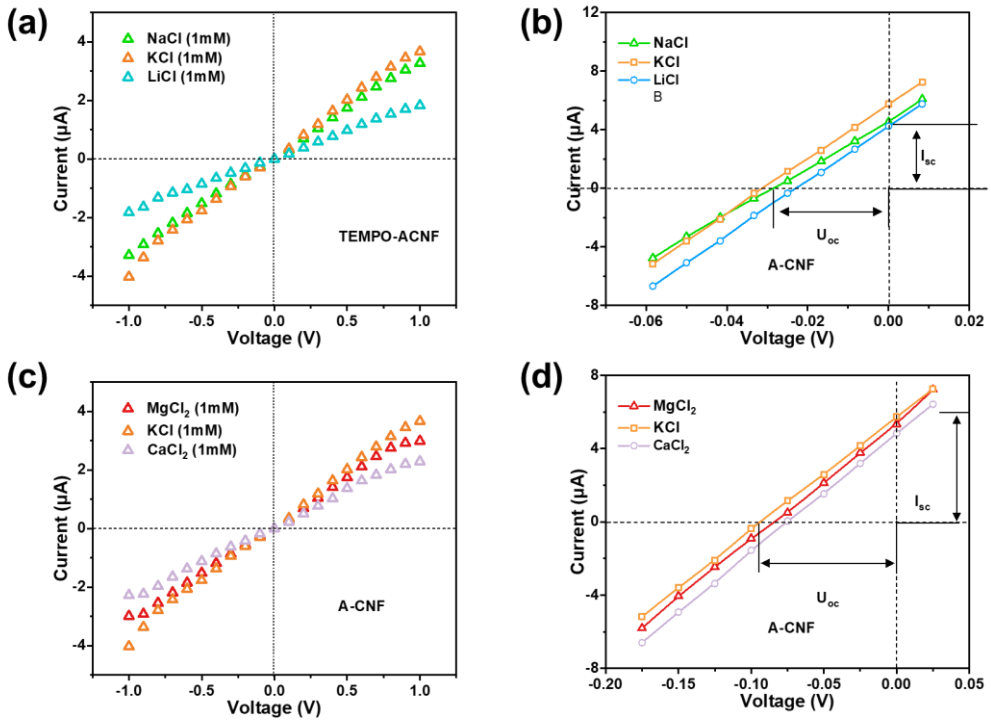

Figure 6-14. The I-V curves of A-CNF membrane recorded in different types of electrolyte, including KCl, NaCl and LiCl. (b) Measurement of current-voltage (I-V) curves for A-CNF membrane recorded in 50-fold salinity gradient in three types of electrolyte. The low concentration side was set to 1 mM.

The prepared A-CNF membrane could also be utilized in other electrolyte systems for selective ion transport. As shown in Table 6-1, with reference to K^+, the transport of Li^+ and Na^+ ions inside the nanochannel was more challenging due to their lower diffusion efficiency and electrophoretic mobility. However, as depicted in Figure 6-14a, both Li^+ and Na^+ ions could be effectively transported inside the nanochannel, and their ion transport behavior aligned well with that of K^+ ions. Besides, the internal resistance in these two electrolytes was also evaluated, as shown in Figure 6-14b. The values were found to be 5.34 kΩ for Li^+ and 6.15 kΩ for Na^+ which was slightly higher than K^+, and this could be attributed to the larger hydrated ionic radius of Na^+ and Li^+, which increased the hindrance of ion transport inside the nanochannel.

In addition to monovalent ions, the A-CNF membrane was also capable of selectively transporting multivalent ions with larger hydrated radii, such as Ca^{2+} and Mg^{2+}. As shown in Figure 6-14c, at low voltage regions, the electrochemical behavior was consistent with that of monovalent ions.

However, a slight polarization was observed at high voltages (±1 V), indicating the kinetic limitation of multivalent ion transport at high voltages. The U_{oc} and I_{sc} for Ca^{2+} and Mg^{2+} were also evaluated. Although these ions were more difficult to transport inside the nanochannel, their higher intrinsic charge led to higher short-circuit currents during ion transport. It's worth mentioning that multivalent ions normally have difficulty passing through nanochannels due to the strong intermolecular interactions between the ions and the walls of the nanochannels. However, in our A-CNF membrane-based nanochannels, the functional groups form hydrogen bonds with water molecules, generating a hydration layer around the functional groups. This reduced the intermolecular force between the ions and nanochannel walls while increasing the charge interaction with the functional groups. Under the influence of external forces such as applied voltage or osmotic forces, ions could hop from one negatively charged functional group (carboxylate in A-CNF membrane) to another through a process known as "Grotthuss hopping", achieving the rapid and selectively ion transport behavior.

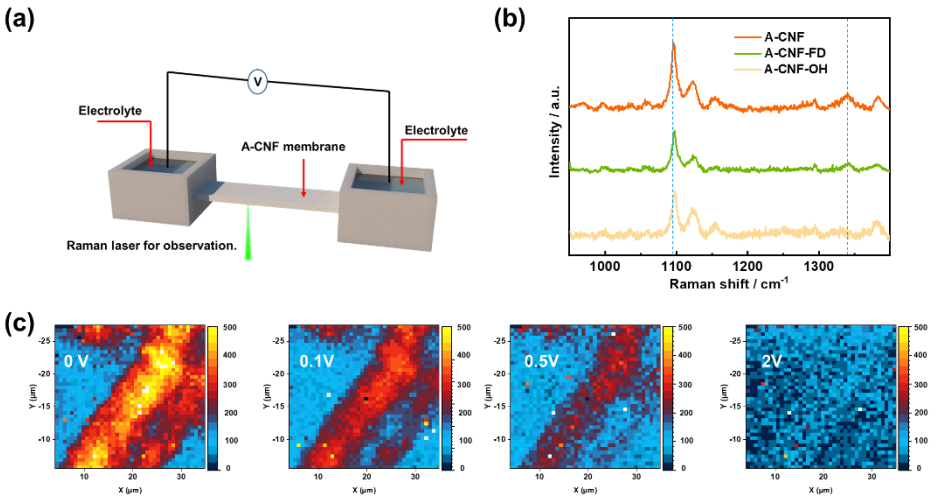

Figure 6-15. (a) The illustration of in-situ Raman observation device for ion transport in A-CNF membrane. (b) The Raman spectrum measurement for A-CNF, A-CNF-FD and A-CNF-OH membrane. (c) The 2D Raman image obtained by in-situ analyzing changes in the carboxyl signal intensity, showing the incorporation between the K^+ and A-CNF membrane.

The strong interaction between the cations and carboxylate groups on the surface of A-CNF could be monitored using in-situ Raman mapping. Initially, the Raman spectra were obtained for three samples: A-CNF, A-CNF-FD, and A-CNF-OH. As shown in Figure 6-14b, the peak at 1100 cm^{-1}

corresponded to the glycosidic bond of cellulose nanofibers, which was present in all three samples, indicating that the molecular chain did not change after the structural reorganization. The peak around 1335 cm^{-1} could be attributed to the carboxylate groups on the membrane's surface, which were present in A-CNF and A-CNF-FD due to the pre-TEMPO oxidation process before membrane construction but was absent in A-CNF-OH.

To investigate the incorporation of the cations between carboxyl groups, a bundle of TEMPO-oxidized CNFs was subjected to 2D Raman mapping that monitored the signal intensity variation of the carboxylate groups. The measurement setup is illustrated in Figure 6-15a, where the nanofluidic membrane was mounted between two reservoirs containing the same type of electrolyte but with different concentrations (at very low concentrations, 10^{-4} M/10^{-5} M, when the electrostatic double layer covers the entire nanochannel). To increase the ion flux inside the nanochannel, an external potential was applied to induce a higher flux of cations to enter the nanochannel while excluding anions due to the membrane's selectivity. As shown in Figure 6-15c, when no voltage was applied between the two electrolyte reservoirs, the morphology of the CNF bundle could be clearly observed by monitoring the signals of the carboxyl groups. This is because the extremely low concentration of K^+ ions did not occupy all the negatively charged functional groups inside the nanochannel. However, the signal intensity gradually decreased when a voltage of 0.1 V was applied, indicating a higher flux of cations entering the nanochannel and occupying more carboxylate regions for transport. The signal intensity decreased further when a voltage of 0.5 V was applied and eventually disappeared at a high voltage around 2 V, indicating that all the carboxyl groups participated with cations for transport. However, it is important to note that while the Raman mapping demonstrated the incorporation of negatively charged functional groups and cations during ion transport, the actual movement of ions needed to be further demonstrated through model simulations and density functional theory (DFT) calculations to confirm the detailed ion transport behavior inside the charged nanochannel.

6.3.4 The osmotic energy harvesting of A-CNF membrane

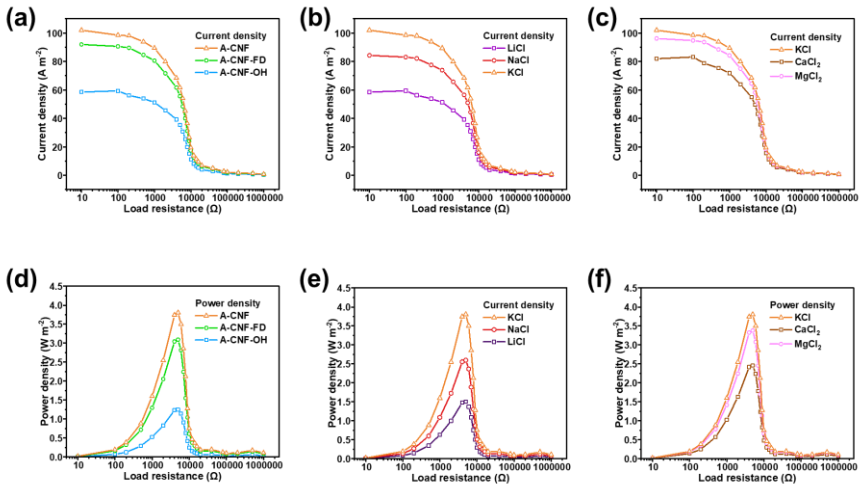

Figure 6-16. Current density (a) and output power density (d) of A-CNF, A-CNF-FD and A-CNF-OH based reverse electrochemical dialysis system as function of load resistance under the placement of electrolyte solution (artificial sea water and river water, 0.5M/0.01M KCl electrolyte) in the central cell. (b) and (c) Current density measurement of A-CNF membrane under different electrolyte systems. (e) and (f) The output power density of A-CNF membrane under different electrolyte systems.

The osmotic energy conversion performance of the A-CNF membrane was evaluated by applying a concentration gradient across the membrane. The concentration gradient generated a net flow of cations across the membrane, resulting in the diffusion current and voltage. The three samples, A-CNF, A-CNF-FD, and A-CNF-OH, were initially evaluated in a 50-fold gradient KCl electrolyte solution (0.5 M and 0.01 M KCl), and an external resistance was connected to the system to measure the output current density and power density. As shown in Figure 6-16a and d, A-CNF exhibited the highest diffusion current density that gradually decreased with increasing external resistance. The calculated power density reached 3.95 W/m^2 with a very low internal resistance of around 5.3 kΩ, close to the theoretically calculated internal resistance based on the open-circuit voltage and short-circuit current. It is worth noting that A-CNF-FD possessed a relatively lower output power density of approximately 3.09 W/m^2. This is because A-CNF-FD possessed larger nanochannels, and the increased spacing between the charged cellulose chains reduced the selectivity of the nanochannel. As a result, a higher concentration of anions entered the nanochannel, generating a reverse diffusion

current resulting in a reduced power density output. In contrast, A-CNF-OH exhibited the lowest power density of about 1.23 W/m^2. Although this membrane possessed a similar nanochannel diameter as A-CNF, the poor performance was attributed to the lower content of negatively charged functional groups. This resulted in lower charge density and capacity of the nanochannel system, reducing the ion flux inside the nanochannel that yielded a lower power density. This demonstrated that both high charge density and the geometry of the nanochannel are important for selective ion transport. The energy conversion behaviors of the A-CNF membrane with various electrolytes were also separately tested. As shown in Figure 6-16b and e, the lower diffusion coefficient and electrophoretic mobility of Na^+ and Li^+ resulted in a lower current density and power density, which is a typical behavior of cation-selective membranes. Additionally, the system exhibited considerable power output for divalent ions such as Ca^{2+} and Mg^{2+}, which is different from traditional ion exchange membrane-based reverse electrodialysis systems, where the negative effects of divalent ions, such as uphill transport, chelation, and electrostatic loading, largely weakened the power output. It is worth mentioning that although these divalent ions have lower diffusion coefficients, the obtained power density was higher than that in the electrolytes containing Li^+ and Na^+ due to their stronger electrostatic interactions due to their larger intrinsic charge. This successful utilization of A-CNF in divalent ion transport demonstrated the membrane's potential for real-world applications, considering the diverse types of salts that coexist in seawater environments.

6.4 Conclusions

In conclusion, we have successfully developed a “bottom-up” process to fabricate nanofluidic membrane based on oxidized cellulose nanofibers (A-CNF) that displayed excellent water transport and selective ion transport performance. Through ion transport measurements and osmotic based concentration gradient experiments, we verified the membrane's ability to selectively transport monovalent and divalent ions, generating significant diffusion currents and voltages under high concentration gradients. In-situ Raman mapping further confirmed the strong interaction between the carboxylate groups on the A-CNF membrane surface and cations, supporting the mechanism of selective ion transport. The A-CNF membrane displayed low internal resistance and high flux for diverse types of ions, making it a promising material for energy conversion applications in the real-world sea water and river water. Under concentration gradient conditions, the membrane achieved

substantial osmotic energy conversion, yielding high power densities of approximately 3.92W m^{-2}.

Chapter 7 Conclusions and recommendation for future studies

7.1 Conclusions

In this thesis, sustainable materials, such as cellulose nanocrystal, cellulose nanofiber and plant pollens were functionalized and formulated with other materials or structurally re-organized to construct surfaces with special wettability and functionalities. These superwettable surfaces have been successfully used in the areas of environment and energy, including non-loss water transport, oil/water emulsion separation, selectivity ion transport and osmotic energy harvesting. In **chapter 3**, we investigated the utilization of cellulose nanocrystals (CNC) functionalized with positively charged functional groups as an emulsifier for preparing wax-in-water Pickering emulsions and superhydrophobic surface with tunable adhesive force. The size, surface charge, and morphology of the CNC-GTMAC particles were characterized after the functionalization process. Besides, the interfacial properties of the wax-water interface, including interfacial tension and surface coverage, were evaluated. The prepared Pickering emulsions, containing CNC-GTMAC particles of different sizes, were utilized to construct superhydrophobic surfaces with tunable adhesive forces towards water droplets. Through various techniques such as contact angle, contact angle hysteresis, and sliding angle measurements, we successfully demonstrated the construction of these surfaces with adjustable adhesive properties, ranging from extremely low adhesion (5.7 μN) to high adhesion (79 μN). Additionally, two-dimensional adhesive force measurements further confirmed the homogeneity of the surface, ensuring consistent adhesive behavior across the sample. Finally, as a demonstration of the potential applications of these special superhydrophobic surfaces, we utilized a non-loss micro droplet transportation method, showcasing one of the future directions for these surfaces. These findings highlight the ability to tailor the adhesive properties of superhydrophobic surfaces through the manipulation of emulsion particle size, opening up possibilities for various applications where controlled adhesion to water droplets is desired.

Besides the surperhydrophobic surface, a new type of under liquid dual superlyophobic surface was constructed and investigated in **Chapter 4** by incorporating the superhydrophilic CNF and superhydrophobic plant pollens that offers unique applications in various field involving multiphase fluids. The hierarchical 3D topography of the treated pollen provided the rough structure, which could generate superhydrophobicity in air by grafting hydrophobic materials onto its surface. The

CNF, on the other hand, introduced surface hydrophilicity and facilitated the construction of compact membranes due to the presence of hydroxyl and carboxyl groups. By combining superhydrophilic CNF and superhydrophobic ODA.SES particles, we were able to tune the wettability and surface free energy of the composite membranes over a wide range, from highly hydrophobic to superhydrophilic in air. Morphological and contact angle analyses revealed that increasing the CNF content enhanced the water affinity of the system both in air, water, and oil environments. Besides, the hierarchical structure provided by the superhydrophobic ODA.SES particles effectively trapped water or oil for creating "liquid cushion" for superlyophobicity, depending on the environment. The model analysis energy analysis and experiments demonstrated that the propel surface free energy (56 to 40 mJ m^{-2}) tuning would let the surface maintain a meta-stable oil-water-solid interface, letting the overall system is favorable to these two contradictory wetting states (noted as under water superoleophobicity and under oil superhydrophobicity in this part). Also, an emulsion separation experiment demonstrates the importance of this kind of underliquid superlyophobic surface for the future multiphase fluid applications such as soild-oil-water systems, such as the oil recovery, particle phase transfer and liquid–liquid interface assembly. The intercalation of highly hydrophilic CNC into the hydrophobic GO system would increase the water affinity of system, creating the potential applications of selective ion transport and "blue energy harvesting". In **chapter 5**, we intercalated the charged CNC into oppositely charged graphene oxide system, successful making the hydrophilic NCNC/GO and PCNC/pGO. the oppositely charged 2D CNC intercalated GO membranes were constructed via a facile vacuum-assisted assembly process to harvest osmotic energy from nature. The introduction of small amounts (6%wt) of 1D CNC nanorod into GO lamellar could significantly enhance the structural and mechanical stability, achieving a high ultimate strength up to 272 and 309 MPa for NCNC/GO and PCNC/pGO, respectively, thus satisfying the requirements for practical application. Additionally, due to the special geometry and morphology of CNC nanorod, it could also expand the interlayer spacing of 2D nanosheet for faster ion transport without generating extra transmembrane resistance and physical hinderance. Due to the chemical flexibility of CNC, its surface charge could be easily tuned with either negative or positive by modifying it with charged polymer. The NCNC and PCNC with high charge density could introduce space charge inside the 2D nanochannel. Combined with the surface charge of GO and pGO, they could synergistically improve the energy conversion

performance. In this study, the composite membranes of ChCNC/GO produced a power density of 4.73 W m^{-2} under 50-fold salinity gradient, which was very close to the standard commercialization benchmark (5 W m^{-2}).

Additionally, the superhydrophilic membrane was constructed to further enhance the water conduction performance and selective ion transport capability. In **Chapter 6**, we successfully developed a “bottom-up” method for the fabrication of nanofluidic membrane based on oxidized cellulose nanofibers (A-CNF) that exhibited excellent water transport and selective ion transport performance. Through ion transport measurements and osmotic based concentration gradient experiments, we verified the membrane's ability to selectively transport monovalent and divalent ions, generating significant diffusion currents and voltages under high concentration gradients. In-situ Raman mapping further confirmed the strong interaction between the carboxylate groups on the A-CNF membrane surface and cations, supporting the mechanism of selective ion transport. The A-CNF membrane demonstrated low internal resistance and high flux for diverse types of ions, making it a promising material for energy conversion applications in the real-world sea water and river water. Under concentration gradient conditions, the membrane achieved substantial osmotic energy conversion, yielding high power densities approximately 3.92 W m^{-2}.

In this thesis, sustainable materials were used to prepare surfaces with special wettability and functionality. The research goes beyond the traditional characteristics of superwettable surfaces by introducing novel capabilities to manipulate water behavior, opening up advanced applications: (i) the superhydrophobic surface not only resists water but also allows for controllable adhesion to droplets, achieved through topography regulation and surface functionality using modified CNC. (ii) Secondly, the combination of materials with contradictory wettability resulted in a new type of superlyophobic surface. By finely tuning the surface free energy, this surface exhibited both superhydrophobicity under oil and superoleophobicity under water simultaneously, offering opportunities for future multiphase fluid applications. (iii) incorporating sustainable materials into existing fluidic systems enhanced their wettability and functionality, leading to improved performance. For example, the CNC/GO membrane pair with high hydrophilicity and charge capacity could effectively harvest osmotic energy. (iv) a facile "bottom-up" method reorganized the structure of sustainable materials, significantly enhancing their water manipulation performances. The resulting membrane demonstrated superhydrophilic and superspreading characteristics, making

it suitable for selective ion transport and "blue energy" harvesting.

7.2 Future recommendations

Based on the studies conducted in this thesis, the following recommendations are proposed for future work:

(1) Advanced modification of sustainable materials: While this thesis focuses on surface charge modification and surface hydrophilicity manipulation of sustainable materials, there is a need for further exploration of additional modifications. This can involve membrane polymer coating, responsive polymer grafting, and incorporating inorganic materials for broader modifications such as metal particle deposition or coating. By introducing various functional materials into the sustainable materials system, the inherent merits and structural advantages can be further expanded and utilized for future applications.

(2) Construction of new types of superwettable surfaces: Although this thesis introduces a special superwettable surface with unique water manipulation abilities, there are still numerous other types of surfaces that are not fully understood and controlled in their construction. Some of the examples include anti-icing surfaces, blood repellent surfaces, liquid-infused slippery surfaces, super-spreading surfaces, and directional transport surfaces. The use of sustainable materials derived from nature provides opportunities for the fabrication of these new types of superwettable surfaces.

(3) Advanced application utilization: Gaining a deeper understanding on the mechanisms underlying superwettable surfaces can facilitate their integration into current real-world applications, thereby improving their performance, stability, and longevity. For example, understanding the wettability and interfacial phenomena can aid in designing catalysts with better interaction with electrolytes, thereby increasing their performance. The discovery of new water/oil wetting behavior can facilitate the creation of superwettable membranes for improved separation technologies.

By pursuing these recommendations, future research can advance the field of superwettable surfaces, leading to enhanced utilization of sustainable materials, proposing novel surface functionalities, and expanded their applications in various domains.

Letters of Copyright Permissions

License Details

This Agreement between Mr. weinan zhao ("You") and John Wiley and Sons ("John Wiley and Sons") consists of your license details and the terms and conditions provided by John Wiley and Sons and Copyright Clearance Center.

Print Copy

License Number	5573741510428
License date	Jun 21, 2023
Licensed Content Publisher	John Wiley and Sons
Licensed Content Publication	Chemistry - A European Journal
Licensed Content Title	Frontispiece: Surface Modification, Topographic Design and Applications of Superhydrophobic Systems
Licensed Content Author	Weinan Zhao, Yi Wang, Mei Han, et al
Licensed Content Date	Dec 8, 2022
Licensed Content Volume	28
Licensed Content Issue	68
Licensed Content Pages	1

ELSEVIER

Osmotic energy generation with mechanically robust and oppositely charged cellulose nanocrystal intercalating GO membranes

Author: Weinan Zhao,Yi Wang,Mei Han,Jiaxin Xu,Lian Han,Kam Chiu Tam
Publication: Nano Energy
Publisher: Elsevier
Date: July 2022

Journal Author Rights

Please note that, as the author of this Elsevier article, you retain the right to include it in a thesis or dissertation, provided it is not published commercially. Permission is not required, but please ensure that you reference the journal as the original source. For more information on this and on your other retained rights, please visit: https://www.elsevier.com/about/our-business/policies/copyright#Author-rights

Sustainable Superhydrophobic Surface with Tunable Nanoscale Hydrophilicity for Water Harvesting Applications

Author: Yi Wang, Weinan Zhao, Mei Han, et al
Publication: Angewandte Chemie International Edition
Publisher: John Wiley and Sons
Date: Jan 14, 2022

Review Order

Please review the order details and the associated terms and conditions.

No royalties will be charged for this reuse request although you are required to obtain a license and comply with the license terms and conditions. To obtain the license, click the Accept button below.

Superhydrophobic surfaces from sustainable colloidal systems

Author: Yi Wang,Weinan Zhao,Lian Han,Kam Chiu Tam
Publication: Current Opinion in Colloid & Interface Science
Publisher: Elsevier
Date: February 2022

Journal Author Rights

Please note that, as the author of this Elsevier article, you retain the right to include it in a thesis or dissertation, provided it is not published commercially. Permission is not required, but please ensure that you reference the journal as the original source. For more information on this and on your other retained rights, please visit: https://www.elsevier.com/about/our-business/policies/copyright#Author-rights

References

[1] K. Liu, X. Yao, L. Jiang, Recent developments in bio-inspired special wettability, Chemical Society Reviews 39 (8) (2010) 3240-3255.

[2] N.K. Adam, Use of the Term ‘Young's Equation’ for Contact Angles, Nature 180 (4590) (1957) 809-810.

[3] Y. Si, Z. Dong, L. Jiang, Bioinspired Designs of Superhydrophobic and Superhydrophilic Materials, ACS Central Science 4 (9) (2018) 1102-1112.

[4] A. Chunder, K. Etcheverry, G. Londe, H.J. Cho, L. Zhai, Conformal switchable superhydrophobic/hydrophilic surfaces for microscale flow control, Colloids and Surfaces A: Physicochemical and Engineering Aspects 333 (1) (2009) 187-193.

[5] X. Tian, V. Jokinen, J. Li, J. Sainio, R.H.A. Ras, Unusual Dual Superlyophobic Surfaces in Oil–Water Systems: The Design Principles, Advanced Materials 28 (48) (2016) 10652-10658.

[6] D. Chen, J. Li, J. Zhao, J. Guo, S. Zhang, T.A. Sherazi, Ambreen, S. Li, Bioinspired superhydrophilic-hydrophobic integrated surface with conical pattern-shape for self-driven fog collection, Journal of Colloid and Interface Science 530 (2018) 274-281.

[7] S. Zhang, J. Huang, Z. Chen, Y. Lai, Bioinspired Special Wettability Surfaces: From Fundamental Research to Water Harvesting Applications, Small 13 (3) (2017) 1602992.

[8] M. Nosonovsky, B. Bhushan, Superhydrophobic surfaces and emerging applications: Non-adhesion, energy, green engineering, Current Opinion in Colloid & Interface Science 14 (4) (2009) 270-280.

[9] Y. Wang, W. Zhao, L. Han, K.C. Tam, Superhydrophobic surfaces from sustainable colloidal systems, Current Opinion in Colloid & Interface Science 57 (2022) 101534.

[10] E.S. Ferreira, C.A. Rezende, E.D. Cranston, Fundamentals of cellulose lightweight materials: bio-based assemblies with tailored properties, Green Chemistry 23 (10) (2021) 3542-3568.

[11] F. Rol, M.N. Belgacem, A. Gandini, J. Bras, Recent advances in surface-modified cellulose nanofibrils, Progress in Polymer Science 88 (2019) 241-264.

[12] T.-F. Fan, S. Park, Q. Shi, X. Zhang, Q. Liu, Y. Song, H. Chin, M.S.B. Ibrahim, N. Mokrzecka, Y. Yang, H. Li, J. Song, S. Suresh, N.-J. Cho, Transformation of hard pollen into soft matter, Nature Communications 11 (1) (2020) 1449.

[13] R.S.S. Raja, P. Selvakumar, P.D. Babu, B.J. Rubasingh, K. Suresh, Influence of laser parameters on superhydrophobicity- A review, Engineering Research Express 3 (2) (2021) 022001.

[14] W. Miao, Y. Tian, L. Jiang, Bioinspired Superspreading Surface: From Essential Mechanism to Application, Accounts of Chemical Research 55 (11) (2022) 1467-1479.

[15] Y. Wang, W. Zhao, M. Han, J. Xu, X. Zhou, W. Luu, L. Han, K.C. Tam, Topographical Design and Thermal-Induced Organization of Interfacial Water Structure to Regulate the Wetting State of Surfaces, JACS Au 2 (9) (2022) 1989-2000.

[16] T. Nishino, M. Meguro, K. Nakamae, M. Matsushita, Y. Ueda, The Lowest Surface Free Energy Based on −CF3 Alignment, Langmuir 15 (13) (1999) 4321-4323.

[17] G.E. Fogg, Diurnal Fluctuation in a Physical Property of Leaf Cuticle, Nature 154 (3912) (1944) 515-515.

[18] R.N. Wenzel, Resistance of solid surfaces to wetting by water, Industrial & Engineering Chemistry 28 (8) (1936) 988-994.

[19] A.B.D. Cassie, S. Baxter, Wettability of porous surfaces, Transactions of the Faraday Society 40 (0) (1944) 546-551.
[20] R. David, A.W. Neumann, Energy barriers between the Cassie and Wenzel states on random, superhydrophobic surfaces, Colloids and Surfaces A: Physicochemical and Engineering Aspects 425 (2013) 51-58.
[21] T. Huhtamäki, X. Tian, J.T. Korhonen, R.H.A. Ras, Surface-wetting characterization using contact-angle measurements, Nature Protocols 13 (7) (2018) 1521-1538.
[22] C.N.C. Lam, R. Wu, D. Li, M.L. Hair, A.W. Neumann, Study of the advancing and receding contact angles: liquid sorption as a cause of contact angle hysteresis, Advances in Colloid and Interface Science 96 (1) (2002) 169-191.
[23] Y.L. Chen, C.A. Helm, J.N. Israelachvili, Molecular mechanisms associated with adhesion and contact angle hysteresis of monolayer surfaces, The Journal of Physical Chemistry 95 (26) (1991) 10736-10747.
[24] Y. Xiu, L. Zhu, D.W. Hess, C.P. Wong, Relationship between Work of Adhesion and Contact Angle Hysteresis on Superhydrophobic Surfaces, The Journal of Physical Chemistry C 112 (30) (2008) 11403-11407.
[25] K.L. Johnson, Mechanics of adhesion, Tribology International 31 (8) (1998) 413-418.
[26] S.P. Pujari, L. Scheres, A.T.M. Marcelis, H. Zuilhof, Covalent Surface Modification of Oxide Surfaces, Angewandte Chemie International Edition 53 (25) (2014) 6322-6356.
[27] K. Wen, R. Maoz, H. Cohen, J. Sagiv, A. Gibaud, A. Desert, B.M. Ocko, Postassembly Chemical Modification of a Highly Ordered Organosilane Multilayer: New Insights into the Structure, Bonding, and Dynamics of Self-Assembling Silane Monolayers, ACS Nano 2 (3) (2008) 579-599.
[28] D.-M. Yoon, B.-J. Yoon, K.-H. Lee, H.S. Kim, C.G. Park, Synthesis of carbon nanotubes from solid carbon sources by direct microwave irradiation, Carbon 44 (7) (2006) 1339-1343.
[29] L. Zhang, A.G. Zhou, B.R. Sun, K.S. Chen, H.-Z. Yu, Functional and versatile superhydrophobic coatings via stoichiometric silanization, Nature Communications 12 (1) (2021) 982.
[30] D. Wang, Q. Sun, M.J. Hokkanen, C. Zhang, F.-Y. Lin, Q. Liu, S.-P. Zhu, T. Zhou, Q. Chang, B. He, Q. Zhou, L. Chen, Z. Wang, R.H.A. Ras, X. Deng, Design of robust superhydrophobic surfaces, Nature 582 (7810) (2020) 55-59.
[31] S.M.R. Razavi, J. Oh, S. Sett, L. Feng, X. Yan, M.J. Hoque, A. Liu, R.T. Haasch, M. Masoomi, R. Bagheri, N. Miljkovic, Superhydrophobic Surfaces Made from Naturally Derived Hydrophobic Materials, ACS Sustainable Chemistry & Engineering 5 (12) (2017) 11362-11370.
[32] R.M. Hensarling, V.A. Doughty, J.W. Chan, D.L. Patton, "Clicking" Polymer Brushes with Thiol-yne Chemistry: Indoors and Out, Journal of the American Chemical Society 131 (41) (2009) 14673-14675.
[33] W. Feng, L. Li, E. Ueda, J. Li, S. Heißler, A. Welle, O. Trapp, P.A. Levkin, Surface Patterning via Thiol-Yne Click Chemistry: An Extremely Fast and Versatile Approach to Superhydrophilic-Superhydrophobic Micropatterns, Advanced Materials Interfaces 1 (7) (2014) 1400269.
[34] W. Feng, L. Li, C. Yang, A. Welle, O. Trapp, P.A. Levkin, UV-Induced Tetrazole-Thiol Reaction for Polymer Conjugation and Surface Functionalization, Angewandte Chemie International Edition 54 (30) (2015) 8732-8735.
[35] M.E. Buck, D.M. Lynn, Azlactone-functionalized polymers as reactive platforms for the design of advanced materials: Progress in the last ten years, Polymer Chemistry 3 (1) (2012) 66-80.
[36] U. Manna, M.J. Kratochvil, D.M. Lynn, Superhydrophobic Polymer Multilayers that Promote the

Extended, Long-Term Release of Embedded Water-Soluble Agents, Advanced Materials 25 (44) (2013) 6405-6409.
[37] U. Manna, D.M. Lynn, Synthetic Surfaces with Robust and Tunable Underwater Superoleophobicity, Advanced Functional Materials 25 (11) (2015) 1672-1681.
[38] M.E. Buck, S.C. Schwartz, D.M. Lynn, Superhydrophobic Thin Films Fabricated by Reactive Layer-by-Layer Assembly of Azlactone-Functionalized Polymers, Chemistry of Materials 22 (23) (2010) 6319-6327.
[39] M.C.D. Carter, D.M. Lynn, Covalently Crosslinked and Physically Stable Polymer Coatings with Chemically Labile and Dynamic Surface Features Fabricated by Treatment of Azlactone-Containing Multilayers with Alcohol-, Thiol-, and Hydrazine-Based Nucleophiles, Chemistry of Materials 28 (14) (2016) 5063-5072.
[40] A. Shome, A. Das, A. Borbora, M. Dhar, U. Manna, Role of chemistry in bio-inspired liquid wettability, Chemical Society Reviews 51 (13) (2022) 5452-5497.
[41] N. Jana, D. Parbat, U. Manna, Rational Use of Dual Chemical Reactivity in a Single Interface for Optimizing Both Superhydrophobicity and Underwater Superoleophobicity, Chemistry of Materials 31 (5) (2019) 1479-1484.
[42] Y. Li, H. Li, J. Wu, X. Yang, X. Jia, J. Yang, D. Shao, L. Feng, S. Wang, H. Song, One-pot synthesis of superhydrophobic photothermal materials with self-healing for efficient ice removal, Applied Surface Science 600 (2022) 154177.
[43] L.M. Cox, A.M. Martinez, A.K. Blevins, N. Sowan, Y. Ding, C.N. Bowman, Nanoimprint lithography: Emergent materials and methods of actuation, Nano Today 31 (2020) 100838.
[44] C.W. Extrand, Designing for Optimum Liquid Repellency, Langmuir 22 (4) (2006) 1711-1714.
[45] H.J. Butt, D. Vollmer, P. Papadopoulos, Super liquid-repellent layers: The smaller the better, Adv Colloid Interface Sci 222 (2015) 104-109.
[46] J. Song, L. Huang, C. Zhao, S. Wu, H. Liu, Y. Lu, X. Deng, C.J. Carmalt, I.P. Parkin, Y. Sun, Robust Superhydrophobic Conical Pillars from Syringe Needle Shape to Straight Conical Pillar Shape for Droplet Pancake Bouncing, ACS Appl Mater Interfaces 11 (48) (2019) 45345-45353.
[47] Y. Liu, L. Moevius, X. Xu, T. Qian, J.M. Yeomans, Z. Wang, Pancake bouncing on superhydrophobic surfaces, Nature Physics 10 (7) (2014) 515-519.
[48] T.L. Liu, C.J. Kim, Repellent surfaces. Turning a surface superrepellent even to completely wetting liquids, Science 346 (6213) (2014) 1096-1100.
[49] W.E. Teo, S. Ramakrishna, A review on electrospinning design and nanofibre assemblies, Nanotechnology 17 (14) (2006) R89-R106.
[50] L. Jiang, Y. Zhao, J. Zhai, A Lotus-Leaf-like Superhydrophobic Surface: A Porous Microsphere/Nanofiber Composite Film Prepared by Electrohydrodynamics, Angewandte Chemie International Edition 43 (33) (2004) 4338-4341.
[51] M. Kang, R. Jung, H.-S. Kim, H.-J. Jin, Preparation of superhydrophobic polystyrene membranes by electrospinning, Colloids and Surfaces A: Physicochemical and Engineering Aspects 313-314 (2008) 411-414.
[52] L. Zhou, C.L. Li, P.T. Chang, S.H. Tan, A.L. Ahmad, S.C. Low, Intrinsic microspheres structure of electrospun nanofibrous membrane with rational superhydrophobicity for desalination via membrane distillation, Desalination 527 (2022).
[53] Y.C. Woo, M. Yao, W.-G. Shim, Y. Kim, L.D. Tijing, B. Jung, S.-H. Kim, H.K. Shon, Co-axially electrospun superhydrophobic nanofiber membranes with 3D-hierarchically structured surface for

desalination by long-term membrane distillation, Journal of Membrane Science 623 (2021).
[54] J. Zeng, X. Ji, Y. Ma, Z. Zhang, S. Wang, Z. Ren, C. Zhi, J. Yu, 3D Graphene Fibers Grown by Thermal Chemical Vapor Deposition, Adv Mater 30 (12) (2018) e1705380.
[55] F. Zou, G. Li, X. Wang, A.L. Yarin, Dynamic hydrophobicity of superhydrophobic PTFE-SiO2 electrospun fibrous membranes, Journal of Membrane Science 619 (2021).
[56] J. Cai, T. Wang, W. Hao, H. Ling, T. Hang, Y.-W. Chung, M. Li, Fabrication of superamphiphobic Cu surfaces using hierarchical surface morphology and fluorocarbon attachment facilitated by plasma activation, Applied Surface Science 464 (2019) 140-145.
[57] Y. Wu, T. Hang, Z. Yu, L. Xu, M. Li, Lotus leaf-like dual-scale silver film applied as a superhydrophobic and self-cleaning substrate, Chem Commun (Camb) 50 (61) (2014) 8405-8407.
[58] W. Zhang, Z. Yu, Z. Chen, M. Li, Preparation of super-hydrophobic Cu/Ni coating with micro-nano hierarchical structure, Materials Letters 67 (1) (2012) 327-330.
[59] C. Cao, J. Cheng, Fabrication of robust surfaces with special wettability on porous copper substrates for various oil/water separations, Chemical Engineering Journal 347 (2018) 585-594.
[60] S. Xu, Q. Wang, N. Wang, Fabrication of pre-wetting induced superamphiphobic meshes for on-demand oil-water separation of light or heavy oil-water mixtures, Colloids and Surfaces A: Physicochemical and Engineering Aspects 602 (2020).
[61] M. Qu, B. Zhang, S. Song, L. Chen, J. Zhang, X. Cao, Fabrication of Superhydrophobic Surfaces on Engineering Materials by a Solution-Immersion Process, Advanced Functional Materials 17 (4) (2007) 593-596.
[62] X. Yao, Q. Chen, L. Xu, Q. Li, Y. Song, X. Gao, D. Quéré, L. Jiang, Bioinspired Ribbed Nanoneedles with Robust Superhydrophobicity, Advanced Functional Materials 20 (4) (2010) 656-662.
[63] C. Yu, W. Zhang, Y. Gao, D. Ni, J. Ye, C. Zhu, K. Ma, The super-hydrophobic thermite film of the Co3O4/Al core/shell nanowires for an underwater ignition with a favorable aging-resistance, Chemical Engineering Journal 338 (2018) 99-106.
[64] L. Wang, X. Zhang, B. Li, P. Sun, J. Yang, H. Xu, Y. Liu, Superhydrophobic and ultraviolet-blocking cotton textiles, ACS Appl Mater Interfaces 3 (4) (2011) 1277-1281.
[65] X. Zhang, S. Liu, A. Salim, S. Seeger, Hierarchical Structured Multifunctional Self-Cleaning Material with Durable Superhydrophobicity and Photocatalytic Functionalities, Small 15 (34) (2019) e1901822.
[66] Q.F. Xu, J.N. Wang, K.D. Sanderson, Organic−Inorganic Composite Nanocoatings with Superhydrophobicity, Good Transparency, and Thermal Stability, ACS Nano 4 (4) (2010) 2201-2209.
[67] M. Sun, C. Luo, L. Xu, H. Ji, Q. Ouyang, D. Yu, Y. Chen, Artificial Lotus Leaf by Nanocasting, Langmuir 21 (19) (2005) 8978-8981.
[68] R. Fürstner, W. Barthlott, C. Neinhuis, P. Walzel, Wetting and Self-Cleaning Properties of Artificial Superhydrophobic Surfaces, Langmuir 21 (3) (2005) 956-961.
[69] Y. Yang, X. Li, X. Zheng, Z. Chen, Q. Zhou, Y. Chen, 3D-Printed Biomimetic Super-Hydrophobic Structure for Microdroplet Manipulation and Oil/Water Separation, Adv Mater 30 (9) (2018).
[70] H.K. Webb, R.J. Crawford, E.P. Ivanova, Wettability of natural superhydrophobic surfaces, Advances in Colloid and Interface Science 210 (2014) 58-64.
[71] S.G. Lee, H.S. Lim, D.Y. Lee, D. Kwak, K. Cho, Tunable Anisotropic Wettability of Rice Leaf-Like Wavy Surfaces, Advanced Functional Materials 23 (5) (2013) 547-553.
[72] Y. Zheng, X. Gao, L. Jiang, Directional adhesion of superhydrophobic butterfly wings, Soft Matter 3 (2) (2007) 178-182.

[73] K. Liu, J. Du, J. Wu, L. Jiang, Superhydrophobic gecko feet with high adhesive forces towards water and their bio-inspired materials, Nanoscale 4 (3) (2012) 768-772.
[74] W. Lee, K. Nielsch, U. Gösele, Self-ordering behavior of nanoporous anodic aluminum oxide (AAO) in malonic acid anodization, Nanotechnology 18 (47) (2007) 475713.
[75] X. Deng, L. Mammen, H.-J. Butt, D. Vollmer, Candle Soot as a Template for a Transparent Robust Superamphiphobic Coating, Science 335 (6064) (2012) 67-70.
[76] M. Machida, K. Norimoto, T. Watanabe, K. Hashimoto, A. Fujishima, The effect of SiO2 addition in super-hydrophilic property of TiO2 photocatalyst, Journal of Materials Science 34 (11) (1999) 2569-2574.
[77] J. Kim, S. Jun, J. Lee, J. Godinez, S.M. You, Effect of Surface Roughness on Pool Boiling Heat Transfer of Water on a Superhydrophilic Aluminum Surface, Journal of Heat Transfer 139 (10) (2017).
[78] S. Starinskiy, E. Starinskaya, N. Miskiv, A. Rodionov, F. Ronshin, A. Safonov, M.-K. Lei, V. Terekhov, in: Water, 2023.
[79] S. Wang, K. Liu, X. Yao, L. Jiang, Bioinspired Surfaces with Superwettability: New Insight on Theory, Design, and Applications, Chemical Reviews 115 (16) (2015) 8230-8293.
[80] Y. Takata, S. Hidaka, M. Masuda, T. Ito, Pool boiling on a superhydrophilic surface, International Journal of Energy Research 27 (2) (2003) 111-119.
[81] F. Palumbo, R. Di Mundo, D. Cappelluti, R. d'Agostino, SuperHydrophobic and SuperHydrophilic Polycarbonate by Tailoring Chemistry and Nano-texture with Plasma Processing, Plasma Processes and Polymers 8 (2) (2011) 118-126.
[82] L.-Y. Yao, X.-Q. Yu, Y.-J. Zhao, A.-P. Fan, An aptamer-based chemiluminescence method for ultrasensitive detection of platelet-derived growth factor by cascade amplification combining rolling circle amplification with hydroxylamine-enlarged gold nanoparticles, Analytical Methods 7 (20) (2015) 8786-8792.
[83] W. Miao, S. Zheng, J. Zhou, B. Zhang, R. Fang, D. Hao, L. Sun, D. Wang, Z. Zhu, X. Jin, Y. Tian, L. Jiang, Microchannel and Nanofiber Array Morphology Enhanced Rapid Superspreading on Animals' Corneas, Advanced Materials 33 (23) (2021) 2007152.
[84] J. Chun, C. Xu, Y. Zhang, Q. Li, R. Wen, X. Ma, Fast Capillary Wicking on Hierarchical Copper Nanowired Surfaces with Interconnected V-Grooves: Implications for Thermal Management, ACS Applied Nano Materials 4 (5) (2021) 5360-5371.
[85] B. Bhushan, M. Nosonovsky, The rose petal effect and the modes of superhydrophobicity, Philosophical Transactions of the Royal Society A: Mathematical, Physical and Engineering Sciences 368 (1929) (2010) 4713-4728.
[86] Y. Zhan, S. Yu, A. Amirfazli, A.R. Siddiqui, W. Li, Magnetically Responsive Superhydrophobic Surfaces for Microdroplet Manipulation, Advanced Materials Interfaces 9 (5) (2022) 2102010.
[87] M. Jin, X. Feng, L. Feng, T. Sun, J. Zhai, T. Li, L. Jiang, Superhydrophobic Aligned Polystyrene Nanotube Films with High Adhesive Force, Advanced Materials 17 (16) (2005) 1977-1981.
[88] Y. Lai, X. Gao, H. Zhuang, J. Huang, C. Lin, L. Jiang, Designing Superhydrophobic Porous Nanostructures with Tunable Water Adhesion, Advanced Materials 21 (37) (2009) 3799-3803.
[89] W. Kim, J. Eun, S. Jeon, Anti-splashing properties of sticky superhydrophobic surfaces, Applied Surface Science 542 (2021) 148617.
[90] W. Weng, M. Tenjimbayashi, W.H. Hu, M. Naito, Evolution of and Disparity among Biomimetic Superhydrophobic Surfaces with Gecko, Petal, and Lotus Effect, Small 18 (18) (2022) 2200349.
[91] C. Chen, M. Liu, L. Zhang, Y. Hou, M. Yu, S. Fu, Mimicking from Rose Petal to Lotus Leaf:

Biomimetic Multiscale Hierarchical Particles with Tunable Water Adhesion, ACS Applied Materials & Interfaces 11 (7) (2019) 7431-7440.
[92] P. Xu, T.W. Coyle, L. Pershin, J. Mostaghimi, From lotus effect to petal effect: Tuning the water adhesion of non-wetting rare earth oxide coatings, Journal of the European Ceramic Society 40 (4) (2020) 1692-1702.
[93] Y. Tan, B. Hu, Z. Chu, W. Wu, Bioinspired Superhydrophobic Papillae with Tunable Adhesive Force and Ultralarge Liquid Capacity for Microdroplet Manipulation, Advanced Functional Materials 29 (15) (2019) 1900266.
[94] Y. Lai, C. Lin, J. Huang, H. Zhuang, L. Sun, T. Nguyen, Markedly Controllable Adhesion of Superhydrophobic Spongelike Nanostructure TiO2 Films, Langmuir 24 (8) (2008) 3867-3873.
[95] N. Jana, D. Parbat, B. Mondal, S. Das, U. Manna, A biodegradable polymer-based common chemical avenue for optimizing switchable, chemically reactive and tunable adhesive superhydrophobicity, Journal of Materials Chemistry A 7 (15) (2019) 9120-9129.
[96] X.-P. Li, Y.-L. Sun, Y.-Y. Xu, Z.-S. Chao, UV-Resistant and Thermally Stable Superhydrophobic CeO2 Nanotubes with High Water Adhesion, Small 14 (27) (2018) 1801040.
[97] K.-H. Nam, M. Abdulhafez, G. Najaf Tomaraei, M. Bedewy, Laser-Induced fluorinated graphene for superhydrophobic surfaces with anisotropic wetting and switchable adhesion, Applied Surface Science 574 (2022) 151339.
[98] A.J. Mazaltarim, A. Torres, S.A. Morin, Mechanically Tunable Superhydrophobic Surfaces Enabled by the Rational Manipulation of Microcrack Networks in Nanoporous Films, Advanced Materials Interfaces 8 (17) (2021) 2100869.
[99] J. Li, W. Jiao, Y. Wang, Y. Yin, X. He, Spraying pressure-tuning for the fabrication of the tunable adhesion superhydrophobic coatings between Lotus effect and Petal effect and their anti-icing performance, Chemical Engineering Journal 434 (2022) 134710.
[100] Z. Cheng, D. Zhang, T. Lv, H. Lai, E. Zhang, H. Kang, Y. Wang, P. Liu, Y. Liu, Y. Du, S. Dou, L. Jiang, Superhydrophobic Shape Memory Polymer Arrays with Switchable Isotropic/Anisotropic Wetting, Advanced Functional Materials 28 (7) (2018) 1705002.
[101] X. Bai, Q. Yang, Y. Fang, J. Yong, Y. Bai, J. Zhang, X. Hou, F. Chen, Anisotropic, adhesion-switchable, and thermal-responsive superhydrophobicity on the femtosecond laser-structured shape-memory polymer for droplet manipulation, Chemical Engineering Journal 400 (2020) 125930.
[102] H. Zhang, H. Lai, Z. Cheng, D. Zhang, W. Wang, P. Liu, X. Yu, Z. Xie, Y. Liu, Superhydrophobic shape memory film with switchable adhesion to both water and solid, Chemical Engineering Journal 420 (2021) 129862.
[103] S. Anand, A.T. Paxson, R. Dhiman, J.D. Smith, K.K. Varanasi, Enhanced Condensation on Lubricant-Impregnated Nanotextured Surfaces, ACS Nano 6 (11) (2012) 10122-10129.
[104] P. Papadopoulos, L. Mammen, X. Deng, D. Vollmer, H.-J. Butt, How superhydrophobicity breaks down, Proceedings of the National Academy of Sciences 110 (9) (2013) 3254-3258.
[105] J. Yoon, M. Ryu, H. Kim, G.-N. Ahn, S.-J. Yim, D.-P. Kim, H. Lee, Wet-Style Superhydrophobic Antifogging Coatings for Optical Sensors, Advanced Materials 32 (34) (2020) 2002710.
[106] Y. Chen, J. Meng, Z. Zhu, F. Zhang, L. Wang, Z. Gu, L. Jiang, S. Wang, Controlled Growth of Patterned Conducting Polymer Microsuckers on Superhydrophobic Micropillar-Structured Templates, Advanced Functional Materials 28 (49) (2018) 1800240.
[107] Y. Gurumukhi, S. Chavan, S. Sett, K. Boyina, S. Ramesh, P. Sokalski, K. Fortelka, M. Lira, D. Park, J.-Y. Chen, S. Hegde, N. Miljkovic, Dynamic Defrosting on Superhydrophobic and Biphilic

Surfaces, Matter 3 (4) (2020) 1178-1195.
[108] C.-W. Lo, Y.-C. Chu, M.-H. Yen, M.-C. Lu, Enhancing Condensation Heat Transfer on Three-Dimensional Hybrid Surfaces, Joule 3 (11) (2019) 2806-2823.
[109] M. Leitgeb, D. Nees, S. Ruttloff, U. Palfinger, J. Götz, R. Liska, M.R. Belegratis, B. Stadlober, Multilength Scale Patterning of Functional Layers by Roll-to-Roll Ultraviolet-Light-Assisted Nanoimprint Lithography, ACS Nano 10 (5) (2016) 4926-4941.
[110] J. Oh, J.B. Hoffman, S. Hong, K.D. Jo, J. Román-Kustas, J.H. Reed, C.E. Dana, D.M. Cropek, M. Alleyne, N. Miljkovic, Dissolvable Template Nanoimprint Lithography: A Facile and Versatile Nanoscale Replication Technique, Nano Letters 20 (10) (2020) 6989-6997.
[111] L.P. Singh, S.K. Bhattacharyya, R. Kumar, G. Mishra, U. Sharma, G. Singh, S. Ahalawat, Sol-Gel processing of silica nanoparticles and their applications, Advances in Colloid and Interface Science 214 (2014) 17-37.
[112] S. Liu, X. Liu, S.S. Latthe, L. Gao, S. An, S.S. Yoon, B. Liu, R. Xing, Self-cleaning transparent superhydrophobic coatings through simple sol–gel processing of fluoroalkylsilane, Applied Surface Science 351 (2015) 897-903.
[113] H. Liu, W.-Y. Xie, F. Song, X.-L. Wang, Y.-Z. Wang, Constructing hierarchically hydrophilic/superhydrophobic ZIF-8 pattern on soy protein towards a biomimetic efficient water harvesting material, Chemical Engineering Journal 369 (2019) 1040-1048.
[114] X. Yang, J. Song, J. Liu, X. Liu, Z. Jin, A Twice Electrochemical-Etching Method to Fabricate Superhydrophobic-Superhydrophilic Patterns for Biomimetic Fog Harvest, Scientific Reports 7 (1) (2017) 8816.
[115] L. Wu, Z. Dong, M. Kuang, Y. Li, F. Li, L. Jiang, Y. Song, Printing Patterned Fine 3D Structures by Manipulating the Three Phase Contact Line, Advanced Functional Materials 25 (15) (2015) 2237-2242.
[116] Y. Wang, W. Zhao, M. Han, L. Guan, L. Han, A. Hemraj, K.C. Tam, Sustainable Superhydrophobic Surface with Tunable Nanoscale Hydrophilicity for Water Harvesting Applications, Angewandte Chemie International Edition 61 (10) (2022) e202115238.
[117] T. Ishizaki, N. Saito, O. Takai, Correlation of Cell Adhesive Behaviors on Superhydrophobic, Superhydrophilic, and Micropatterned Superhydrophobic/Superhydrophilic Surfaces to Their Surface Chemistry, Langmuir 26 (11) (2010) 8147-8154.
[118] S.M. Oliveira, W. Song, N.M. Alves, J.F. Mano, Chemical modification of bioinspired superhydrophobic polystyrene surfaces to control cell attachment/proliferation, Soft Matter 7 (19) (2011) 8932-8941.
[119] J. Zhang, Y. Wang, J. Zhang, Z. Lin, F. Huang, J. Yu, Enhanced Photocatalytic Hydrogen Production Activities of Au-Loaded ZnS Flowers, ACS Applied Materials & Interfaces 5 (3) (2013) 1031-1037.
[120] W. Feng, E. Ueda, P.A. Levkin, Droplet Microarrays: From Surface Patterning to High-Throughput Applications, Advanced Materials 30 (20) (2018) 1706111.
[121] A.I. Neto, K. Demir, A.A. Popova, M.B. Oliveira, J.F. Mano, P.A. Levkin, Fabrication of Hydrogel Particles of Defined Shapes Using Superhydrophobic-Hydrophilic Micropatterns, Advanced Materials 28 (35) (2016) 7613-7619.
[122] L. Li, W. Feng, A. Welle, P.A. Levkin, UV-Induced Disulfide Formation and Reduction for Dynamic Photopatterning, Angewandte Chemie International Edition 55 (44) (2016) 13765-13769.
[123] X. Du, M. Wang, A. Welle, F. Behboodi-Sadabad, Y. Wang, P.A. Levkin, Z. Gu, Reparable

Superhydrophobic Surface with Hidden Reactivity, Its Photofunctionalization and Photopatterning, Advanced Functional Materials 28 (41) (2018) 1803765.
[124] H. Bai, L. Wang, J. Ju, R. Sun, Y. Zheng, L. Jiang, Efficient Water Collection on Integrative Bioinspired Surfaces with Star-Shaped Wettability Patterns, Advanced Materials 26 (29) (2014) 5025-5030.
[125] L. Zhang, J. Wu, M.N. Hedhili, X. Yang, P. Wang, Inkjet printing for direct micropatterning of a superhydrophobic surface: toward biomimetic fog harvesting surfaces, Journal of Materials Chemistry A 3 (6) (2015) 2844-2852.
[126] L. Mishchenko, M. Khan, J. Aizenberg, B.D. Hatton, Spatial Control of Condensation and Freezing on Superhydrophobic Surfaces with Hydrophilic Patches, Advanced Functional Materials 23 (36) (2013) 4577-4584.
[127] K. Ichimura, S.-K. Oh, M. Nakagawa, Light-Driven Motion of Liquids on a Photoresponsive Surface, Science 288 (5471) (2000) 1624-1626.
[128] G. Kwon, D. Panchanathan, S.R. Mahmoudi, M.A. Gondal, G.H. McKinley, K.K. Varanasi, Visible light guided manipulation of liquid wettability on photoresponsive surfaces, Nature Communications 8 (1) (2017) 14968.
[129] B. Yuan, G. Gou, T. Fan, M. Liu, Y. Ma, R. Matsuda, L. Li, Delicate and Fast Photochemical Surface Modification of 2D Photoresponsive Organosilicon Metal–Organic Frameworks, Angewandte Chemie International Edition 61 (28) (2022) e202204568.
[130] T. Sun, G. Wang, L. Feng, B. Liu, Y. Ma, L. Jiang, D. Zhu, Reversible Switching between Superhydrophilicity and Superhydrophobicity, Angewandte Chemie International Edition 43 (3) (2004) 357-360.
[131] Q. Fu, G.V. Rama Rao, S.B. Basame, D.J. Keller, K. Artyushkova, J.E. Fulghum, G.P. López, Reversible Control of Free Energy and Topography of Nanostructured Surfaces, Journal of the American Chemical Society 126 (29) (2004) 8904-8905.
[132] J. Lin, J. Hu, W. Wang, K. Liu, C. Zhou, Z. Liu, S. Kong, S. Lin, Y. Deng, Z. Guo, Thermo and light-responsive strategies of smart titanium-containing composite material surface for enhancing bacterially anti-adhesive property, Chemical Engineering Journal 407 (2021) 125783.
[133] K. Nagase, Thermoresponsive interfaces obtained using poly(N-isopropylacrylamide)-based copolymer for bioseparation and tissue engineering applications, Advances in Colloid and Interface Science 295 (2021) 102487.
[134] Y. Zhou, S. Wang, J. Peng, Y. Tan, C. Li, F.Y.C. Boey, Y. Long, Liquid Thermo-Responsive Smart Window Derived from Hydrogel, Joule 4 (11) (2020) 2458-2474.
[135] F. Zhao, X. Zhou, Y. Liu, Y. Shi, Y. Dai, G. Yu, Super Moisture-Absorbent Gels for All-Weather Atmospheric Water Harvesting, Advanced Materials 31 (10) (2019) 1806446.
[136] H. Geng, Q. Xu, M. Wu, H. Ma, P. Zhang, T. Gao, L. Qu, T. Ma, C. Li, Plant leaves inspired sunlight-driven purifier for high-efficiency clean water production, Nature Communications 10 (1) (2019) 1512.
[137] J. Brito, K. Asawa, A. Marin, A.K. Andrianov, C.-H. Choi, S.A. Sukhishvili, Hierarchically Structured, All-Aqueous-Coated Hydrophobic Surfaces with pH-Selective Droplet Transfer Capability, ACS Applied Materials & Interfaces 14 (22) (2022) 26225-26237.
[138] T. Lv, Z. Cheng, D. Zhang, E. Zhang, Q. Zhao, Y. Liu, L. Jiang, Superhydrophobic Surface With Shape Memory Micro/Nanostructure and Its Application in Rewritable Chip for Droplet Storage, ACS Nano 10 (10) (2016) 9379-9386.

[139] L. Sun, F. Bian, Y. Wang, Y. Wang, X. Zhang, Y. Zhao, Bioinspired programmable wettability arrays for droplets manipulation, Proceedings of the National Academy of Sciences 117 (9) (2020) 4527-4532.
[140] J. Cao, D. Gao, C. Li, X. Si, J. Jia, J. Qi, Bioinspired Metal-Intermetallic Laminated Composites for the Fabrication of Superhydrophobic Surfaces with Responsive Wettability, ACS Applied Materials & Interfaces 13 (4) (2021) 5834-5843.
[141] F. Wang, R. Chang, R. Ma, H. Qiu, Y. Tian, Eco-Friendly and pH-Responsive Nano-Starch-Based Superhydrophobic Coatings for Liquid-Food Residue Reduction and Freshness Monitoring, ACS Sustainable Chemistry & Engineering 9 (30) (2021) 10142-10153.
[142] Y. Guo, F. Xia, L. Xu, J. Li, W. Yang, L. Jiang, Switchable Wettability on Cooperative Dual-Responsive Poly-l-lysine Surface, Langmuir 26 (2) (2010) 1024-1028.
[143] Y. Liu, X. Wang, B. Fei, H. Hu, C. Lai, J.H. Xin, Bioinspired, Stimuli-Responsive, Multifunctional Superhydrophobic Surface with Directional Wetting, Adhesion, and Transport of Water, Advanced Functional Materials 25 (31) (2015) 5047-5056.
[144] Y. Huang, B.B. Stogin, N. Sun, J. Wang, S. Yang, T.-S. Wong, A Switchable Cross-Species Liquid Repellent Surface, Advanced Materials 29 (8) (2017) 1604641.
[145] H.-D. Wang, C.-H. Xue, X.-J. Guo, B.-Y. Liu, Z.-Y. Ji, M.-C. Huang, S.-T. Jia, Superhydrophobic porous film for daytime radiative cooling, Applied Materials Today 24 (2021) 101100.
[146] Y. Chen, Z. Zhu, X. Jiang, L. Jiang, Superhydrophobic-Substrate-Assisted Construction of Free-Standing Microcavity-Patterned Conducting Polymer Films, Advanced Science 8 (17) (2021) 2100949.
[147] Y. Chen, Z. Zhu, X. Jiang, L. Jiang, Construction of Free-Standing MOF Sheets through Electrochemical Printing on Superhydrophobic Substrates, ACS Materials Letters 4 (4) (2022) 609-617.
[148] B. Zhang, P.W. Wong, J. Guo, Y. Zhou, Y. Wang, J. Sun, M. Jiang, Z. Wang, A.K. An, Transforming Ti3C2Tx MXene's intrinsic hydrophilicity into superhydrophobicity for efficient photothermal membrane desalination, Nature Communications 13 (1) (2022) 3315.
[149] D. Yoo, S.J. Kim, Y. Joung, S. Jang, D. Choi, D.S. Kim, Lotus leaf-inspired droplet-based electricity generator with low-adhesive superhydrophobicity for a wide operational droplet volume range and boosted electricity output, Nano Energy 99 (2022) 107361.
[150] Z. Ma, J. Ai, Y. Yue, K. Wang, B. Su, A superhydrophobic magnetoelectric generator for high-performance conversion from raindrops to electricity, Nano Energy 83 (2021) 105846.
[151] Z. Ma, J. Ai, Y. Shi, K. Wang, B. Su, A Superhydrophobic Droplet-Based Magnetoelectric Hybrid System to Generate Electricity and Collect Water Simultaneously, Advanced Materials 32 (50) (2020) 2006839.
[152] Z. Shao, Y. Wang, H. Bai, A superhydrophobic textile inspired by polar bear hair for both in air and underwater thermal insulation, Chemical Engineering Journal 397 (2020) 125441.
[153] F. Sahin, N. Celik, A. Ceylan, S. Pekdemir, M. Ruzi, M.S. Onses, Antifouling superhydrophobic surfaces with bactericidal and SERS activity, Chemical Engineering Journal 431 (2022) 133445.
[154] Z. Ma, X. Liu, X. Xu, L. Liu, B. Yu, C. Maluk, G. Huang, H. Wang, P. Song, Bioinspired, Highly Adhesive, Nanostructured Polymeric Coatings for Superhydrophobic Fire-Extinguishing Thermal Insulation Foam, ACS Nano 15 (7) (2021) 11667-11680.
[155] S. Wang, D. Li, W. Meng, L. Jiang, D. Fang, Scalable, superelastic, and superhydrophobic MXene/silver nanowire/melamine hybrid sponges for high-performance electromagnetic interference shielding, Journal of Materials Chemistry C 10 (13) (2022) 5336-5344.
[156] J. Long, P. Fan, D. Gong, D. Jiang, H. Zhang, L. Li, M. Zhong, Superhydrophobic Surfaces

Fabricated by Femtosecond Laser with Tunable Water Adhesion: From Lotus Leaf to Rose Petal, ACS Applied Materials & Interfaces 7 (18) (2015) 9858-9865.
[157] E. Yilgör, C.K. Söz, I. Yilgör, Wetting behavior of superhydrophobic poly(methyl methacrylate), Progress in Organic Coatings 125 (2018) 530-536.
[158] S. Kancharla, P. Alexandridis, M. Tsianou, Sequestration of per- and polyfluoroalkyl substances (PFAS) by adsorption: Surfactant and surface aspects, Current Opinion in Colloid & Interface Science 58 (2022) 101571.
[159] L. Cao, A.K. Jones, V.K. Sikka, J. Wu, D. Gao, Anti-Icing Superhydrophobic Coatings, Langmuir 25 (21) (2009) 12444-12448.
[160] Y. Meng, W. Sun, H. Yang, W. Wang, N. Jin, Y. Zhao, X. Zhang, H. Lü, Fine tuning of surface properties of SiO2 nanoparticles for the regulation of Pickering emulsions, Colloids and Surfaces A: Physicochemical and Engineering Aspects 592 (2020) 124603.
[161] M. Tang, X. Wang, F. Wu, Y. Liu, S. Zhang, X. Pang, X. Li, H. Qiu, Au nanoparticle/graphene oxide hybrids as stabilizers for Pickering emulsions and Au nanoparticle/graphene oxide@polystyrene microspheres, Carbon 71 (2014) 238-248.
[162] F. Cui, S. Zhao, X. Guan, D.J. McClements, X. Liu, F. Liu, T. Ngai, Polysaccharide-based Pickering emulsions: Formation, stabilization and applications, Food Hydrocolloids 119 (2021) 106812.
[163] J. Tang, P.J. Quinlan, K.C. Tam, Stimuli-responsive Pickering emulsions: recent advances and potential applications, Soft Matter 11 (18) (2015) 3512-3529.
[164] S.P. Akhlaghi, R.C. Berry, K.C. Tam, Surface modification of cellulose nanocrystal with chitosan oligosaccharide for drug delivery applications, Cellulose 20 (4) (2013) 1747-1764.
[165] S. Bhattacharjee, DLS and zeta potential – What they are and what they are not?, Journal of Controlled Release 235 (2016) 337-351.
[166] Z. Sekhavat Pour, P. Makvandi, M. Ghaemy, Performance properties and antibacterial activity of crosslinked films of quaternary ammonium modified starch and poly(vinyl alcohol), International Journal of Biological Macromolecules 80 (2015) 596-604.
[167] Y. Wang, X. Gong, Special oleophobic and hydrophilic surfaces: approaches, mechanisms, and applications, Journal of Materials Chemistry A 5 (8) (2017) 3759-3773.
[168] Q. Ma, H. Cheng, A.G. Fane, R. Wang, H. Zhang, Recent Development of Advanced Materials with Special Wettability for Selective Oil/Water Separation, Small 12 (16) (2016) 2186-2202.
[169] X. Li, T. Zhang, Z. Xu, H. Chi, Z. Wu, Y. Zhao, Amphiphobic polyHIPEs with pH-triggered transition to hydrophilicity–oleophobicity for the controlled removal of water from oil–water mixtures, Polymer Chemistry 11 (43) (2020) 6935-6943.
[170] J. Chen, Y. Zhang, C. Chen, M. Xu, G. Wang, Z. Zeng, L. Wang, Q. Xue, Cellulose Sponge with Superhydrophilicity and High Oleophobicity Both in Air and under Water for Efficient Oil–Water Emulsion Separation, Macromolecular Materials and Engineering 302 (9) (2017) 1700086.
[171] F. Xia, L. Jiang, Bio-Inspired, Smart, Multiscale Interfacial Materials, Advanced Materials 20 (15) (2008) 2842-2858.
[172] N. Li, L. Thia, X. Wang, A CO2-responsive surface with an amidine-terminated self-assembled monolayer for stimuli-induced selective adsorption, Chemical Communications 50 (30) (2014) 4003-4006.
[173] N. Nath, A. Chilkoti, Creating “Smart” Surfaces Using Stimuli Responsive Polymers, Advanced Materials 14 (17) (2002) 1243-1247.
[174] M. Cheng, Q. Liu, G. Ju, Y. Zhang, L. Jiang, F. Shi, Bell-Shaped Superhydrophilic–

Superhydrophobic–Superhydrophilic Double Transformation on a pH-Responsive Smart Surface, Advanced Materials 26 (2) (2014) 306-310.
[175] L. Kang, B. Wang, J. Zeng, Z. Cheng, J. Li, J. Xu, W. Gao, K. Chen, Degradable dual superlyophobic lignocellulosic fibers for high-efficiency oil/water separation, Green Chemistry 22 (2) (2020) 504-512.
[176] Z. Zhao, Y. Ning, X. Jin, S. Ben, J. Zha, B. Su, D. Tian, K. Liu, L. Jiang, Molecular-Structure-Induced Under-Liquid Dual Superlyophobic Surfaces, ACS Nano 14 (11) (2020) 14869-14877.
[177] Q. Wang, Y. Wang, B. Wang, Z. Liang, J. Di, J. Yu, Under-liquid dual superlyophobic nanofibrous polymer membranes achieved by coating thin-film composites: a design principle, Chemical Science 10 (25) (2019) 6382-6389.
[178] Z. Wang, M. Guan, X. Jiang, J. Xiao, Y. Shao, S. Li, Y. Chen, Bioinspired Under-Liquid Dual Superlyophobic Surface for On-Demand Oil/Water Separation, Langmuir 39 (2) (2023) 870-877.
[179] C.-L. Xu, Y. Luo, S. Liu, G. Wang, C. Chen, G. Lv, Z. Cheng, Z. Yang, X. Xu, J. Cai, X. Zhang, G. Yang, J. Wu, S. Zhang, Dual Superlyophobic Materials for Under-Liquid Microfluid Manipulation, Immiscible Solvent Separation, and CO2 Blockage, ACS Applied Materials & Interfaces 15 (15) (2023) 19761-19772.
[180] P. Zhang, S. Wang, S. Wang, L. Jiang, Superwetting Surfaces under Different Media: Effects of Surface Topography on Wettability, Small 11 (16) (2015) 1939-1946.
[181] A. Alicke, S. Simon, J. Sjöblom, J. Vermant, Assessing the Interfacial Activity of Insoluble Asphaltene Layers: Interfacial Rheology versus Interfacial Tension, Langmuir 36 (49) (2020) 14942-14959.
[182] X.-M. Li, T. He, M. Crego-Calama, D.N. Reinhoudt, Conversion of a Metastable Superhydrophobic Surface to an Ultraphobic Surface, Langmuir 24 (15) (2008) 8008-8012.
[183] A. Giacomello, M. Chinappi, S. Meloni, C.M. Casciola, Metastable Wetting on Superhydrophobic Surfaces: Continuum and Atomistic Views of the Cassie-Baxter--Wenzel Transition, Physical Review Letters 109 (22) (2012) 226102.
[184] R. Poetes, K. Holtzmann, K. Franze, U. Steiner, Metastable Underwater Superhydrophobicity, Physical Review Letters 105 (16) (2010) 166104.
[185] W. Liu, X. Bai, Y. Shen, P. Mu, Y. Yang, J. Li, Efficient separation of free organic liquid mixtures based on underliquid superlyophobic coconut shell coated meshes, Separation and Purification Technology 231 (2020) 115899.
[186] T. Maric, M.Z.M. Nasir, N.F. Rosli, M. Budanović, R.D. Webster, N.-J. Cho, M. Pumera, Microrobots Derived from Variety Plant Pollen Grains for Efficient Environmental Clean Up and as an Anti-Cancer Drug Carrier, Advanced Functional Materials 30 (19) (2020) 2000112.
[187] J.L. Sanchez-Salvador, C. Campano, C. Negro, M.C. Monte, A. Blanco, Increasing the Possibilities of TEMPO-Mediated Oxidation in the Production of Cellulose Nanofibers by Reducing the Reaction Time and Reusing the Reaction Medium, Advanced Sustainable Systems 5 (4) (2021) 2000277.
[188] S. Iravani, R.S. Varma, Plant Pollen Grains: A Move Towards Green Drug and Vaccine Delivery Systems, Nano-Micro Letters 13 (1) (2021) 128.
[189] J. Shin, C. Andreas Hutomo, J. Kim, J. Jang, C.B. Park, Natural pollen exine-templated synthesis of photocatalytic metal oxides with high surface area and oxygen vacancies, Applied Surface Science 599 (2022) 154064.
[190] H. Noei, H. Qiu, Y. Wang, E. Löffler, C. Wöll, M. Muhler, The identification of hydroxyl groups on ZnO nanoparticles by infrared spectroscopy, Physical Chemistry Chemical Physics 10 (47) (2008)

7092-7097.
[191] L.-h. Teng, T.-d. Tang, IR study on surface chemical properties of catalytic grown carbon nanotubes and nanofibers, Journal of Zhejiang University-SCIENCE A 9 (5) (2008) 720-726.
[192] N. Meng, J. Ren, Y. Liu, Y. Huang, T. Petit, B. Zhang, Engineering oxygen-containing and amino groups into two-dimensional atomically-thin porous polymeric carbon nitrogen for enhanced photocatalytic hydrogen production, Energy & Environmental Science 11 (3) (2018) 566-571.
[193] X. Yu, S. Tong, M. Ge, L. Wu, J. Zuo, C. Cao, W. Song, Adsorption of heavy metal ions from aqueous solution by carboxylated cellulose nanocrystals, Journal of Environmental Sciences 25 (5) (2013) 933-943.
[194] H. Hashemi Gahruie, E. Ziaee, M.H. Eskandari, S.M.H. Hosseini, Characterization of basil seed gum-based edible films incorporated with Zataria multiflora essential oil nanoemulsion, Carbohydrate Polymers 166 (2017) 93-103.
[195] Y. Wang, J. Di, L. Wang, X. Li, N. Wang, B. Wang, Y. Tian, L. Jiang, J. Yu, Infused-liquid-switchable porous nanofibrous membranes for multiphase liquid separation, Nature Communications 8 (1) (2017) 575.
[196] D.K. Owens, R.C. Wendt, Estimation of the surface free energy of polymers, Journal of Applied Polymer Science 13 (8) (1969) 1741-1747.
[197] S. Chu, A. Majumdar, Opportunities and challenges for a sustainable energy future, Nature 488 (7411) (2012) 294-303.
[198] R.E. Pattle, Production of Electric Power by mixing Fresh and Salt Water in the Hydroelectric Pile, Nature 174 (4431) (1954) 660-660.
[199] J. Maier, Nanoionics: ion transport and electrochemical storage in confined systems, Nat. Mater. 4 (11) (2005) 805-815.
[200] P. Długołęcki, A. Gambier, K. Nijmeijer, M. Wessling, Practical Potential of Reverse Electrodialysis As Process for Sustainable Energy Generation, Environmental Science & Technology 43 (17) (2009) 6888-6894.
[201] E. Güler, W. van Baak, M. Saakes, K. Nijmeijer, Monovalent-ion-selective membranes for reverse electrodialysis, Journal of Membrane Science 455 (1) (2014) 254-270.
[202] J. Xu, D.A. Lavan, Designing artificial cells to harness the biological ion concentration gradient, Nature Nanotechnology 3 (11) (2008) 666-670.
[203] J. Veerman, R.M. de Jong, M. Saakes, S.J. Metz, G.J. Harmsen, Reverse electrodialysis: Comparison of six commercial membrane pairs on the thermodynamic efficiency and power density, Journal of Membrane Science 343 (1) (2009) 7-15.
[204] R.B. Schoch, J. Han, P. Renaud, Transport phenomena in nanofluidics, Reviews of Modern Physics 80 (3) (2008) 839-883.
[205] B.E. Logan, M. Elimelech, Membrane-based processes for sustainable power generation using water, Nature 488 (7411) (2012) 313-319.
[206] G.Z. Ramon, B.J. Feinberg, E.M.V. Hoek, Membrane-based production of salinity-gradient power, Energy & Environmental Science 4 (11) (2011) 4423-4434.
[207] J. Ji, Q. Kang, Y. Zhou, Y. Feng, X. Chen, J. Yuan, W. Guo, Y. Wei, L. Jiang, Osmotic Power Generation with Positively and Negatively Charged 2D Nanofluidic Membrane Pairs, Advanced Functional Materials 27 (2) (2017).
[208] L. Ding, D. Xiao, Z. Lu, J. Deng, Y. Wei, J. Caro, H. Wang, Oppositely Charged Ti3 C2 Tx MXene Membranes with 2D Nanofluidic Channels for Osmotic Energy Harvesting, Angew Chem Int Ed Engl

59 (22) (2020) 8720-8726.
[209] C. Zhu, P. Liu, B. Niu, Y. Liu, W. Xin, W. Chen, X.-Y. Kong, Z. Zhang, L. Jiang, L. Wen, Metallic Two-Dimensional MoS2 Composites as High-Performance Osmotic Energy Conversion Membranes, Journal of the American Chemical Society 143 (4) (2021) 1932-1940.
[210] W. Sparreboom, A. van den Berg, J.C.T. Eijkel, Principles and applications of nanofluidic transport, Nature Nanotechnology 4 (11) (2009) 713-720.
[211] W. Guo, L. Cao, J. Xia, F.-Q. Nie, W. Ma, J. Xue, Y. Song, D. Zhu, Y. Wang, L. Jiang, Energy Harvesting with Single-Ion-Selective Nanopores: A Concentration-Gradient-Driven Nanofluidic Power Source, Advanced Functional Materials 20 (8) (2010) 1339-1344.
[212] D.-K. Kim, C. Duan, Y.-F. Chen, A. Majumdar, Power generation from concentration gradient by reverse electrodialysis in ion-selective nanochannels, Microfluidics and Nanofluidics 9 (6) (2010) 1215-1224.
[213] C. Cheng, G. Jiang, C.J. Garvey, Y. Wang, G.P. Simon, J.Z. Liu, D. Li, Ion transport in complex layered graphene-based membranes with tuneable interlayer spacing, Science Advances 2 (2) (2016) e1501272.
[214] S. Hong, C. Constans, M.V. Surmani Martins, Y.C. Seow, J.A. Guevara Carrió, S. Garaj, Scalable Graphene-Based Membranes for Ionic Sieving with Ultrahigh Charge Selectivity, Nano Letters 17 (2) (2017) 728-732.
[215] S. Zheng, Q. Tu, J.J. Urban, S. Li, B. Mi, Swelling of Graphene Oxide Membranes in Aqueous Solution: Characterization of Interlayer Spacing and Insight into Water Transport Mechanisms, ACS Nano 11 (6) (2017) 6440-6450.
[216] Y. Zhou, C. Chen, X. Zhang, D. Liu, L. Xu, J. Dai, S.-C. Liou, Y. Wang, C. Li, H. Xie, Q. Wu, B. Foster, T. Li, R.M. Briber, L. Hu, Decoupling Ionic and Electronic Pathways in Low-Dimensional Hybrid Conductors, Journal of the American Chemical Society 141 (44) (2019) 17830-17837.
[217] M. Sivakumar, D.-K. Liu, Y.-H. Chiao, W.-S. Hung, Synergistic effect of one-dimensional silk nanofiber and two-dimensional graphene oxide composite membrane for enhanced water purification, Journal of Membrane Science 606 (1) (2020) 118142.
[218] Z. Zhang, S. Yang, P. Zhang, J. Zhang, G. Chen, X. Feng, Mechanically strong MXene/Kevlar nanofiber composite membranes as high-performance nanofluidic osmotic power generators, Nature Communications 10 (1) (2019) 2920.
[219] Y. Wu, W. Xin, X.-Y. Kong, J. Chen, Y. Qian, Y. Sun, X. Zhao, W. Chen, L. Jiang, L. Wen, Enhanced ion transport by graphene oxide/cellulose nanofibers assembled membranes for high-performance osmotic energy harvesting, Materials Horizons 7 (10) (2020) 2702-2709.
[220] N. Sheng, S. Chen, M. Zhang, Z. Wu, Q. Liang, P. Ji, H. Wang, TEMPO-Oxidized Bacterial Cellulose Nanofibers/Graphene Oxide Fibers for Osmotic Energy Conversion, ACS Applied Materials & Interfaces 13 (19) (2021) 22416-22425.
[221] Z. Jia, B. Wang, S. Song, Y. Fan, Blue energy: Current technologies for sustainable power generation from water salinity gradient, Renewable and Sustainable Energy Reviews 31 (2014) 91-100.
[222] N. Grishkewich, N. Mohammed, J. Tang, K.C. Tam, Recent advances in the application of cellulose nanocrystals, Current Opinion in Colloid & Interface Science 29 (2017) 32-45.
[223] M.S. Islam, L. Chen, J. Sisler, K.C. Tam, Cellulose nanocrystal (CNC)–inorganic hybrid systems: synthesis, properties and applications, Journal of Materials Chemistry B 6 (6) (2018) 864-883.
[224] G. Chen, T. Chen, K. Hou, W. Ma, M. Tebyetekerwa, Y. Cheng, W. Weng, M. Zhu, Robust, hydrophilic graphene/cellulose nanocrystal fiber-based electrode with high capacitive performance and

conductivity, Carbon 127 (2018) 218-227.
[225] J. Tang, J. Sisler, N. Grishkewich, K.C. Tam, Functionalization of cellulose nanocrystals for advanced applications, Journal of Colloid and Interface Science 494 (2017) 397-409.
[226] D.C. Marcano, D.V. Kosynkin, J.M. Berlin, A. Sinitskii, Z. Sun, A. Slesarev, L.B. Alemany, W. Lu, J.M. Tour, Improved synthesis of graphene oxide, ACS nano 4 (8) (2010) 4806-4814.
[227] R. Batmaz, N. Mohammed, M. Zaman, G. Minhas, R.M. Berry, K.C. Tam, Cellulose nanocrystals as promising adsorbents for the removal of cationic dyes, Cellulose 21 (3) (2014) 1655-1665.
[228] R. Xiong, K. Hu, A.M. Grant, R. Ma, W. Xu, C. Lu, X. Zhang, V.V. Tsukruk, Ultrarobust Transparent Cellulose Nanocrystal-Graphene Membranes with High Electrical Conductivity, Advanced Materials 28 (7) (2016) 1501-1509.
[229] H. Yang, H. Hu, Y. Wang, T. Yu, Rapid and non-destructive identification of graphene oxide thickness using white light contrast spectroscopy, Carbon 52 (2013) 528-534.
[230] T. Szabó, O. Berkesi, P. Forgó, K. Josepovits, Y. Sanakis, D. Petridis, I. Dékány, Evolution of Surface Functional Groups in a Series of Progressively Oxidized Graphite Oxides, Chemistry of Materials 18 (11) (2006) 2740-2749.
[231] M. Zhang, K. Guan, Y. Ji, G. Liu, W. Jin, N. Xu, Controllable ion transport by surface-charged graphene oxide membrane, Nature Communications 10 (1) (2019) 1253.
[232] A. Razmjou, M. Asadnia, E. Hosseini, A. Habibnejad Korayem, V. Chen, Design principles of ion selective nanostructured membranes for the extraction of lithium ions, Nature Communications 10 (1) (2019) 5793.
[233] Y. Huang, D. Hu, S. Wen, M. Shen, M. Zhu, X. Shi, Selective removal of mercury ions using thymine-grafted electrospun polymer nanofibers, New Journal of Chemistry 38 (4) (2014) 1533-1539.
[234] M. Zhang, L. Huang, J. Chen, C. Li, G. Shi, Ultratough, ultrastrong, and highly conductive graphene films with arbitrary sizes, Adv Mater 26 (45) (2014) 7588-7592.
[235] Z. Rao, H. Ge, L. Liu, C. Zhu, L. Min, M. Liu, L. Fan, D. Li, Carboxymethyl cellulose modified graphene oxide as pH-sensitive drug delivery system, Int J Biol Macromol 107 (Pt A) (2018) 1184-1192.
[236] H.D. Espinosa, A.L. Juster, F.J. Latourte, O.Y. Loh, D. Gregoire, P.D. Zavattieri, Tablet-level origin of toughening in abalone shells and translation to synthetic composite materials, Nat Commun 2 (2011) 173.
[237] Y. Li, H. Zhu, S. Zhu, J. Wan, Z. Liu, O. Vaaland, S. Lacey, Z. Fang, H. Dai, T. Li, L. Hu, Hybridizing wood cellulose and graphene oxide toward high-performance fibers, NPG Asia Materials 7 (1) (2015) e150-e150.
[238] L. Cao, W. Guo, W. Ma, L. Wang, F. Xia, S. Wang, Y. Wang, L. Jiang, D. Zhu, Towards understanding the nanofluidic reverse electrodialysis system: well matched charge selectivity and ionic composition, Energy & Environmental Science 4 (6) (2011) 2259-2266.
[239] W. Xin, Z. Zhang, X. Huang, Y. Hu, T. Zhou, C. Zhu, X.Y. Kong, L. Jiang, L. Wen, High-performance silk-based hybrid membranes employed for osmotic energy conversion, Nat Commun 10 (1) (2019) 3876.
[240] L.B. Mao, S.H. Yu, Biomimetic Nacrelike Membranes for Selective Ion Transport, ACS Cent Sci 7 (9) (2021) 1467-1469.
[241] J. Chen, W. Xin, W. Chen, X. Zhao, Y. Qian, X.Y. Kong, L. Jiang, L. Wen, Biomimetic Nanocomposite Membranes with Ultrahigh Ion Selectivity for Osmotic Power Conversion, ACS Cent Sci 7 (9) (2021) 1486-1492.
[242] Z. Zhang, W. Shen, L. Lin, M. Wang, N. Li, Z. Zheng, F. Liu, L. Cao, Vertically Transported

Graphene Oxide for High-Performance Osmotic Energy Conversion, Adv Sci (Weinh) 7 (12) (2020) 2000286.
[243] D.D. Ordinario, L. Phan, W.G.t. Walkup, J.M. Jocson, E. Karshalev, N. Husken, A.A. Gorodetsky, Bulk protonic conductivity in a cephalopod structural protein, Nat Chem 6 (7) (2014) 596-602.
[244] J. Abraham, K.S. Vasu, C.D. Williams, K. Gopinadhan, Y. Su, C.T. Cherian, J. Dix, E. Prestat, S.J. Haigh, I.V. Grigorieva, P. Carbone, A.K. Geim, R.R. Nair, Tunable sieving of ions using graphene oxide membranes, Nature Nanotechnology 12 (6) (2017) 546-550.
[245] J. Hwang, T. Sekimoto, W.L. Hsu, S. Kataoka, A. Endo, H. Daiguji, Thermal dependence of nanofluidic energy conversion by reverse electrodialysis, Nanoscale 9 (33) (2017) 12068-12076.
[246] S.F. Jones, G.M. Evans, K.P. Galvin, Bubble nucleation from gas cavities-a review, Advances in colloid and Interface Science 80 (1) (1999) 27-80.
[247] Y. Wu, C.-F. Fu, Q. Huang, P. Zhang, P. Cui, J. Ran, J. Yang, T. Xu, 2D Heterostructured Nanofluidic Channels for Enhanced Desalination Performance of Graphene Oxide Membranes, ACS Nano 15 (4) (2021) 7586-7595.
[248] L. Xie, J. Tang, R. Qin, Q. Zhang, J. Liu, Y. Jin, H. Wang, Surface Charge Modification on 2D Nanofluidic Membrane for Regulating Ion Transport, Advanced Functional Materials 33 (4) (2023) 2208959.
[249] G. Laucirica, M.E. Toimil-Molares, C. Trautmann, W. Marmisollé, O. Azzaroni, Nanofluidic osmotic power generators – advanced nanoporous membranes and nanochannels for blue energy harvesting, Chemical Science 12 (39) (2021) 12874-12910.
[250] J. Zhou, J. Hao, R. Wu, L. Su, J. Wang, M. Qiu, B. Bao, C. Ning, C. Teng, Y. Zhou, L. Jiang, Maximizing Ion Permselectivity in MXene/MOF Nanofluidic Membranes for High-Efficient Blue Energy Generation, Advanced Functional Materials 32 (49) (2022) 2209767.
[251] Y. Feng, W. Zhu, W. Guo, L. Jiang, Bioinspired Energy Conversion in Nanofluidics: A Paradigm of Material Evolution, Advanced Materials 29 (45) (2017) 1702773.
[252] M.I.U. Hoque, A.-N. Chowdhury, M.S.H. Firoz, M.K. Biswas, U. Luba, Y. Haque, K. Kani, M. Kim, S.H.A. Ahmad, A.U. Rehman, R. Holze, S. Rahman, S.W. Donne, K. Ariga, Y. Bando, M.S.A. Hossain, J. Na, V. Malgras, Y. Yamauchi, One-dimensional Sn(iv) hydroxide nanofluid toward nonlinear optical switching, Materials Horizons 7 (4) (2020) 1150-1159.
[253] D. Mijatovic, J.C.T. Eijkel, A. van den Berg, Technologies for nanofluidic systems: top-down vs. bottom-up—a review, Lab on a Chip 5 (5) (2005) 492-500.
[254] A. Kiy, S. Dutt, C. Notthoff, M.E. Toimil-Molares, N. Kirby, P. Kluth, Highly Rectifying Conical Nanopores in Amorphous SiO2 Membranes for Nanofluidic Osmotic Power Generation and Electroosmotic Pumps, ACS Applied Nano Materials 6 (10) (2023) 8564-8573.
[255] L.-H. Yeh, Z.-Y. Huang, Y.-C. Liu, M.-J. Deng, T.-H. Chou, H.-C. Ou Yang, T. Ahamad, Saad M. Alshehri, K.C.W. Wu, A nanofluidic osmotic power generator demonstrated in polymer gel electrolytes with substantially enhanced performance, Journal of Materials Chemistry A 7 (47) (2019) 26791-26796.
[256] V. Amendola, L. Fabbrizzi, L. Mosca, Anion recognition by hydrogen bonding: urea-based receptors, Chemical Society Reviews 39 (10) (2010) 3889-3915.
[257] Y. Okamoto, Cationic Ring-Opening Polymerization of Epichlorohydrin in the Presence of Ethylene Glycol, in: Ring-Opening Polymerization, American Chemical Society, 1985, pp. 361-372.
[258] S. Wang, T. Li, C. Chen, W. Kong, S. Zhu, J. Dai, A.J. Diaz, E. Hitz, S.D. Solares, T. Li, L. Hu, Transparent, Anisotropic Biofilm with Aligned Bacterial Cellulose Nanofibers, Advanced Functional

Materials 28 (24) (2018).
[259] R. Pastor, J.I. Calvo, P. Prádanos, A. Hernández, Surface charges and zeta potentials on polyethersulphone heteroporous membranes, Journal of Membrane Science 137 (1) (1997) 109-119.
[260] S.X. Li, W. Guan, B. Weiner, M.A. Reed, Direct Observation of Charge Inversion in Divalent Nanofluidic Devices, Nano Letters 15 (8) (2015) 5046-5051.